universität wien

DISSERTATION / DOCTORAL THESIS

Titel der Dissertation / Title of the Doctoral Thesis

„The Role of Jahn-Teller Effects in Homogeneous Water Oxidation Catalysis“

verfasst von / submitted by

Ludwig Schwiedrzik, BSc MSc

angestrebter akademischer Grad / in partial fulfilment of the requirements for the degree of

Doktor der Naturwissenschaften (Dr. rer. nat.)

Wien, 2023 / Vienna, 2023

Studienkennzahl lt. Studienblatt / degree programme code as it appears on the student record sheet:	A 796 605 419
Dissertationsgebiet lt. Studienblatt / field of study as it appears on the student record sheet:	Chemie
Betreut von / Supervisor:	Univ.-Prof. Dr. Dr. h.c. Leticia González Herrero

I see, yes, if you play around with it there must be a way to make it work.

- G. Cárdenas

... e allora si capí che l'ora era venuta. Accendemmo fuochi nel bosco,
e nessuno dormí: passammo il resto della notte cantando e ballando,
raccontandoci a vicenda le avventure passate, e ricordando i compagni perduti:
poiché non è dato all'uomo di godere gioie incontaminate.

- P. Levi, La Tregua

Acknowledgements

The four years and a bit I have spent working on my PhD have been, for a variety of reasons, some of the most stressful of my life so far. While I know this is not a unique experience by any means, and certainly one shared by everyone who has written their thesis during the Covid pandemic, I am still not sure I would have made it to the end, were it not for the help and support I have received along the way from colleagues, friends and family, each of whom I would now like to take the time to thank accordingly.

First, I would like to thank Prof. Leticia González. It is because of her that I had the opportunity to work as a PhD researcher in the first place, an opportunity I might not have seized were it not for her encouragement. As my supervisor, she helped me through the difficulties of many firsts, such as my first poster presentation, the first conference I helped organize, and the first paper I wrote. And while we did not agree on all things, I learned to appreciate her unique perspective and value her insightful feedback. It is thanks to her that I learned what working as a researcher in theoretical chemistry really means, and it is this knowledge that has enabled me to take the next steps in my career with confidence.

Next, I would like to thank my good friend and colleague Gustavo Cárdenas. His research laid the foundations for much of my own, and the many discussions, scientific and otherwise, that we had even after his time in Vienna had come to a close are some of my most cherished memories from my time as a PhD student. I would further like to especially thank David Hernández-Castillo, Ricardo Meyrelles, Roman Ochsenreiter, Veronika Zeindlhofer, Ivan Trentin, Boris Maryasin, Sebastian Mai, and Carsten Streb for freely contributing their time and expertise throughout many discussions and one-on-one brainstorming sessions and thereby helping me immensely in developing my dissertation. I am also deeply indebted to Vera Brieskorn and Tina Rajkovic, both of whom I had the good fortune to supervise as they wrote their bachelor theses in the González group. The research they carried out formed the nucleus around which I was eventually able to build the two major publications that make up the bulk of this thesis, and I am immensely proud to have been able to co-author a paper with each of them.

Furthermore, I would like to express my gratitude to all the members of the González research group as well as everyone involved in CataLight for their acceptance, their support, and the many happy memories I got to share with them. I'd particularly like to thank Markus Oppel, Denis Hoxha, Simon Kropf, Monika

Schett, and Sophie Gröber for keeping our institute running through some tough times, during which particular strain was placed on all things infrastructure and administration.

I would also like to thank my CYSS co-organizers Mathias Micheel, Julian Hniopek, Elisabeth Hofmeister, Carolin Müller, Miftahussurur Hamidi Putra, Pascal Wintergerst, Jannik Brückmann, and Simon Clausing for being amazing colleagues and walking the rocky road of organizing two online conferences for junior researchers on a shoestring budget together. I immensely enjoyed running CYSS together for two years, and I'm very proud of everything we accomplished during that time. On a related note, I'd like to thank Vera Krewald, Leon Freitag, Maren Podewitz, Pedro Sánchez Murcia, and Moritz Heindl for helping me at crucial points during my PhD journey in deciding what direction I wanted to turn to next.

Finally, I would like to thank my parents, my family, and all my friends for their continued support throughout the time I have spent working on my dissertation. I would also like to thank everyone in the ASO, the Enchoir, and the Partisans for providing welcome distractions and refuges from the stress of academia whenever I needed them. And last but emphatically not least, I would like to express my deepest gratitude to my partner, Irene. Without her unceasing support, I would not be who I am today. I owe her a debt I well never be able to fully repay, and no words written in a dissertation can express my feelings for her, so I will end by simply saying: Thank you.

Vienna
June 27th, 2023

Abstract

Artificial photosynthesis is seen as a key technology for the transition from fossil to renewable energy sources, and its application to the production of green hydrogen is an area of ongoing research. While hydrogen can be synthesized from water through straightforward electrolytic water splitting, the substantial overpotential required to drive this process makes it economically infeasible due to the typically high cost of electrical power. Therefore, catalysts able to reduce the overpotential of the water splitting reaction are of interest both from an economic as well as an ecological point of view.

Water splitting is a redox reaction consisting of two half-reactions, water oxidation and hydrogen evolution. Of the two, water oxidation is considered to be the thermodynamically more challenging. In recent years, catalyst development efforts in the field of water oxidation have increasingly focused on polyoxometalate clusters. These molecular catalysts offer both high stability and reactivity; furthermore, they are able to act as models for complex biomolecular systems as well as solid metal oxide surface catalysts, allowing researchers to gain crucial insights into the workings of various types of catalytic systems.

The goal of this PhD thesis is to understand in the greatest possible mechanistic detail the catalytic cycle of $[Mn_4V_4O_{13}(OAc)_3]^{3-}$, a promising bioinspired polyoxometalate catalyst, in order to better comprehend what drives its high reactivity and generate design ideas for improved catalysts. To this end, I have carried out theoretical simulations of this catalyst covering its large variety of oxidation states and ligand configurations using density functional theory. Together with crucial experimental work carried out by research collaborators at Ulm University as well as complementary calculations carried out by my colleagues here in Vienna, these simulations have allowed me to propose for the first time a complete model of the catalytic cycle of $[Mn_4V_4O_{13}(OAc)_3]^{3-}$, including key elements such as O-O bond formation, catalyst regeneration, and possible degradation pathways. I have further found that Jahn-Teller effects play a central role in determining the reactivity and stability of $[Mn_4V_4O_{13}(OAc)_3]^{3-}$, suggesting their intentional inclusion in the design of future catalysts could lead to further improvements in performance.

Zusammenfassung

Künstliche Photosynthese gilt als Schlüsseltechnologie für den Umstieg von fossilen auf erneuerbare Energiequellen, und ihre Anwendung auf die Synthese von grünem Wasserstoff wird laufend erforscht. Zwar kann Wasserstoff mittels direkter elektrolytischer Wasserspaltung aus Wasser synthetisiert werden, doch benötigt dieser Prozess eine erhebliche Überspannung, die ihn aufgrund hoher Strompreise in den meisten Fällen unwirtschaftlich macht. Aus diesem Grunde sind Katalysatoren, die die Überspannung der Wasserspaltungsreaktion verringen können, sowohl von ökonomischem als auch von ökologischem Interesse.

Die Wasserspaltung ist eine Redoxreaktion, die aus zwei Halbreaktionen besteht: Wasseroxidation und Wasserstoffevolution. Von den beiden Halbreaktionen gilt die Wasseroxidation als thermodynamisch anspruchsvoller. In den letzten Jahren haben sich Bemühungen zur Entwicklung von Wasserspaltungskatalysatoren zunehmend auf Polyoxometalatcluster konzentriert. Diese molekularen Katalysatoren zeichen sich durch hohe Stabilität und Reaktivität aus. Des Weiteren dienen Polyoxometalate als Modellsysteme für biomolekulare wie auch Metalloxid-Feststoffkatalysatoren, mit deren Hilfe Erkentnisse zu verschiedensten Arten von Katalysatoren gewonnen werden können.

Das Ziel meiner Dissertation ist, den Katalysezyklus von $[Mn_4V_4O_{13}(OAc)_3]^{3-}$, einem vielversprechenden Polyoxometalatkatalysator, in größtmöglichem mechanistischem Detail zu verstehen, um nachvollziehen zu können, woraus sich die hohe Reaktivität dieses Katalysators speist, und so neue Motive für den Entwurf verbesserter Katalysatoren zu schaffen. Zu diesem Zwecke habe ich mithilfe der Dichtefunktionaltheorie theoretische Simulationen dieses Katalysators durchgeführt, die die gesamte Bandbreite seiner Oxidationszustände und Ligandenkonfigurationen abbilden. Gemeinsam mit experimentellen Arbeiten, die von Kooperationspartner:innen an der Universität Ulm ausgeführt wurden, sowie komplementären Rechnungen meiner Kolleg:innen hier in Wien haben diese Simulationen es mir erlaubt, erstmals ein vollständiges Modell des Katalysezyklus von $[Mn_4V_4O_{13}(OAc)_3]^{3-}$ vorzuschlagen - inklusive wichtiger Details wie der Bildung der O-O Brückenbindung, der Regeneration des Katalysators sowie möglicher Zerfallsmechanismen. Des Weiteren habe ich entdeckt, dass Jahn-Teller-Effekte eine zentrale Rolle für Reaktivität und Stabilität dieses Katalysators spielen. Das wiederum legt nahe, dass die bewusste Einbindung solcher Effekte beim Entwurf neuer Katalysatoren sich positiv auf deren Leistungspotential auswirken könnte.

Contents

Acknowledgements **5**

Abstract **7**

List of Abbreviations **10**

List of Figures **13**

1 Introduction **17**
1.1 Water Splitting 17
1.2 Water Oxidation Catalysis 18
1.3 A Biomimetic Polyoxometalate Catalyst 19
1.4 Thesis Goals and Structure 22

2 Methods **23**
2.1 The Thermodynamics of Water Oxidation 23
2.1.1 Practical Accuracy 25
2.1.2 Solvent Effects 26
2.1.3 Energy Corrections 26
2.2 Catalyst Structures 27
2.2.1 Nomenclature 27
2.2.2 Structural Sampling 29
2.3 Exploring Catalysis: the *ab initio* Nanoreactor 32

3 Results and Discussion **35**
3.1 Catalyst Activation 35
3.2 Water Oxidation 39
3.3 Regeneration and Degradation 42

4 Conclusion **47**

A Paper Reprints **51**
A.1 Activation by oxidation and ligand exchange in a molecular manganese vanadium oxide water oxidation catalyst 53
A.2 Flexibility Enhances Reactivity: Redox Isomerism and Jahn-Teller Effects in a Bioinspired Mn4O4 Cubane Water Oxidation Catalyst . 73

A.3 Regeneration and Degradation in a Biomimetic Polyoxometalate Water Oxidation Catalyst 93

Bibliography **127**

List of Abbreviations

OEC	Oxygen Evolving Complex
POM	Polyoxometalate
Mn4V4	$[Mn_4V_4O_{13}(OAc)_3]^{3-}$
JT	Jahn-Teller
XRD	X-Ray Diffraction
WNA	Water Nucleophilic Attack
DC	Direct Coupling
DFT	Density Functional Theory
ACN	Acetonitrile
NEB	Nudged Elastic Band
PCET	Proton-Coupled Electron Transfer
ET	Electron Transfer

List of Figures

1.1 The structure of the $[Mn_4V_4O_{13}(OAc)_3]^{3-}$ catalyst as synthesized, illustrated as a ball-and-stick model with color legend and as a ChemDraw structure. 20

1.2 All bonds of an Mn^{4+} atom in octahedral coordination are of equal length due to the degeneracy of the metal center's d orbitals. The addition of a single electron (i.e. reduction to Mn^{3+}) leads to further splitting of the d orbitals, resulting in a more stable configuration overall. However, this orbital splitting also causes bonds along one bond axis to be lengthened, making them weaker; the other bonds, meanwhile, are slightly shortened and therefore stronger. This form of structural distortion is termed the Jahn-Teller effect. 21

2.1 The thermodynamic limit of water oxidation overcome by the ideal catalyst and two proposed pathways of a real catalyst. While the ideal catalyst overcomes the thermodynamic limit in four steps of equal potential, the real catalyst pathways both deviate significantly from this behavior: In both, the largest and therefore potential-determining step is from 1 to 2a or 2b, respectively. As 2b is more stable than 2a, the pathway featuring 2b results in a lower thermodynamic overpotential. 24

2.2 a) Full ChemDraw structure of the Mn4V4 precatalyst. b) Abbreviated ChemDraw structure of the precatalyst with Mn centers labeled A-D and O atoms labeled 1-6. The accompanying text box contains a descriptor representing the oxidation state of the cubane core, $Mn_2^{3+}Mn_2^{4+}$, and the ligand configuration, a bidentate acetate ligand. c) Abbreviated ChemDraw structures and descriptors representing three ligand configurations, with ligands colored blue. d) Abbreviated ChemDraw structures and descriptors representing three specific JT isomers. Mn^{3+} centers and their JT axes are colored red and represented in the descriptor by letter codes corresponding to the JT axis orientation. 28

2.3 Catalyst structural sampling workflow: From a single starting geometry without JT distortions, six distinct unrelaxed sampling target structures are obtained through constrained preoptimizations; unconstrained optimizations of these six structures converge to a single stable minimum; desired properties of the final optimized structure such as ΔG_{TZ} are obtained through further single point and frequency calculations. 31

3.1 Reduction potentials of experimentally observed redox processes P1-P5 and theoretically computed reduction potentials corresponding to P1, P2, and P4, respectively versus water content in percentage of solvent volume. 36
3.2 Investigated oxidation (Ox) and ligand exchange (LEx) processes as well as intermediate structures involved in these processes. Structural changes resulting from each reaction step are highlighted in orange. Two possible sequences of reaction steps were investigated: Ox-Ox-LEx and Ox-LEx-Ox. 37
3.3 Overlapping ligand exchange pathways Ia and Ib with structures of intermediates and transition states. In each structure, the location of the Mn^{3+} center and the orientation of its main JT axis are highlighted in red. 38
3.4 Four possible pathways for water oxidation, with PCET steps marked by blue arrows and ET steps marked by green arrows. Intermediates are labeled **1**-**6**, and their relative energy is given in eV. In each intermediate structure, Mn^{4+} centers are highlighted in magenta, while Mn^{3+} and their main JT axes are highlighted in red. 40
3.5 Detailed reaction diagram for the iWNA-type O-O bond formation reaction observed in Mn4V4. Note the transfer of an electron from the OH ligand to the Mn^{4+} center binding it, an example of intramolecular oxidation yielding Mn^{3+}. The reactant structure corresponds to a deprotonated **2b**, while the product is **2a** (see figure 3.4). In each intermediate and transition state structure, the Mn^{3+} centers and their main JT axes are highlighted in red; meanwhile, the attacking OH ligand is highlighted in blue. 41

3.6 The investigated network of intermediates, with each row corresponding to one redox state of the cubane core and each column to one ligand configuration (for reference, see figure 2.2). For each type of intermediate, the most stable isomer obtained from sampling is represented by a text box containing its JT configuration, relative energy, and Boltzmann population at 298.15 K. The initial reactant and final product structures of regeneration are highlighted in gold; intermediates with populations greater than 5% are in white, while unpopulated intermediates are shaded in grey. Formal oxidation steps are represented by black arrows, while formal ligand exchange steps are represented by blue arrows. 44

3.7 NEB simulations of two degradation processes, with initial and final structures as well as energy profiles. On the left (NEB 3), cubane opening and protonation of O4 by the neighboring ligand can be observed. On the right (NEB 4), an H_2O ligand is dissociated from its Mn center, remaining loosely bound to the complex via H-bond. Mn^{3+} centers and their main JT axes are highlighted in red, while ligands at the active face of the catalyst are highlighted in blue. 45

4.1 The full proposed catalytic cycle of Mn4V4, consisting of activation of the precatalyst, water oxidation, and catalyst regeneration. The Mn4V4 catalyst is represented as an abbreviated ChemDraw structure; for reference, the full ChemDraw structure of the precatalyst **3344-OAc** is shown in the top left insert. 48

Chapter 1

Introduction

Many of the greatest problems facing humanity today are directly or indirectly caused by our overreliance on fossil fuels. [1] Being our primary energy carrier, fluctuations in their price and availability, whether for political or economic reasons, can result in dramatic upheaval in affected communities. [2] At the same time, climate change caused by the release of anthropogenic CO_2 into the atmosphere is continuously threatening the homes and lives of millions through flooding, heat waves, and other forms of extreme weather. [3] In an effort to curtail CO_2 output, great leaps have been made in switching to renewable energy sources for electricity generation, such as wind and solar power, in recent years. [3] While this approach is effective in targeting the greatest producer of anthropogenic CO_2, the energy sector, [4] it is somewhat limiting in that renewable energies can only be effectively utilized wherever the electricity grid reaches, either through direct cable connection or by portable batteries. Renewables are also famously dependent on circumstances outside of the human sphere of influence, such as weather and the time of day, which can result in fluctuations in the availability of electricity generation capacity. Thus, to enable the storage as well as ease transportation and distribution of renewable energy, a chemical energy carrier is required. [5, 6]

1.1 Water Splitting

Hydrogen is a prime candidate for the role of a sustainable chemical energy carrier. [6] It can be produced through electrolysis of water, which is far more widely available than fossil fuels. Burning hydrogen produces water vapor, whereas alternatives such as methane gas or organic alcohols produce CO_2. Unfortunately, the electrolysis of water is an extremely energy-intensive process that requires huge quantities of electricity. [6] Much research has therefore been devoted to reducing the energetic cost of hydrogen production through the use of catalysts. [7] These come in a variety of flavors and overlapping categories: electrocatalysts are intended to improve the efficiency of electrolysis itself, while photocatalysts attempt to emulate the natural process of photosynthesis, using sunlight to produce H_2 directly. [7, 8] Heterogeneous catalysts such as IrO_2 [9] are solid mate-

rials that catalyze water splitting at their surface, generally thought to be most useful for industrial-scale applications. Meanwhile, homogeneous catalysts such as the so-called *blue dimer*, $[(bpy)_2Ru(H_2O)(\mu\text{-}O)(H_2O)Ru(bpy)_2]^{4+}$, [10, 11, 12] are molecular systems that are dissolved in the catalytic solution they act upon. These are generally viewed as development models for laboratory-scale research, although recent years have seen increasing efforts to utilize molecular catalysts at larger scale by binding them to various surfaces (e.g. functionalized polymers), combining their high tunability and activity with the stability and scalability of heterogeneous catalysts. [7, 13, 14]

Formally, the water splitting reaction that forms the basis of hydrogen production is a redox reaction

$$2\,H_2O \longrightarrow O_2 + 2\,H_2 \tag{1.1}$$

that consists of two half reactions

$$2\,H_2O \longrightarrow O_2 + 4\,H^+ + 4\,e^- \tag{1.2}$$

$$4\,H^+ + 4\,e^- \longrightarrow 2\,H_2 \tag{1.3}$$

termed water oxidation and hydrogen evolution, respectively. Of the two, the water oxidation reaction is considered the thermodynamically more challenging one, as it consists of four sequential single-electron oxidations. [7] In nature, water oxidation is carried out as part of the photosynthetic cycle by the oxygen-evolving complex (OEC), the active center of the protein Photosystem II. [8] While the exact mechanism of water oxidation at the OEC is still being debated, it has been established that the Mn centers attain the oxidation states Mn^{3+} and Mn^{4+} during the reaction. [15, 16, 17, 18] Especially in the field of photocatalytic water splitting, the highly efficient OEC has inspired many attempts to develop similar synthetic water oxidation catalysts.

1.2 Water Oxidation Catalysis

The OEC has an Mn_3CaO_4 cubane core, with a fourth Mn center dangling off to the side. [19] However, as the exact structure of the OEC was not fully uncovered until 2015 [19], the type of biomimetic design mentioned above has only been developed during recent years. Early synthetic water oxidation catalysts such as the aforementioned *blue dimer* utilized just one or two active metal centers. These metal centers had to undergo multiple oxidation state changes and attain high, often unstable oxidation states in order to catalyze the four single-electron oxidations that comprise water oxidation. This has in turn generated much research interest in multicenter catalysts with four active metal centers, each of which would have to undergo just a single oxidation state change during water oxidation catalysis. In particular, catalysts with M_4O_4 cubane cores (similar but not identical in

structure to the OEC) have been shown to be able to flexibly redistribute electrons between metal centers, thereby fulfilling this design goal. [20, 21, 22] Co_4O_4 and Mn_4O_4 catalysts especially have been intensively studied, with a variety of reaction mechanisms being proposed. [23, 24, 25, 26, 27, 28, 29, 30, 31, 32, 33, 34]

Furthermore, many homogeneous water oxidation catalysts are plagued by low stability under oxidative conditions. This issue can be addressed in a number of ways, such as binding them permanently to a solid electrode surface. [13] However, this can lead to loss of activity in some catalysts, and generally makes these systems harder to investigate in detail. In recent years, water oxidation catalysts with polyoxometalate (POM) ligands have been investigated by several groups. [35, 36, 37, 38, 39, 40, 41, 42, 43, 28, 44, 45] The large, stable POM ligands can serve to stabilize otherwise-volatile molecular catalysts; furthermore, catalysts incorporating such ligands can be seen as model systems for heterogeneous catalysts, making it easier to study their reaction mechanisms in detail.

As is exemplified above, issues that were identified with early water oxidation catalysts have led to the development of a core set of design criteria for water oxidation catalysts: [7, 46]

1. Most fundamentally, they must be capable of catalyzing the water oxidation reaction from a structural point of view, having at least one (and preferably four) active metal center(s) able to bind an H_2O molecule, which can then react to form O_2.

2. They should catalyze water oxidation at the lowest possible overpotential by appropriately stabilizing intermediates and transition states along the reaction pathway. [7, 47, 48]

3. They must demonstrate sufficient stability under oxidative conditions to catalyze a high number of turnovers. [7, 49]

4. They should contain only earth-abundant elements; particularly for the catalytically active metal centers, this can be a challenge. [49]

5. The activity of any synthetic catalyst is measured against that of the OEC; the ultimate goal of catalyst design is to attain or even surpass that high threshold. [24, 29]

1.3 A Biomimetic Polyoxometalate Catalyst

One catalyst that apparently fulfills most of (if not all) the design criteria listed above is $[Mn_4V_4O_{13}(OAc)_3]^{3-}$ (abbreviated herein as Mn4V4, see figure 1.1). Combining an Mn_4O_4 cubane core with a multidentate POM ligand, Mn4V4 boasts high activity and stability (turnover frequency greater than 200 min^{-1}, turnover number greater than 12000). [51, 52] Due to its structure that incorporates biological as well as inorganic design elements, it is a useful model system

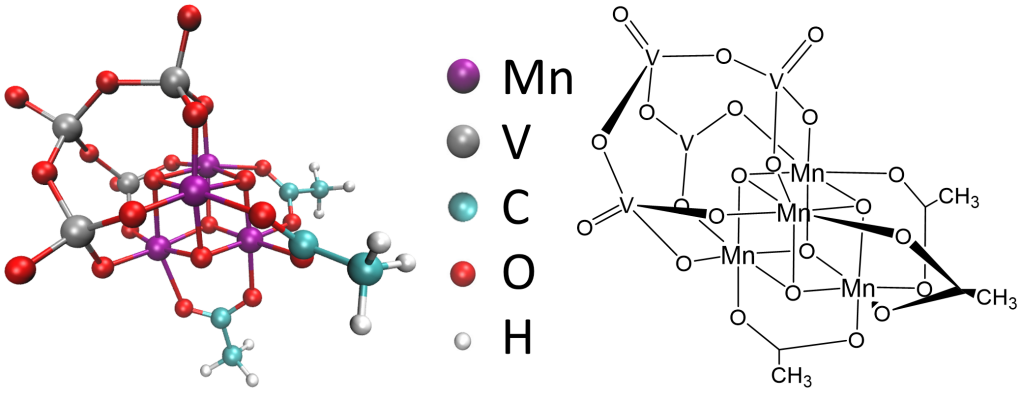

Figure 1.1: The structure of the $[Mn_4V_4O_{13}(OAc)_3]^{3-}$ catalyst as synthesized, illustrated as a ball-and-stick model with color legend (left) and as a ChemDraw structure (right). Adapted from [50].

both for studying the OEC as well as industrially relevant heterogeneous Mn oxide catalysts, in addition to being a promising homogeneous catalyst in its own right. Though the activity and stability of Mn4V4 have been verified in experiment, purely experimental approaches are limited in the level of mechanistic insight that can be obtained through their use - not just in Mn4V4, but in catalysis in general. In particular, studying short-lived and transient species that are intermittently formed as part of the catalytic cycle is extremely challenging. To isolate such species requires advanced experimental techniques (e.g. spectroelectrochemistry [53]) that allow the user to essentially halt the catalytic reaction and probe it in discrete steps. Here, theoretical approaches such as the ones utilized in this work can offer new perspectives through their ability to model the elemental steps that make up a catalytic cycle.

A first attempt to leverage theoretical methods in the study of Mn4V4 was our combined study of precatalyst activation, which is described in section 3.1. In the course of this investigation, it became clear that Jahn-Teller (JT) effects play an important role in influencing the reactivity of Mn4V4. JT effects are present in d^4 metal ions such as Mn^{3+} and result from a favorable splitting of the d-orbitals (see figure 1.2). In an octahedral coordination environment, this leads to one bond axis being weakened, with the bonds along that axis being longer than usual, while the other two bond axes are strengthened, with correspondingly shorter bonds. If the bonds along two bond axes bind different ligands, two non-symmetry equivalent isomers result from the two possible orientations of the main JT-distorted axis; these are termed JT isomers. [54]

In Mn4V4 as in other tetramanganese catalysts such as the OEC, the presence of up to four Mn^{3+} centers as well as the variability of the ligand configuration can result in a large number of JT isomers, adding to the complexity of structure elucidation in those systems. [56, 57, 58, 59, 60, 61, 62, 63] Furthermore, the aforementioned flexibility of cubane catalysts with regard to the localization of elec-

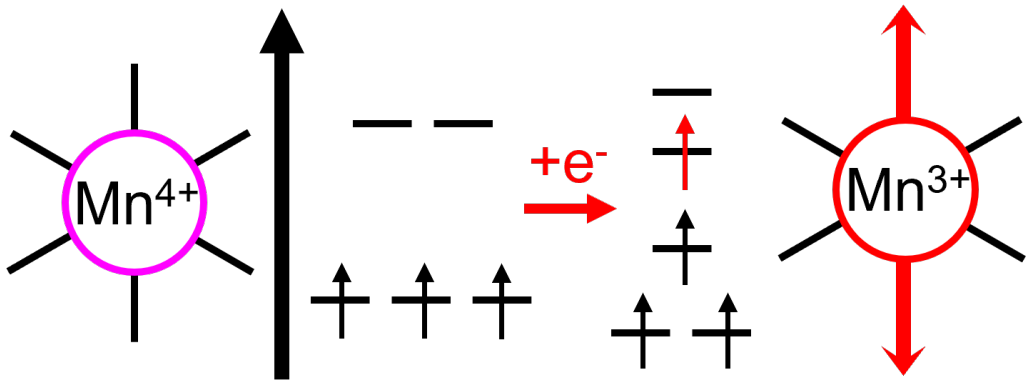

Figure 1.2: All bonds of an Mn^{4+} atom in octahedral coordination are of equal length due to the degeneracy of the metal center's d orbitals (left). The addition of a single electron (i.e. reduction to Mn^{3+}) leads to further splitting of the d orbitals (right), resulting in a more stable configuration overall. However, this orbital splitting also causes bonds along one bond axis (marked in red) to be lengthened, making them weaker; the other bonds, meanwhile, are slightly shortened and therefore stronger. This form of structural distortion is termed the Jahn-Teller effect. Adapted from [55].

trons between the four metal centers also results in so-called redox isomerism at mixed oxidation states. Redox isomers are structures that differ in their formal assignment of oxidation states to the individual, non-symmetry equivalent Mn centers. Extensive computational sampling of redox and JT isomers and comparison to X-ray diffraction (XRD) experiments had already been leveraged by Krewald et al. to gain insight into the structure of the OEC across its multiple oxidation states. [64] Furthermore, JT effects have been previously identified as playing a crucial role in facilitating the water oxidation activity of certain Mn-oxo polymorphs; only those with Mn^{3+} centers at their surface were shown to be active catalysts, which was explained by Robinson et al. as being due to the presence of JT effects at these active surfaces.[65, 66, 67] Finally, Drosou et al. showed in 2021 that populating one of two distinct JT isomers of the OEC at one oxidation state can lead to two different oxidation products, which are themselves redox isomers. [68]

Against this background of increased interest in JT effects in Mn-containing water oxidation catalysts, closer scrutiny of JT effects in Mn4V4 was to be required in order to fully understand its catalytic cycle. Spurred on by the success of the brute-force sampling approach used in our initial investigation of catalyst activation, Mai et al. carried out two studies [53, 69] in which they attempted to sample a large number of isomers of Mn4V4. In the course of that work, they were able to identify a correlation between catalyst oxidation state and infrared peak shifts that could be reproduced in experiment; rationalize a previously un-

explained interatomic interaction that had been observed in the XRD structure of Mn4V4; and (most crucially for my own work) develop an effective workflow for sampling catalyst isomers. Finally, Mai et al. proposed heuristic rules for the relative stability of Mn4V4 isomers, which I was able to leverage to increase sampling efficiency in my study of catalyst regeneration. [69]

My own work focused on the catalytic cycle of Mn4V4. In the absence of experimental evidence, again a large number of structures bearing different ligand configurations needed to be sampled. Two different types of cycles were considered based on known mechanisms from literature, differentiated by how O-O bond formation is achieved: In water nucleophilic attack (WNA), an H_2O or OH attacks a terminal oxo or oxyl group bound to a catalyst metal center. [70, 71, 23] Herein, the attacking molecule can come from the solvent, or alternatively the attack can be carried out intramolecularly by a ligand already bound to the catalyst. By contrast, in direct coupling (DC), two terminal oxo or oxyl groups react with one another directly to form a peroxo bridge. [26, 71, 23] This can be achieved by such ligands if they are bound to two neighboring metal centers, such as those found on each face of a cubane catalyst, or it can occur where two catalyst molecules react with one another to form a dimer. Many sub-variations of these two general types of mechanisms have been described, [71, 23] and both have been proposed as feasible water oxidation mechanisms for the OEC, [15, 16, 17, 18] though the DC mechanism is now generally preferred.

1.4 Thesis Goals and Structure

My research focused on developing a feasible model of the catalytic cycle of Mn4V4, starting with the initial steps of a WNA-type mechanism. [55] With this work complete, I turned to the regeneration half of the WNA cycle, while also investigating catalyst degradation and regeneration in an alternative DC-type cycle. [50]. Overall, the goal of this thesis project is to gain mechanistic insight into the reactivity and stability of Mn4V4 using theoretical methods in order to enable the rational design of improved catalysts.

In the following, I will discuss some of the methodological aspects of this work and how my approach to studying Mn4V4 evolved over the course of my investigation. I will then shortly summarize my most important results, starting with catalyst activation, then moving on to WNA-style water oxidation, and ending with regeneration and degradation. The papers corresponding to these three studies, which go into much greater detail, are reprinted in appendix A. Finally, I will attempt to draw overall conclusions from what I have learned throughout the course of my research, focusing on the multiple roles played by JT effects in determining reactivity and stability in homogeneous water oxidation catalysis.

Chapter 2

Methods

Throughout the course of my research project, I had the opportunity to use a variety of theoretical methods, some of which had to be adapted in some ways in order to study water oxidation catalysis. In the following, I want to give a brief overview of how the methods and approaches I utilized evolved over the course of the project. First, it is necessary to briefly discuss the thermodynamics of water oxidation, both in a general sense and in how they pertain to certain aspects of the calculations carried out herein: the practical accuracy of theoretical mechanistic proposals, how solvent effects were accounted for, and what energy corrections were applied to ensure comparability between diverse reaction pathways. The following section will give a brief overview of the most important points; for a more detailed discussion, the reader is directed to the excellent reviews of Dau et al. and Betley et al. referenced herein. [7, 46] Second, I will discuss how the large variety of catalyst structures studied throughout this thesis was handled. A particular nomenclature of ligand configurations and JT and redox isomers of Mn4V4 was adopted early on and continuously refined as more and more structures came under investigation. This nomenclature is shortly presented here and used consistently throughout the present thesis, with the exception of the first two papers [54, 55], which utilized earlier iterations of the same system. I will also describe how the structural sampling-based approach to studying catalysis I utilized to develop the proposed catalytic cycle came about and why I chose it over other methods. Finally, one other method for studying reactions in an exploratory manner that I tested during the course of my research, the *ab initio* nanoreactor, is described and compared to the more traditional approach preferred herein.

2.1 The Thermodynamics of Water Oxidation

The water oxidation reaction consists of four sequential single-electron oxidations. An ideal catalyst would stabilize the intermediates of these four reactions such that they are equidistant in energy; thus, the potential required to reach each intermediate step would be identical, and the potential required to drive the over-

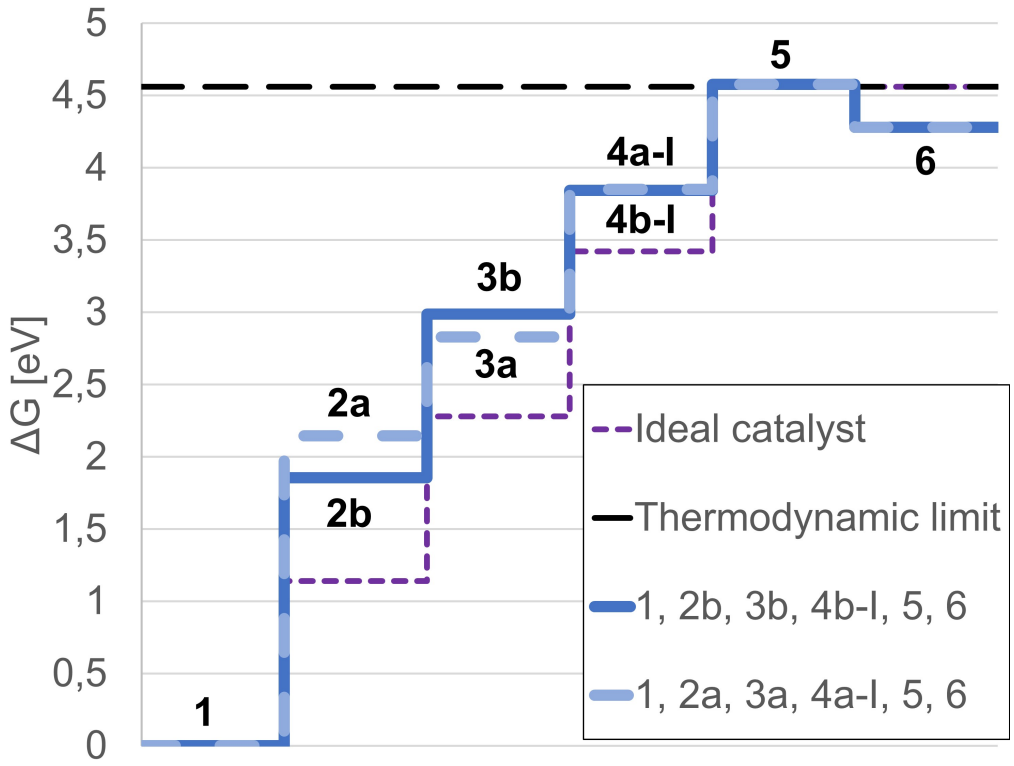

Figure 2.1: The thermodynamic limit of water oxidation (black, dashed) overcome by the ideal catalyst (purple, dashed) and two proposed pathways of a real catalyst (blue, dashed and solid). While the ideal catalyst overcomes the thermodynamic limit in four steps of equal potential, the real catalyst pathways both deviate significantly from this behavior: In both, the largest and therefore potential-determining step is from 1 to 2a or 2b, respectively. As 2b is more stable than 2a, the pathway featuring 2b (solid blue line) results in a lower thermodynamic overpotential. Adapted from [55].

all reaction would be minimal. [7] Given that the reaction free energy of the overall reaction is 4.56 eV when computed using B3LYP [42] (4.92 eV in experiment), this value is effectively the thermodynamic limit of water oxidation, as no catalyst can achieve the reaction at a lower reaction free energy. Rather, theoretical proposals of water oxidation catalytic cycles must have an overall reaction energy greater than this limit in order to demonstrate they are at least thermodynamically feasible. [41] An ideal catalyst would therefore overcome this limit in four equal steps of 1.14 eV each, and any overpotential required beyond that would be entirely kinetic in origin. Real catalysts cannot achieve such an ideal stabilization of reaction intermediates due to inherent scaling relationships that exist between these intermediates, [7] resulting in one of the four reaction steps being associated with the largest potential, thus being termed the potential-determining step (see figure 2.1). [7] The difference between the potential-determining step of the real catalyst $\Delta G^{\max}_{\text{real}}$ and the fixed step size of the ideal catalyst ΔG_{ideal} is termed

the thermodynamic overpotential of water oxidation,

$$\eta = \Delta G^{\max}_{\text{real}} - \Delta G_{\text{ideal}}, \tag{2.1}$$

and minimizing this thermodynamic overpotential is considered an important target in catalyst design. [47]

2.1.1 Practical Accuracy

Early in the course of the present thesis project, a number of reduction potentials ΔE^0_{red} were computed [54] according to

$$\Delta E^0_{\text{red}} = -\frac{\Delta G^0_{\text{red}}}{nF} - E^{\text{abs}}_{\text{elec}}, \tag{2.2}$$

wherein ΔG^0_{red} is the reaction free energy of the reduction reaction, n is the number of electrons transferred ($n = 1$ for single-electron reactions), F is Faraday's constant, and $E^{\text{abs}}_{\text{elec}}$ is the absolute reduction potential of the electrode in use. In order to obtain the greatest possible accuracy when comparing theoretically computed and experimentally measured potentials, several different density functional theory (DFT) functionals were tested, with B3LYP [72, 73] producing the results closest to the experimental values. It is for this reason that B3LYP was used throughout all mechanistic calculations. Furthermore, in these initial reduction potential calculations, the broken symmetry formalism was employed to determine the spin ground state of each investigated structure and thereby obtain yet more accurate energies. Similar to what has been previously noted in literature, [74] the energy difference between the most stable broken symmetry and high spin solutions was found to be less than 0.1 eV in all investigated configurations of the Mn4V4 catalyst. The broken symmetry formalism was therefore not used in any of the theoretical mechanistic calculations, as such small energy differences would not significantly affect the conclusions of these studies and would greatly increase computational costs due to the number of spin configurations that would need to be sampled for each catalyst structure of interest.

Conversely, while double-ζ basis sets such as def2-SVP [75] are considered sufficient to obtain optimized catalyst geometries and thermal corrections, it was found that the energy ordering of JT and redox isomers is not consistent between using double-ζ- and triple-ζ-derived electronic energies. [55] Triple-ζ-derived electronic energies were used throughout to ensure maximum practical accuracy. Thus, the absolute Gibbs free energy of a given structure i is defined as

$$\Delta G_{\text{TZ}}(i) = \Delta E_{\text{TZ}}(i) + \Delta H(i) - T\Delta S(i), \tag{2.3}$$

wherein $\Delta E_{\text{TZ}}(i)$ is the electronic energy of species i computed using a triple-ζ basis set, $\Delta H(i)$ is the thermal correction of the enthalpy derived from frequency calculations carried out using a double-ζ basis set, $T = 298.15$ K, and $\Delta S(i)$ is

the thermal correction to the entropy, also derived from frequency calculations carried out using a double-ζ basis set.

2.1.2 Solvent Effects

As the stability and activity of the Mn4V4 catalyst depends strongly on the composition of the reaction mixture, it was necessary to account for solvent effects in the simulations. Due to the extremely high computational costs associated with explicit solvation and the large number of structures that needed to be investigated, it was decided to instead employ implicit solvation, specifically the conductor-like polarized continuum model. [76] To account for the varying solvent compositions used in experiments particularly during the study of catalyst activation, the solvent model parameters of acetonitrile (ACN), which in all cases comprises the largest proportion of the solvent mixture, were combined with custom dielectric constant values computed as

$$\varepsilon_{\text{mix}} = \varphi(\text{H}_2\text{O})\varepsilon(\text{H}_2\text{O}) + \varphi(\text{ACN})\varepsilon(\text{ACN}), \tag{2.4}$$

wherein $\varphi(i)$ is the volumetric fraction of solvent i and $\varepsilon(i)$ is the dielectric constant of pure solvent i.

2.1.3 Energy Corrections

Energetic comparison between catalyst structures of varying ligand configurations necessitated the calculation of the absolute energies of H_2O and O_2, carried out at the same level of theory as the catalyst structures themselves. Furthermore, free energies for reactions that include proton transfers to solution had to be corrected for the energy of the abstracted H^+. As the energy of H^+ cannot be computed in the same way as that of an H_2O ligand, the formalism used by Van Voorhis et al., [70] a derivation of the so-called Nørskov method, was employed. [47] Therein, the energy value assigned to one abstracted H^+ is the standard free energy of a proton in solution. To account for the non-uniform solvent composition of the catalytic solution, the correction to the Gibbs energy for one abstracted H^+ in the solvent mixture was defined as the weighted average of the standard free energy of a proton in ACN and H_2O,

$$\Delta G^{\text{H}^+}_{\text{corr}} = \varphi(\text{H}_2\text{O})\Delta G^{H^+}_{\text{solv}}(\text{H}_2\text{O}) + \varphi(\text{ACN})\Delta G^{H^+}_{\text{solv}}(\text{ACN}), \tag{2.5}$$

giving a value of $\Delta G^{H^+}_{\text{corr}} = 11.1090$ eV for a single proton. [77] Thus, the Gibbs free energy of a given structure i relative to a reference structure j was computed as

$$\Delta G_{\text{TZ, rel}}(i) = (\Delta G_{\text{TZ}}(i) - n_{\text{L}}\Delta G_{\text{L}} - n_{\text{H}^+}\Delta G^{\text{H}^+}_{\text{corr}}) - \Delta G_{\text{TZ}}(j), \tag{2.6}$$

wherein $\Delta G_{\text{TZ}}(i)$ is the absolute Gibbs free energy of structure i (see equation 2.3), n_{L} is the number of ligands L present in species i but not species j,

ΔG_{L} is the absolute Gibbs free energy of ligand L, $n_{\mathrm{H^+}}$ is the number of protons transferred to solution to form species i from species j, $\Delta G^{\mathrm{H^+}}_{\mathrm{corr}}$ is the correction to the Gibbs energy for one abstracted $\mathrm{H^+}$ (see equation 2.5), and $\Delta G_{\mathrm{TZ}}(j)$ is the absolute Gibbs free energy of reference structure j.

2.2 Catalyst Structures

The Mn4V4 catalyst is synthesized in a precatalytic form (see figure 2.2a) consisting of an $\mathrm{Mn_4O_4}$ cubane core that is surrounded on three sides by a hexadentate $\mathrm{V_4O_{13}}$ ligand and one acetate ligand each on the remaining sides. [51] The reactive Mn centers achieve two oxidation states throughout the catalytic cycle: $\mathrm{Mn^{3+}}$ and $\mathrm{Mn^{4+}}$. On one face of the cubane core, an acetate ligand is replaced during catalyst activation by an $\mathrm{H_2O}$ and an OH ligand. [54] This lowers the symmetry of the idealized catalyst from C_{3v} to C_s. To differentiate between the various oxidation states, ligand configurations, and isomers of the catalyst, I developed a system of nomenclature throughout the course of the present thesis project, resulting in the following form: [50]

2.2.1 Nomenclature

The most important atoms to participate in catalytic reactions are labeled as follows (see figure 2.2b):

- MnA is the apical Mn atom that in the precatalyst faces away from the vanadate ligand, binding to all three acetate ligands.
- MnB is its cofacial neighbor on the active face of the catalyst, binding an OH ligand in the activated species.
- MnC and MnD are (ideally) symmetry-equivalent Mn centers on the cubane face opposite from the active face.
- The cubane O atoms are labeled O1 through O4, with O1 being the apical O atom diagonally opposite MnA and closest to the bulk of the vanadate ligand, and each O atom in turn being diagonally opposite its corresponding Mn center: O2 to MnB, O3 to MnC, and O4 to MnD.
- O5 is the O atom of ligands binding to MnB on the active face of the catalyst, and O6 is the O atom of ligands binding to MnA on the active face of the catalyst.

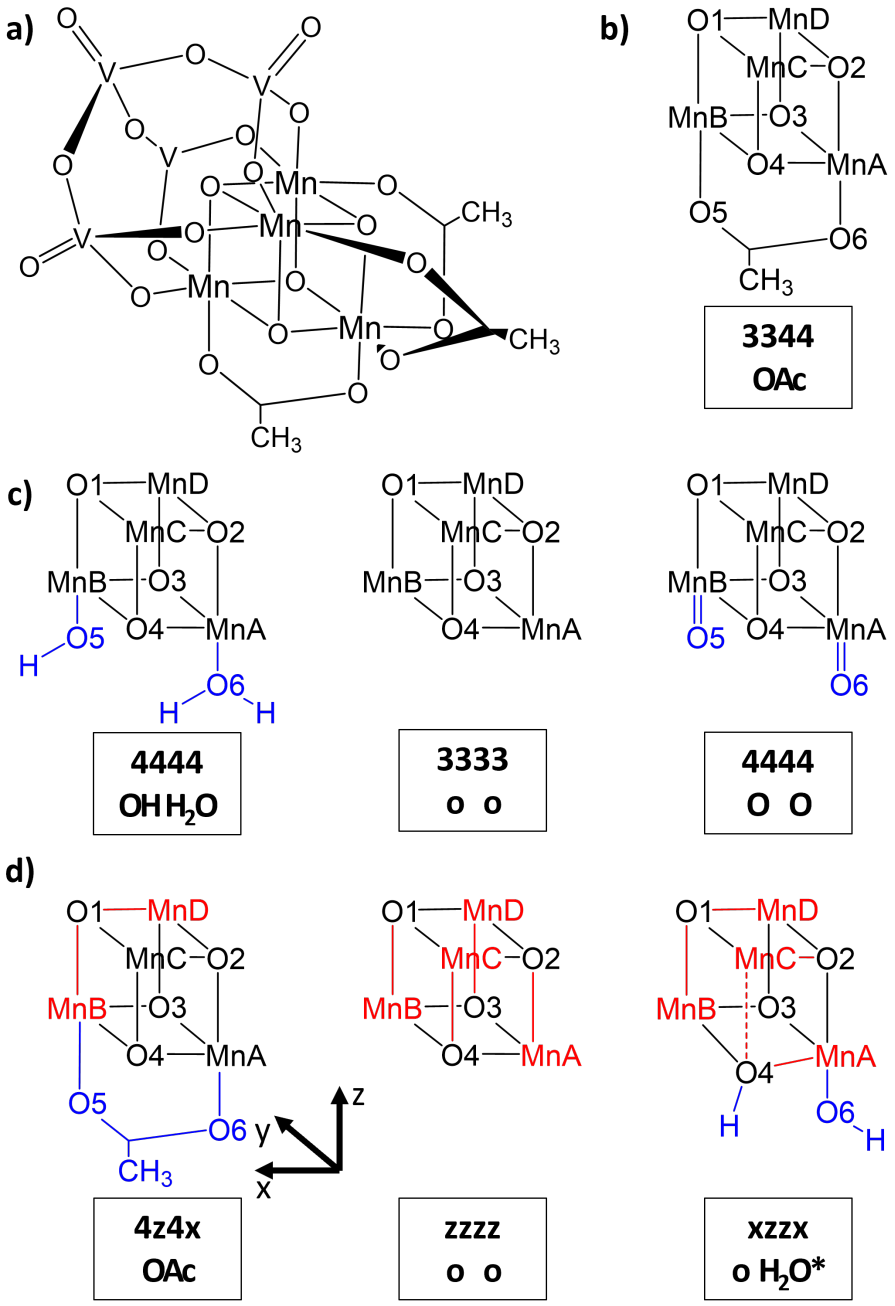

Figure 2.2: a) Full ChemDraw structure of the Mn4V4 precatalyst. b) Abbreviated ChemDraw structure of the precatalyst with Mn centers labeled A-D and O atoms labeled 1-6. The accompanying text box contains a descriptor representing the oxidation state of the cubane core, $Mn_2^{3+}Mn_2^{4+}$, and the ligand configuration, a bidentate acetate ligand. c) Abbreviated ChemDraw structures and descriptors representing three ligand configurations, with ligands colored blue. d) Abbreviated ChemDraw structures and descriptors representing three specific JT isomers. Mn^{3+} centers and their JT axes are colored red and represented in the descriptor by letter codes corresponding to the JT axis orientation. Adapted from [50].

The oxidation states of the catalyst accessed throughout the proposed cycle are referred to by abbreviation of the formal charges of the Mn centers:

- **3333** represents an Mn_4^{3+} configuration of the cubane core,
- **3334** represents an $Mn_3^{3+}Mn^{4+}$ configuration of the cubane core,
- **3344** represents an $Mn_2^{3+}Mn_2^{4+}$ configuration of the cubane core,
- **3444** represents an $Mn^{3+}Mn_3^{4+}$ configuration of the cubane core, and
- **4444** represents an Mn_4^{4+} configuration of the cubane core.

Simultaneously, the ligand configuration at the active face of the cubane core is represented (taking the precatalyst as an example) as **3344-OAc**, wherein a bidentate acetate ligand is bound to MnB and MnA, the Mn centers of the catalyst's active face (see figure 2.2b). Thus, as shown in figure 2.2c the activated species would be **4444-OH-H_2O**, with an OH ligand bound to MnB and an H_2O ligand bound to the apical MnA; the deactivated species would be **3333-o-o**, with each **-o** representing an open coordination site; and the hypothesized activated species of the iDC cycle would be **4444-O-O**, wherein a terminal oxo ligand each is bound to MnB and MnA, respectively.

To further differentiate between specific redox and JT isomers where relevant, the representation of the oxidation state is rendered more precisely to yield the localization of formal charges at the individual Mn centers **ABCD** and simultaneously give the orientation of the main JT axis at each Mn^{3+} center (**x**, **y**, or **z**). Thus, as shown in figure 2.2d the most stable isomer of the precatalyst would be **4z4x-OAC**, representing a JT axis in z-direction at MnB^{3+} and a further JT axis in x-direction at MnD^{3+}, while the most stable isomer of the deactivated species would be **zzzz-o-o**, with JT axes in z-direction at all four Mn^{3+} centers. Catalyst structures at the **4444** oxidation state are unaffected by this, as they do not possess JT axes. Finally, structures bearing distortions that are sufficiently strong to be considered potentially degraded are marked with an asterisk (*), e.g. the O4-protonated degraded structure **xzzx-o-H_2O*** (again, see figure 2.2d).

2.2.2 Structural Sampling

While the presence of JT effects across most of the Mn4V4 catalyst's oxidation states was recognized early in its development, their importance to catalytic reactivity was only realized in the course of investigating catalyst activation. [54] Certain ligand exchange pathways featured noticeably lower kinetic barriers than others, and these were associated with new ligands attacking at Mn^{3+} centers. Analyzing the orientation of the JT axes at those centers, the reason for the lower barriers became clear: new ligands were able to attack along the JT-distorted bond axis, with the longer and therefore weaker bond to the old ligand breaking more

easily than would have been possible at an Mn^{3+} center. This discovery strongly influenced further research into the reactivity of Mn4V4, as it became clear that JT effects could play a number of roles in determining the catalyst's structure and reactivity. Previous studies of the OEC by Krewald et al. had already made use of extensive sampling of JT and redox isomers to interpret XRD structures of the OEC; [64] similar work was later carried out by Mai et al. on Mn4V4. [69] While the discovery of the direct influence of JT effects on the kinetics of catalytic processes on Mn4V4 was a first in homogeneous catalysis, the same connection had already been postulated in heterogeneous Mn-oxo surface catalysts some years before. [65] Finally, Drosou et al. have found that in the OEC, the population of different JT isomers in the S1 could even determine which one out of two oxidation pathways leading to distinct products in the S2 would be favored. [68] Against this background of increasing interest in JT effects in water oxidation catalysis, an approach to studying catalytic reactivity that accounted for the large variety of accessible JT and redox isomers was required.

In Mn4V4, such an approach was inspired by the earlier work of Krewald et al. [64] and first utilized in studying catalyst activation. The basic workflow is illustrated exemplarily in figure 2.3: from a starting geometry with the desired ligand configuration and no JT distortions (**4444-OAc**), six isomers of the 3444 state are sampled by first performing preoptimizations constrained to produce catalyst geometries corresponding to each of the sampling targets (marked with **†**). Subsequent unconstrained optimizations of the six unrelaxed structures then converge to the same stable minimum on the potential energy surface (PES) (**4z44-OAc**). Finally, desired properties such as ΔG_{TZ} (see equation 2.3) are obtained from further single point and frequency calculations.

This approach was essentially followed and expanded upon in all further theoretical work carried out on Mn4V4. While the requisite calculations could be easily set up by hand and carried out individually on such a limited scale, parts of this workflow needed to be streamlined in order to sample especially the lower oxidation states that feature more than one JT axis. Mai et al. systematically studied all redox and JT isomers of the precatalyst, using a standard file framework in ORCA that allowed easy setup of preoptimizations and optimizations by manually adapting a master input file. [69] Working on this basis, I automated the workflow to better suit the requirements of larger-scale mechanistic studies. By employing a series of python and bash scripts, I was able to automate the setup of whole arrays of calculations at all stages as well as the analysis of the resulting geometries and other molecular properties, making the large-scale sampling of redox and JT isomers of Mn4V4 far more tractable. However, sampling all possible isomers across multiple ligand configurations still wastes substantial computational resources, as many sampling target structures converge to the same minimum.

To address this issue and reduce the expenditure of computational resources on calculations unlikely to contribute useful results to the overall investigation, I decided to limit sampling to only the most stable isomers of each ligand configu-

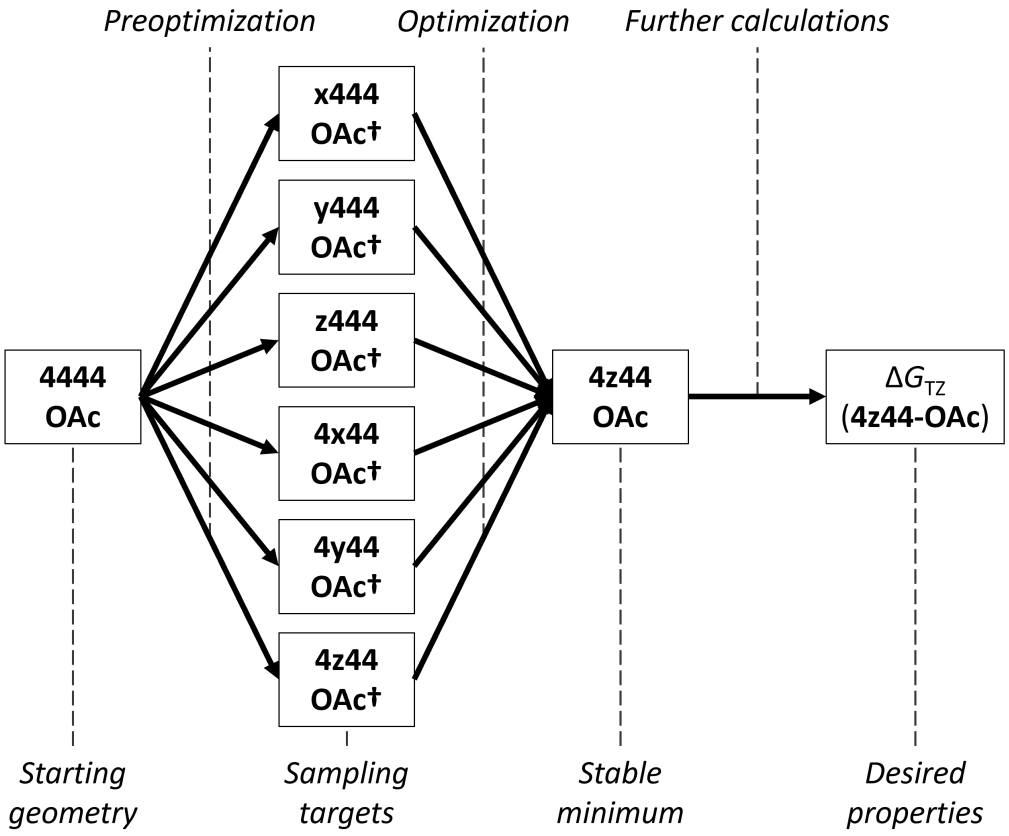

Figure 2.3: Catalyst structural sampling workflow: From a single starting geometry without JT distortions, six distinct unrelaxed (marked as †) sampling target structures are obtained through constrained preoptimizations; unconstrained optimizations of these six structures converge to a single stable minimum; desired properties of the final optimized structure such as ΔG_{TZ} are obtained through further single point and frequency calculations.

ration and oxidation state. To this end, I employed the heuristic rules derived by Mai et al. for the relative stability of redox and JT isomers of Mn4V4. [69] These heuristics allow the prediction of relative energies for all isomers of a given oxidation state; by only targeting those isomers predicted by heuristics to be within a certain threshold of the most stable isomer for a given oxidation state, I was able to further limit the computational costs of structural sampling.

While this largely automated workflow ended up saving a lot of time in setting up and analyzing calculations, it still comes with a number of drawbacks. Even when using the heuristics to select sampling targets, many of the calculations end up being redundant, as only some of the isomers predicted by heuristics to be most energetically favorable correspond to stable minima on the PES - thus, many of the unconstrained optimizations still produce virtually identical geometries. Furthermore, the workflow as described here with its particular inputs and

scripts is only useful under very specific conditions - essentially water oxidation catalysts with an Mn_4O_4 cubane core that can access oxidation states featuring Mn^{3+} centers. An alternative approach that automatically samples the potential energy surface of any given catalyst in an exploratory manner would be much more generally useful - in this vein, I attempted to use the *ab-initio* nanoreactor in my investigations of Mn4V4, as will be described in the following section.

2.3 Exploring Catalysis: the *ab initio* Nanoreactor

The *ab initio* nanoreactor is a method for exploring the ground state potential energy surface of a molecular system based on Born-Oppenheimer molecular dynamics. [78, 79] It employs three tools to increase the simulation speed as well as the likelihood of rare events occurring during a simulation:

1. The *ab initio* nanoreactor is implemented in TeraChem, [80, 81, 82, 83] a quantum chemistry package that leverages graphical processing units to speed up calculations.

2. Nanoreactor simulations are run at high temperature in order to supply sufficient thermal energy to easily overcome reaction barriers.

3. A so-called virtual piston, a periodically contracting spherical potential, is employed to increase the likelihood of collisions between reactive components of the simulated system.

In practice, the nanoreactor simulations form part of a larger workflow: Once a nanoreactor trajectory has been obtained, reactive trajectory segments must be first identified and then refined using e.g. nudged elastic band (NEB) calculations. Thus, reaction pathways of both previously known and unknown reactions can be characterized without requiring any initial information on their reactants, intermediates, transition states, or products - even an unoptimized starting geometry is in principle sufficient. As the method's authors point out, while the nanoreactor method is applicable to any system that can be simulated in TeraChem, a certain amount of parameter optimization is needed if useful results are to be obtained. The temperature must be chosen such that non-covalent interactions are rapidly broken while covalent bonds are largely preserved. Also, the composition of the simulated system requires some thought: explicit solvent molecules may be required if reactions of interest involve solvent interactions, as is the case in proton transfer reactions. [78, 79]

I initially attempted to leverage the nanoreactor to investigate the catalytic cycle of Mn4V4. In this, I quickly found that the open-ended, exploratory nature of the nanoreactor makes it less suitable to studying individual reactions of interest, as the likelihood of any particular reaction occurring within the simulation time is still quite low when using this form of non-directed dynamics. I therefore

attempted to utilize the nanoreactor for an exploratory study of catalyst degradation pathways, using a variety of reactive intermediates spanning all relevant oxidation states of the catalyst as starting geometries.

In this, I was first hampered by the virtual piston - a spherical potential that encourages centripetal movement of small molecules is not best suited to enhance the quasi-centrifugal forces that operate in the degradation of a large molecular catalyst. Nevertheless, after much parameter optimization, some structures were obtained that looked promising enough to prompt further investigation. However, in attempting to optimize them, I encountered a more substantial problem: The commercial release of TeraChem is somewhat limited in its electronic structure modeling of transition metals, eschewing the use of f orbitals for effective core potentials, exclusively. This produced structures with highly unrealistic spin populations that could not be reproduced or otherwise optimized in other quantum chemistry software.

Faced with these insurmountable issues, I elected to focus instead on more immediately promising avenues of research. While an exploration-based approach to studying transition metal catalysts would surely be welcomed by many theoretical chemists working in this field, the nanoreactor in its current form would require significant additional development in general as well as some degree of adaptation to the types of problems most studied in catalysis. This, in turn, would render the resulting method less generally useful, calling into question whether such method development is truly constructive at this point in time.

Ultimately, the nanoreactor is not best-suited to studying catalysts on a conceptual level - it excels at untethered exploration of the chemical space of a single reactive system, enabling the discovery of reactions no one has even considered before. [78] However, in studying individual catalysts, the focus lies much more on characterizing very specific reaction pathways in depth, rendering more traditional approaches that focus on sampling a multitude of structures along those pathways attractive.

Expanding the scope of catalytic investigations to entire families of related structures, recent methods developed specifically for the study of catalysis such as augmented volcano plots focus instead on a data-driven approach. [48, 59, 84, 85, 86] By leveraging statistical analysis and machine learning-based approaches, linear scaling relationships between certain catalyst properties and catalytic activity can be derived from available theoretical and experimental data. In this way, many different catalysts are screened *in silico*, allowing the user to identify promising candidates for further experimental study and understand important structure-property relationships.

Chapter 3

Results and Discussion

This thesis project is made up of three main studies. Each of these studies corresponds to a paper that is reprinted in appendix A. The first study concerns the activation of the precatalyst Mn4V4 to its activated form and is reprinted in section A.1. The second study concerns the mechanism of water oxidation in Mn4V4 and is reprinted in section A.2. The third and final study concerns catalyst regeneration, degradation, and a hypothesized alternative catalytic mechanism; it is reprinted in section A.3. In the following, each of the studies that make up the present thesis are shortly presented, and their most important results are summarized; for a more detailed presentation, the reader is referred to the paper reprints.

3.1 Catalyst Activation

The first study that forms part of this thesis concerns the activation of the Mn4V4 catalyst. [54] It had been observed in previous experiments that the precatalytic species **3344-OAc** must undergo a lengthy induction period of about 3 minutes under photocatalytic conditions before water oxidation can be observed; furthermore, two oxidation processes had been observed before water oxidation onset under electrocatalytic conditions. [51] Therefore, it appeared that these two oxidations along with the binding of water ligands are the necessary steps involved in transforming the inactive precatalyst into an activated species able to enter the water oxidation cycle. A combined theoretical and experimental study of the mechanism of catalyst activation was consequently launched.

The aims of this study were threefold: First, to characterize oxidative processes observed at potentials less positive than the onset of electrocatalytic water oxidation. Secondly, to model the mechanism of ligand exchange involved in binding water ligands to the catalyst. And thirdly, to determine the identity of the activated species as well as the preferred order of oxidation and ligand exchange steps that leads to its formation. To this end, infrared spectroscopy and square wave voltammetry experiments were carried out along with mechanistic DFT calculations and simulations of redox processes employing broken symmetry. It was hoped that, by combining these diverse approaches, additional insight be-

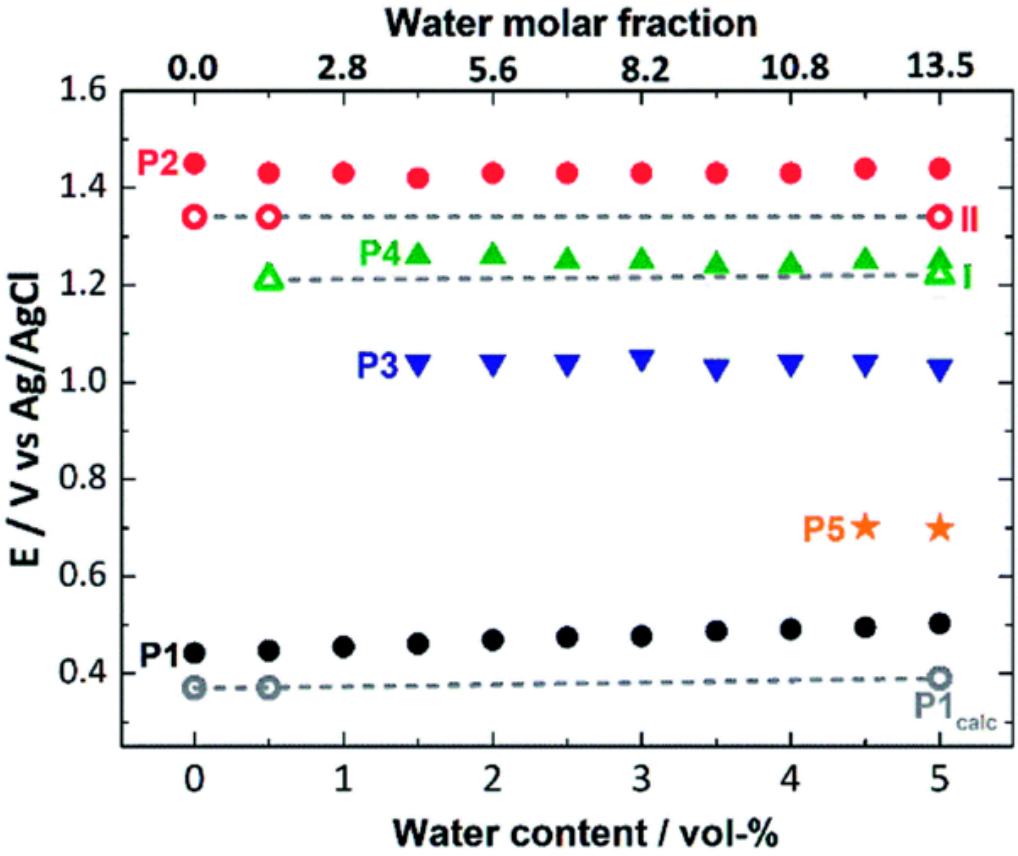

Figure 3.1: Reduction potentials of experimentally observed redox processes P1-P5 (full symbols) and theoretically computed reduction potentials corresponding to P1, P2, and P4, respectively (empty symbols linked by dashed lines) versus water content in percentage of solvent volume. Adapted from [54].

yond the results of the individual experiments and calculations could be gained. In the following, the most important results of this study will be summarized.

Starting with purely experimental results (see figure 3.1, full symbols), the square wave voltammogram of the precatalyst in dry ACN shows two oxidations, labeled P1 and P2; in the absence of water, these can be unambiguously assigned as P1: **3344-OAc** $\longrightarrow$ **3444-OAc** and P2: **3444-OAc** $\longrightarrow$ **4444-OAc** (corresponding to the black and red oxidation arrows in figure 3.2, respectively). Upon addition of water, water oxidation onset is observed at potentials more positive than P2, suggesting an activated species of oxidation state **4444**. Infrared experiments confirm that the precatalyst is stable in ACN solutions containing up to 5% H_2O on the timescale of the electrocatalytic experiments, indicating that neither ligand exchange nor degradation reactions play any significant role at the **3344** oxidation state. Meanwhile, adding water to the reaction solution causes new oxidative processes P3, P4, and P5 to appear on the square wave voltammogram of the precatalyst between the potentials of P1 and P2. The appearance of these pro-

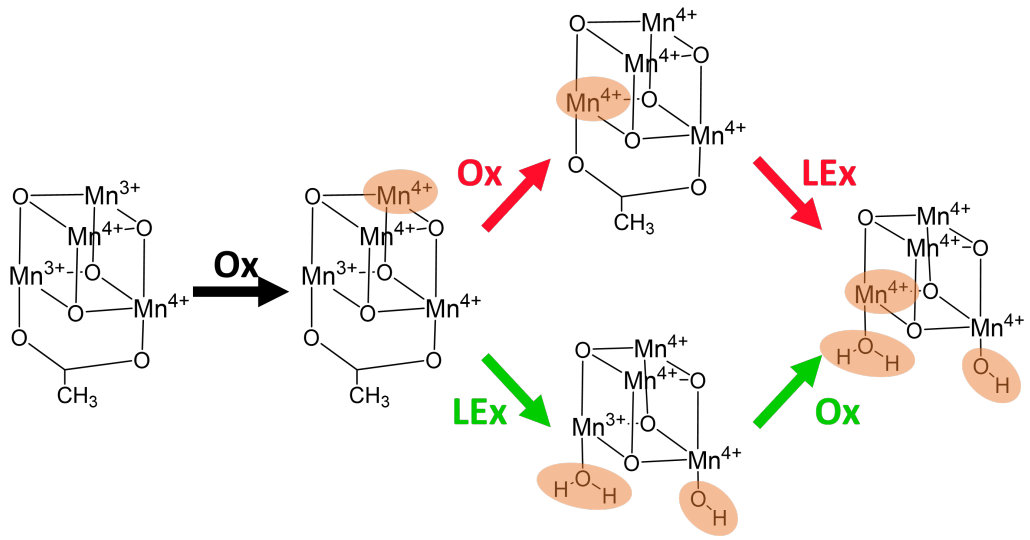

Figure 3.2: Investigated oxidation (Ox) and ligand exchange (LEx) processes (arrows in colors corresponding to appropriate reduction potentials in figure 3.1) as well as intermediate structures involved in these processes. Structural changes resulting from each reaction step are highlighted in orange. Two possible sequences of reaction steps were investigated: Ox-Ox-LEx (top pathway) and Ox-LEx-Ox (bottom pathway). Adapted from [54].

cesses is accompanied by a significant decrease in the current of P2, showing that they compete in some way with the **3444-OAc** $\longrightarrow$ **4444-OAc** oxidation. The most straightforward interpretation of these competing processes is that they involve some form of ligand exchange.

To better understand the nature of the hypothesized ligand exchange processes, DFT mechanistic calculations[1] were employed to model several possible pathways corresponding to two ligand exchange reactions: (I) **3444-OAC** $\longrightarrow$ **3444-OH-H_2O** and (II) **4444-OAC** $\longrightarrow$ **4444-OH-H_2O** (green and red ligand exchange arrows in figure 3.2, respectively). It should be noted at this point that, while it was initially assumed that ligand exchange would produce a catalyst species bearing two H_2O ligands, the calculations showed that the preferred products of both investigated ligand reactions (I and II) feature one H_2O and one OH ligand. Five pathways were modeled in detail, and all but one were found to be associated with kinetic barriers of more than 20 kcal/mol. The one exception is pathway Ia (see figure 3.3, in black), where the first H_2O-for-acetate ligand exchange takes place at a Mn^{3+} center and is associated with a low barrier of just 7.3 kcal/mol. Rather counterintuitively, an electron is then transferred from the Mn center binding the new H_2O ligand to the cofacial Mn center binding the departing, now-monodentate acetate ligand. This allows the second H_2O-for-acetate ligand exchange to also take place at a Mn^{3+} center, yielding another low barrier

[1]These calculations were carried out by G. Cárdenas.

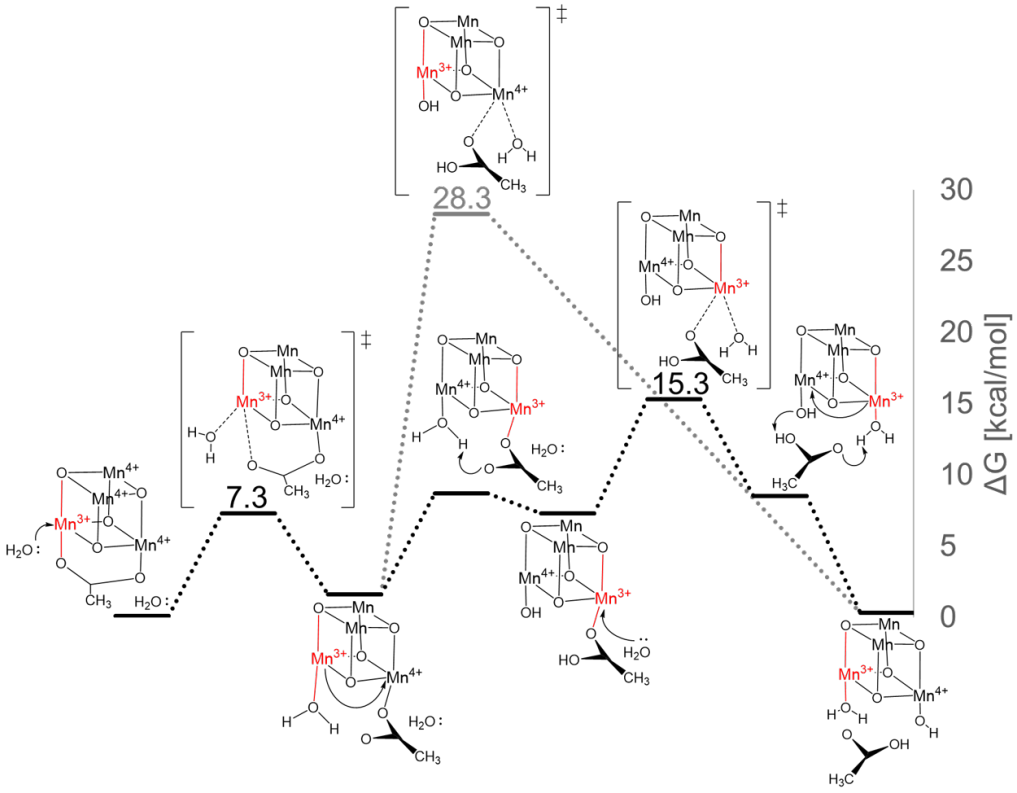

Figure 3.3: Overlapping ligand exchange pathways Ia (black) and Ib (grey) with structures of intermediates and transition states. In each structure, the location of the Mn^{3+} center and the orientation of its main JT axis are highlighted in red. Adapted from [54].

of only 8.0 kcal/mol. Without this crucial step, the barrier for the second ligand exchange step would be significantly higher (see pathway Ib, grey in figure 3.3). The wandering electron is then transferred back to its original Mn center, and along with a series of proton transfers, this yields the ligand-exchanged species **3444-OH-H_2O**.

Upon closer inspection, I found that the reason for the unusually low barriers in ligand exchange pathway Ia was that in both cases, the water molecule was able to attack along the JT bond axis of a Mn^{3+} center, utilizing the weaker, distorted bond to hasten the kinetics of ligand exchange. Having now modeled the **3444-OAC**, **3444-OH-H_2O**, **4444-OAc**, and **4444-OH-H_2O** species, we were able to compute highly accurate theoretical redox potentials[2] for processes P1 and P2, as well as a new process, **3444-OH-H_2O** $\longrightarrow$ **4444-OH-H_2O**, which could then be assigned to the experimental P4 (see empty symbols in figure 3.1). Based on these results, the thermodynamically and kinetically most favorable activation pathway for the precatalyst **3344-OAC** was determined to consist of three key steps: 1. **3344-OAc** $\longrightarrow$ **3444-OAc** oxidation (P1); 2. **3444-OAC** $\longrightarrow$ **3444-OH-H_2O** lig-

[2]These calculations were carried out by D. Hernández-Castillo and L. Schwiedrzik.

and exchange according to pathway Ia; and 3. **3444-OH-H_2O** $\longrightarrow$ **4444-OH-H_2O** oxidation (P4) (the lower pathway in figure 3.2). Formally, the reaction leading to the formation of the activated species from the precatalyst can be described as

$$[Mn_4V_4O_{13}(OAc)_3]^{3-} + 2H_2O \longrightarrow [Mn_4V_4O_{13}(OAc)_2(H_2O)(OH)]^{-} + AcOH + 2e^{-} \tag{3.1}$$

The activated species was determined to be **4444-OH-H_2O**. The experimental processes P3 and P5 could not be characterized, but were hypothesized to involve intermediate, electrode surface-adsorbed species and not play a major role in the activation of the catalyst.

This initial study of how the Mn4V4 catalyst is activated contributed to my overall research project in a number of ways. Firstly, the identity of the activated species was established, defining a clear point of departure for future mechanistic studies of the catalytic cycle of Mn4V4. Secondly, it was demonstrated that theoretical calculations could contribute significantly to better understanding the reactivity of Mn4V4. The catalyst had previously been studied using purely experimental methods, and it was only through the combination of theory and experiment that the full mechanism of catalyst activation could be uncovered. Finally and most unexpectedly, the unique role played by JT distortions in lowering the kinetic barriers of ligand exchange reactions first pointed toward the importance of JT effects for the reactivity of Mn4V4, a research topic that was to greatly increase in importance during my subsequent investigations of Mn4V4.

3.2 Water Oxidation

The second study presented in this thesis investigates the mechanism of water oxidation catalyzed by Mn4V4. [55] Having previously identified the activated species that enters the catalytic cycle as **4444-OH-H_2O**, this structure was chosen as the starting point for the following mechanistic investigations. The presence of cofacial H_2O and OH ligands in the activated species led us to focus on studying multicenter mechanisms of catalysis that involved at least these two ligands and the metal centers binding them in some fashion. As no experimental insight into the speciation of the catalyst beyond the activated species was available, our purely theoretical study design had to account for a large number of variables in terms of catalyst reactivity. We therefore investigated a variety of diverse pathways and compared them with one another in order to find the most favorable mechanism of water oxidation.

This study had three main goals: Firstly, to determine the relative stability of catalyst intermediates that could be involved in water oxidation catalysis. Secondly, to predict the most likely mechanism of O-O bond formation. And thirdly, to elucidate the role of redox and JT isomerism in the catalytic cycle of Mn4V4. To achieve these goals, we carried out mechanistic DFT calculations in a multistep sampling approach described above, as well as NEB simulations of some

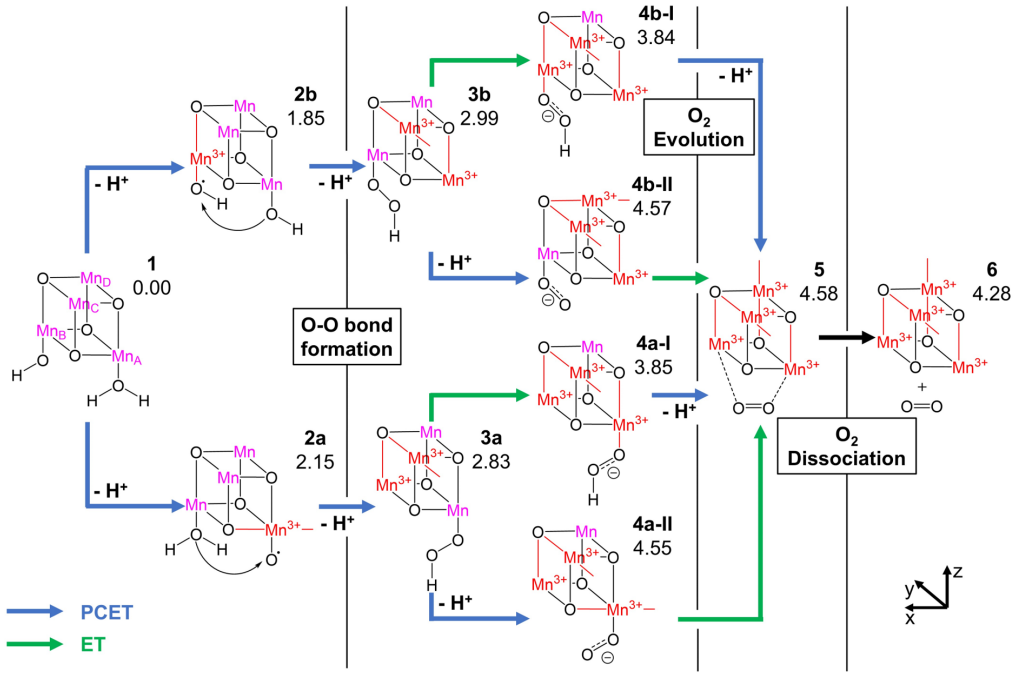

Figure 3.4: Four possible pathways for water oxidation, with PCET steps marked by blue arrows and ET steps marked by green arrows. Intermediates are labeled **1-6**, and their relative energy is given in eV. In each intermediate structure, Mn^{4+} centers are highlighted in magenta, while Mn^{3+} and their main JT axes are highlighted in red. Adapted from [55].

individual reaction steps. Ultimately, we aimed to gain greater insight into the reactivity of Mn4V4 in order to identify areas in which the design of the catalyst could be improved (e.g. by lowering the thermodynamic overpotential) and ways in which such improvements could be achieved (e.g. by favoring certain redox and JT isomers). In the following, the most important results of our work will be summarized.

From **4444-OH-H_2O**, water oxidation formally involves four single-electron oxidations and three deprotonations; as is typically done in literature, we assumed these are coupled, though the exact order of steps - 3 proton-coupled electron transfers (PCET) and 1 electron transfer (ET) - was initially unknown, resulting in 4 possible pathways. Both proton acceptors and oxidizing agents are readily available in the catalytic reaction mixture, leading us to consider two types of oxidation steps: intermolecular oxidation would involve just the water ligands and an oxidizer in solution (i.e. $[Ru(bpy)_3]^{2+}$), leaving the catalyst proper to play the role of a supporting scaffold. Alternatively, intramolecular oxidation would consist of electron transfers from the water ligands to the Mn^{4+} centers of the catalyst, which would in that reaction play the role of redox equivalent storage, much as the Mn centers in the OEC are known to do. Considering both inter- and intramolecular oxidation for each oxidation step resulted in a total of

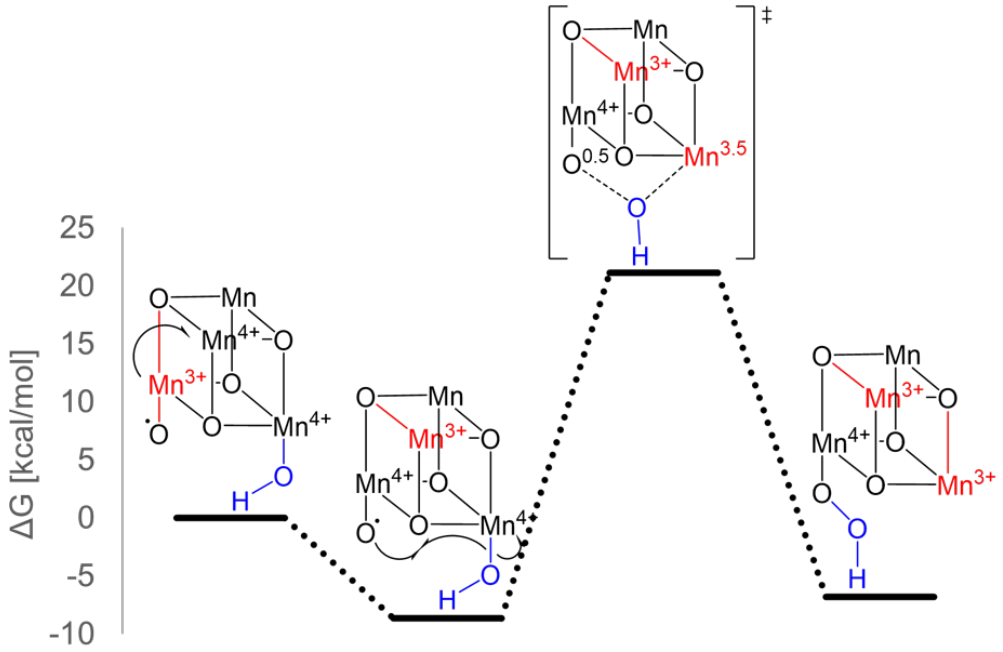

Figure 3.5: Detailed reaction diagram for the iWNA-type O-O bond formation reaction observed in Mn4V4. Note the transfer of an electron from the OH ligand to the Mn^{4+} center binding it, an example of intramolecular oxidation yielding Mn^{3+}. The reactant structure corresponds to a deprotonated **2b**, while the product is **2a** (see figure 3.4). In each intermediate and transition state structure, the Mn^{3+} centers and their main JT axes are highlighted in red; meanwhile, the attacking OH ligand is highlighted in blue. Adapted from [55].

64 pathways to be characterized.

The initial focus of the study was to optimize[3] just one structure per intermediate involved in the various pathways we were investigating, as the energy differences between the intermediates involved in the oxidation and deprotonation steps of water oxidation are known to be much larger than the energy differences between conformers or redox/JT isomers of the catalyst. This approach resulted in a number of key insights, namely that not all orders of the 3 PCET and 1 ET steps were feasible; that intramolecular oxidation was heavily favored thermodynamically over intermolecular oxidation; and that the mechanism of O-O bond formation most likely involved a nucleophilic attack of an OH ligand on a neighboring terminal oxyl radical (termed iWNA). Next, I decided to expand the sampling to include a number of ligand conformers as well as redox and JT isomers for every intermediate previously modeled.

This expanded sampling approach resulted in four possible pathways for water oxidation (see figure 3.4), which can be quickly narrowed down to one ther-

[3]These initial calculations were carried out by V. Brieskorn under the supervision of L. Schwiedrzik. All further calculations were carried out by L. Schwiedrzik.

modynamically most favorable one (**1**, **2b**, **3b**, **4b-I**, **5**, **6**) when considering the resulting thermodynamic overpotentials, specifically 0.71 V for the most favorable pathway. Further investigation of the O-O bond formation and O_2 evolution steps reveals additional roles played by JT and redox isomerism in the water oxidation cycle: In O_2 evolution, JT axes are involved in lowering the barrier to Mn-O bond cleavage in a manner similar to that already observed during catalyst activation. In O-O bond formation (see figure 3.5), NEB simulations and subsequent optimization of stationary points showed that O-O bond formation is preceded by deprotonation and then a redox isomerization; finally, the O-O bond formation step is a concerted reaction consisting of homolytic Mn-OH bond cleavage, homolytic O-OH bond formation, and the emergence of a new JT axis at the Mn^{3+} center thus newly created. The resulting most favorable pathway of water oxidation on Mn4V4 consists of the following steps: PCET, O-O bond formation by iWNA-type nucleophilic attack of an OH ligand on a neighboring terminal oxyl, another PCET, intramolecular ET, another PCET, and finally O_2 evolution. Formally, the water oxidation reaction at Mn4V4 can be described as

$$[Mn_4V_4O_{13}(OAc)_2(H_2O)(OH)]^{-} \longrightarrow [Mn_4V_4O_{13}(OAc)_2]^{4-} + O_2 + 3H^{+} \quad (3.2)$$

Our study of how Mn4V4 catalyzes water oxidation made several major contributions to the research project overall. Firstly, a feasible mechanism of water oxidation in Mn4V4 was proposed for the first time on the basis of a purely theoretical investigation. Secondly, I was able to model the O-O bond formation process in great detail, gaining for the first time key insights into this unusual type of multicenter, intramolecular water attack. Thirdly, I was able to expand on my previous discovery of the importance of redox and JT isomerism in the reactivity of the catalyst, establishing their role in the catalytic cycle proper. And finally, I was able to rationalize the high catalytic activity of Mn4V4 observed in experiment as being due to a combination of low thermodynamic overpotential and relatively low kinetic barriers thanks to the involvement of JT distortions. As the catalyst is left at its lowest oxidation state with two open coordination sites (**3333-o-o**, see also structure **6** in figure 3.4) at the end of the proposed mechanism, the next step was to close the catalytic cycle and, if possible, explain the somewhat lacking stability of Mn4V4 under catalytic conditions.

3.3 Regeneration and Degradation

The final study that contributes to this thesis attempts to complete the proposed theoretical model of the catalytic reactivity of Mn4V4. [50] The deactivated catalyst species **3333-o-o** that results from the proposed water oxidation mechanism is formally separated by four metal-centered oxidation steps, the binding of two new water ligands, and a deprotonation from the activated species able to restart

the water oxidation cycle, **4444-OH-H_2O**. The overall regeneration reaction can be represented as

$$[Mn_4V_4O_{13}(OAc)_2]^{4-} + 2H_2O \longrightarrow [Mn_4V_4O_{13}(OAc)_2(H_2O)(OH)]^{-} + H^{+} + 4e^{-} \tag{3.3}$$

In the absence of experimental evidence, it fell to theory to elucidate the mechanism of catalyst regeneration. At the same time, the proposed cycle involving an iWNA-style mechanism of water oxidation is not the only possible pathway along which water oxidation could be achieved - alternatives might prove to be more favorable. Finally, a marked decrease in activity over time had been observed in photocatalytic experiments, explained by colloid formation via electrostatic aggregation of the anionic catalyst with the cationic photosensitizer. Understanding how this and other degradation processes occur would enable the design of improved catalysts that avoid such deactivation pathways.

Our study thus aimed to answer a number of interconnected questions: How is the activated species **4444-OH-H_2O** regenerated from the deactivated species **3333-o-o** formed after O_2 evolution? Is an alternative form of O-O bond formation, involving the direct coupling of two terminal oxo groups (iDC), feasible in Mn4V4? Can theory explain why and how the activity of the catalyst decreases over time? And finally, what is the role played by JT distortions in all this? To answer all these questions, a large scale *in silico* sampling effort[4] was undertaken, which together with further NEB simulations unearthed a number of surprising results; the most important of these are summarized in the following.

To study the processes of catalyst regeneration that connect **3333-o-o** to **4444-OH-H_2O**, a network of intermediates covering all oxidation states **3333** through **4444** and ligand configurations, including having two open coordination sites, one H_2O or OH ligand bound to either MnA or MnB, and the OH-H_2O configuration of the activated species, was drawn up (see figure 3.6). Furthermore, two sets of intermediates connecting **3333-o-o** via **3333-OH-H_2O** to **4444-O-O,** a species hypothesized to play a central role in an alternative iDC-type mechanism, were also investigated. To limit the computational cost of these extensive calculations, the heuristic rules describing the relative stability of redox and JT isomers developed by Mai et al. [69] were operationalized to predict which isomers of each oxidation state are likely to be the most stable ones; only those under an energy threshold of 12 kcal/mol were targeted for sampling using the multistage approach already employed in our study of the water oxidation mechanism of Mn4V4 (see section 2.2.2). In this way, 159 stable minima covering the entire network of intermediates of interest were obtained.

In the absence of experimental evidence concerning at which oxidation state the binding of new water ligands might occur, I decided to limit the characterization of possible regeneration pathways to the purely thermodynamic perspective.

[4]Part of these calculations was carried out by T. Rajkovic under the supervision of L. Schwiedrzik, with the rest carried out by L. Schwiedrzik

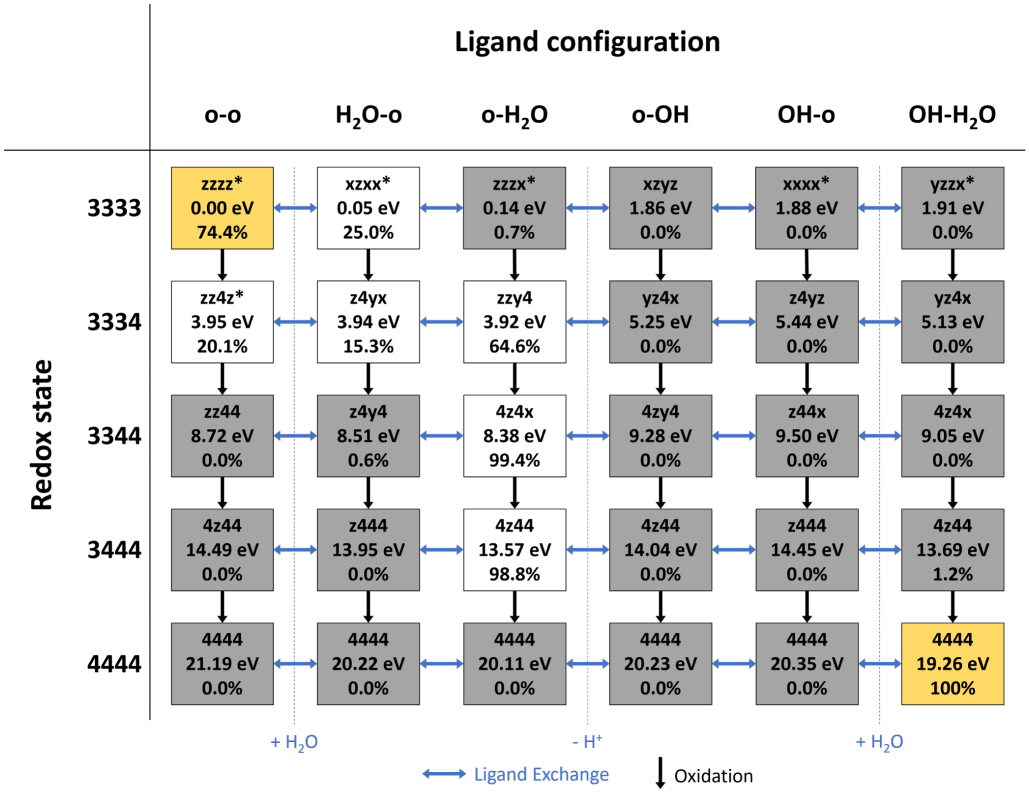

Figure 3.6: The investigated network of intermediates, with each row corresponding to one redox state of the cubane core and each column to one ligand configuration (for reference, see figure 2.2). For each type of intermediate, the most stable isomer obtained from sampling is represented by a text box containing its JT configuration, relative energy, and Boltzmann population at 298.15 K. The initial reactant and final product structures of regeneration are highlighted in gold; intermediates with populations greater than 5% are in white, while unpopulated intermediates are shaded in grey. Formal oxidation steps are represented by black arrows, while formal ligand exchange steps are represented by blue arrows. Adapted from [50].

From this, one can judge which intermediates are most stable at each oxidation state - a pathway consisting of these intermediates would result in the lowest thermodynamic overpotential of regeneration, even if they are almost certainly not the only intermediates formed during catalyst regeneration *in vitro*. I thus uncovered that the first H_2O ligand is bound to Mn4V4 during the first of four oxidation steps, and the second H_2O ligand is bound and deprotonated during the final oxidation step (see gold and white boxes in figure 3.6). The redox potential of the final oxidation step was found to be comparable to the experimental potential obtained for the **3444-OH-H_2O** to **4444-OH-H_2O** step of catalyst activation. The alternative iDC-type pathway studied herein was found to be thermodynamically infeasible.

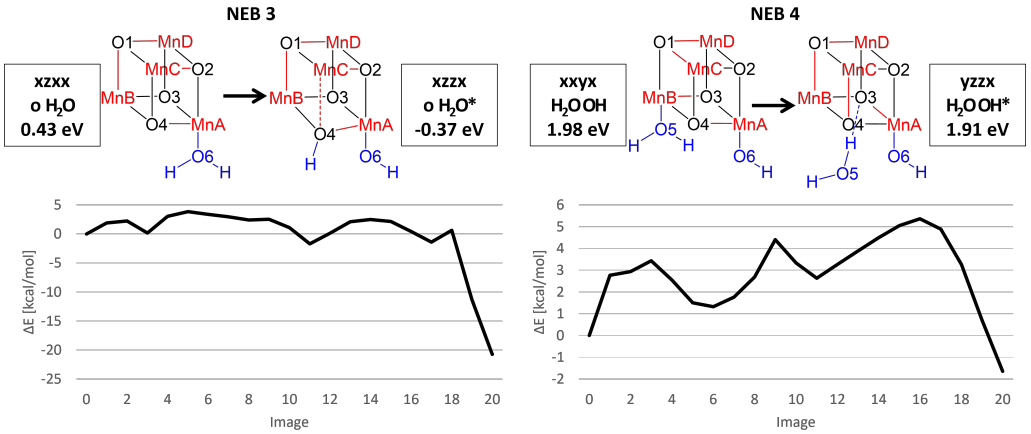

Figure 3.7: NEB simulations of two degradation processes, with initial and final structures as well as energy profiles. On the left (NEB 3), cubane opening and protonation of O4 by the neighboring ligand can be observed. On the right (NEB 4), an H_2O ligand is dissociated from its Mn center, remaining loosely bound to the complex via H-bond. Mn^{3+} centers and their main JT axes are highlighted in red, while ligands at the active face of the catalyst are highlighted in blue. Adapted from [50].

An analysis of bond length distributions across the obtained minima yielded some unexpected results. The vanadate ligand appears to be far more chemically active than previously thought, being able to accommodate JT axes and even interact directly with the apical O atom of the cubane core at lower oxidation states. Furthermore, a number of structures bearing unusually large interatomic distances along JT-distorted bonds were identified and studied in greater detail, as these could represent intermediates of potential catalyst degradation processes.

Two types of catalyst degradation processes were identified: cubane opening and ligand dissociation. NEB calculations were then used to approximate the kinetics of these processes, showing that all examples studied herein are associated with low barriers - hardly a surprising result, as the bond openings in these degradation processes appear to universally occur along pre-existing JT axes. Several of these apparent degradation processes were found to be fully reversible, showing that while the abundance of JT axes at lower oxidation states opens up many forms of unexpected side reactions for the Mn4V4 catalyst, not all of these need be detrimental to its activity or ability to be regenerated (see for example NEB 4 in figure 3.7).

One unique degradation product (**xzzx-o-H_2O***, see NEB 3 in figure 3.7) was found that features a partially open, protonated μ-oxo bridge. The opening of μ-oxo bridges could feasibly interrupt the free exchange of electrons within the cubane core of the catalyst, potentially decreasing its activity. As this degradation product is also significantly more stable than the deactivated species **3333-o-o**, its

formation could represent an irreversible degradation of the catalyst, leading to rapid loss of activity. However, a low kinetic barrier for this process was found only when starting from a reactant complex already binding an H_2O ligand, a thermodynamically quite unstable structure. As Mn4V4 is known to catalyze a significant number of turnovers in experiment, one can safely assume that the kinetic barrier to the formation of **xzzx-o-H_2O*** by direct solvent attack on the catalyst must be quite high. Nevertheless, this μ-oxo-protonated structure offers a first glimpse at how loss of activity could occur in Mn4V4 over time and should be studied in greater detail in future work.

This final study of catalyst regeneration and degradation serves to complete a number of avenues of investigation begun during the course of my research. I was able to complete the proposed iWNA-type catalytic cycle centering on the activated species **4444-OH-H_2O**, showing how that species can be regenerated from the deactivated **3333-o-o**. Furthermore, one alternative type of catalytic cycle that features a species with two terminal oxo ligands, **4444-O-O**, was studied; such an intermediate would be required in order to achieve O-O bond formation according to the iDC type of mechanism, but was found to be highly unstable. As a byproduct of our extensive sampling, I was able to serendipitously identify a number of partially degraded species and study the processes of their formation, shedding some light on how the catalyst might decrease in activity over time. And finally, I was able to uncover another role played by JT effects in the reactivity of Mn4V4: In addition to facilitating ligand exchange and O-O bond formation steps, JT distortions can weaken key bonds in the catalyst, possibly leading to its eventual degradation. These results serve to underline the importance of a catalyst design concept that has been known in heterogeneous catalysis for some time: JT effects are key to increasing the catalytic activity of d^4 metal centers.

Chapter 4

Conclusion

The overall goal of this research project was to gain mechanistic insight into the reactivity and stability of Mn4V4 in order to enable the design of an improved catalyst. To this end, a theoretical approach using static DFT calculations and NEB simulations was taken, resulting in three papers that were covered in the previous chapters. In summary, I propose a feasible catalytic cycle for Mn4V4 that is comprised of three parts: first, activation, where the precatalyst is oxidized and exchanges one of its ligands with water, enabling entry into the water oxidation cycle proper. [54] Second, in the initial half of that cycle, a series of coupled deprotonations and intramolecular electron transfers lead to the formation of an O-O bond by way of nucleophilic attack of an OH ligand on a neighboring terminal oxyl radical; [55] from this, O_2 is then formed, leaving all Mn centers of the catalyst at their lowest oxidation state. Third, catalyst regeneration commences, consisting of the binding of new water ligands and renewed oxidation of the four Mn centers. [50] This entire process is illustrated in figure 4.1.

Within the proposed catalytic cycle, I found that JT effects play several prominent roles. They weaken key metal-ligand bonds during catalyst activation, opening up a low-barrier pathway for ligand exchange. JT and redox isomerizations are also crucial to enabling the formation of the O-O bond during water oxidation as well as the eventual evolution of O_2 from the complex. Finally, JT axes can lower the barriers for a variety of degradation processes discovered during the study of catalyst regeneration, showing they not only influence the water oxidation activity of Mn4V4, but also its stability.

In terms of catalyst design, this thesis demonstrates the (theoretical) feasibility of several key design concepts already noted elsewhere, such as the ability of cubane-core catalysts to flexibly redistribute electrons between their metal centers, reducing the need to achieve high oxidation states during water oxidation catalysis. [20, 21, 22] Furthermore, the POM ligand of Mn4V4 does seem to serve as a form of stabilizer to the catalyst, as it is not involved in any of the discovered degradation mechanisms and generally appears to disfavor JT effects. [51, 69]

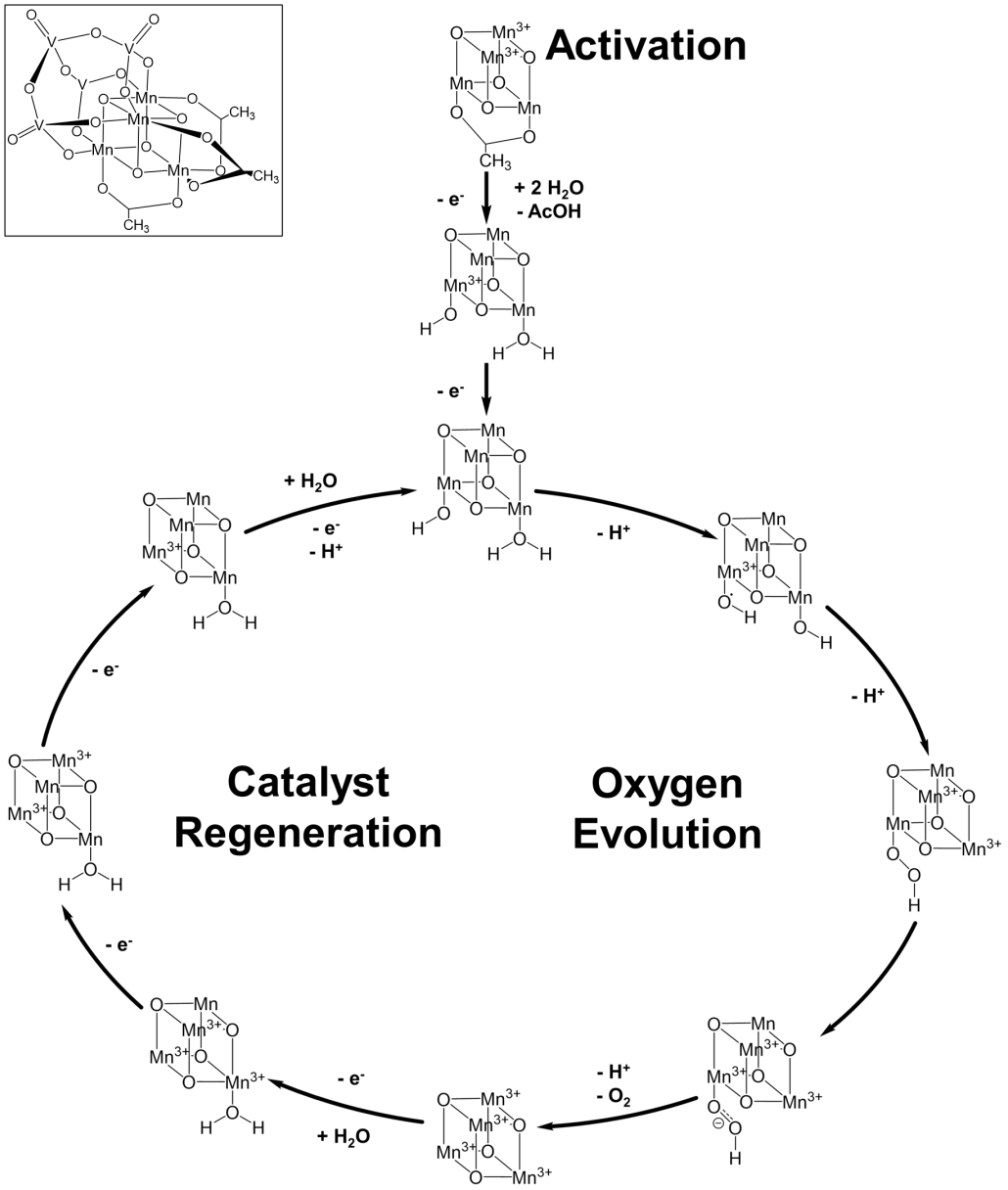

Figure 4.1: The full proposed catalytic cycle of Mn4V4, consisting of activation of the precatalyst (top), water oxidation (right half of cycle), and catalyst regeneration (left half of cycle). The Mn4V4 catalyst is represented as an abbreviated ChemDraw structure; for reference, the full ChemDraw structure of the precatalyst **3344-OAc** is shown in the top left insert. See also figure 2.2.

Finally, the present work proposes one design paradigm that is (to the best of my knowledge) new to the field of homogeneous catalysis, though already known in heterogeneous catalysis [65, 66, 67]: d^4 ions can be utilized to lower key barriers during water oxidation catalysis through JT effects. As JT effects depend on both the metal center and the ligand environment, one could imagine

that these effects could be fine-tuned to favor reaction steps that facilitate catalysis while avoiding those that lead to catalyst degradation.

Future work on the effective utilization of JT effects could focus on clarifying their role in the catalytic cycle of the natural OEC, as has already been begun by Drosou et al. [68] However, perhaps greater immediate benefit could be gained from applying the lessons learned here to the design of multicomponent, polymer-based systems for water splitting. In such systems, the binding of a cubane core featuring d^4 ions could be achieved by way of a stable POM, while the other faces of the cubane would be highly catalytically active due to the presence of favorable JT effects.

Finally, data-driven approaches to catalyst design by way of *in-silico* screening of potential catalyst structures for desirable qualities have been gaining popularity in recent years. [48, 59, 84, 85, 86] I would propose that the presence of (multiple) d^4 ions is such a desirable quality in water oxidation (and probably other types of) catalysts. This is not the only example of structural flexibility being shown to be crucial to the high activity of a water oxidation catalyst, [21] but it is perhaps the most accessible form thereof, as JT effects can be easily detected in a given system by monitoring of formal oxidation states through Mulliken spin densities as well as relative bond lengths. It is my hope that, by using these and other new insights gained into the functionality of water oxidation and hydrogen evolution catalysts in recent years, the affordable production of green hydrogen using nothing but water and sunlight can become a reality in the near future.

Appendix A

Paper Reprints

Reprints of the publications that contribute to the present thesis are listed in this appendix. The paper discussing catalyst activation is found in Appendix A.1. The paper covering the mechanism of water oxidation is found in Appendix A.2. Finally, the paper on catalyst regeneration, degradation, and an alternative water oxidation mechanism is found in Appendix A.3.

A.1 Activation by oxidation and ligand exchange in a molecular manganese vanadium oxide water oxidation catalyst

GUSTAVO CÁRDENAS, IVAN TRENTIN, LUDWIG SCHWIEDRZIK, DAVID HERNÁNDEZ-CASTILLO, GRACE A. LOWE, JULIAN KUND, CHRISTINE KRANZ, SARAH KLINGLER, ROBERT STACH, BORIS MIZAIKOFF, PHILIPP MARQUETAND, JUAN J. NOGUEIRA, CARSTEN STREB, AND LETICIA GONZÁLEZ

Chem. Sci., **2021**, 12, 12918-12927.
https://doi.org/10.1039/D1SC03239A

Contributions:

Gustavo Cárdenas performed and analyzed calculations, co-wrote the original draft, discussed, and commented on the manuscript.

Ivan Trentin synthesized the compound, provided electrochemical analyses, co-wrote the original draft, discussed, and commented on the manuscript.

Ludwig Schwiedrzik performed and analyzed calculations, discussed, and commented on the manuscript.

David Hernández-Castillo performed and analyzed calculations, co-wrote the original draft, discussed, and commented on the manuscript.

Grace A. Lowe provided electrochemical analyses, discussed, and commented on the manuscript.

Julian Kund provide IR-spectroscopic analyses, discussed, and commented on the manuscript.

Christine Kranz provided electrochemical analyses, discussed, commented on the manuscript, and acquired funding.

Sarah Klingler provided IR-spectroscopic analyses, discussed, and commented on the manuscript.

Robert Stach provided IR-spectroscopic analyses, discussed, commented on the manuscript, and acquired funding.

Boris Mizaikoff provided IR-spectroscopic analyses, discussed, commented on the manuscript, and acquired funding.

Philipp Marquetand supervised theoretical work, discussed, and commented on the manuscript.

Juan J. Nogueira supervised theoretical work, discussed, and commented on the manuscript.

Carsten Streb designed the study, provided electrochemical analyses, reviewed and edited the manuscript, discussed, commented on the manuscript, and acquired funding.

Leticia González designed the study, supervised theoretical work, reviewed and edited the manuscript, discussed, commented on the manuscript, and acquired funding.

Chemical Science

ROYAL SOCIETY OF CHEMISTRY

EDGE ARTICLE

View Article Online
View Journal | View Issue

Cite this: *Chem. Sci.*, 2021, **12**, 12918

All publication charges for this article have been paid for by the Royal Society of Chemistry

Activation by oxidation and ligand exchange in a molecular manganese vanadium oxide water oxidation catalyst†

Gustavo Cárdenas,[ab] Ivan Trentin,[c] Ludwig Schwiedrzik,[a] David Hernández-Castillo,[a] Grace A. Lowe,[c] Julian Kund,[d] Christine Kranz,[d] Sarah Klingler,[d] Robert Stach,[d] Boris Mizaikoff,[d] Philipp Marquetand,[af] Juan J. Nogueira,[bf] Carsten Streb *[c] and Leticia González *[ae]

Despite their technological importance for water splitting, the reaction mechanisms of most water oxidation catalysts (WOCs) are poorly understood. This paper combines theoretical and experimental methods to reveal mechanistic insights into the reactivity of the highly active molecular manganese vanadium oxide WOC $[Mn_4V_4O_{17}(OAc)_3]^{3-}$ in aqueous acetonitrile solutions. Using density functional theory together with electrochemistry and IR-spectroscopy, we propose a sequential three-step activation mechanism including a one-electron oxidation of the catalyst from $[Mn_2^{3+}Mn_2^{4+}]$ to $[Mn^{3+}Mn_3^{4+}]$, acetate-to-water ligand exchange, and a second one-electron oxidation from $[Mn^{3+}Mn_3^{4+}]$ to $[Mn_4^{4+}]$. Analysis of several plausible ligand exchange pathways shows that nucleophilic attack of water molecules along the Jahn–Teller axis of the Mn^{3+} centers leads to significantly lower activation barriers compared with attack at Mn^{4+} centers. Deprotonation of one water ligand by the leaving acetate group leads to the formation of the activated species $[Mn_4V_4O_{17}(OAc)_2(H_2O)(OH)]^-$ featuring one H_2O and one OH ligand. Redox potentials based on the computed intermediates are in excellent agreement with electrochemical measurements at various solvent compositions. This intricate interplay between redox chemistry and ligand exchange controls the formation of the catalytically active species. These results provide key reactivity information essential to further study bio-inspired molecular WOCs and solid-state manganese oxide catalysts.

Received 14th June 2021
Accepted 30th August 2021

DOI: 10.1039/d1sc03239a

rsc.li/chemical-science

Introduction

The development of noble metal-free water oxidation catalysts[1,2] (WOCs) is often inspired by natural photosynthesis, where a calcium manganese oxide cubane (the oxygen evolving complex, OEC) oxidizes water near the thermodynamic potential.[3,4] Molecular model complexes are often used in mechanistic studies of the catalytic cycle.[5–8] Meanwhile, the design of solid-state metal oxide WOCs comes with its own set of challenges: structural complexity, typically mixed metal sites, and scarce information on the nature of their active sites.[9] On the quest to surmount these challenges, molecular mixed metal oxides – so-called polyoxometalates (POMs) – have emerged as prototypes useful for homogeneous water oxidation catalysis and as models to correlate molecular reactivity with heterogeneous solid-state catalysts.[10] Typically, POM-WOCs are engineered by functionalizing chemically robust POMs (mainly tungstates) with redox-active transition metals[11–13] such as Ru,[14,15] Co[16,17] or Mn.[18,19] Much research on POM-WOCs has focused on stabilizing bio-inspired polynuclear metal-oxo-aggregates $[M_xO_y]$ using POM ligands, as this approach limits the oxidation state changes required per metal site during water oxidation.[11–13,20]

While the last decade has seen tremendous progress in POM-WOC synthesis and catalysis, mechanistic studies are rare, in part due to challenges related to POM-WOC stability.[21,22] Early studies by Musaev and colleagues explored the electronic structure and accessible oxidation states of ruthenium tungstate POM-WOCs.[23] Later, pioneering studies by Poblet and colleagues provided a water oxidation mechanism for cobalt

[a]*Institute of Theoretical Chemistry, University of Vienna, Währinger Str. 17, 1090 Vienna, Austria. E-mail: leticia.gonzalez@univie.ac.at*
[b]*Chemistry Department, Universidad Autónoma de Madrid, Calle Francisco Tomás y Valiente, 7, 28049 Madrid, Spain*
[c]*Institute of Inorganic Chemistry I, Ulm University, Albert-Einstein-Allee 11, 89081, Ulm, Germany. E-mail: carsten.streb@uni-ulm.de*
[d]*Institute of Analytical and Bioanalytical Chemistry, Ulm University, Albert-Einstein-Allee 11, 89081 Ulm, Germany*
[e]*Vienna Research Platform on Accelerating Reaction Discovery, University of Vienna, Währinger Str. 17, 1090 Vienna, Austria*
[f]*IADCHEM, Institute for Advanced Research in Chemistry, Universidad Autónoma de Madrid, Madrid, Spain*

† Electronic supplementary information (ESI) available: Electrochemical, spectroscopic and theoretical data. See DOI: 10.1039/d1sc03239a

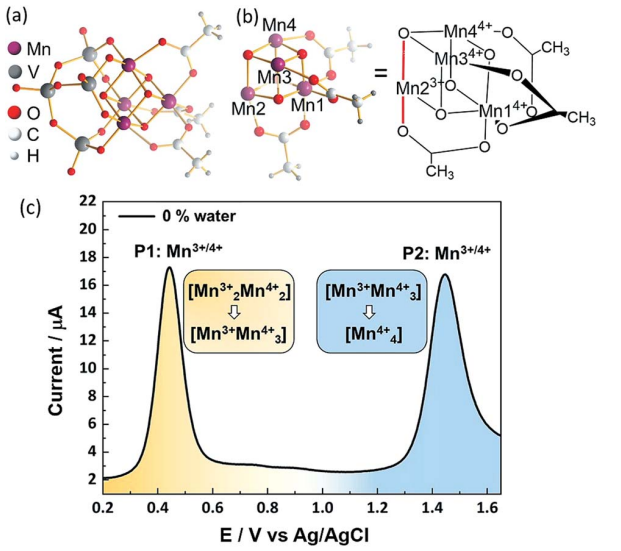

Fig. 1 (a) Complete structure of the POM-WOC $[Mn_4V_4O_{17}(OAc)_3]^{3-}$ (={Mn_4V_4}). (b) Simplified manganese oxo cubane core structure of the one-electron-oxidized species with Mn numbering scheme. Oxidation states of the Mn centres are indicated by superscripts. Jahn–Teller axis highlighted in red. (c) Square wave voltammogram of $[Mn_4V_4O_{17}(OAc)_3]^{3-}$. Conditions: $f = 25$ Hz, $E_{SW} = 25$ mV, $E_{step} = 2$ mV water-free MeCN containing 0.1 M nBu$_4$NPF$_6$ as electrolyte, working electrode: glassy carbon; counter-electrode Pt wire, reference electrode: Ag/AgCl (3.5 M KCl).

tungstate POM-WOCs using density functional theory (DFT).[17,24] Also, Llobet, Bo, Bonchio and colleagues combined spectroscopic and spectro-electrochemical studies with DFT calculations to investigate the redox chemistry during water oxidation by ruthenium-containing POM-WOCs.[25] However, for many POM-WOCs[11,12,21] mechanistic understanding of their mode of action in water oxidation catalysis is lacking.

To date, most POM-WOC research is focused on metal-functionalized lacunary polyoxotungstates.[11–13,21] In contrast, the use of vanadates to stabilize metal-oxo ligands is limited, possibly due to their more complex reactivity.[26] Recently, some of us reported[19] the embedding of OEC-inspired manganese oxo reaction centers[3] into a molecular vanadium oxide WOC, $[Mn_4V_4O_{17}(OAc)_3]^{3-}$ (={Mn_4V_4}), see Fig. 1. This compound is capable of electrochemical and photochemical water oxidation when operated under homogeneous conditions in aqueous acetonitrile solutions with turnover numbers > 12 000 and turnover frequencies > 200 min^{-1},[19,27] but any knowledge related to its catalytic activity remains elusive. This insight is urgently required not only because this catalyst is one of the best-performing POM-WOCs reported, but also because it can be considered a model for the OEC and for technologically important manganese oxide water oxidation catalysts.

Herein, we report the activation mechanism of the POM-WOC $[Mn_4V_4O_{17}(OAc)_3]^{3-}$ as a fundamental step towards understanding speciation in solution under catalytic conditions and elucidating the complete water oxidation cycle. Combining electrochemical measurements and theoretical calculations we unravel a three-step activation mechanism consisting of a one-electron oxidation of the catalyst, acetate-to-water ligand exchange, and a second one-electron oxidation. The calculations of the ligand exchange pathways and redox potentials allow us to precisely determine the nature of the experimentally observed redox transitions. Further, the complex interplay of proton-coupled redox processes is of general importance for understanding water oxidation catalysis and advancing the design of other efficient POM-WOCs.

Experimental

Electrochemistry

Voltammograms were recorded using a Gamry 1010B potentiostat and a three-electrode setup. A 3 mm diameter glassy carbon disk working electrode (CH Instruments, USA), Pt wire counter-electrode and a leakless miniature Ag/AgCl reference electrode were used. The reference electrode potential was measured against a standard calomel reference electrode (CH Instruments, USA) in pure electrolyte solution before and after each measurement. As pre-treatment, the glassy carbon (GC) electrode was cycled 10 times in 0.2 M aqueous H_2SO_4 between −0.5 V and 0.5 V to remove impurities. Between each square wave voltammetry (SWV) experiment, the electrode was polished with an alumina slurry. The counter-electrode Pt wire was polished with a 0.05 µm alumina slurry prior to use. Samples with varying water content were prepared by mixing the required amounts of water and acetonitrile with nBu$_4$NPF$_6$ (0.1 M) and background SWV were collected for each solvent mixture in the absence of {Mn_4V_4}. Successively, (nBu$_4$N)$_3$[$Mn_4V_4O_{17}$(AcO)$_3$] (32 mg, 2 mM) was added to the solution and stirred until dissolved (*ca.* 1 min).[19] After *ca.* 5 min equilibration, the SWV was performed. Each experiment was performed at least in triplicate to ensure reproducibility. Between each experiment, the working electrode was polished to avoid interferences from possible electrode fouling (*e.g.* adsorption of intermediate species). SWV parameters were as follows: Frequency $f = 25$ Hz, pulse amplitude $E_{SW} = 25$ mV, potential step $E_{step} = 2$ mV in a range between 0.2 and 1.7 V *vs.* Ag/AgCl (3.5 M KCl) at room temperature.

Infrared spectroscopy

IR spectra were recorded using a Fourier-transform infrared (FT-IR) spectrometer (Alpha I, Bruker Optik GmbH, Ettlingen, Germany) equipped with a zinc selenide multi-bounce attenuated total reflection (ATR) accessory (Multi ATR, Bruker Optik GmbH, Ettlingen, Germany). The spectra were collected at a spectral resolution of 4 cm^{-1} averaging 42 spectra per measurement. For each measurement, an aliquot of 0.6 ml of the sample solution (4 mM) was deposited onto the ATR crystal inside a closed sampling cell to prevent evaporation of the solvent during the measurement.

Computational

Ligand exchange mechanistic calculations

As in Siegbahn's studies of the OEC in photosystem II,[28,29] calculations were carried out using the high-spin configuration

and assuming that antiferromagnetic effects do not significantly affect either the reaction barriers or the geometry of the complex.[30] Geometries were optimized using DFT and the B3LYP functional[31,32] – as widely used in other studies of OEC model systems[33–37] and polyoxometalate WOCs[24,38–45]— combined with the def2-SVP basis set.[46] Local minima were confirmed by the absence of imaginary frequencies. Solvation effects were considered using the SMD implicit solvation model[47] with a dielectric constant of 40.98. We use Grimme's D3 empirical dispersion correction[48] and the zeroth-order DKH relativistic Hamiltonian.[49] Electronic energies were refined using B3LYP with def2-TZVP[46] for Mn, V, O atoms, and def2-SVP for C and H atoms. All these calculations were performed with the Gaussian 16 software package.[50]

Redox potentials calculations

The geometries employed for the redox potential calculations were also optimized at the B3LYP/def2-SVP level of theory. Dielectric constants between 36.60 (0% water) and 38.79 (5% water) account for the variation of the solvent composition, as dictated by the experiment. The value of the dielectric constant of the mixture is calculated as:

$$\varepsilon_{\text{mixture}} = \varphi_{\text{water}}\varepsilon_{\text{water}} + \varphi_{\text{acetonitrile}}\varepsilon_{\text{acetonitrile}} \quad (1)$$

where $\varepsilon_{\text{mixture}}$, $\varepsilon_{\text{water}}$ and $\varepsilon_{\text{acetonitrile}}$ are the dielectric constants of the mixture, water (80.4) and acetonitrile (36.6), respectively, and φ_{water}, $\varphi_{\text{acetonitrile}}$ are the volumetric fractions of the respective solvents. Unlike the ligand exchange calculations, accurate redox potentials for OEC similar systems require the consideration of antiferromagnetic effects. This was done by employing the Orca 4.2.1 (ref. 51) suite, which enables the computation of antiferromagnetic electronic configurations using the broken-symmetry[52] approach including implicit solvation effects. To this end, electronic energies entering the redox potentials were refined using the zeroth-order regular approximation (ZORA) for relativistic effects,[53] along with the ZORA-Def2-SVP (C, H) and ZORA-Def2-TZVP (Mn, V, O) basis sets. The calculations used the most stable antiferromagnetic electronic configurations for the complexes in the broken-symmetry framework.[52] Implicit solvent effects, on the single point energies, were included through the conductor-like polarizable continuum model.[54]

The standard reduction potentials ($\Delta E^{\circ}_{\text{reduction}}$) were calculated relative to the Ag/AgCl electrode as:

$$\Delta E^{\circ}_{\text{reduction}} = -\frac{\Delta G^{\circ}_{\text{reduction}}}{nF} - E^{\text{absolute}}_{\text{Ag/AgCl}} \quad (2)$$

where $\Delta G^{\circ}_{\text{reduction}}$ is the change in Gibbs free energy in the reduction reaction, n and F are the number of electrons transferred and the Faraday constant, respectively, and $E^{\text{absolute}}_{\text{Ag/AgCl}}$ is the absolute reduction potential of the Ag/AgCl electrode. The value of $E^{\text{absolute}}_{\text{Ag/AgCl}}$ was obtained considering an absolute reduction potential for the Standard Hydrogen Electrode (SHE) of 4.28 V (ref. 55) and a reduction potential of 0.22 V (ref. 56) for the Ag/AgCl electrode relative to the SHE. The Gibbs free energy of reduction was computed here by the so-called direct approach,[57] in which the solution phase reaction energy is computed as the difference between the Gibbs free energy of the product and the reactant, each obtained from an optimization-frequency calculation in a continuum solvation model. Alternatively, thermodynamic cycles can be used to compute solution phase reaction energies, as they are parametrized to obtain accurate solvation free energies.[55,57] When computing the Gibbs free energy of solvation in a thermodynamic cycle using implicit solvation models to obtain the solution phase reaction energy, explicit vibrational corrections are not included,[58] although there are cases in which solvation can induce changes in vibrational frequencies. Therefore, it is advisable to consider these vibrational corrections,[57,59] as we have done here using the direct approach. We note that the direct approach has also been applied in the computation of the redox potentials of POMs analogous to the one presented in this work.[60,61]

Results and discussion

The POM-WOC $[Mn_4V_4O_{17}(OAc)_3]^{3-}$ is based on a tripodal tetravanadate ligand that coordinates to a $[Mn_4O_4]$ cubane (abbreviated as $[Mn_x^{3+}Mn_{4-x}^{4+}]$); the manganese centers are further stabilized by three bridging acetate ligands, see Fig. 1a and b. Square wave voltammograms and cyclic voltammograms recorded in water-free acetonitrile show that the catalyst undergoes two quasi-reversible Mn-based oxidation reactions, $[Mn_2^{3+}Mn_2^{4+}] \rightarrow [Mn^{3+}Mn_3^{4+}]$ and $[Mn^{3+}Mn_3^{4+}] \rightarrow [Mn_4^{4+}]$ (labelled P1 and P2, respectively, in Fig. 1c, see also Fig. S1 and Table S1 of the ESI†).[19] Previous studies have shown that water oxidation occurs at potentials more positive than P2, suggesting that $[Mn_4^{4+}]$ is the species that enters the water oxidation cycle.[19] Note that no protonation of the cluster is observed by crystallography, spectroscopy or mass spectrometry,[19] unlike other POM-WOCs discussed in the literature.[62]

In order to study the full catalytic cycle, first it is essential to understand how the catalyst reaches its active state. To this end, here, we investigate the P1 and P2 oxidation processes to elucidate the electronic and structural changes required to access the catalytically active species. We propose that the first step in the cluster activation is the $[Mn_2^{3+}Mn_2^{4+}] \rightarrow [Mn^{3+}Mn_3^{4+}]$ oxidation (rather than ligand exchange). This is based on *in situ* IR-spectroscopic data, which was recorded at conditions identical to the experimental electrochemistry discussed below (*i.e.*, acetonitrile solutions containing up to 5 vol% water). The analysis of the characteristic metal oxide and acetate vibrations of $[Mn_4V_4O_{17}(OAc)_3]^{3-}$ in the 700–1600 cm^{-1} spectral range shows no significant changes during the experimental electrochemical timescale (*i.e.*, sample preparation and experiment *approx.* 20 min; see Fig. 2a). Only the vanadate signature appears less well resolved at high water content, yet, no significant peak shift or change in intensity was observed.[63,64] This suggests that the structural integrity of the cluster is maintained, and that no acetate-to-water ligand exchange is observed during this period. Consequently, we focus on mechanisms starting by oxidation of the native $[Mn_4V_4O_{17}(OAc)_3]^{3-}$ species. Particular focus is put on exploring (i) the formation of the highly oxidized $[Mn_4^{4+}]$ state through the $[Mn^{3+}Mn_3^{4+}] \rightarrow$

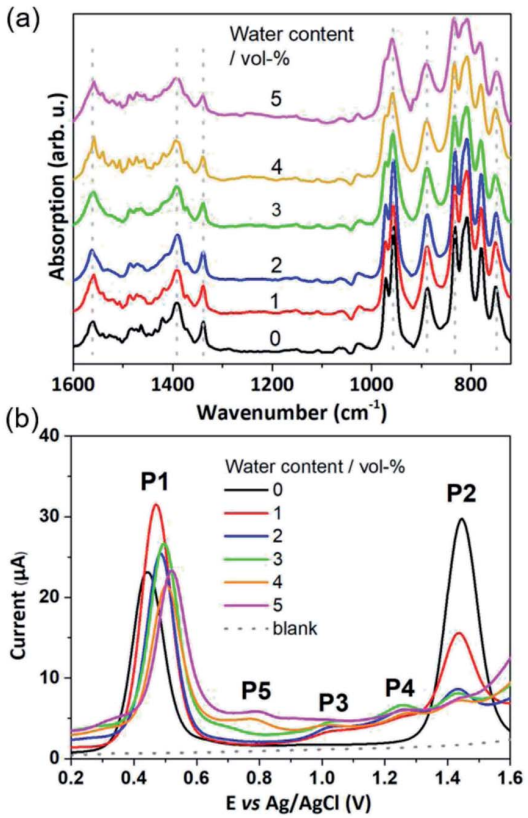

Fig. 2 (a) IR-spectra of $\{Mn_4V_4\}$ in acetonitrile containing 0–5 vol% of water. Each spectrum was collected after a $t = 20$ min equilibration period, which is in line with the time required for collecting the SWV data shown in (b). Note that no evidence for structural changes, ligand exchange or metal oxo framework degradation is evident. (b) Square wave voltammetry (SWV) of $\{Mn_4V_4\}$, MeCN : H_2O solutions at varying water content (0–5 vol%), $f = 25$ Hz, $E_{SW} = 25$ mV, $E_{step} = 2$ mV containing 0.2 mM $\{Mn_4V_4\}$ and 0.1 M nBu$_4$NPF$_6$ as electrolyte.

$[Mn_4^{4+}]$ redox reaction and (ii) the acetate ligand exchange reaction with water to generate the water-binding species required for subsequent O–O bond formation and oxygen evolution. Note that more complex reaction paths (including protonation or partial/full metal oxo framework hydrolysis) are principally possible but are not considered here, based on the stability studies discussed above.

To determine which redox pathways dominate at different water concentrations, the experimental redox potentials of the oxidation reaction P1 and P2 were determined at different MeCN : H_2O ratios as a basis for subsequent theoretical calculations. To this end, we employed SWV that eliminates the capacitive current component and thus is by a few orders of magnitude more sensitive than cyclic voltammetry (CV). By varying pulse frequency and pulse amplitude and recording the forward and backward scan, information on reaction mechanism and kinetics can be obtained.[64] In the context of this study, plotting the difference of the forward and reverse current against potential gives well-defined SWV peaks (Fig. 1c, 2b and ESI Fig. S2–S5†). These mark the experimental oxidation potentials, which can subsequently be used to compare with the calculated values derived from theory.[65] Square wave voltammograms were recorded for the native cluster (oxidation state $[Mn_2^{3+}Mn_2^{4+}]$) in MeCN : H_2O solutions (containing 0.1 M nBu$_4$NPF$_6$ as electrolyte) with the water content varied from 0–5 vol%. Each electrochemical experiment (*i.e.*, each MeCN : H_2O ratio) was performed using a freshly prepared catalyst solution and freshly cleaned electrodes to ensure maximum reliability and reproducibility. Each measurement was performed in triplicate. All data given are referenced against a Ag/AgCl (3.5 M) reference electrode.

In water-free, MeCN, the SWV results (Fig. 1c and 2b) correspond to the CV signals originally observed (ESI, Fig. S1†), showing an oxidative wave for the $[Mn_2^{3+}Mn_2^{4+}] \rightarrow [Mn^{3+}Mn_3^{4+}]$ transition at 0.45 V (labeled P1 in Fig. 2b), and the $[Mn^{3+}Mn_2^{4+}] \rightarrow [Mn_4^{4+}]$ transition at 1.45 V (P2 in Fig. 2b). When increasing the water content to 5 vol%, we observed a positive potential shift of 80 mV. In addition, the current associated with P1 initially increases when going from 0% to 1% water content. At higher water content, the P1 current decreases again as shown in Fig. 2b. With increasing water content, P2 shows a significant decrease in current, while simultaneously three new signals at less positive potentials appear. The signals are labelled in their order of appearance: P3 (1.05 V), P4 (1.25 V), and P5 (0.70 V), see Fig. 2b and ESI Fig. S2.† Initial data interpretation suggests, that the $[Mn^{3+}Mn_3^{4+}] \rightarrow [Mn_4^{4+}]$ transition is strongly influenced by the presence of water, leading us to suggest that for the one-electron oxidized species $[Mn^{3+}Mn_3^{4+}]$, there may be two competing reaction pathways, *i.e.*, further oxidation (to give $[Mn_4^{4+}]$) or acetate-to-water ligand exchange.

Based on these experimental data, we now use theory to calculate reaction energies and activation barriers to unravel which of the two plausible mechanisms—proposed in Scheme 1— follows the first $[Mn_2^{3+}Mn_2^{4+}] \rightarrow [Mn^{3+}Mn_3^{4+}]$ oxidation (Ox) step. In mechanism I (green in Scheme 1), the first oxidation is followed by the acetate ligand exchange (LEx) with water, after which the second $[Mn^{3+}Mn_2^{4+}] \rightarrow [Mn_4^{4+}]$ oxidation step (Ox) takes place (globally summarized as Ox–LEx–Ox). In mechanism II (red), the first and second oxidations occur before the acetate ligand exchange (summarized as Ox–Ox–LEx). As the highest reactivity (based on turnover frequencies and electrochemical current densities) was observed in a 9 : 1 MeCN : H_2O (v/v) mixture,[19] these calculations were carried out considering the same solvent composition.

The X-ray structrure of the native catalyst[19] has an idealized C_{3v} symmetry (due to the appearence of delocalized electrons on the Mn-centres), so that in the $[Mn_4O_4]$ cubane (Fig. 1b), Mn1 is located on the C_3 axis, while the three manganese centers Mn2, Mn3 and Mn4 are symmetry equivalent. However, when considering the electronic structure of the one-electron-oxidized species $[Mn^{3+}Mn_3^{4+}]$, the crystallographic C_{3v} symmetry[19] is lowered due to the presence of three Mn^{4+} centers and one Mn^{3+} center (which could correspond to any of the four Mn positions). Furthermore, Mn^{3+} (d^4) ions in an octahedral environment show Jahn–Teller (JT) distortions, with one of the axes – the JT axis – elongated and the other two shortened. Such JT distortions have previously been identified in the analogous

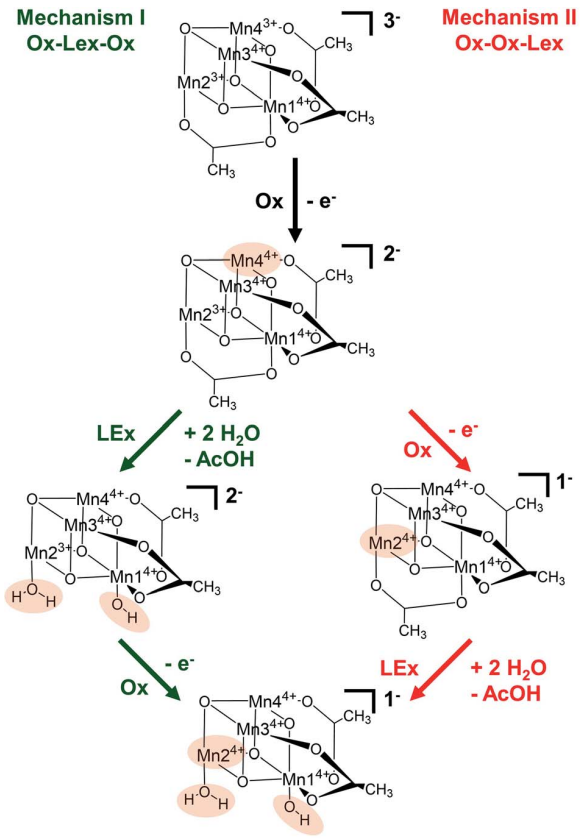

Scheme 1 Schematic representation of the two proposed reaction mechanisms (I and II) involving oxidation (Ox) and ligand exchange (LEx) of the catalyst. Chemical changes relative to the previous step are highlighted in beige. Note that all calculations showed that the acetate ligand dissociates as a protonated acetic acid molecule due to the higher basicity of acetate compared with water. Thus, in both reactions the calculations show that the acetate is replaced by a H_2O and an OH ligand.

S_2 oxidation state of the OEC,[66,67] and in other related model complexes.[28,61,68] The JT distortion implies that for each possible position of the Mn^{3+} ion, there are three possible JT axes, giving rise to three different structures. Due to the symmetry equivalence of Mn2, Mn3 and Mn4, we only have to consider localization of the Mn^{3+} ion at the positions Mn1 or Mn2, resulting in six possible structures (Fig. S6†). Accordingly, we performed geometry optimizations based on the six possible locations of the JT axes. In all cases, the geometries converged towards a minimum where the Mn^{3+} was localized at the Mn2 position, and the JT axis pointed along the Mn–acetate bond (red axis in Fig. 1b). This minimum energy structure was used hereafter. However, identifying the preferred JT axis localization does not yield any information on the acetate-to-water ligand exchange step, which could still occur at any of the Mn centers. Accordingly, in both mechanisms I and II, several ligand exchange pathways need to be considered (depicted in Fig. 3 and labelled (a)–(e)). The resulting intermediates and transition states (TS),

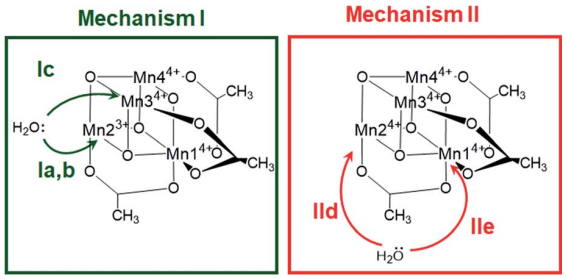

Fig. 3 Possible water attack sites for the proposed ligand exchange pathways in mechanism I (Ox–LEx–Ox) and mechanism II (Ox–Ox–LEx), labelled (a)–(e).

together with their associated Gibbs free energies (Table S2†) and spin assignments (Tables S3 and S4†), are shown in Fig. 4.

Both ligand exchange pathways Ia and Ib involve the nucleophilic attack of the first water molecule at the Mn2 center, and the second water molecule at the Mn1 center. The first step of pathway Ia (Fig. 4, green solid line) is the ligand exchange of one oxygen donor of the acetate group by a water molecule at $Mn2^{3+}$ (step 1a → 2a) with an activation barrier of 7.3 kcal mol^{-1} (TS1a/b). A sequential intramolecular electron transfer (ET) from Mn2 to Mn1 takes place (2a → 3a), followed by a proton transfer (PT) from the coordinated water molecule to the acetate ligand (3a → 4a), resulting in the formation of a Mn–OH group. This PT reaction is not water mediated (unlike analogous PT reactions reported by Maksimchuk *et al.*[69]) as the second water molecule does not actively participate in it. The second acetate ligand exchange at $Mn1^{3+}$ (4a → 5a) represents the rate determining step of this path, with an activation Gibbs free energy of 8.0 kcal mol^{-1} (TS2a). Finally, an intramolecular concerted electron-proton transfer (5a → 6a) gives rise to a more stable product featuring one Mn–OH_2 and one Mn–OH group, where the JT axis is again localized on the Mn2 atom.

The initial step of pathway Ib (Fig. 4, green dashed line) is identical to pathway Ia (1b → 2b). However, the second ligand exchange occurs at $Mn1^{4+}$ (2b → 3b) *via* TS2b to give 3b, which is identical to 6a. Although thermodynamically possible, this pathway is kinetically unfavorable with an activation barrier of 26.7 kcal mol^{-1} and is therefore disregarded.

Pathway Ic (Fig. 4, green dashed-dotted line) starts with the nucleophilic attack of a water molecule at a Mn^{4+} atom (either the symmetry equivalent Mn3/Mn4 or Mn1). The attack on Mn3/4 gives an activation barrier of 21 kcal mol^{-1} (1c → TS1c → 2c). During the second ligand exchange, a proton is transferred from a Mn-coordinated water molecule to the departing acetate ligand, forming a Mn^{4+}–OH moiety. This step (2c → 3c) presents a prohibitively high activation barrier of 33.1 kcal mol^{-1} (TS2c). An additional ligand exchange pathway initiated by water attacking the Mn1 center has not been explored further as no transition states for this pathway were found.

Pathways IId and IIe describe the ligand exchange within mechanism II, *i.e.*, after the oxidation to [Mn_4^{4+}] has taken place. The first ligand exchange can either occur at $Mn2^{4+}$ (pathway IId, Mn3 and Mn4 are symmetry equivalent to Mn2) or

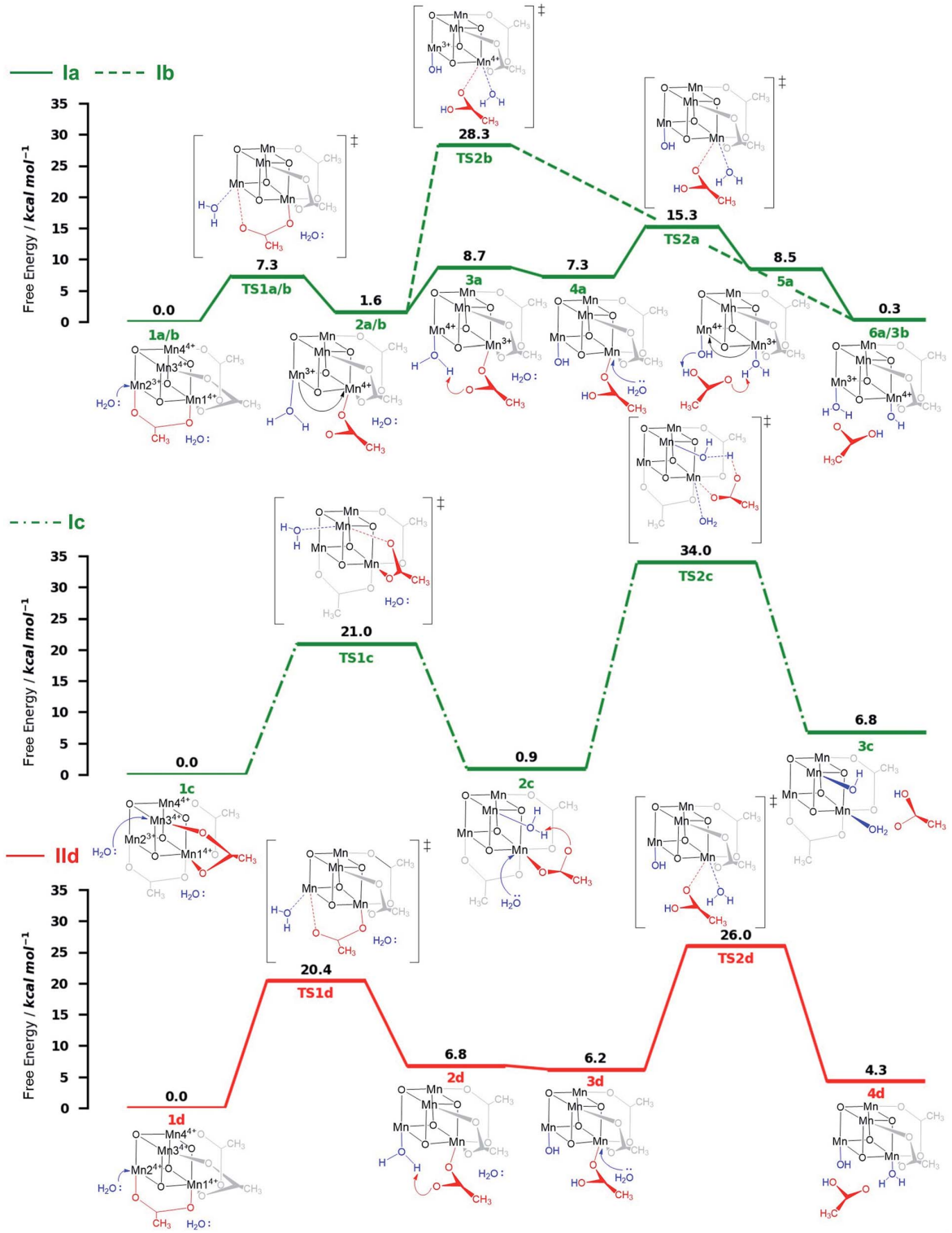

Fig. 4 Energy diagrams (ΔG free energy in kcal mol^{-1}) of the ligand exchange pathways studied at the B3LYP-D3/Def2-TZVP(Mn,V,O)-Def2-SVP(C,H)//B3LYP-D3/Def2-SVP level of theory with implicit solvent in a 9 : 1 MeCN : H_2O ratio. Oxidation numbers at the Mn-cubane are only shown where they change. Pathways Ia–Ic (green) correspond to ligand exchange reactions which occur before the second oxidation step (Ox–LEx–Ox); pathway IId (red) corresponds to ligand exchange which occurs after the second oxidation process (Ox–Ox–LEx). The structures below and above each energy diagram are reaction intermediates and transition states, respectively. Energies are given relative to the reactant species.

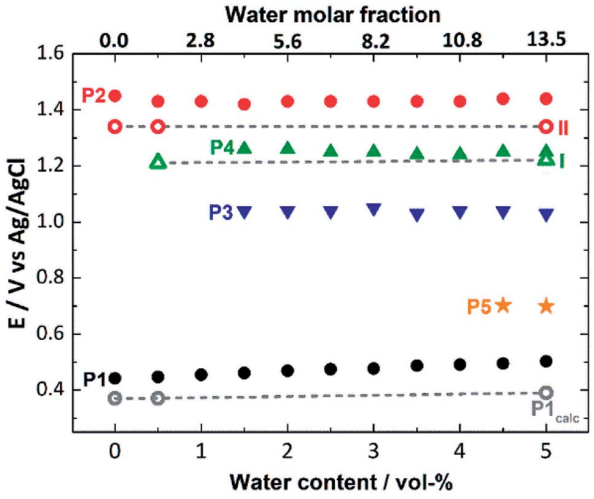

Fig. 5 Comparison of experimental (full symbols) and theoretical (empty symbols, linked by gray dashed lines) oxidation potentials for the processes P1 to P5 (also see Fig. 2), depending on the water content (0–5 vol%) of the SWV electrolyte.

at $Mn1^{4+}$ (pathway IIe). The first ligand exchange in pathway IId (1d → 2d) has a barrier of 20.3 kcal mol^{-1} (TS1d) and is thus the rate limiting step. This step is followed by PT from the coordinated water to the acetate ligand (2d → 3d), generating again an OH group coordinated to Mn2. The second ligand exchange occurs at Mn1 with an activation barrier of 19.8 kcal mol^{-1} (TS2d). The structures and energetics of pathway IIe are very similar to those of pathway IId and thus are only shown in the ESI (Fig. S7†).

Pathways Ia and Ib are the most thermodynamically favorable ones with a total reaction free energy of 0.3 kcal mol^{-1}. However, pathway Ib presents a very large energy barrier of 26.7 kcal mol^{-1} in the process 2b→3b *via* TS2b, in contrast to the 8 kcal mol^{-1} of pathway Ia in the step 4a → 5a *via* TS2a. The low barriers found only in pathway Ia appear to result from both acetate ligand exchange steps taking place at the Mn^{3+} centers, mirroring behavior observed in the OEC.[28] Furthermore, all substitutions at Mn^{3+} centers occur along their JT axis, so that it is plausible to infer that the lower energy barriers evidenced for these ligand substitutions are associated with the elongated Mn^{3+}–O bond being easier to cleave, with respect to its shorter Mn^{4+}–O counterpart (see also Table S5†).

The calculations thus suggest that ligand exchange in mechanism I (Ox–LEx–Ox) is most likely to occur *via* pathway Ia. Concerning mechanism II (Ox–Ox–LEx), pathways IId and IIe have reaction free energies of 4.3 and 3.9 kcal mol^{-1}, respectively, and are less favorable than pathways Ia and Ib, albeit still thermodynamically feasible. However, their large activation barriers (>20 kcal mol^{-1}) make them both kinetically unfavorable. Interestingly, all pathways investigated end in a species with a water and an OH group as ligands.

Next, we used this detailed theoretical assessment to gain further insight into the catalyst activation by correlating theoretically calculated redox potentials with the experimental SWV data measured at different solvent water contents (Fig. 5, Table S6†). Since P1 can be unambiguously assigned to the $[Mn_2^{3+}Mn_2^{4+}] \rightarrow [Mn^{3+}Mn_3^{4+}]$ oxidation, the value of the redox potential obtained theoretically provides an estimate of the errors involved. Based on three calculated MeCN : H_2O ratios, the mean error in P1 is 0.09 V, which shows good agreement between theory and experiment and is in line with the literature.[70–72] In addition, the shift of the experimental redox-potential to more positive values (80 mV when going from 0 vol% to 5 vol% water content, Fig. 5, black dots) is qualitatively reproduced by theory, where a shift of 20 mV (between 0 vol% and 5 vol% water content) is calculated (Fig. 5, gray dashed line).

The experimental P2 signal (1.45 V at 0 vol% water content) can then be assigned to the $[Mn^{3+}Mn_3^{4+}] \rightarrow [Mn_4^{4+}]$ transition, as acetate-to-water ligand exchange cannot occur under water-free conditions. Comparison with the theoretical potential calculated in mechanism II (Ox–Ox–LEx, 1.34 V) gives a good agreement (mean error: 0.1 V). In the presence of water, the Ox–LEx–Ox mechanism I becomes possible, and our redox calculations predict that the $[Mn^{3+}Mn_3^{4+}] \rightarrow [Mn_3^{4+}]$ oxidation following the most favorable pathway Ia in mechanism I (Scheme 1) will occur at a potential of 1.22 V. This is in line with the appearance of the new oxidation peak P4 (1.25 V, mean error 0.03 V) in the presence of water (Fig. 5). To gain further insights into the correlation between peaks P2 and P4, variable-frequency SWV analyses were used. This method (in analogy to scan rate variation in CV) allows frequency-dependent study of the kinetics of electron transfer processes, while retaining the advantages of SWV over CV. Variation of the SWV frequency between 5 and 50 Hz showed that with increasing frequency (analogous to higher scan rate in CV), process P2 is partially recovered (ESI, Fig. S4†). This is in line with the interpretation that at higher SWV frequencies, the oxidation step to $[Mn_4^{4+}]$ (ESI, Fig. S3,† step 2a) can now compete with the acetate-to-water ligand exchange (ESI, Fig. S3,† step 2b). Note that this suggestion is also in agreement with our initial hypothesis that under the given electrochemical conditions, ligand exchange occurs only after the $[Mn_2^{3+}Mn_2^{4+}] \rightarrow [Mn^{3+}Mn_3^{4+}]$ oxidation. This is also supported by IR-spectroscopic data described earlier (Fig. 2a) and will in the future be studied by *in situ* spectroelectrochemistry. Finally, the experimentally observed redox peaks P3 and P5 are at this point assigned to intermediate, electrode-surface-adsorbed species (ESI, Fig. S5†), which will be analyzed in more detail in a follow-up study.

In summary, these data support the hypothesis that mechanism I is most favorable at the given experimental conditions following these steps: (i) $[Mn_2^{3+}Mn_2^{4+}] \rightarrow [Mn^{3+}Mn_3^{4+}]$ oxidation, (ii) acetate for water ligand exchange and deprotonation of one water ligand, according to pathway Ia, and (iii) $[Mn^{3+}Mn_3^{4+}] \rightarrow [Mn_4^{4+}]$ oxidation, *i.e.* Ox–LEx–Ox.

Conclusions

This work presents theoretical and experimental insights into the redox and ligand exchange processes of the initial activation steps of the molecular manganese vanadium oxide water

oxidation catalyst $[Mn_4V_4O_{17}(AcO_3)]^{3-}$. Extensive DFT calculations were used to model redox properties and the ligand exchange pathways of the catalyst prior to entering the water oxidation cycle. We demonstrate that the currently most plausible activation mechanism involves a one-electron oxidation of the catalyst $[Mn_2^{3+}Mn_2^{4+}] \rightarrow [Mn^{3+}Mn_3^{4+}]$, followed by acetate-to-water ligand exchange and a second one-electron oxidation from $[Mn^{3+}Mn_3^{4+}]$ to $[Mn_4^{4+}]$. The ligand exchange pathways investigated show that the kinetically most favorable pathway is characterized by two nucleophilic attacks of water molecules along the Jahn–Teller axis of Mn^{3+} centers. Theory predicts that the oxidized species $[Mn_4V_4O_{17}(OAc)_2(H_2O)(OH)]^-$ features one H_2O and one OH ligand, as a result of deprotonation of one water ligand and proton transfer to the leaving acetate group during the ligand exchange. The final products derived from the proposed mechanism allowed us to calculate redox potentials that are in excellent agreement with electrochemical measurements carried out at various solvent compositions, supporting our speciation assignment. This study therefore offers a comprehensive understanding of the complex interplay between electronic structure, redox chemistry, and acid–base ligand exchange in molecular metal-oxide water oxidation catalysts. Further, we provide a blueprint for how experimental electrochemistry and IR spectroscopy together with theoretical calculations can be utilized to explore complex mechanisms in multi-electron catalytic systems. We expect similar studies to guide the design of advanced mixed metal oxide water oxidation catalysts. Future work will focus on studying the speciation of the catalyst at higher oxidation states as a starting point for the water oxidation cycle.

Data availability

Inputs/outputs as well as experimental results are available upon reasonable request.

Author contributions

LG and CS designed the study. GC, DHC, and LS performed and analyzed the calculations. JJN, PM and LG supervised the theoretical work. IT synthesised the compound. JK, RS, SK and BM provided IR-spectroscopic analyses. IT, GL, CK and CS provided electrochemical analyses. GC, DHC and IT wrote the original draft. CS and LG reviewed and edited the manuscript. All authors discussed and commented on the manuscript. LG, CS, BM and CK acquired funding.

Conflicts of interest

There are no conflicts to declare.

Acknowledgements

This work is funded by the Deutsche Forschungsgemeinschaft DFG (TRR234 "CataLight", project ID 364549901 (projects B3, C2, C3 and C4) and project STR1164/4), the Austrian Science Fund FWF (project no. I3987-N28) and the Comunidad de Madrid through the Attraction of Talent Program 2018 (Grant Ref. 2018-T1/BMD-10261). The Vienna Scientific Cluster is thanked for generous computational resources. Prof. Vera Krewald (TU Darmstadt) is acknowledged for initial fruitful discussions about the catalyst computations.

References

1 R. Matheu, P. Garrido-Barros, M. Gil-Sepulcre, M. Z. Ertem, X. Sala, C. Gimbert-Suriñach and A. Llobet, *Nat. Rev. Chem.*, 2019, **3**, 331–341.
2 M. D. Kärkäs, O. Verho, E. V. Johnston and B. Åkermark, *Chem. Rev.*, 2014, **114**, 11863–12001.
3 J. Kern, R. Chatterjee, I. D. Young, F. D. Fuller, L. Lassalle, M. Ibrahim, S. Gul, T. Fransson, A. S. Brewster, R. Alonso-Mori, R. Hussein, M. Zhang, L. Douthit, C. de Lichtenberg, M. H. Cheah, D. Shevela, J. Wersig, I. Seuffert, D. Sokaras, E. Pastor, C. Weninger, T. Kroll, R. G. Sierra, P. Aller, A. Butryn, A. M. Orville, M. Liang, A. Batyuk, J. E. Koglin, S. Carbajo, S. Boutet, N. W. Moriarty, J. M. Holton, H. Dobbek, P. D. Adams, U. Bergmann, N. K. Sauter, A. Zouni, J. Messinger, J. Yano and V. K. Yachandra, *Nature*, 2018, **563**, 421–425.
4 Y. Umena, K. Kawakami, J.-R. R. Shen and N. Kamiya, *Nature*, 2011, **473**, 55–60.
5 G. C. Dismukes, R. Brimblecombe, G. A. N. Felton, R. S. Pryadun, J. E. Sheats, L. Spiccia and G. F. Swiegers, *Acc. Chem. Res.*, 2009, **42**, 1935–1943.
6 X. Liu and F. Wang, *Coord. Chem. Rev.*, 2012, **256**, 1115–1136.
7 H. B. Lee, A. A. Shiau, P. H. Oyala, D. A. Marchiori, S. Gul, R. Chatterjee, J. Yano, R. D. Britt and T. Agapie, *J. Am. Chem. Soc.*, 2018, **140**, 17175–17187.
8 J. S. Kanady, P.-H. Lin, K. M. Carsch, R. J. Nielsen, M. K. Takase, W. A. Goddard and T. Agapie, *J. Am. Chem. Soc.*, 2014, **136**, 14373–14376.
9 B. M. Hunter, H. B. Gray and A. M. Müller, *Chem. Rev.*, 2016, **116**, 14120–14136.
10 L. Cronin and A. Müller, *Chem. Soc. Rev.*, 2012, **41**, 7325–7648.
11 H. Lv, Y. V. Geletii, C. Zhao, J. W. Vickers, G. Zhu, Z. Luo, J. Song, T. Lian, D. G. Musaev and C. L. Hill, *Chem. Soc. Rev.*, 2012, **41**, 7572–7589.
12 A. Sartorel, M. Carraro, F. M. Toma, M. Prato and M. Bonchio, *Energy Environ. Sci.*, 2012, **5**, 5592–5603.
13 H. Dau, C. Limberg, T. Reier, M. Risch, S. Roggan and P. Strasser, *ChemCatChem*, 2010, **2**, 724–761.
14 A. Sartorel, M. Carraro, G. Scorrano, R. De Zorzi, S. Geremia, N. D. McDaniel, S. Bernhard and M. Bonchio, *J. Am. Chem. Soc.*, 2008, **130**, 5006–5007.
15 Y. V. Geletii, B. Botar, P. Kögerler, D. a. Hillesheim, D. G. Musaev and C. L. Hill, *Angew. Chem., Int. Ed.*, 2008, **47**, 3896–3899.
16 Q. Yin, J. M. Tan, C. Besson, Y. V. Geletii, D. G. Musaev, A. E. Kuznetsov, Z. Luo, K. I. Hardcastle and C. L. Hill, *Science*, 2010, **328**, 342–345.
17 M. Blasco-Ahicart, J. Soriano-Lopez, J. J. Carbo, J. M. Poblet and J. R. Galan-Mascaros, *Nat. Chem.*, 2018, **10**, 24–30.

18 R. Al-Oweini, A. Sartorel, B. S. Bassil, M. Natali, S. Berardi, F. Scandola, U. Kortz and M. Bonchio, *Angew. Chem., Int. Ed.*, 2014, 11182–11185.
19 B. Schwarz, J. Forster, M. K. Goetz, D. Yücel, C. Berger, T. Jacob and C. Streb, *Angew. Chem., Int. Ed.*, 2016, **55**, 6329–6333.
20 J. J. Stracke and R. G. Finke, *ACS Catal.*, 2014, **4**, 909–933.
21 D. Gao, I. Trentin, L. Schwiedrzik, L. González and C. Streb, *Molecules*, 2020, **25**, 157.
22 J. W. Vickers, H. Lv, J. M. Sumliner, G. Zhu, Z. Luo, D. G. Musaev, Y. V. Geletii and C. L. Hill, *J. Am. Chem. Soc.*, 2013, **135**, 14110–14118.
23 D. Quiñonero, A. L. Kaledin, A. E. Kuznetsov, Y. V. Geletii, C. Besson, C. L. Hill and D. G. Musaev, *J. Phys. Chem. A*, 2010, **114**, 535–542.
24 J. Soriano-López, D. G. Musaev, C. L. Hill, J. R. Galán-Mascarós, J. J. Carbó and J. M. Poblet, *J. Catal.*, 2017, **350**, 56–63.
25 A. Sartorel, P. Miró, E. Salvadori, S. Romain, M. Carraro, G. Scorrano, M. Di Valentin, A. Llobet, C. Bo and M. Bonchio, *J. Am. Chem. Soc.*, 2009, **131**, 16051–16053.
26 C. Streb, Structure and Bonding in Molecular Vanadium Oxides: From Templates *via* Host–Guest Chemistry to Applications, in *Polyoxometalate-Based Assemblies and Functional Materials*, ed. Y.-F Song, Springer, Cham, 2018, vol. 176, DOI: 10.1007/430_2017_2.
27 F. L. Huber, S. Amthor, B. Schwarz, B. Mizaikoff, C. Streb and S. Rau, *Sustainable Energy Fuels*, 2018, **2**, 1974–1978.
28 P. E. M. Siegbahn, *J. Am. Chem. Soc.*, 2013, **135**, 9442–9449.
29 P. E. M. Siegbahn, *Phys. Chem. Chem. Phys.*, 2018, **20**, 22926–22931.
30 P. E. M. Siegbahn, *Chem.–Eur. J.*, 2006, **12**, 9217–9227.
31 A. D. Becke, *J. Chem. Phys.*, 1993, **98**, 5648–5652.
32 C. Lee, W. Yang and R. G. Parr, *Phys. Rev. B*, 1988, **37**, 785–789.
33 E. M. Sproviero, *J. Inorg. Biochem.*, 2017, **171**, 52–66.
34 T. Wang, G. Brudvig and V. S. Batista, *J. Chem. Theory Comput.*, 2010, **6**, 755–760.
35 M. Shoji, H. Isobe, T. Nakajima and K. Yamaguchi, *Chem. Phys. Lett.*, 2015, **640**, 23–30.
36 M. Shoji, H. Isobe, S. Yamanaka, M. Suga, F. Akita, J.-R. Shen and K. Yamaguchi, *Chem. Phys. Lett.*, 2015, **623**, 1–7.
37 H. Isobe, M. Shoji, S. Yamanaka, Y. Umena, K. Kawakami, N. Kamiya, J.-R. Shen and K. Yamaguchi, *Dalton Trans.*, 2012, **41**, 13727–13740.
38 K. Nishiki, N. Umehara, Y. Kadota, X. López, J. M. Poblet, C. A. Mezui, A. L. Teillout, I. M. Mbomekalle, P. De Oliveira, M. Miyamoto, T. Sano and M. Sadakane, *Dalton Trans.*, 2016, **45**, 3715–3726.
39 Z. L. Lang, G. C. Yang, N. N. Ma, S. Z. Wen, L. K. Yan, W. Guan and Z. M. Su, *Dalton Trans.*, 2013, **42**, 10617–10625.
40 A. E. Kuznetsov, Y. V. Geletii, C. L. Hill, K. Morokuma and D. G. Musaev, *J. Am. Chem. Soc.*, 2009, **131**, 6844–6854.
41 S. Piccinin and S. Fabris, *Phys. Chem. Chem. Phys.*, 2011, **13**, 7666–7674.
42 S. Piccinin, A. Sartorel, G. Aquilanti, A. Goldoni, M. Bonchio and S. Fabris, *Proc. Natl. Acad. Sci. U. S. A.*, 2013, **110**, 4917–4922.
43 S. Piccinin and S. Fabris, *Inorganics*, 2015, **3**, 374–387.
44 X.-F. Su, W. Guan, L.-K. Yan, Z.-L. Lang and Z.-M. Su, *J. Catal.*, 2019, **376**, 146–149.
45 X.-F. Su, L.-K. Yan and Z.-M. Su, *Inorg. Chem.*, 2019, **58**, 15751–15757.
46 F. Weigend and R. Ahlrichs, *Phys. Chem. Chem. Phys.*, 2005, **7**, 3297.
47 A. V. Marenich, C. J. Cramer and D. G. Truhlar, *J. Phys. Chem. B*, 2009, **113**, 6378–6396.
48 S. Grimme, J. Antony, S. Ehrlich and H. Krieg, *J. Chem. Phys.*, 2010, **132**, 154104.
49 M. Douglas and N. M. Kroll, *Ann. Phys.*, 1974, **82**, 89–155.
50 M. J. Frisch, G. W. Trucks, H. B. Schlegel, G. E. Scuseria, M. A. Robb, J. R. Cheeseman, G. Scalmani, V. Barone, G. A. Petersson, H. Nakatsuji, X. Li, M. Caricato, A. V. Marenich, J. Bloino, B. G. Janesko, R. Gomperts, B. Mennucci, H. P. Hratchian, J. V. Ortiz, A. F. Izmaylov, J. L. Sonnenberg, D. Williams-Young, F. Ding, F. Lipparini, F. Egidi, J. Goings, B. Peng, A. Petrone, T. Henderson, D. Ranasinghe, V. G. Zakrzewski, J. Gao, N. Rega, G. Zheng, W. Liang, M. Hada, M. Ehara, K. Toyota, R. Fukuda, J. Hasegawa, M. Ishida, T. Nakajima, Y. Honda, O. Kitao, H. Nakai, T. Vreven, K. Throssell, J. A. Montgomery Jr, J. E. Peralta, F. Ogliaro, M. J. Bearpark, J. J. Heyd, E. N. Brothers, K. N. Kudin, V. N. Staroverov, T. A. Keith, R. Kobayashi, J. Normand, K. Raghavachari, A. P. Rendell, J. C. Burant, S. S. Iyengar, J. Tomasi, M. Cossi, J. M. Millam, M. Klene, C. Adamo, R. Cammi, J. W. Ochterski, R. L. Martin, K. Morokuma, O. Farkas, J. B. Foresman and D. J. Fox, *Gaussian 16, Revision C.01*, Gaussian, Inc., Wallingford CT, 2016.
51 F. Neese, *Wiley Interdiscip. Rev.: Comput. Mol. Sci.*, 2018, **8**, e3127.
52 L. Noodleman, *J. Chem. Phys.*, 1981, **74**, 5737–5743.
53 E. Van Lenthe, J. G. Snijders and E. J. Baerends, *J. Chem. Phys.*, 1996, **105**, 6505–6516.
54 V. Barone and M. Cossi, *J. Phys. Chem. A*, 1998, **102**, 1995–2001.
55 A. V. Marenich, J. Ho, M. L. Coote, C. J. Cramer and D. G. Truhlar, *Phys. Chem. Chem. Phys.*, 2014, **16**, 15068–15106.
56 R. G. Bates and J. B. Macaskill, *Pure Appl. Chem.*, 1978, **50**, 1701–1706.
57 J. Ho, *Phys. Chem. Chem. Phys.*, 2015, **17**, 2859–2868.
58 J. Ho, A. Klamt and M. L. Coote, *J. Phys. Chem. A*, 2010, **114**, 13442–13444.
59 R. F. Ribeiro, A. V. Marenich, C. J. Cramer and D. G. Truhlar, *J. Phys. Chem. B*, 2011, **115**, 14556–14562.
60 V. Krewald, F. Neese and D. A. Pantazis, *Phys. Chem. Chem. Phys.*, 2016, **18**, 10739–10750.
61 V. Krewald and D. A. Pantazis, *Dalton Trans.*, 2016, **45**, 18900–18908.
62 C. A. Ohlin and M. Pascual-Borràs, *Dalton Trans.*, 2018, **47**, 13602–13607.

63 C. M. Julien, M. Massot and C. Poinsignon, *Spectrochim. Acta, Part A*, 2004, **60**, 689–700.
64 A. Chen and B. Shah, *Anal. Methods*, 2013, **5**, 2158–2173.
65 A. Molina, J. González, E. Laborda, Y. Wang and R. G. Compton, *Phys. Chem. Chem. Phys.*, 2011, **13**, 16748–16755.
66 N. Cox, M. Retegan, F. Neese, D. A. Pantazis, A. Boussac and W. Lubitz, *Science*, 2014, **345**, 804–808.
67 V. Krewald, M. Retegan, N. Cox, J. Messinger, W. Lubitz, S. DeBeer, F. Neese and D. A. Pantazis, *Chem. Sci.*, 2015, **6**, 1676–1695.
68 V. Krewald, F. Neese and D. A. Pantazis, *J. Am. Chem. Soc.*, 2013, **135**, 5726–5739.
69 N. V. Maksimchuk, I. D. Ivanchikova, G. M. Maksimov, I. V. Eltsov, V. Y. Evtushok, O. A. Kholdeeva, D. Lebbie, R. J. Errington, A. Solé-Daura, J. M. Poblet and J. J. Carbó, *ACS Catal.*, 2019, **9**, 6262–6275.
70 S. Schönweiz, M. Heiland, M. Anjass, T. Jacob, S. Rau and C. Streb, *Chem.–Eur. J.*, 2017, **23**, 15370–15376.
71 M. H. Anjass, K. Kastner, F. Nägele, M. Ringenberg, J. F. Boas, J. Zhang, A. M. Bond, T. Jacob and C. Streb, *Angew. Chem., Int. Ed.*, 2017, **56**, 14749–14752.
72 E. Falbo and T. J. Penfold, *J. Phys. Chem. C*, 2020, **124**, 15045–15056.

Supporting Information

Activation by oxidation and ligand exchange in a molecular manganese vanadium oxide water oxidation catalyst

Gustavo Cardenas,[a,b] Ivan Trentin,[c] Ludwig Schwiedrzik,[a] David Hernández-Castillo,[a] Grace A. Lowe,[c] Julian Kund,[d] Christine Kranz,[d] Sarah Klingler,[d] Robert Stach[d] Boris Mizaikoff,[d] Philipp Marquetand,[a,e] Juan J. Nogueira,[b,e] Carsten Streb,*[c] and Leticia González*[a,f]

a. Institute of Theoretical Chemistry, University of Vienna, Währinger Str. 17, 1090 Vienna, Austria.

b. Chemistry Department, Universidad Autónoma de Madrid, Calle Francisco Tomás y Valiente, 7, 28049 Madrid, Spain.

c. Institute of Inorganic Chemistry I, Ulm University, Albert-Einstein-Allee 11, 89081, Ulm, Germany.

d. Institute of Analytical and Bioanalytical Chemistry, Ulm University, Albert-Einstein-Allee 11, 89081 Ulm, Germany

e. IADCHEM, Institute for Advanced Research in Chemistry, Universidad Autónoma de Madrid, Madrid, Spain

f. Vienna Research Platform on Accelerating Reaction Discovery, University of Vienna Währinger Str. 17, 1090 Vienna, Austria

Table of Contents

S1. Electrochemistry

S2. Calculation of Ligand Exchange Pathways

S3. Calculation of Redox Potentials

S1. Electrochemistry

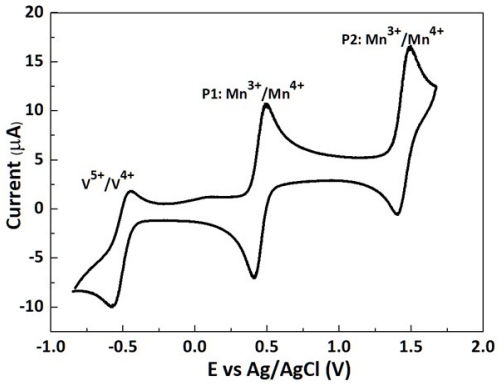

Figure S1. Exemplary cyclovoltammogram of the native cluster $\{Mn_4V_4\}$ (2 mM, oxidation state $[Mn^{3+}{}_2Mn^{4+}{}_2]$) in water-free MeCN solution (containing 0.1 M nBu$_4$NPF$_6$ as electrolyte) recorded at a glassy carbon electrode (3 mm diam.) scan rate: 50 mV/s vs. Ag/AgCl.

Square wave voltammetry

While cyclic voltammetry (CV) is a standard method to evaluate electron transfer kinetic data and reaction mechanisms in electrochemical experiments, square-wave voltammetry (SWV) offers significant advantages for the system studied here. In contrast to CV, where capacitive current may mask the faradaic signal for redox active species evolving at low concentration, SWV eliminates the capacitive current component as it is a differential method and thus achieves significantly higher sensitivity (up to at least 3 magnitudes, also see Figure S2).[1] In addition, recording the forward and backward scan and varying either the scan frequency *f* or the current amplitude E_{SW} allows the effective study of electron transfer kinetics and reaction mechanisms.[2] Depending on the experimental conditions, SWV can differentiate two or more closely spaced redox processes by providing a better peak separation (resolution) in comparison to CV. Hence, SWV was chosen here as electrochemical method to study the electrochemistry of $[Mn_4V_4O_{17}(OAc)_3]^{3-}$ (abbreviated hereafter as **{Mn$_4$V$_4$}**).

As shown in Figure S2, when comparing CV and SWV data for the first two oxidation redox processes (P1, P2) at different water concentrations, marked differences are observed. While the CV data is dominated by capacitive currents, the SWV data is more sensitive and allows observations of five distinguishable redox processes. Based on the CV data, the quasi-reversibility of P1 and P2 are observed. In addition, we note that the peak separation ΔE_p increases with increasing water content, see Table S1.

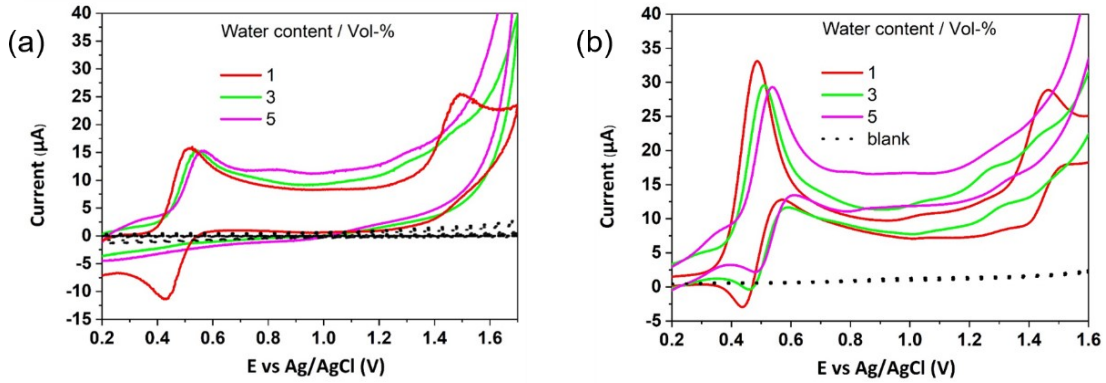

Figure S2: (a) CV of **{Mn$_4$V$_4$}** at 1, 3, 5 vol-% water content, scan rate = 50 mV/s; (b) SWV of **{Mn$_4$V$_4$}** at 1, 3, 5 vol-% water content *f*= 25 Hz, E_{SW} = 25 mV, E_{step}= 2 mV. Conditions: solvent: MeCN with added demineralized water and 0.1 M nBu$_4$NPF$_6$; **[{Mn$_4$V$_4$}]** = 2 Mm.

Table S1: CV peak separation depending on water content of the solvent

Water content / vol-%	ΔE_p, P1 / mV	ΔE_p, P2 / mV
0	73	90
1	84	>100[a]
2	>100[a]	-[b]

[a]reductive peak shows low S/N ratio; [b]reductive peak not observed

SWV analysis of the individual oxidation and ligand exchange processes

For the non-oxidized, native catalyst [$Mn^{3+}_2Mn^{4+}_2$], no acetate-to-water water ligand exchange is observed on the timescale of SWV experiments, as shown by time-dependent ATR-IR spectroscopy (Figure 2a in the ms). However, for the one-electron oxidized species [$Mn^{3+}Mn^{4+}_3$] electrochemical data and theory suggest that this ligand exchange is significantly faster. This is in line with SWV data, where the current of the second oxidation step P2 reduces significantly with increasing water content, while a new redox active species, P4, appears at slightly less positive potentials than P2. Theoretical data suggests that P4 could be due to the oxidation of the ligand-exchanged [$Mn^{3+}Mn^{4+}_3$], see Figure S3. In sum, these observations and calculations suggest that two independent oxidation paths, *i.e.* P2 (2nd oxidation step without ligand exchange) and P4 (ligand exchanged species that undergoes a second oxidation), are accessible starting from the non-ligand exchanged species [$Mn^{3+}Mn^{4+}_3$], see Figure S3.

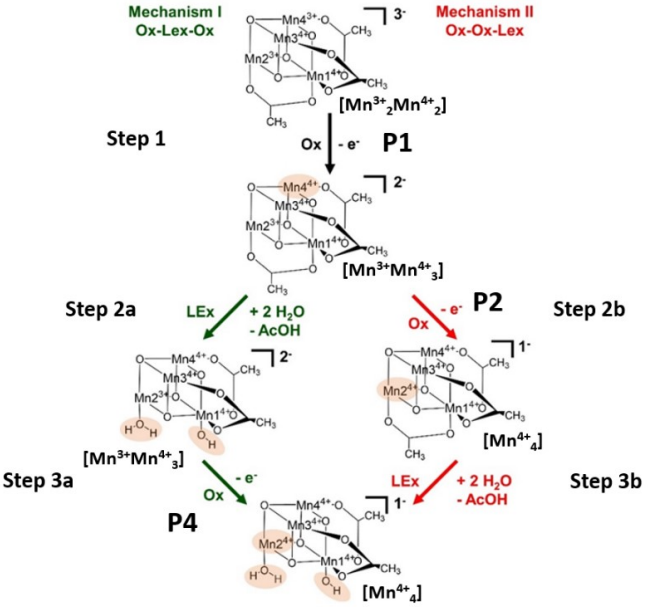

Figure S3: Proposed oxidation (Ox) and ligand exchange (LEx) mechanisms together with oxidation peak assignments P1, P2, P4. Also see discussion in main text.

The correlation of the peaks P2 and P4 was further investigated by variation of the SWV frequency. This method (in analogy to scan rate variation in CV) allows frequency-dependent analyses of electron transfer processes and their kinetics, while retaining the advantages of SWV over CV. Here, we used frequency-variation SWV to gain further insights into the observed electrochemical processes P1 – P5. Variation of the SWV frequency between 5 and 50 Hz showed that with increasing frequency (analogous to faster scan rate in CV), process P2 is partially recovered (Figure S4a,b). This is in line with the interpretation that at higher frequency, the [$Mn^{3+}Mn^{4+}_3$] → [Mn^{4+}_4] oxidation is preferred, as the rate constant for ligand exchange is lower than the electron transfer rate constant for

this oxidation step. (Figure S3, Step 2a). Thus, at high frequency, the oxidation can compete with the acetate-to-water ligand exchange, see Figure S3, Step 2b.

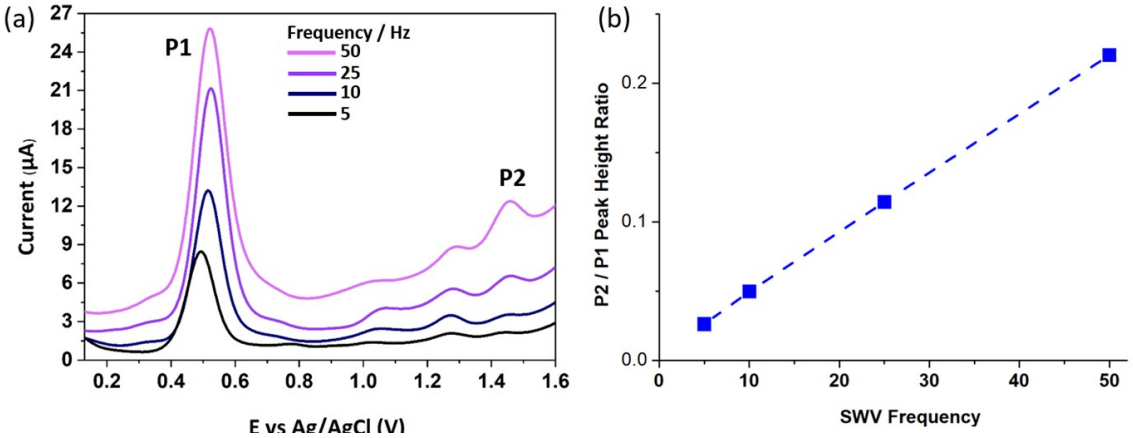

Figure S4: (a) Frequency-dependent SWV, with frequency variation from 5 Hz to 50 Hz, E_{SW} = 25 mV, E_{step} = 2 mV, [**{Mn_4V_4}**] = 2 mM, solvent: acetonitrile containing 3 vol-% water and 0.1 M $n$$Bu_4NPF_6$. (b) Ratio of P2 / P1 peak heights, showing the partial recovery of peak P2 at increasing SWV frequencies.

Analysis of 10 consecutive SWV scans shows decreasing currents which are indicative of surface deposition of {Mn_4V_4}-related species, as shown in Figure S5.

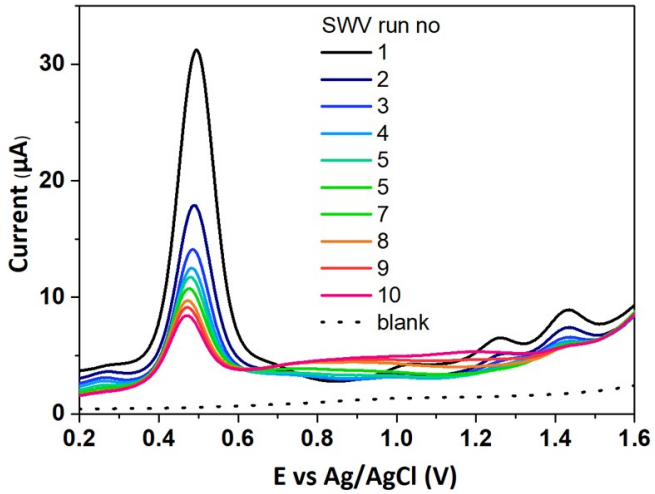

Figure S5: Ten consecutive SWV sweeps. Conditions: [**{Mn_4V_4}**] = 2 mM, f = 25 Hz, E_{SW} = 25 mV, E_{step} = 2 mV, solvent: acetonitrile containing 3 vol-% water and 0.1 M $n$$Bu_4NPF_6$.

S2. Calculation of ligand exchange pathways

In pathways Ia-Ic (Ox-LEx-Ox mechanism), the presence of a Mn^{3+} ion in an octahedral environment gives rise to Jahn-Teller (JT) distortions, elongating one bond axis (the JT axis) and shortening the other two. Due to the different positions where the Mn^{3+} ion could be located, but also due to the symmetry equivalence of the Mn2, Mn3 and Mn4 atoms (in the C_{3v} group), there are six possible orientations of the JT axis in the [$Mn^{3+}Mn^{4+}_3$] reactant species (Figure S6). For this reason, geometry optimizations were carried out starting from six guess structures, where elongated Mn-O bonds corresponding to each possible orientation of the JT axis were deliberately constrained. Upon releasing the constraints, all optimizations converged toward one structure, where the Mn^{3+} ion is Mn2, with the JT axis along the Mn-acetate bond (Figure S6, e).

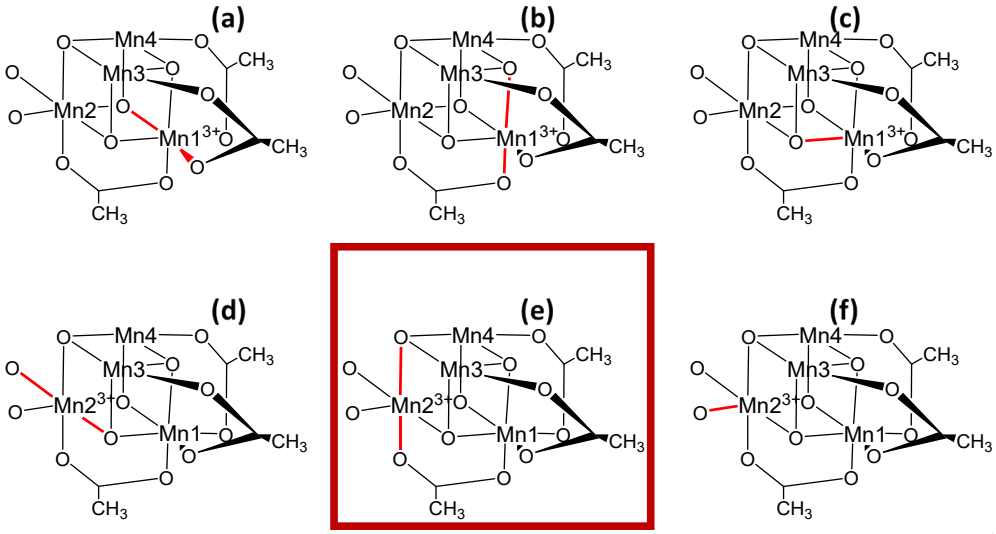

Figure S6. Schematic representation of the six possible orientations of the Jahn-Teller (JT) axis due to the presence of a Mn^{3+} ion. The geometry optimizations of the guess structures (Mn-O bonds deliberately elongated to constrain the localization of the JT axis are shown in red) converged in all cases towards the structure represented by (e).

All pathways Ia-Ic and IId-IIe were determined stepwise, by first optimizing the transition state (TS) of a ligand exchange reaction, followed by the optimization of the two intermediates connected by the TS using the two extrema of the oscillation associated with the imaginary frequency as guess structures for the reactant and the product. This process was repeated for the structures involved in the second ligand exchange reaction of each pathway. More specifically, for the TS determination we first performed a constrained geometry optimization, in which the atoms participating in the ligand substitution were frozen, followed by a relaxed TS optimization. The Gibbs free energies of all structures considered are collected in Table S2 and depicted in Figure 4 of the main manuscript (pathways Ia-Ic and IId), and Figure S7 (pathway IIe). Cartesian coordinates of all geometries are provided separately (file coordinates.pdf).

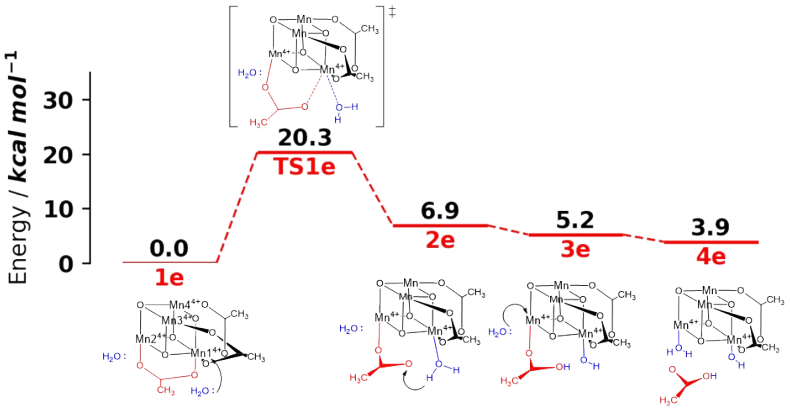

Figure S7. Energy diagram (ΔG free energy in kcal/mol) of the ligand exchange pathway IIe (Ox-Ox-LEx) studied at the B3LYP-D3/Def2-TZVP(Mn,V,O)-Def2-SVP(C,H)//B3LYP-D3/Def2-SVP level of theory. Oxidation numbers are only shown at the cubane center when they change. The structures below and above the energy diagram are reaction intermediates and transition states, respectively. Energies relative to the reactant species. Note that a species with a OH group and a H_2O molecule as ligands is formed.

Localization of the Mn^{3+} and Mn^{4+} ions is monitored along all pathways by inspecting Mulliken spin populations (Tables S3 and S4). Spin populations close to the ideal values of 4 and 3 correspond to Mn^{3+} and Mn^{4+} ions, respectively, so that electron transfer processes can be easily shown, *e.g,* as in **2a→3a**. These electron transfer processes can also be evinced structurally, by observing the Mn ion that presents a JT distortion characteristic of a Mn^{3+} ion. On the one hand, in **2a** the Mn2-OH_2 bond length is 2.17 Å and the parallel Mn2-O_{cub} bond (with a cubane oxygen atom O_{cub}) length amounts to 2.30 Å, whereas the Mn1-OAc bond is 1.90 Å, and the parallel Mn1-O_{cub} bond length amounts to 1.85 Å. On the other hand, for **3a** the analogous bonds involving Mn2 present distances of 1.96 Å (Mn2-OH_2) and 1.92 Å (Mn2-O_{cub}), whereas bonds involving Mn1 have bond lengths of 2.06 Å (Mn1-OH_2) and of 2.15 Å (Mn1-O_{cub}). The latter clearly evidences the JT axis displacement concomitant with the electron transfer process from Mn2 to Mn1 (see table S5 for a comprehensive list of all Mn-O bond lengths of the bonds involved in the ligand substitution reactions).

Table S2. Gibbs Free Energies (in kcal/mol) of all ligand exchange pathways studied in the present work.

Path Ia		**Path Ib**		**Path Ic**		**Path IId**		**Path IIe**	
Structure	**ΔG (kcal/mol)**	**Structure**	**ΔG (kcal/mol)**	**Structure**	**ΔG (kcal/mol)**	**Structure**	**ΔG (kcal/mol)**	**Structure**	**ΔG (kcal/mol)**
1a	0.0	1b	0.0	1c	0.0	1d	0.0	1e	0.0
TS1a	7.3	TS1b	7.3	TS1c	21.0	TS1d	20.4	TS1e	20.3
2a	1.6	2b	1.6	2c	0.9	2d	6.8	2e	6.9
3a	8.7	TS2b	28.3	TS2c	34.0	3d	6.2	3e	5.2
4a	7.3	3b	0.3	3c	6.8	TS2d	26.0	4e	3.9
TS2a	15.3					4d	4.3		
5a	8.5								
6a	0.3								

Table S3. Mulliken spin populations of the Mn ions of all structures involved in pathways in which the ligand exchange reactions occur before the oxidation reaction (Ox-LEx-OX).

Pathway	**Structure**	**Mn1**	**Mn2**	**Mn3**	**Mn4**
Ia and Ib	1a/1b	2.98	3.87	3.04	2.98
	TS1a/TS1b	2.97	3.90	3.05	2.98
	2a/2b	3.02	3.89	3.05	3.02
	TS2b	2.97	3.87	3.18	2.97
	3a	3.89	2.99	2.99	2.98
	4a	3.90	3.00	2.99	2.99
	TS2a	3.92	2.99	2.98	2.99
	5a	3.91	3.00	2.98	3.00
	6a	3.00	3.88	3.01	2.99
Ic	1c	3.01	3.87	3.06	3.01
	TS1c	3.14	3.88	3.06	3.02
	2c	3.03	3.88	3.06	3.01
	TS2c	3.03	3.86	3.16	2.97
	3c	3.03	3.88	3.08	3.02

Table S4. Mulliken spin populations of the Mn ions of all structures involved in pathways in which the ligand exchange reactions occur after the oxidation reaction (Ox-Ox-LEx).

Pathway	Structure	Mn1	Mn2	Mn3	Mn4
IId	1d/1e	3.06	2.95	2.93	2.93
	TS1d	3.03	3.05	2.92	2.92
	2d	3.03	2.96	2.95	2.94
	3d	3.07	2.95	2.95	2.95
	TS2d	3.17	2.96	2.94	2.93
	4d	3.07	2.96	2.95	2.95
IIe	TS1e	3.16	2.97	2.93	2.94
	2e	3.07	2.94	2.95	2.94
	3e	3.03	2.96	2.95	2.95
	4e	3.03	2.93	2.94	2.92

Table S5. Bond lengths of the Mn-O bonds involved in the ligand exchange reactions of all the intermediates involved in the pathways studied in this work. The bond lengths of the bonds breaking/formatting on the TS structures are not indicated, and are simply referred to as "TS bonds".

		Mn (VO-bound)		Mn (apex)	
Pathway	Species	Bond	Bond Length (Å)	Bond	Bond Length (Å)
Ia	1a/b	Mn2-OAc	2.19	Mn1-OAc	1.91
		Mn2-O_{cub}	2.31	Mn1-O_{cub}	1.86
	TS1a/b	Mn2 (TS bonds)		Mn1-OAc	1.89
		Mn2-O_{cub}	2.29	Mn1-O_{cub}	1.85
	2a/b	Mn2-OH	2.17	Mn1-OAc	1.90
		Mn2-O_{cub}	2.30	Mn1-O_{cub}	1.85
	3a/b	Mn2-OH	1.96	Mn1-OAc	2.06
		Mn2-O_{cub}	1.91	Mn1-O_{cub}	2.15
	4a	Mn2-OH	1.85	Mn1-OAc	2.13
		Mn2-O_{cub}	1.98	Mn1-O_{cub}	2.12
	TS2a	Mn2-OH	1.84	Mn1 (TS bonds)	
		Mn2-O_{cub}	2.00	Mn1-O_{cub}	2.12
	5a	Mn2-OH	1.84	Mn1-OH_2	2.18
		Mn2-O_{cub}	2.00	Mn1-O_{cub}	2.15
	6a	Mn2-OH_2	2.18	Mn1-OH	1.85
		Mn2-O_{cub}	2.30	Mn1-O_{cub}	1.88
Ib	TS2b	Mn2-OH_2	2.15	Mn1-O_{cub}	1.85
		Mn2-O_{cub}	2.32	Mn1 (TS bonds)	
Ic	1c	Mn3-OAc	2.00	Mn1-OAc	1.96
		Mn3-O_{cub}	1.87	Mn1-O_{cub}	1.84
	TS1c	Mn3 (TS bonds)		Mn1-OAc	1.90
		Mn3-O_{cub}	1.84	Mn1-O_{cub}	1.86
	2c	Mn3-OH_2	2.00	Mn1-OAc	1.92
		Mn3-O_{cub}	1.85	Mn1-O_{cub}	1.83
	TS2c	Mn3-OH_2	1.96	Mn1-O_{cub}	1.80
		Mn3-O_{cub}	1.87	Mn1 (TS bonds)	
	3c	Mn3-OH	1.91	Mn1-OH_2	2.00
		Mn3-O_{cub}	1.90	Mn1-O_{cub}	1.82

S3. Calculation of Redox Potentials

The redox processes considered were (also see step-labelling in Figure S3):

I. **Step 1**: First oxidation of the manganese vanadium oxide: $[Mn^{3+}{}_2Mn^{4+}{}_2]\rightarrow[Mn^{3+}Mn^{4+}{}_3] + e^-$

II. **Step 2b:** Second oxidation of the manganese vanadium oxide: $[Mn^{3+}Mn^{4+}{}_3]\rightarrow[Mn^{4+}{}_4] + e^-$

III. **Step 3a:** Second oxidation of the manganese vanadium oxide after ligand exchange and deprotonation (Step 2a): $[(Mn^{3+}Mn^{4+}{}_3)(H_2O)(OH)]\rightarrow[(Mn^{4+}{}_4)(H_2O)(OH)] + e^-$

IV. Second oxidation of the manganese vanadium oxide after ligand exchange only (for comparison): $[(Mn^{3+}Mn^{4+}{}_3)(H_2O)_2]\rightarrow[(Mn^{4+}{}_4)(H_2O)_2] + e^-$

For the species $[Mn^{3+}Mn^{4+}{}_3]$, $[Mn^{4+}{}_4]$, $[(Mn^{3+}Mn^{4+}{}_3)(H_2O)(OH)]$ and $[(Mn^{4+}{}_4)(H_2O)(OH)]$, initial guesses were taken from the ligand exchange pathway studies. In the native manganese vanadium oxide $[Mn^{3+}{}_2Mn^{4+}{}_2]$, it was found that the JT distortion is located along the Mn-acetate bond of two symmetry equivalent Mn^{3+}, see Figure S8. Thus, this configuration was used as an initial guess structure for the calculations.

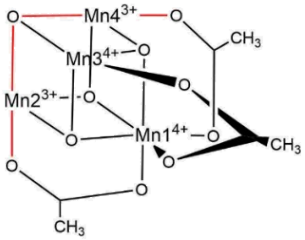

Figure S8. Schematic representation of the JT axes in the most stable configuration found for the $[Mn_3{}^{+2}Mn_4{}^{+2}]$ species.

The standard reduction potentials $\Delta E^{\circ}_{reduction}$ resulting from our calculations are in Table S6. No calculations were carried out at 0% water for the $[(Mn^{3+}Mn^{4+}{}_3)(H_2O)(OH)]\rightarrow[(Mn^{4+}{}_4)(H_2O)(OH)] + e^-$ reaction involving the manganese vanadium oxide with an H_2O and an OH ligand as well as the $[(Mn^{3+}Mn^{4+}{}_3)(H_2O)_2]\rightarrow[(Mn^{4+}{}_4)(H_2O)_2] + e^-$ reaction involving the manganese vanadium oxide with two H_2O ligands, as these species can only be formed in the presence of water. The significantly higher reduction potential of the reaction involving the species with two H_2O ligands (1.62 V on average) compared to that of the species involving an H_2O and an OH ligand that was predicted by our pathway calculations (1.22 V on average) further supports the conclusion that ligand exchange is most likely followed by immediate deprotonation, as seen in pathway Ia.

Table S6. Calculated standard reduction potentials $\Delta E^{\circ}_{reduction}$ for all redox processes and solvent compositions discussed in this section.

Reaction	0% water	0,5% water	5%water
$[Mn^{3+}{}_2Mn^{4+}{}_2]\rightarrow[Mn^{3+}Mn^{4+}{}_3] + e^-$	0.37	0.37	0.39
$[Mn^{3+}Mn^{4+}{}_3]\rightarrow[Mn^{4+}{}_4] + e^-$	1.34	1.34	1.34
$[(Mn^{3+}Mn^{4+}{}_3)(H_2O)(OH)]\rightarrow[(Mn^{4+}{}_4)(H_2O)(OH)] + e^-$	-	1.21	1.22
$[(Mn^{3+}Mn^{4+}{}_3)(H_2O)_2]\rightarrow[(Mn^{4+}{}_4)(H_2O)_2] + e^-$	-	1.62	1.62

Literature

1 A. Chen and B. Shah, *Anal. Methods*, 2013, **5**, 2158.
2 S. N. Vettorelo and F. Garay, *J. Solid State Electrochem.*, 2016, **20**, 3271–3278.

A.2 Flexibility Enhances Reactivity: Redox Isomerism and Jahn-Teller Effects in a Bioinspired Mn4O4 Cubane Water Oxidation Catalyst

LUDWIG SCHWIEDRZIK, VERA BRIESKORN, AND LETICIA GONZÁLEZ

ACS Catal., **2021**, 11, 13320-13329.
https://doi.org/10.1021/acscatal.1c03566

Contributions:

Ludwig Schwiedrzik designed the research, performed the research, analyzed the data, and wrote the paper.

Vera Brieskorn performed the research.

Leticia González designed the research and wrote the paper.

ACS Catalysis

pubs.acs.org/acscatalysis

Research Article

Flexibility Enhances Reactivity: Redox Isomerism and Jahn−Teller Effects in a Bioinspired Mn_4O_4 Cubane Water Oxidation Catalyst

Ludwig Schwiedrzik,* Vera Brieskorn, and Leticia González*

Cite This: *ACS Catal.* 2021, 11, 13320−13329

Read Online

ACCESS | Metrics & More | Article Recommendations | Supporting Information

ABSTRACT: Understanding how water oxidation to molecular oxygen proceeds in molecular metal-oxo catalysts is a challenging endeavor due to their structural complexity. In this report, we unravel the water oxidation mechanism of the highly active water oxidation catalyst $[Mn_4V_4O_{17}(OAc)_3]^{3-}$, a polyoxometalate catalyst with a $[Mn_4O_4]^{6+}$ cubane core reminiscent of the natural oxygen-evolving complex. Starting from the activated species $[Mn_4^{4+}V_4O_{17}(OAc)_2(H_2O)(OH)]^{1-}$, we scrutinized multiple pathways to find that water oxidation proceeds via a sequential proton-coupled electron transfer (PCET), O−O bond formation, another PCET, an intramolecular electron transfer, and another PCET resulting in O_2 evolution, with a predicted thermodynamic overpotential of 0.71 V. An in-depth investigation of the O−O bond formation process revealed an essential interplay between redox isomerism and Jahn−Teller effects, responsible for enhancing reactivity in the catalytic cycle. This is achieved by redistributing electrons between metal centers and weakening relevant bonds through Jahn−Teller distortions, introducing flexibility to the otherwise rigid cubane core of the catalyst. These mechanistic insights are expected to advance the design of efficient bioinspired Mn cubane water-splitting catalysts.

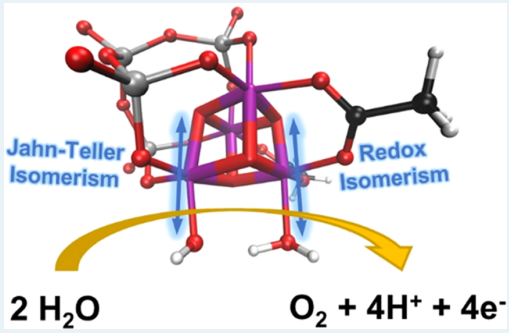

KEYWORDS: *artificial photosynthesis, polyoxometalate, Jahn−Teller axis, O−O bond formation, density functional theory*

INTRODUCTION

Climate change caused by the emission of anthropogenic CO_2 and other greenhouse gases into the atmosphere is one of the greatest challenges facing humanity today.[1,2] Among the many technologies being developed to reduce CO_2 emissions, artificial water splitting promises to replace fossil fuels with a clean-burning alternative, hydrogen gas.[3,4] Inspired by the natural process of photosynthesis, artificial water splitting aims to produce oxygen and hydrogen according to

$$2\,H_2O \rightarrow O_2 + 2\,H_2 \quad (1)$$

consisting of the half-reactions

$$2\,H_2O \rightarrow O_2 + 4\,H^+ + 4e^- \quad (2)$$

$$4\,H^+ + 4\,e^- \rightarrow 2\,H_2 \quad (3)$$

wherein eq 2 is referred to as water oxidation and eq 3 as hydrogen evolution.[5,6] Of the two, water oxidation is thermodynamically more challenging, as it comprises four one-electron oxidations and four deprotonations, usually assumed to be coupled.[6] This has inspired a massive research effort to come up with ever-more effective water oxidation catalysts (WOCs).[6−13]

In the development of synthetic molecular WOCs, a number of central design criteria have emerged:[6,10] (i) the WOC should catalyze water oxidation at a low thermodynamic overpotential, that is, the overall reaction potential should be overcome in four equal steps;[6,14,15] (ii) the WOC should be stable under the oxidative conditions typically found in experimental photo- or electrocatalytic water-splitting set-ups;[6,16] (iii) earth-abundant elements should be used for the metal centers to minimize the cost and environmental impact of future industrial-scale usage;[16] and (iv) every synthetic WOC is judged by its activity, with the ultimate goal of approaching or even surpassing the natural oxygen-evolving complex (OEC).[17,18]

Given this variety of difficult-to-reconcile goals, it is not surprising that the design of many WOCs is inspired by nature, attempting to copy one or several aspects of the OEC. As the OEC is centered on a Mn_3CaO_4 cubane structure with a dangling fourth Mn center,[19] such cubane structures have received considerable attention. In particular, Co cubane WOCs have been extensively studied both experimentally and

Received: August 7, 2021
Revised: September 28, 2021
Published: October 18, 2021

theoretically.[13,17,20] It was found that terminal Co-oxo or -oxyl groups play a central role in O−O bond formation on Co cubanes, with a variety of water oxidation cycles being described.[21−26] The relatively high water oxidation activity of these systems has been linked to the ability of cubanes to flexibly redistribute electrons between the metal centers.[23−25] A number of Mn cubane WOCs have also been investigated, often as model systems for the OEC.[18,27−31] In these model systems, it has been noted that Jahn−Teller (JT) effects present on Mn^{3+} centers can lead to significant distortions of the cubane[32−40] and even influence ligand exchange kinetics or oxidation pathways.[41,42] Such JT distortions arise from d^4 ions such as Mn^{3+} due to the energetically favorable splitting of the octahedral ligand field, resulting in the elongation and concomitant weakening of one bond axis (see Scheme 1).

Scheme 1. Reduction of Mn^{4+} Leads to the Emergence of Jahn−Teller (JT) Distortions Due to Splitting of the Octahedral Ligand Field in Mn^{3+}, Resulting in the Elongation and Weakening of One Bond Axis (Marked in Red)

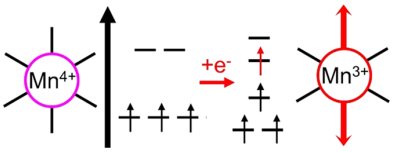

Here, we focus on a promising bioinspired catalyst, $[Mn_4V_4O_{17}(OAc)_3]^{3-}$, a highly active synthetic WOC with a TON > 12 000 and a TOF > 200 min^{-1}.[43,44] It consists of a Mn_4O_4 cubane core, surrounded on three sides by a multidentate V_4O_{13} vanadate ligand and three acetate ligands on the remaining sides (Figure 1a). A recent theoretical and experimental study[45] uncovered the activation mechanism of the precatalytic species $[Mn_2^{3+}Mn_2^{4+}V_4O_{17}(OAc)_3]^{3-}$, consisting of a one-electron oxidation, ligand exchange accompanied by deprotonation, and further one-electron oxidation, resulting in the activated species $[Mn_4^{4+}V_4O_{17}(OAc)_2(H_2O)(OH)]^{1-}$ (**1**) (Figure 1b). In that work, **1** was assigned an experimental redox potential of 1.25 V, which is below the onset of water oxidation observed at 1.6 eV under electrochemical conditions, suggesting that **1** initiates the water oxidation cycle. It was also found that during the acetate-to-water ligand exchange, the first water molecule attacks along the JT-distorted bond axis of Mn_B^{3+} (see Figure 1c), taking advantage of the weaker Mn^{3+}−OAc bond present at that metal center. A subsequent electron transfer from Mn_B to Mn_A allows the second water molecule to also attack a weak JT-distorted bond, resulting in a much lower reaction barrier than an attack at a Mn^{4+} center would (8.0 vs 26.7 kcal/mol). These findings hinted at a possible role of the JT axes controlling the reactivity of $[Mn_4V_4O_{17}(OAc)_3]^{3-}$.[45] It is well known that the OEC[41] sports a large variety of stable JT isomers (structures that differ in the relative orientation of their JT axes) at its lower oxidation states,[38] and in the S1 oxidation state, these favor oxidation leading to distinct redox isomers (structures that differ in the assignment of oxidation states to specific atoms) in the S2, possibly influencing the water oxidation cycle of the OEC.[42]

A detailed investigation of JT and redox isomers of the precatalytic and activated forms of $[Mn_4V_4O_{17}(OAc)_3]^{3-}$ at various oxidation states found that JT axes prefer an

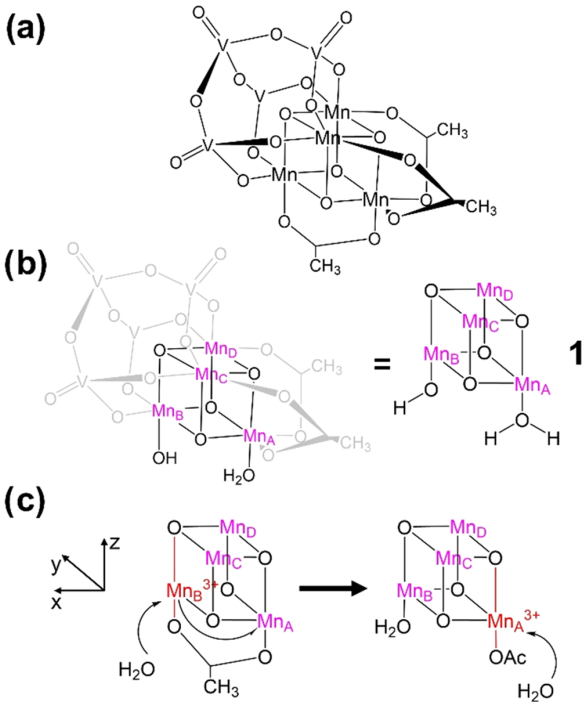

Figure 1. (a) Structural formula of the pristine water oxidation catalyst $[Mn_4V_4O_{17}(OAc)_3]^{3-}$. (b) Activated species $[Mn_4^{4+}V_4O_{17}(OAc)_2(H_2O)(OH)]^{1-}$ (**1**), with Mn^{4+} centers labeled A−D in purple (left). Abbreviated structure of **1** showing only the cubane core and reactive ligands (right). (c) Intermediates during catalyst activation with Mn^{3+} centers and Jahn−Teller (JT) axes marked in red: a redox isomerization (half arrow, left) lowers the barrier for the second water attack (full arrow, right), as the Mn_A^{3+}-OAc bond is weakened by JT distortion.

orientation toward the weaker acetate, water, or OH ligands over the stronger vanadate ligand.[46] Further, interconversion between redox isomers appears to be associated with low barriers (between 1.5 and 7.6 kcal/mol), while interconversion between JT isomers is almost barrierless (between 0.6 and 1.6 kcal/mol), showing that various redox and JT isomers can be easily accessed in the course of reactions on $[Mn_4V_4O_{17}(OAc)_3]^{3-}$.[46]

In this work, we unravel the water oxidation cycle for $[Mn_4V_4O_{17}(OAc)_3]^{3-}$ starting from **1**. Density functional theory (DFT) is used to optimize possible intermediates along multiple reaction pathways. A subsequent in-depth sampling of reaction intermediates revealed the multiple roles played by redox isomers and their JT effects in the water oxidation cycle, which introduce a high degree of structural flexibility to the otherwise rigid cubane core. These flexibility effects were further studied by optimizing the minimum energy paths (MEPs) for O−O bond formation including all stationary points, giving a complete picture of this important reaction step. These results are of general importance not only for understanding water oxidation on molecular catalysts but also for advancing the design of Mn-containing WOCs.

METHODS

In the first step, unconstrained geometry optimizations were carried out on guess structures representing possible

https://doi.org/10.1021/acscatal.1c03566
ACS Catal. 2021, 11, 13320−13329

intermediates of the reaction. As a starting point for the optimization of these guess structures, the activated species **1** was adapted by deleting hydrogen atoms as necessary. The different oxidation states of the reactive oxygen and manganese atoms were specifically targeted by adjusting the multiplicity and charge accordingly. Optimized structures and their Gibbs free energies were obtained using the Gaussian16 package[47] at the B3LYP/def2-SVP level of theory[48−50] with Grimme's D3 dispersion correction.[51] Solvent effects were accounted for by employing the Polarizable Continuum Model (PCM), an implicit solvation model;[52] the acetonitrile/H_2O 9:1 (v/v) solvent composition used in photocatalytic experiments[43,44] was approximated using the parameters for acetonitrile with a custom epsilon value of 41.589. All calculations were carried out on an all-atom model of the complex using the high-spin configuration.[53−55] Oxidation states of individual atoms are reported based on their computed Mulliken spin populations.

The results of these initial unconstrained optimizations indicated that both Mn^{3+} and Mn^{4+} centers play a role in the water oxidation mechanism of the cluster. As Mn^{3+} is a d^4 ion that shows JT distortions in an octahedral coordination environment, these effects were accounted for as follows. For each Mn^{3+} center in a given structure, three orientations of the elongated JT bond axis are possible: in the *x*-, *y*-, or *z*-direction. The global minimum on the potential energy surface is obtained by sampling all three possible JT orientations for each Mn^{3+} center, which results in a large number of distinct isomers.[34,38] We adopted the sampling procedure of ref 46, wherein individual isomers are obtained from guesses that used constrained preoptimizations; specifically, the two bonds corresponding to the desired JT axis for each Mn^{3+} center are elongated. Additionally, we sampled possible ligand conformers for each protonation state of the cluster. Constrained preoptimizations were carried out using the ORCA 4.2.1 package[56,57] at the BP86/def2-SVP level of theory,[50,58,59] with D3 dispersion correction[51] and PCM (acetonitrile);[52] the looseopt keyword was employed, as full convergence of these constrained structures was not required. All preoptimized structures were then subjected to an unconstrained optimization to obtain final geometries and energies, again using Gaussian16 at the B3LYP/def2-SVP level of theory. Final JT configurations of the intermediates were determined by comparing the lengths of Mn^{3+}−O bonds, with the two longest coaxial bonds indicating the *x*-, *y*-, or *z*-orientation of the JT axis on a given Mn^{3+} center. As in the precatalyst,[46] not every conceivable redox and JT isomer of an individual intermediate corresponds to a stable minimum on that intermediate's potential energy surface. In the following, only the most stable isomers for each intermediate in the proposed water oxidation cycle shall be discussed (see Table S1 for a list of all stable isomers and conformers).

Complex **1** and its various reaction intermediates show CS symmetry. No explicit symmetry was employed in our calculations; however, we did not consider symmetry-equivalent redox and JT isomers separately. Furthermore, isomers featuring JT axes oriented toward the vanadate ligand were not specifically targeted, as these had been previously found to be energetically unfavorable.[46]

To study the O−O bond formation, Climbing Image-Nudged Elastic Band (CI-NEB) calculations were carried out using the ORCA 5.0.0 package.[56,57] We used B3LYP[48,49] with the def2-SVP basis set,[50,60] employing D3 dispersion correction[51] and conductor-like PCM (acetonitrile)[52] with a custom epsilon value of 41.589 and surface type vdw_gaussian. All stationary points found by NEB calculations were optimized using Gaussian16 at the B3LYP/def2-SVP level of theory, as described above.

To ensure full convergence, the electronic energies of all species discussed herein were refined at the B3LYP/def2-TZVP level of theory. Taken together with thermochemical corrections obtained from frequency calculations at the B3LYP/def2-SVP level of theory at T = 298.150 K, we calculated final Gibbs free energies relative to **1** (unless otherwise noted). To account for differing protonation states between structures, an energy correction term is calculated using the approach proposed by Van Voorhis et al.,[7] wherein the standard free energy of a proton in solution is added for each proton removed from the cluster. To approximate the standard free energy of a proton in the acetonitrile/H_2O 9:1 (v/v) mixture used in the experiment, we used a 9:1 weighted average of the standard free energy of a proton in acetonitrile (11.0622 eV) and the standard free energy of a proton in water (11.5305 eV),[61] giving a value of 11.1090 eV for each proton transferred to the solution. A detailed breakdown of the final Gibbs free energies is provided in Table S2.

The thermodynamic limit of water oxidation is defined in this work as the free energy of the reaction (2), computed using B3LYP as 4.56 eV.[62] According to the Sabatier principle,[63] a thermodynamically ideal catalyst would overcome this limit in four equal steps, each with a potential of 1.14 eV. Thus, the overpotential of water oxidation using such an ideal catalyst would be entirely kinetic, possibly originating from the reaction barriers of O−O bond formation or O_2 evolution. In contrast, in a real catalyst, some intermediates are more stabilized than others, resulting in one potential step being larger than the others—the potential-determining step.[6] The thermodynamic overpotential η of water oxidation is defined as the difference between the potential-determining step of the real catalyst and the step size of an ideal catalyst[14,64]

$$\eta = \Delta G_{\text{real}}^{\max} - \Delta G_{\text{ideal}} \tag{4}$$

RESULTS AND DISCUSSION

The starting point of our study is the activated species $[Mn_4^{4+}V_4O_{17}(OAc)_2(H_2O)(OH)]^{1-}$ (**1**) (recall Figure 1b).[45] As **1** features cofacial H_2O and OH ligands in close proximity, we assume that water oxidation involves both ligands and their respective metal centers. While a variety of single-center mechanisms could also be imagined, here we focus exclusively on plausible multicenter mechanisms. The two ligands must formally undergo four oxidation and three deprotonation steps, which are assumed to be coupled[6] (i.e., three proton-coupled electron transfer (PCET) steps and one-electron transfer (ET) step). A priori, the order of these steps is unknown. As proton acceptors are readily available in solution under the photocatalytic conditions used in experiment (acetonitrile/H_2O 9:1 (v/v), $[Ru(bpy)_3]^{2+}$, $Na_2S_2O_8$),[43,44] deprotonation of the cluster is most likely carried out by the solvent.

Oxidation of the reactive H_2O and OH ligands could occur in two ways, either intermolecularly by an oxidizing agent present under photocatalytic conditions, i.e., $[Ru(bpy)_3]^{3+}$, or intramolecularly, with a concomitant reduction of each Mn^{4+} center to Mn^{3+}. In the case of intermolecular oxidation, the cluster would serve primarily as a structural support and activator of the ligands, without being directly involved in their redox chemistry. Alternatively, as all Mn centers are in the

https://doi.org/10.1021/acscatal.1c03566
ACS Catal. 2021, 11, 13320−13329

Mn^{4+} oxidation state in **1**, one can argue that the cluster is storing up to four redox equivalents (much like the OEC),[65] allowing intramolecular oxidation of the ligands to occur. Both possibilities were accounted for in our calculations for each step of the reaction. This, along with the multiple possible orders of the PCET and ET steps, results in 64 possible pathways for O_2 formation. These pathways were compared according to the Gibbs free energies of their intermediates, with only the thermodynamically most favorable pathways being discussed here (further results are in Table S1). It should be noted that a recent in situ IR spectroscopy study[66] has shown that changes of the catalyst under oxidative conditions occur at the Mn centers, while the vanadate ligand remains unaffected. We therefore focus on those redox pathways that involve primarily the Mn_4O_4 cubane core and the reactive ligands.

The uncertainty regarding the order of PCET and ET steps results in four possible arrangements of the reaction steps: PCET-PCET-PCET-ET, PCET-PCET-ET-PCET, PCET-ET-PCET-PCET, and ET-PCET-PCET-PCET (see Figure 2).

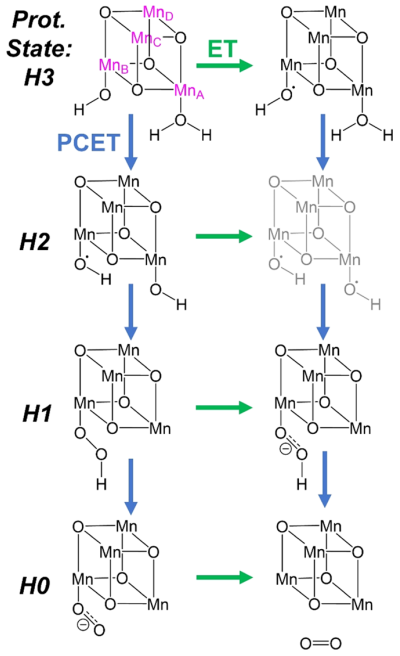

Figure 2. Types of intermediates investigated by direct optimization, starting from **1** (top left) and resulting from the four possible orders of proton-coupled electron transfer (PCET, blue) and electron transfer (ET, green) steps. The protonation state *Hn* (n = 0, 1, 2, 3) for each pair of structures is noted on the left. The grayed-out structure could not be optimized, leading to the exclusion of pathways involving such an intermediate from further consideration.

First, we directly optimized intermediates corresponding to each of the structures shown in Figure 2 considering all accessible oxidation states of the Mn centers. The results obtained proved to be pivotal for our further investigation, as will be described next (for a detailed overview of results of these direct optimizations, see Table S1).

We note that the species with two protonated oxyl groups (gray in Figure 2) could not be optimized, indicating that the PCET-ET-PCET-PCET and ET-PCET-PCET-PCET pathways, which necessarily include such a species, may not be feasible. Importantly, the investigation of both intermolecular and intramolecular oxidation for each reaction step showed that intramolecular oxidation of the ligands by the Mn^{4+} centers appears to be thermodynamically favored over intermolecular oxidation, regardless of the order of PCET and ET steps. Finally, our results pointed toward an intramolecular water nucleophilic attack of an OH ligand on the neighboring oxyl radical as a possible mechanism of O−O bond formation, an i-WNA(OH)-type mechanism within the classification proposed by Schilling and Luber.[13] We therefore expanded our sampling of reaction intermediates to include a greater variety of isomers and conformers.

As redox and JT isomerism were previously shown to play an important role in the reactivity of $[Mn_4V_4O_{17}(OAc)_3]^{3-}$,[45,46] we decided to target the most important isomers and conformers of each intermediate of interest. To this end, we extended the sampling procedure of ref 46 by also targeting multiple ligand arrangements for each redox and JT isomer. Accordingly, we next investigated all four arrangements of reaction steps (PCET-PCET-PCET-ET, PCET-PCET-ET-PCET, PCET-ET-PCET-PCET, and ET-PCET-PCET-PCET) as well as both inter- and intramolecular oxidations. Table 1 gives an overview of which specific redox and JT isomers were targeted at each oxidation state of the cubane core (designated as Mn4444 for Mn_4^{4+} and Mn3333 for Mn_3^{3+}) and the protonation state of the reactive ligands (designated as *Hn*, where *n* is the number of protons). In total, we investigated 91 unique isomers and 203 individual conformers (considering the various ligand arrangements sampled at each protonation state). A full overview of the resulting 80 optimized geometries can be found in Table S1.

This extended sampling approach largely confirmed our initial observations. An intermediate with two protonated oxyl groups that would be essential for the ET-PCET-PCET-PCET and PCET-ET-PCET-PCET mechanisms could not be optimized, leading to the conclusion that such an intermediate is too unstable to play any significant role in the water oxidation mechanism of **1**. Furthermore, the energy difference between **1** and the most stable intermediate resulting from a single intermolecular PCET step was found to be 7.50 eV (at the B3LYP/def2-SVP level of theory, see Table S1), which is significantly above the computed thermodynamic limit of water oxidation at 4.56 eV.[62] It appears therefore that intermolecular ETs are highly unfavorable in the context of the water oxidation cycle of **1**, allowing us to focus exclusively on pathways that feature intramolecular ETs.

The additional sampling of various conformations of the reactive ligands for each intermediate revealed that the nucleophilic attack of OH on the neighboring Mn-oxyl group could take place at either Mn_B (Figure 3, top) or Mn_A (Figure 3, bottom), with relatively minute differences in the stability of the respective intermediates. Figure 3 shows the most stable isomers found for each intermediate between the activated species **1** and the deactivated catalyst after O_2 evolution and dissociation **6**.

Starting from **1**, an intramolecular ET from the OH ligand to its Mn_B^{4+} center, coupled to deprotonation of the neighboring H_2O ligand, results in intermediate **2b** with a JT axis on Mn_B^{3+} pointing in the *z*-direction toward the protonated oxyl species, with a reaction energy of 1.85 eV. The next PCET step leads to the formation of the O−O bond (**3b**, 2.99 eV), with some internal rearrangement resulting in Mn_A^{3+} having a JT axis in

https://doi.org/10.1021/acscatal.1c03566
ACS Catal. 2021, 11, 13320−13329

Table 1. Redox and Jahn–Teller (JT) Isomers Targeted for Sampling at Each Oxidation State[a]

Ox. State	JT conformers	Prot. State
Mn4444	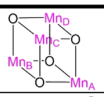	H3, H2, H1, H0
Mn3444	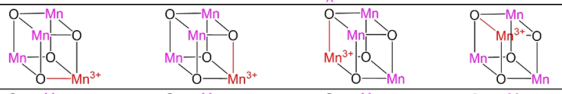	H3, H2, H1, H0
Mn3344	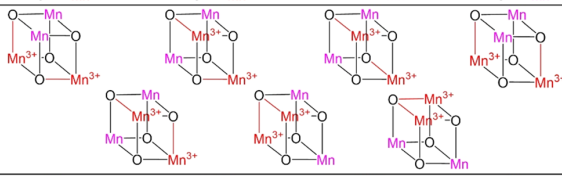	H2, H1, H0
Mn3334	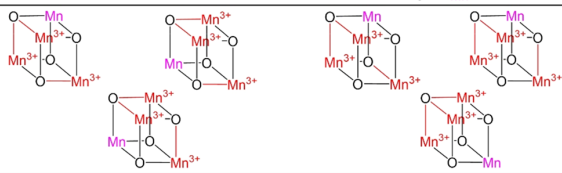	H1, H0
Mn3333	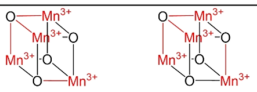	H0

[a]The nomenclature MnXXXX (left column) indicates the oxidation state of the four Mn atoms, e.g., Mn3333 corresponds to a Mn_4^{3+} configuration and Mn4444 to a Mn_4^{4+} configuration of the cubane core. At each oxidation state, a variety of ligand conformations for each relevant protonation state *Hn*, where *n* is the number of protons, were targeted (right column). Mn^{3+} centers and the orientation of their JT axes are marked in red and Mn^{4+} centers in purple.

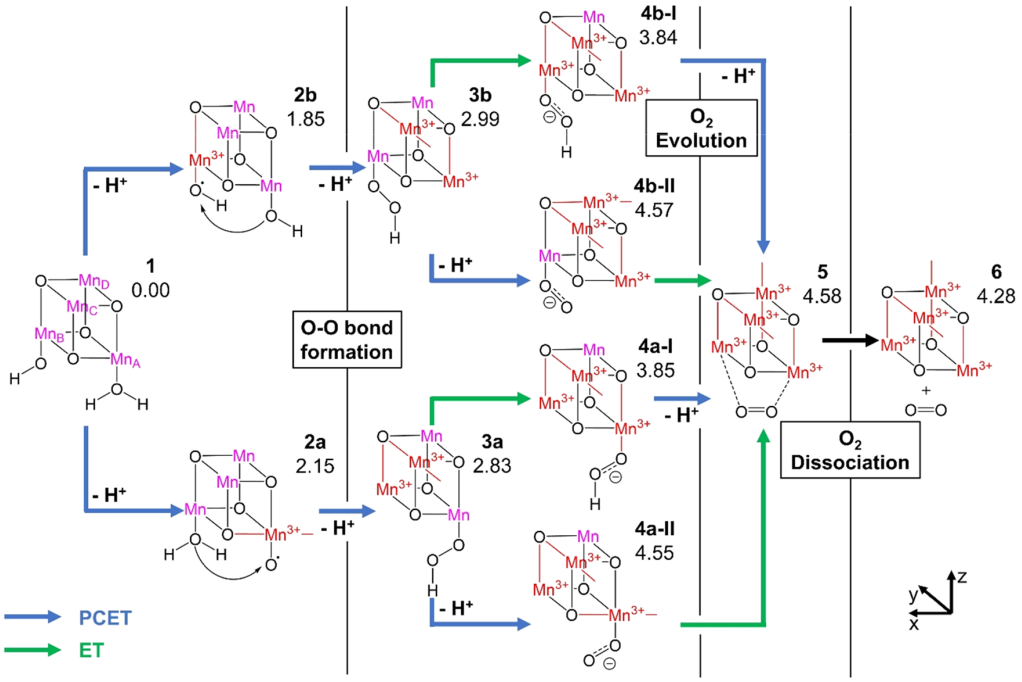

Figure 3. Most stable isomers of intermediates along the thermodynamically most favorable pathways for the PCET-PCET-ET-PCET and PCET-PCET-PCET-ET orders of steps. PCETs are marked by blue arrows, ETs by green arrows, and other reactions by black boxes. Mn^{4+} centers are in purple, and Mn^{3+} centers and their JT axes are in red. Intermediates are labeled **1** through **6**, and their relative Gibbs free energies are presented in eV at the B3LYP/def2-SVP/def2-TZVP level of theory.

https://doi.org/10.1021/acscatal.1c03566
ACS Catal. 2021, 11, 13320–13329

the *z*-direction toward an open coordination site and Mn_C^{3+} having a JT axis in the *y*-direction toward an acetate ligand. The resulting peroxo species is bound to Mn_B^{4+}. Subsequently, an ET step without deprotonation produces **4b-I**, which adds a JT axis on Mn_B^{3+} in the *z*-direction toward the peroxyl species with a resulting relative energy of 3.84 eV. In contrast, a PCET from **3b** results in **4b-II**, with a new JT axis in the *x*-direction (toward an acetate ligand) on Mn_D^{3+} and a far higher relative energy of 4.57 eV. In either case, the final redox step leads to the product complex **5** (4.58 eV), in which molecular O_2 has been formed and is no longer directly bound to any Mn center but loosely associated with the complex (product complex). The species **5** features JT axes on Mn_A^{3+} and Mn_B^{3+} in the *z*-direction toward the loosely associated O_2, on Mn_C^{3+} in the *y*-direction toward an acetate ligand, and on Mn_D^{3+} in the *z*-direction toward the vanadate ligand. Dissociation of O_2 gives the final product **6**, with an identical arrangement of JT axes and a relative energy of 4.28 eV.

Alternatively, an intramolecular PCET at the H_2O ligand bound to Mn_A^{4+} results in **2a**, with a proton transfer to the OH ligand yielding an oxyl species bound to Mn_A^{3+} with a JT axis in the *x*-direction toward a neighboring acetate ligand and a reaction energy of 2.15 eV. The O−O bond formation once again occurs with the next PCET step, resulting in the intermediate **3a** at 2.83 eV. This features JT axes at Mn_B^{3+} in the *z*-direction toward the open coordination site and at Mn_C^{3+} in the *y*-direction toward an acetate ligand, with the peroxo species bound to Mn_A^{4+}. Next, either a simple ET results in **4a-I**, with a new JT axis in the *z*-direction on Mn_A^{3+} toward the peroxyl species (3.85 eV) or a PCET step results in **4a-II**, with a JT axis added in the *x*-direction on Mn_A^{3+} toward an acetate ligand (4.55 eV). The final steps converge to the product complex **5** and final product **6** as described above.

Comparing the relative energies of the species in Figure 3, it is immediately apparent that out of the intermediates resulting from the penultimate redox step, **4b-I** (3.84 eV) is far more stable than **4b-II** (4.57 eV); the same can be observed for **4a-I** (3.85 eV) versus **4a-II** (4.55 eV). From this, we can conclude that PCET-PCET-ET-PCET is the preferred order of redox steps. To determine whether the formation of the peroxo species is thermodynamically favored to take place on Mn_A (pathway: **1**, **2a**, **3a**, **4a-I**, **5**, **6**; light blue in Figure 4) or on Mn_B (pathway: **1**, **2b**, **3b**, **4b-I**, **5**, **6**, dark blue in Figure 4), we compare the two resulting pathways to the behavior of an ideal catalyst that overcomes the computed thermodynamic limit of water oxidation (4.56 eV[62]) in four equal steps of 1.14 eV each (purple in Figure 4). The greater the departure from the ideal catalyst, the larger the resulting thermodynamic overpotential, limiting the efficiency of water oxidation by **1**. Figure 4 discloses that the first redox step has the greatest reaction energy—1.85 eV for **2b** and 2.15 eV for **2a**—and therefore differs most significantly from the value of 1.14 eV for an ideal catalyst, making this the potential-determining step. We can thus conclude that the lowest thermodynamic overpotential should result from forming the peroxo species on Mn_B, following the pathway **1**, **2b**, **3b**, **4b-I**, **5**, **6**. Specifically, the predicted thermodynamic overpotential for this catalytic sequence is 0.71 V, as computed from eq 4.

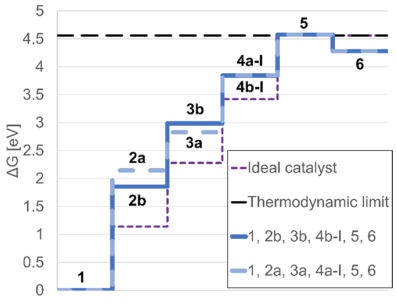

Figure 4. Gibbs free energies of intermediates along the most favorable PCET-PCET-ET-PCET pathways, calculated at the B3LYP/def2-SVP/def2-TZVP level of theory: **1**, **2a**, **3a**, **4a-I**, **5**, **6** (light blue, dashed) vs **1**, **2b**, **3b**, **4b-I**, **5**, **6** (dark blue, continuous). For comparison, the computed thermodynamic limit of water oxidation (black, dashed) and an ideal catalyst with evenly spaced intermediates (purple, dashed).

A closer examination of the intermediates comprising the two most favorable pathways, **1**, **2b**, **3b**, **4b-I**, **5**, **6** and **1**, **2a**, **3a**, **4a-I**, **5**, **6**, reveals the multiple roles that redox isomerizations and JT effects play in enhancing the reactivity of $[Mn_4V_4O_{17}(OAc)_3]^{3-}$ (recall Figure 3). First, one can observe that **4b-I** and **4a-I** prominently feature JT axes in the *z*-direction toward the reactive ligand on Mn_B^{3+} and Mn_A^{3+}, respectively. As JT-distorted bonds break more easily, we can infer that the barrier for the Mn^{3+}−O bond cleavage that occurs in the O_2 evolution step is lowered due to the presence of JT effects in **4b-I** and **4a-I**. Similar behavior has been observed in related OEC model complexes[41] as well as in the activation of $[Mn_4V_4O_{17}(OAc)_3]^{3-}$, where the rate-determining step in the ligand exchange had a lower barrier when a Mn^{3+} center with a JT axis in the direction of the departing ligand was present.[45]

Second, while the redox steps from **3b** via **4b-I** to **5** as well as from **3a** via **4a-I** to **5** require no rearrangement of existing JT axes, but rather involve only the progressive addition of a new JT axis at each emerging Mn^{3+} center, the PCET step from **2b** to **3b** includes significant rearrangement, going from a *z*-axis on Mn_B^{3+} to a *z*-axis on Mn_A^{3+} and a *y*-axis on Mn_C^{3+}. Similarly, the PCET step from **2a** to **3a** involves going from an *x*-axis on Mn_A^{3+} to a *z*-axis on Mn_B^{3+} and a *y*-axis on Mn_C^{3+}. As these steps are key to the O−O bond formation, this seemingly inexplicable behavior awoke our curiosity.

The reaction from **2b** to **3b** comprises at least three elementary steps: deprotonation, ET, and O−O bond formation. As the nucleophilic attack by the OH ligand on the Mn_B^{3+}-oxyl cannot take place as long as the oxyl is protonated, we can safely assume that deprotonation must occur first. We therefore optimized a guess structure based on **2b**, from which the proton on the oxyl ligand has been removed (**OO1**). Next, a CI-NEB calculation was carried out between **OO1** and **3b** to ascertain the order of ET and O−O bond formation steps along the MEP. Figure S1 shows the relative energy along the MEP and pairwise atom distances.

The NEB calculation detected two stationary points along the MEP for O−O bond formation that we subsequently optimized (Figure 5a and Tables S3 and S4). Starting from **OO1**, an ET from Mn_B to Mn_C results in a stable intermediate (**OO2**, −8.7 kcal/mol, r_{O1-O2} = 2.84 Å) that is a redox isomer of **OO1**, featuring a JT axis in the *y*-direction along Mn_C^{3+}−O4 as well as a more electrophilic Mn_B^{4+}-oxyl group (see also Figure 5b, red and yellow). From **OO2**, the expected nucleophilic attack of OH at Mn_B^{4+}-oxyl proceeds via a barrier of 31.0 kcal/mol, which compares favorably to the water nucleophilic attack barriers previously described for related

https://doi.org/10.1021/acscatal.1c03566
ACS Catal. 2021, 11, 13320−13329

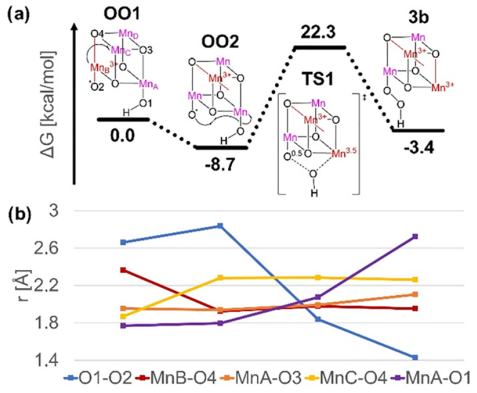

Figure 5. (a) Stationary points along the MEP for O−O bond formation and their relative energies in kcal/mol. (b) Bond lengths for stationary points along the MEP; O1−O2 in blue, Mn_B−O4 along the *z*-axis in red, Mn_A−O3 along the *z*-axis in orange, Mn_C−O4 along the *y*-axis in yellow, and Mn_A−O1 in purple.

WOCs.[24−26] The associated transition state (**TS1**) has the attacking OH ligand suspended halfway between its metal center (r_{MnA-O1} = 2.07 Å) and the oxyl ligand (r_{O1-O2} = 1.84 Å) and features spin populations of 3.56 on Mn_A and 0.53 on O2. This surprising result indicates that O−O bond formation occurs by homolytic cleavage of the Mn_A−O1 bond, resulting in a one-electron reduction of Mn_A^{4+} to Mn_A^{3+} and radical coupling between O1 and O2. As can be seen in Figure 5b, the formation of the O1−O2 bond (blue), the cleavage of the Mn_A−O1 bond (purple), and the ET to Mn_A (shown by the eventual emergence of JT distortions in the *z*-direction along Mn_A−O3, orange) are clearly coupled. Inspection of the normal mode corresponding to the imaginary frequency of **TS1** confirms that all three processes are in fact concerted. The product **3b** has an additional JT axis on Mn_A^{3+} in the *z*-direction toward the now-open coordination site, with the resulting peroxide species (r_{O-O} = 1.43 Å) bound to Mn_B^{4+}, giving an overall reaction energy of −3.4 kcal/mol for O−O bond formation along the **OO1** to **3b** pathway.

We also investigated the alternative O−O bond formation pathway between **2a** and **3a** by first optimizing a deprotonated guess structure based on **2a** (**OO3**). A NEB calculation between **OO3** and **3a** was carried out and is shown in Figure S2, with broadly similar results to the NEB calculation between **OO1** and **3b** described above: A redox isomerization leads to an intermediate **OO4** (−6.1 kcal/mol, r_{O1-O2} = 2.83 Å), featuring a JT axis in the *y*-direction along Mn_C^{3+}−O4 as well as a more electrophilic Mn_A^{4+}-oxyl group. Unfortunately, the transition state between **OO4** and **3a** could not be optimized, but the barrier is expected to be comparable to that presented by **TS1** (see above).

Finally, as **3a** is 3.6 kcal/mol more stable than **3b**, a conversion of **3b** to **3a** via migration of the peroxo species from Mn_B to Mn_A with concomitant redox isomerization would be thermodynamically favorable. A NEB calculation revealed that this is a simple one-step reaction with a single transition state, which was subsequently optimized as **TS3** (see Figure S3). The barrier for conversion from **3a** to **3b** was found to be quite low, only 6.7 kcal/mol, making this process feasible and opening up the possibility of a crossover pathway consisting of **1**, **2b**, **3b**, **3a**, **4a-I**, **5**, **6**.

We thus conclude that structural flexibility in the form of facile redox and JT isomerizations plays an essential role in enhancing the reactivity of the $[Mn_4V_4O_{17}(OAc)_3]^{3-}$ WOC not only during the activation[45] but also in the water oxidation cycle itself. A weak, JT-distorted bond contributes to lowering the barrier for O_2 evolution, and a redox isomerization of **OO1** with its Mn_B^{3+}-oxyl yields **OO2**, which features a more electrophilic Mn_B^{4+}-oxyl group. This redox isomerization must occur first to enable O−O bond formation via attack by a neighboring OH ligand, and that attack takes place in concert with an ET to Mn_A and the emergence of a new JT axis at that metal center. Our observations are reminiscent of the behavior of the OEC recently described by Drosou et al.,[42] who found that different JT isomers in the S1 state influence ligand exchange kinetics as well as favor the formation of distinct redox isomers in the S2, thereby directly influencing the mechanism of water oxidation in the natural system. It should be noted, however, that the high catalytic activity of the OEC relies intimately on the protein environment in which it is embedded, while our calculations deal with $[Mn_4V_4O_{17}(OAc)_3]^{3-}$ in solution. It would therefore be interesting to see whether the integration of $[Mn_4V_4O_{17}(OAc)_3]^{3-}$ into a functionalized soft matter matrix would further increase its activity.

CONCLUSIONS

In this paper, we propose a water oxidation mechanism for the bioinspired water oxidation catalyst $[Mn_4V_4O_{17}(OAc)_3]^{3-}$, starting from the activated species $[Mn_4^{4+}V_4O_{17}(OAc)_2(H_2O)(OH)]^{1-}$ (**1**). After activation, the catalyst holds four redox equivalents in the form of four Mn^{4+} centers; the catalyst also binds cofacial OH and H_2O ligands that are positioned in close proximity, allowing them both to participate in water oxidation. Water oxidation proceeds by an intramolecular ET from the OH ligand of Mn_B to that metal center, coupled with deprotonation of the neighboring H_2O ligand. This is followed by another such PCET and O−O bond formation, with a peroxo species formed on Mn_B. An intramolecular ET and final PCET lead to the evolution and subsequent dissociation of O_2, resulting in the deactivated catalytic species $[Mn_4^{3+}V_4O_{17}(OAc)_2]^{4-}$ with one open coordination site on Mn_A and Mn_B each.

While the presence of JT axes has been noted in OEC models and carefully analyzed to allow for a better comparison with experimental X-ray structures,[32−42] here we investigate the explicit influence of these distortions on the water oxidation cycle. We found that redox isomerism and JT effects play a prominent role in the water oxidation cycle of $[Mn_4V_4O_{17}(OAc)_3]^{3-}$: In the O_2 release step, JT distortions contribute to lowering the barrier of Mn_B^{3+}−O bond cleavage in a straightforward manner. The formation of the O−O bond is preceded by a redox isomerization step and appears to be concerted with an ET from the reactive ligands to Mn_A and the emergence of a new JT axis at that metal center. These findings are of particular interest when one considers the role played by redox isomerism and JT effects in the natural OEC; there, JT effects were shown to influence both ligand exchange kinetics and water oxidation pathways.[41,42] As redox isomerism and JT effects are present in cubane structures with Mn^{3+}/Mn^{4+} centers, we argue that these flexibility-enhancing effects should be harnessed in the design of novel bioinspired WOCs. Future work on $[Mn_4V_4O_{17}(OAc)_3]^{3-}$ will focus on the stability of the

https://doi.org/10.1021/acscatal.1c03566
ACS Catal. 2021, 11, 13320−13329

catalyst, with special attention paid to its regeneration, degradation, and modes of integration in soft matter matrices.

■ ASSOCIATED CONTENT

Supporting Information

The Supporting Information is available free of charge at https://pubs.acs.org/doi/10.1021/acscatal.1c03566.

Molecular structures, Mulliken spin populations, electronic energies, thermochemical contributions, free energies, and nudged elastic band results (PDF)

■ AUTHOR INFORMATION

Corresponding Authors

Ludwig Schwiedrzik − *Institute of Theoretical Chemistry, Faculty of Chemistry, University of Vienna, 1090 Vienna, Austria*; Email: ludwig.schwiedrzik@univie.ac.at

Leticia González − *Institute of Theoretical Chemistry, Faculty of Chemistry, University of Vienna, 1090 Vienna, Austria*; orcid.org/0000-0001-5112-794X; Email: leticia.gonzalez@univie.ac.at

Author

Vera Brieskorn − *Institute of Theoretical Chemistry, Faculty of Chemistry, University of Vienna, 1090 Vienna, Austria*

Complete contact information is available at: https://pubs.acs.org/10.1021/acscatal.1c03566

Notes

The authors declare no competing financial interest.

■ ACKNOWLEDGMENTS

This work is funded by the Austrian Science Fund FWF (project no. I3987-N28) and the Deutsche Forschungsgemeinschaft DFG (TRR234 "CataLight", project ID 364549901, subproject C3). The Vienna Scientific Cluster is acknowledged for the generous allocation of computational resources. The authors would also like to thank Gustavo Cárdenas, Ivan Trentin, Carsten Streb, Sebastian Mai, and Boris Maryasin for insightful discussions.

■ REFERENCES

(1) Chow, J.; Kopp, R. J.; Portney, P. R. Energy Resources and Global Development. *Science* **2003**, *302*, 1528−1531.

(2) Friedlingstein, P.; O'Sullivan, M.; Jones, M. W.; Andrew, R. M.; Hauck, J.; Olsen, A.; Peters, G. P.; Peters, W.; Pongratz, J.; Sitch, S.; Le Quéré, C.; Canadell, J. G.; Ciais, P.; Jackson, R. B.; Alin, S.; Aragão, L. E. O. C.; Arneth, A.; Arora, V.; Bates, N. R.; Becker, M.; Benoit-Cattin, A.; Bittig, H. C.; Bopp, L.; Bultan, S.; Chandra, N.; Chevallier, F.; Chini, L. P.; Evans, W.; Florentie, L.; Forster, P. M.; Gasser, T.; Gehlen, M.; Gilfillan, D.; Gkritzalis, T.; Gregor, L.; Gruber, N.; Harris, I.; Hartung, K.; Haverd, V.; Houghton, R. A.; Ilyina, T.; Jain, A. K.; Joetzjer, E.; Kadono, K.; Kato, E.; Kitidis, V.; Korsbakken, J. I.; Landschützer, P.; Lefèvre, N.; Lenton, A.; Lienert, S.; Liu, Z.; Lombardozzi, D.; Marland, G.; Metzl, N.; Munro, D. R.; Nabel, J. E. M. S.; Nakaoka, S.-I.; Niwa, Y.; O'Brien, K.; Ono, T.; Palmer, P. I.; Pierrot, D.; Poulter, B.; Resplandy, L.; Robertson, E.; Rödenbeck, C.; Schwinger, J.; Séférian, R.; Skjelvan, I.; Smith, A. J. P.; Sutton, A. J.; Tanhua, T.; Tans, P. P.; Tian, H.; Tilbrook, B.; van der Werf, G.; Vuichard, N.; Walker, A. P.; Wanninkhof, R.; Watson, A. J.; Willis, D.; Wiltshire, A. J.; Yuan, W.; Yue, X.; Zaehle, S. Global Carbon Budget 2020. *Earth Syst. Sci. Data* **2020**, *12*, 3269−3340.

(3) Cook, T. R.; Dogutan, D. K.; Reece, S. Y.; Surendranath, Y.; Teets, T. S.; Nocera, D. G. Solar Energy Supply and Storage for the Legacy and Nonlegacy Worlds. *Chem. Rev.* **2010**, *110*, 6474−6502.

(4) Faunce, T. A.; Lubitz, W.; Rutherford, A. W.; MacFarlane, D.; Moore, G. F.; Yang, P.; Nocera, D. G.; Moore, T. A.; Gregory, D. H.; Fukuzumi, S.; Yoon, K. B.; Armstrong, F. A.; Wasielewski, M. R.; Styring, S. Energy and Environment Policy Case for a Global Project on Artificial Photosynthesis. *Energy Environ. Sci.* **2013**, *6*, 695−698.

(5) Lubitz, W.; Reijerse, E. J.; Messinger, J. Solar Water-Splitting into H2 and O2: Design Principles of Photosystem II and Hydrogenases. *Energy Environ. Sci.* **2008**, *1*, 15−31.

(6) Dau, H.; Limberg, C.; Reier, T.; Risch, M.; Roggan, S.; Strasser, P. The Mechanism of Water Oxidation: From Electrolysis via Homogeneous to Biological Catalysis. *ChemCatChem* **2010**, *2*, 724−761.

(7) Wang, L.-P.; Wu, Q.; Van Voorhis, T. Acid−Base Mechanism for Ruthenium Water Oxidation Catalysts. *Inorg. Chem.* **2010**, *49*, 4543−4553.

(8) Hirai, S.; Yagi, S.; Seno, A.; Fujioka, M.; Ohno, T.; Matsuda, T. Enhancement of the Oxygen Evolution Reaction in Mn3+-Based Electrocatalysts: Correlation between Jahn−Teller Distortion and Catalytic Activity. *RSC Adv.* **2016**, *6*, 2019−2023.

(9) Schilling, M.; Böhler, M.; Luber, S. Towards the Rational Design of the Py5-Ligand Framework for Ruthenium-Based Water Oxidation Catalysts. *Dalton Trans.* **2018**, *47*, 10480−10490.

(10) Betley, T. A.; Wu, Q.; Van Voorhis, T.; Nocera, D. G. Electronic Design Criteria for O−O Bond Formation via Metal−Oxo Complexes. *Inorg. Chem.* **2008**, *47*, 1849−1861.

(11) Rivalta, I.; Brudvig, G. W.; Batista, V. S. Oxomanganese Complexes for Natural and Artificial Photosynthesis. *Curr. Opin. Chem. Biol.* **2012**, *16*, 11−18.

(12) Shaffer, D. W.; Xie, Y.; Concepcion, J. J. O−O Bond Formation in Ruthenium-Catalyzed Water Oxidation: Single-Site Nucleophilic Attack vs. O−O Radical Coupling. *Chem. Soc. Rev.* **2017**, *46*, 6170−6193.

(13) Schilling, M.; Luber, S. Computational Modeling of Cobalt-Based Water Oxidation: Current Status and Future Challenges. *Front. Chem* **2018**, *0*, 7202.

(14) Nørskov, J. K.; Rossmeisl, J.; Logadottir, A.; Lindqvist, L.; Kitchin, J. R.; Bligaard, T.; Jónsson, H. Origin of the Overpotential for Oxygen Reduction at a Fuel-Cell Cathode. *J. Phys. Chem. B* **2004**, *108*, 17886−17892.

(15) Man, I. C.; Su, H.-Y.; Calle-Vallejo, F.; Hansen, H. A.; Martínez, J. I.; Inoglu, N. G.; Kitchin, J.; Jaramillo, T. F.; Nørskov, J. K.; Rossmeisl, J. Universality in Oxygen Evolution Electrocatalysis on Oxide Surfaces. *ChemCatChem* **2011**, *3*, 1159−1165.

(16) Blasco-Ahicart, M.; Soriano-López, J.; Carbó, J. J.; Poblet, J. M.; Galan-Mascaros, J. R. Polyoxometalate Electrocatalysts Based on Earth-Abundant Metals for Efficient Water Oxidation in Acidic Media. *Nat. Chem.* **2018**, *10*, 24−30.

(17) Li, X.; Siegbahn, P. E. M. Water Oxidation Mechanism for Synthetic Co−Oxides with Small Nuclearity. *J. Am. Chem. Soc.* **2013**, *135*, 13804−13813.

(18) Liao, R.-Z.; Kärkäs, M. D.; Lee, B.-L.; Åkermark, B.; Siegbahn, P. E. M. Photosystem II Like Water Oxidation Mechanism in a Bioinspired Tetranuclear Manganese Complex. *Inorg. Chem.* **2015**, *54*, 342−351.

(19) Suga, M.; Akita, F.; Hirata, K.; Ueno, G.; Murakami, H.; Nakajima, Y.; Shimizu, T.; Yamashita, K.; Yamamoto, M.; Ago, H.; Shen, J.-R. Native Structure of Photosystem II at 1.95 Å Resolution Viewed by Femtosecond X-Ray Pulses. *Nature* **2015**, *517*, 99−103.

(20) McCool, N. S.; Robinson, D. M.; Sheats, J. E.; Dismukes, G. C. A Co4O4 "Cubane" Water Oxidation Catalyst Inspired by Photosynthesis. *J. Am. Chem. Soc.* **2011**, *133*, 11446−11449.

(21) Wang, L.-P.; Van Voorhis, T. Direct-Coupling O2 Bond Forming a Pathway in Cobalt Oxide Water Oxidation Catalysts. *J. Phys. Chem. Lett.* **2011**, *2*, 2200−2204.

(22) Fernando, A.; Aikens, C. M. Reaction Pathways for Water Oxidation to Molecular Oxygen Mediated by Model Cobalt Oxide Dimer and Cubane Catalysts. *J. Phys. Chem. C* **2015**, *119*, 11072−11085.

(23) Nguyen, A. I.; Ziegler, M. S.; Oña-Burgos, P.; Sturzbecher-Hohne, M.; Kim, W.; Bellone, D. E.; Tilley, T. D. Mechanistic Investigations of Water Oxidation by a Molecular Cobalt Oxide Analogue: Evidence for a Highly Oxidized Intermediate and Exclusive Terminal Oxo Participation. *J. Am. Chem. Soc.* **2015**, *137*, 12865−12872.
(24) Hodel, F. H.; Luber, S. What Influences the Water Oxidation Activity of a Bioinspired Molecular CoII4O4 Cubane? An In-Depth Exploration of Catalytic Pathways. *ACS Catal* **2016**, *6*, 1505−1517.
(25) Hodel, F. H.; Luber, S. Redox-Inert Cations Enhancing Water Oxidation Activity: The Crucial Role of Flexibility. *ACS Catal* **2016**, *6*, 6750−6761.
(26) Soriano-López, J.; Musaev, D. G.; Hill, C. L.; Galán-Mascarós, J. R.; Carbó, J. J.; Poblet, J. M. Tetracobalt-Polyoxometalate Catalysts for Water Oxidation: Key Mechanistic Details. *J. Catal.* **2017**, *350*, 56−63.
(27) Dismukes, G. C.; Brimblecombe, R.; Felton, G. A. N.; Pryadun, R. S.; Sheats, J. E.; Spiccia, L.; Swiegers, G. F. Development of Bioinspired Mn4O4−Cubane Water Oxidation Catalysts: Lessons from Photosynthesis. *Acc. Chem. Res.* **2009**, *42*, 1935−1943.
(28) Mukherjee, S.; Stull, J. A.; Yano, J.; Stamatatos, T. C.; Pringouri, K.; Stich, T. A.; Abboud, K. A.; Britt, R. D.; Yachandra, V. K.; Christou, G. Synthetic Model of the Asymmetric [Mn3CaO4] Cubane Core of the Oxygen-Evolving Complex of Photosystem II. *Proc. Natl. Acad. Sci.* **2012**, *109*, 2257−2262.
(29) Kanady, J. S.; Lin, P.-H.; Carsch, K. M.; Nielsen, R. J.; Takase, M. K.; Goddard, W. A.; Agapie, T. Toward Models for the Full Oxygen-Evolving Complex of Photosystem II by Ligand Coordination To Lower the Symmetry of the Mn3CaO4 Cubane: Demonstration That Electronic Effects Facilitate Binding of a Fifth Metal. *J. Am. Chem. Soc.* **2014**, *136*, 14373−14376.
(30) Zhang, C.; Chen, C.; Dong, H.; Shen, J.-R.; Dau, H.; Zhao, J. A Synthetic Mn4Ca-Cluster Mimicking the Oxygen-Evolving Center of Photosynthesis. *Science* **2015**, *348*, 690−693.
(31) Lee, H. B.; Agapie, T. Redox Tuning via Ligand-Induced Geometric Distortions at a YMn3O4 Cubane Model of the Biological Oxygen Evolving Complex. *Inorg. Chem.* **2019**, *58*, 14998−15003.
(32) Kanady, J. S.; Tsui, E. Y.; Day, M. W.; Agapie, T. A Synthetic Model of the Mn3Ca Subsite of the Oxygen-Evolving Complex in Photosystem II. *Science* **2011**, *333*, 733−736.
(33) Gatt, P.; Petrie, S.; Stranger, R.; Pace, R. J. Rationalizing the 1.9 Å Crystal Structure of Photosystem II—A Remarkable Jahn−Teller Balancing Act Induced by a Single Proton Transfer. *Angew. Chem., Int. Ed.* **2012**, *51*, 12025−12028.
(34) Krewald, V.; Neese, F.; Pantazis, D. A. On the Magnetic and Spectroscopic Properties of High-Valent Mn3CaO4 Cubanes as Structural Units of Natural and Artificial Water-Oxidizing Catalysts. *J. Am. Chem. Soc.* **2013**, *135*, 5726−5739.
(35) Tsui, E. Y.; Agapie, T. Reduction Potentials of Heterometallic Manganese−Oxido Cubane Complexes Modulated by Redox-Inactive Metals. *Proc. Natl. Acad. Sci. USA* **2013**, *110*, 10084−10088.
(36) Yamaguchi, K.; Yamanaka, S.; Isobe, H.; Saito, T.; Kanda, K.; Umena, Y.; Kawakami, K.; Shen, J.-R.; Kamiya, N.; Okumura, M.; Nakamura, H.; Shoji, M.; Yoshioka, Y. The Nature of Chemical Bonds of the CaMn4O5 Cluster in Oxygen Evolving Complex of Photosystem II: Jahn-Teller Distortion and Its Suppression by Ca Doping in Cubane Structures. *Int. J. Quantum Chem.* **2013**, *113*, 453−473.
(37) Lee, C.; Aikens, C. M. Water Splitting Processes on Mn4O4 and CaMn3O4 Model Cubane Systems. *J. Phys. Chem. A* **2015**, *119*, 9325−9337.
(38) Krewald, V.; Retegan, M.; Cox, N.; Messinger, J.; Lubitz, W.; DeBeer, S.; Neese, F.; Pantazis, D. A. Metal Oxidation States in Biological Water Splitting. *Chem. Sci.* **2015**, *6*, 1676−1695.
(39) Fernando, A.; Aikens, C. M. Theoretical Investigation of Water Oxidation Catalysis by a Model Manganese Cubane Complex. *J. Phys. Chem. C* **2016**, *120*, 21148−21161.
(40) Yamaguchi, K.; Shoji, M.; Isobe, H.; Yamanaka, S.; Umena, Y.; Kawakami, K.; Kamiya, N. On the Guiding Principles for Understanding of Geometrical Structures of the CaMn4O5 Cluster in Oxygen-Evolving Complex of Photosystem II. Proposal of Estimation Formula of Structural Deformations via the Jahn−Teller Effects. *Mol. Phys.* **2017**, *115*, 636−666.
(41) Kanady, J. S.; Mendoza-Cortes, J. L.; Tsui, E. Y.; Nielsen, R. J.; Goddard, W. A.; Agapie, T. Oxygen Atom Transfer and Oxidative Water Incorporation in Cuboidal Mn3MOn Complexes Based on Synthetic, Isotopic Labeling, and Computational Studies. *J. Am. Chem. Soc.* **2013**, *135*, 1073−1082.
(42) Drosou, M.; Zahariou, G.; Pantazis, D. A. Orientational Jahn−Teller Isomerism in the Dark-Stable State of Nature's Water Oxidase. *Angew. Chem., Int. Ed.* **2021**, *60*, 13493−13499.
(43) Schwarz, B.; Forster, J.; Goetz, M. K.; Yücel, D.; Berger, C.; Jacob, T.; Streb, C. Visible-Light-Driven Water Oxidation by a Molecular Manganese Vanadium Oxide Cluster. *Angew. Chem., Int. Ed.* **2016**, *55*, 6329−6333.
(44) Huber, F. L.; Amthor, S.; Schwarz, B.; Mizaikoff, B.; Streb, C.; Rau, S. Multi-Phase Real-Time Monitoring of Oxygen Evolution Enables in Operando Water Oxidation Catalysis Studies. *Sustainable Energy Fuels* **2018**, *2*, 1974−1978.
(45) Cardenas, G.; Trentin, I.; Schwiedrzik, L.; Hernández-Castillo, D.; Lowe, G. A.; Kund, J.; Kranz, C.; Klingler, S.; Stach, R.; Mizaikoff, B.; Marquetand, P.; Nogueira, J. J.; Streb, C.; González, L. Activation by Oxidation and Ligand Exchange in a Molecular Manganese Vanadium Oxide Water Oxidation Catalyst. *Chem. Sci.* **2021**, *12*, 12918−12927.
(46) Mai, S.; Holzer, M.; Andreeva, A.; González, L. Jahn−Teller Effects in a Vanadate-Stabilized Manganese-Oxo Cubane Water Oxidation Catalyst. *Chem. - Eur. J.* **2021**, DOI: 10.1002/chem.202102539.
(47) Frisch, M. J.; Trucks, G. W.; Schlegel, H. B.; Scuseria, G. E.; Robb, M. A.; Cheeseman, J. R.; Scalmani, G.; Barone, V.; Petersson, G. A.; Nakatsuji, H.; Li, X.; Caricato, M.; Marenich, A. V.; Bloino, J.; Janesko, B. G.; Gomperts, R.; Mennucci, B.; Hratchian, H. P.; Ortiz, J. V.; Izmaylov, A. F.; Sonnenberg, J. L.; Williams-Young, D.; Ding, F.; Lipparini, F.; Egidi, F.; Goings, J.; Peng, B.; Petrone, A.; Henderson, T.; Ranasinghe, D.; Zakrzewski, V. G.; Gao, J.; Rega, N.; Zheng, G.; Liang, W.; Hada, M.; Ehara, M.; Toyota, K.; Fukuda, R.; Hasegawa, J.; Ishida, M.; Nakajima, T.; Honda, Y.; Kitao, O.; Nakai, H.; Vreven, T.; Throssell, K.; Montgomery, J. A., Jr; Peralta, J. E.; Ogliaro, F.; Bearpark, M. J.; Heyd, J. J.; Brothers, E. N.; Kudin, K. N.; Staroverov, V. N.; Keith, T. A.; Kobayashi, R.; Normand, J.; Raghavachari, K.; Rendell, A. P.; Burant, J. C.; Iyengar, S. S.; Tomasi, J.; Cossi, M.; Millam, J. M.; Klene, M.; Adamo, C.; Cammi, R.; Ochterski, J. W.; Martin, R. L.; Morokuma, K.; Farkas, O.; Foresman, J. B.; Fox, D. J. *Gaussian 16*, revision C.01: Gaussian Inc.: Wallingford, CT, 2016.
(48) Becke, A. D. Density-functional Thermochemistry. III. The Role of Exact Exchange. *J. Chem. Phys.* **1993**, *98*, 5648−5652.
(49) Lee, C.; Yang, W.; Parr, R. G. Development of the Colle-Salvetti Correlation-Energy Formula into a Functional of the Electron Density. *Phys. Rev. B* **1988**, *37*, 785−789.
(50) Weigend, F.; Ahlrichs, R. Balanced Basis Sets of Split Valence, Triple Zeta Valence and Quadruple Zeta Valence Quality for H to Rn: Design and Assessment of Accuracy. *Phys. Chem. Chem. Phys.* **2005**, *7*, 3297−3305.
(51) Grimme, S.; Antony, J.; Ehrlich, S.; Krieg, H. A Consistent and Accurate Ab Initio Parametrization of Density Functional Dispersion Correction (DFT-D) for the 94 Elements H-Pu. *J. Chem. Phys.* **2010**, *132*, No. 154104.
(52) Barone, V.; Cossi, M. Quantum Calculation of Molecular Energies and Energy Gradients in Solution by a Conductor Solvent Model. *J. Phys. Chem. A* **1998**, *102*, 1995−2001.
(53) Siegbahn, P. E. M. O-O Bond Formation in the S4 State of the Oxygen-Evolving Complex in Photosystem II. *Chem. − Eur. J.* **2006**, *12*, 9217−9227.
(54) Siegbahn, P. E. M. Substrate Water Exchange for the Oxygen Evolving Complex in PSII in the S1, S2, and S3 States. *J. Am. Chem. Soc.* **2013**, *135*, 9442−9449.

(55) Siegbahn, P. E. M. The S2 to S3 Transition for Water Oxidation in PSII (Photosystem II), Revisited. *Phys. Chem. Chem. Phys.* **2018**, *20*, 22926−22931.
(56) Neese, F. The ORCA Program System. *Wiley Interdiscip. Rev.: Comput. Mol. Sci.* **2012**, *2*, 73−78.
(57) Neese, F. Software Update: The ORCA Program System, Version 4.0. *Wiley Interdiscip. Rev.: Comput. Mol. Sci.* **2018**, *8*, No. e1327.
(58) Perdew, J. P. Density-Functional Approximation for the Correlation Energy of the Inhomogeneous Electron Gas. *Phys. Rev. B* **1986**, *33*, 8822−8824.
(59) Becke, A. D. Density-Functional Exchange-Energy Approximation with Correct Asymptotic Behavior. *Phys. Rev. A* **1988**, *38*, 3098−3100.
(60) Pantazis, D. A.; Chen, X.-Y.; Landis, C. R.; Neese, F. All-Electron Scalar Relativistic Basis Sets for Third-Row Transition Metal Atoms. *J. Chem. Theory Comput.* **2008**, *4*, 908−919.
(61) Rossini, E.; Knapp, E.-W. Proton Solvation in Protic and Aprotic Solvents. *J. Comput. Chem.* **2016**, *37*, 1082−1091.
(62) Piccinin, S.; Sartorel, A.; Aquilanti, G.; Goldoni, A.; Bonchio, M.; Fabris, S. Water Oxidation Surface Mechanisms Replicated by a Totally Inorganic Tetraruthenium−Oxo Molecular Complex. *Proc. Natl. Acad. Sci. USA* **2013**, *110*, 4917−4922.
(63) Sabatier, P. *La Catalyse en chimie organique*; Librairie Polytechnique Ch. Béranger: Paris, 1913.
(64) Nørskov, J. K.; Bligaard, T.; Rossmeisl, J.; Christensen, C. H. Towards the Computational Design of Solid Catalysts. *Nat. Chem.* **2009**, *1*, 37−46.
(65) Siegbahn, P. E. M. Water Oxidation Mechanism in Photosystem II, Including Oxidations, Proton Release Pathways, O——O Bond Formation and O2 Release. *Biochim. Biophys. Acta, Bioenerg.* **2013**, *1827*, 1003−1019.
(66) Mai, S.; Klingler, S.; Trentin, I.; Kund, J.; Holzer, M.; Andreeva, A.; Stach, R.; Kranz, C.; Streb, C.; Mizaikoff, B.; González, L. Spectral Signatures of Oxidation States in a Manganese-Oxo Cubane Water Oxidation Catalyst. *Chem. − Eur. J.* **2021**, DOI: 10.1002/chem.202102583.

Supporting Information:

Flexibility Enhances Reactivity: Redox Isomerism and Jahn-Teller Effects in a Bioinspired Mn_4O_4 Cubane Water Oxidation Catalyst

Ludwig Schwiedrzik,[a,*] Vera Brieskorn,[a] Leticia González[a,*]

[a] Institute of Theoretical Chemistry, Faculty of Chemistry, University of Vienna, Währinger Straße 17, 1090 Vienna, Austria

[*] ludwig.schwiedrzik@univie.ac.at, leticia.gonzalez@univie.ac.at

Contents

I.	List of all stable isomers and conformers	S2
II.	Detailed energy breakdown, named Intermediates	S5
III.	Nudged elastic band calculations	S6
IV.	List of O-O bond formation stationary points	S7
V.	Detailed energy breakdown, O-O bond formation stationary points	S8
VI.	Cartesian coordinates of selected intermediates, transition states	S9

I. List of all stable isomers and conformers

Table S1: Unique optimized isomers and conformers of possible intermediates in the water oxidation cycle of $[Mn_4V_4O_{17}(OAc)_3]^{3-}$, grouped according to the overall redox state of the cubane core (e.g Mnx444, corresponding to a $Mn^{4+}{}_3Mn^{3+}$ configuration with a JT axis in x direction on Mn_A), charge q and multiplicity 2S+1. Columns from left to right: Redox and JT configuration of the cubane; configuration of reactive ligands on Mn_B and Mn_A; Gibbs free energy relative to **1**, computed at the B3LYP/def2-SVP level of theory (in eV); spin populations of Mn_{A-D} and of the oxygen atoms of the reactive ligands, where O2 is bound to Mn_B and O1 is bound to Mn_A in **1**; r_{O-O} distance between O1 and O2 atoms (in Å). Further notes: named intermediates in bold, †=structure obtained by direct optimization, ‡=no stable intermediates found.

Cubane config	Ligands		$\Delta G_{DZ,rel}$ [eV]	Spin populations						r_{O-O} [Å]	Notes
	Mn_B-	Mn_A-		Mn_A	Mn_B	Mn_C	Mn_D	O2	O1		
Mn4444	**q=-1**	**2S+1=13**									
Mn4444	OH	OH_2	0.00	3.05	2.93	2.93	2.92	0.01	0.00	2.61	†,**1**
Mn4444	OH_2	OH	0.04	3.00	2.94	2.93	2.92	-0.01	0.05	2.62	
Mn4444	**q=0**	**2S+1=14**									
Mn4444	O*H	OH_2	7.69	3.04	2.85	2.88	2.88	0.93	-0.01	2.88	
Mn4444	OH_2	O*H	7.74	3.00	2.93	2.87	2.87	-0.01	0.98	2.81	†
Mn4444	**q=-1**	**2S+1=14**									
Mn4444	O*	OH_2	7.50	3.05	2.83	2.92	2.92	1.01	-0.01	2.68	†
Mn4444	O*H	OH	7.63	3.02	2.86	2.92	2.92	0.98	0.02	2.51	
Mn4444	OH	O*H	7.65	3.00	2.93	2.92	2.92	0.00	0.99	2.50	
Mn4444	**q=0**	**2S+1=15**									‡
Mn4444	**q=-1**	**2S+1=13**									
Mn4444	OOH		13.89	3.12	2.96	2.92	2.92	-0.04	-0.01	1.42	†
Mn4444		OOH	13.96	3.00	2.99	2.91	2.91	0.03	0.01	1.43	
Mn4444	**q=0**	**2S+1=14**									
Mn4444	OO*H		20.34	3.11	2.91	2.87	2.87	0.62	0.36	1.30	†
Mn4444		OO*H	20.35	2.86	3.03	3.00	2.86	0.38	0.62	1.32	
Mn4444	**q=-1**	**2S+1=14**									
Mn4444	OO*		19.68	3.11	2.99	2.91	2.91	0.40	0.49	1.28	†
Mn4444	**q=0**	**2S+1=15**									
Mn4444	O_2		25.58	3.13	3.00	2.86	2.86	1.00	1.00	1.20	†
Mn3444	**q=-1**	**2S+1=15**									
Mn44y4	O*H	OH_2	1.46	3.03	2.92	3.86	2.96	0.95	-0.01	2.82	
Mn44y4	OH_2	O*H	1.48	2.99	2.97	3.86	2.96	-0.01	0.96	2.77	
Mn4z44	OH_2	O*H	1.50	3.00	3.87	2.96	2.95	0.02	0.97	2.67	
Mn4z44	O*H	OH_2	1.51	3.04	3.85	2.96	2.95	1.03	0.00	2.82	†
Mnz444	O*H	OH_2	1.78	3.92	2.88	2.96	2.97	0.87	0.02	3.27	
Mnx444	O*H	OH_2	1.78	3.92	2.94	2.97	2.95	0.71	0.00	3.82	
Mnz444	OH_2	O*H	1.83	3.90	2.97	2.95	2.96	-0.01	1.02	2.80	
Mnx444	OH_2	O*H	1.89	3.88	2.97	2.93	2.95	-0.01	0.73	2.81	
Mn3444	**q=-2**	**2S+1=15**									

Mn4z44	O*H	OH	1.85	3.03	3.86	2.99	2.99	1.04	0.03	2.57	†,**2b**
Mnx444	O*	OH_2	2.02	3.91	2.92	2.99	2.98	1.00	-0.01	2.65	
Mnx444	OH_2	O*H	2.15	3.87	3.01	2.98	2.98	-0.03	1.01	2.67	**2a**
Mnz444	OH	O*H	2.20	3.89	2.98	3.00	2.99	0.00	1.04	2.55	
Mnz444	OH	O*H	2.31	3.90	2.97	3.00	2.99	0.30	0.75	2.22	
Mn3444	**q=-1**	**2S+1=16**									‡
Mn3444	**q=-2**	**2S+1=14**									
Mn4z44		OOH	7.70	3.05	3.89	2.99	2.99	-0.01	0.01	1.42	
Mnz444	OOH		7.97	3.92	3.04	3.00	3.00	-0.06	-0.01	1.42	†
Mn44y4		OOH	8.09	3.03	3.03	3.88	2.99	0.00	0.00	1.44	
Mn44y4	OOH		8.14	3.07	2.98	3.86	2.99	-0.01	-0.01	1.44	
Mn4z44	OOH		8.41	3.09	3.82	2.99	2.99	0.07	-0.02	1.45	
Mn3444	**q=-1**	**2S+1=15**									
Mn4z44		OO*H	13.74	3.03	3.90	2.95	2.95	0.63	0.36	1.30	
Mn44y4		OO*H	14.00	3.03	3.03	3.86	2.95	0.64	0.35	1.30	
Mnz444	OO*H		14.01	3.93	2.94	2.95	2.95	0.63	0.34	1.30	
Mn4z44	OO*H		14.02	3.10	3.86	2.95	2.94	0.70	0.33	1.31	†
Mn44y4	OO*H		14.03	3.08	2.96	3.86	2.95	0.64	0.34	1.30	
Mn3444	**q=-2**	**2S+1=15**									
Mn4z44		OO*	24.62	3.16	3.88	2.98	2.98	0.30	0.59	1.29	†
Mnz444	OO*		24.78	3.92	3.28	3.00	3.00	0.46	0.21	1.26	
Mn44y4	OO*		24.89	3.07	2.99	3.87	2.98	0.48	0.49	1.29	
Mn3444	**q=-1**	**2S+1=16**									
Mn4z44	O_2		29.97	3.10	3.90	2.94	2.94	1.00	1.00	1.20	†
Mn44y4	O_2		30.20	3.09	3.02	3.86	2.94	1.00	1.00	1.20	
Mnz444	O_2		30.36	3.94	2.98	2.94	2.94	0.91	1.06	1.20	
Mn3344	**q=-2**	**2S+1=17**									‡
Mn3344	**q=-3**	**2S+1=15**									
Mn4zy4		OOH	2.93	3.06	3.87	3.87	3.01	-0.01	0.01	1.43	**3a**
Mnz4y4	OOH		3.08	3.91	3.06	3.90	3.03	-0.03	0.00	1.43	†,**3b**
Mnxz44		OOH	3.12	3.93	3.94	3.03	3.04	-0.05	0.00	1.43	
Mn44yx		OOH	3.19	3.06	2.99	3.89	3.88	-0.01	0.00	1.44	
Mn44yx	OOH		3.46	3.06	2.99	3.86	3.86	0.00	-0.01	1.46	
Mnzz44	OOH		3.58	3.92	3.83	3.05	3.05	0.11	0.04	1.47	
Mn4zy4	OOH		3.61	3.08	3.83	3.87	2.99	0.07	-0.02	1.46	
Mn3344	**q=-2**	**2S+1=16**									
Mnzz44	OO*H		8.36	3.93	3.88	3.02	3.02	0.71	0.32	1.31	†
Mn4zy4		OO*H	8.43	3.02	3.88	3.86	2.98	0.65	0.34	1.31	
Mnz4y4	OO*H		8.51	3.91	2.99	3.90	3.01	0.66	0.33	1.31	
Mn44yx		OO*H	8.65	3.03	2.98	3.87	3.86	0.65	0.34	1.30	
Mn4zy4	OO*H		8.68	3.07	3.85	3.85	2.98	0.71	0.31	1.31	

Mn44yx	OOH*		8.70	3.07	2.95	3.86	3.86	0.67	0.32	1.31	
Mnz4y4		OO*H	8.76	3.89	3.04	3.90	3.01	0.71	0.32	1.31	
Mn3344	**q=-3**		**2S+1=16**								
Mn4zy4		OO*	8.66	3.13	3.87	3.87	3.00	0.59	0.33	1.29	
Mnz4y4	OO*		8.77	3.90	3.10	3.90	3.04	0.57	0.35	1.29	
Mn44yx		OO*	8.85	3.07	2.98	3.87	3.87	0.44	0.52	1.30	
Mnxz44		OO*	8.91	4.01	3.93	3.03	3.03	0.60	0.28	1.30	
Mnzz44	OO*		8.98	3.89	3.86	3.04	3.04	0.57	0.57	1.31	†
Mn3344	**q=-2**		**2S+1=17**								
Mnzz44	O_2		13.19	3.93	3.90	3.01	3.01	1.00	1.00	1.20	†
Mn4zy4	O_2		13.46	3.07	3.88	3.85	2.98	1.00	1.00	1.20	
Mnz4y4	O_2		13.53	3.92	3.03	3.90	3.01	1.00	1.00	1.20	
Mn44yx	O_2		13.63	3.07	2.97	3.86	3.86	1.00	1.00	1.20	
Mn3334	**q=-3**		**2S+1=17**								
Mnzzy4	OO*H		3.89	3.91	3.87	3.89	3.03	0.71	0.31	1.31	†,**4b-I**
Mnzzy4		OO*H	3.90	3.89	3.89	3.89	3.03	0.71	0.31	1.31	**4a-I**
Mnz4yx	OO*H		3.93	3.91	2.98	3.90	3.90	0.67	0.32	1.31	
Mn4zyz		OO*H	4.15	2.99	3.86	3.86	3.90	0.66	0.32	1.31	
Mn3334	**q=-4**		**2S+1=17**								
Mnz4yx	OO*		4.73	3.89	3.04	3.90	3.90	0.41	0.58	1.30	**4b-II**
Mnxzy4		OO*	4.81	3.97	3.91	3.90	3.05	0.61	0.32	1.31	**4a-II**
Mn4zyz		OO*	4.84	3.12	3.86	3.87	3.89	0.58	0.32	1.29	
Mnzzy4		OO*	4.91	3.89	3.87	3.90	3.03	0.56	0.57	1.32	†
Mn4zyx		OO*	4.98	3.14	3.82	3.84	3.84	0.58	0.33	1.29	
Mn4zyy		OO*	5.05	3.08	3.86	3.87	3.89	0.59	0.36	1.30	
Mnzxy4	OO*		5.06	3.92	3.98	3.90	3.07	0.32	0.60	1.30	
Mn3334	**q=-3**		**2S+1=18**								
Mnzzy4	O_2		8.61	3.91	3.89	3.89	3.03	1.00	1.00	1.20	†
Mnz4yx	O_2		8.89	3.91	2.96	3.90	3.90	0.95	1.03	1.20	
Mn3333	**q=-4**		**2S+1=19**								
Mnzzyz	O_2		4.91	3.90	3.86	3.89	3.89	1.00	1.00	1.20	†,**5**
Mn3333	**q=-4**		**2S+1=19**								
Mnzzyz	O_2 ($r = \infty$)		4.70	3.90	3.87	3.89	3.88				†,**6**

II. Detailed energy breakdown, named Intermediates

Table S2: Named intermediates in the water oxidation cycle of $[Mn_4V_4O_{17}(OAc)_3]^{3-}$, with detailed breakdown of electronic and thermochemical contributions to the Gibbs free energy. Columns from left to right: Redox and JT configuration of the cubane; configuration of reactive ligands on Mn_B and Mn_A; electronic energy relative to **1** at the B3LYP/def2-SVP level of theory; electronic energy relative to **1** at the B3LYP/def2-SVP/def2-TZVP level of theory; thermal correction to Enthalpy; thermal correction to Entropy; Grimme-D3 dispersion energy; energy correction for protons transferred to solution; final Gibbs free energy relative to **1**, computed at the B3LYP/def2-SVP/def2-TZVP level of theory. All energy values are given in eV. Further notes: named intermediates in bold.

Cubane config	Ligands		$\Delta E_{DZ,rel}$ [eV]	$\Delta E_{TZ,rel}$ [eV]	ΔH [eV]	ΔS [eV]	$\Delta E_{D3,corr}$ [eV]	ΔG^{H+}_{corr} [eV]	$\Delta G_{TZ,rel}$ [eV]	Notes
	Mn_B-	Mn_A-								
Mn4444	OH	OH_2	-3.91	-3.91	6.90	0.0100	-2.36	0.0000	0.00	**1**
Mnx444	OH_2	O*H	9.74	9.74	6.55	0.0102	-2.29	11.1090	2.15	**2a**
Mn4z44	O*H	OH	9.50	9.50	6.50	0.0102	-2.28	11.1090	1.85	**2b**
Mn4zy4		OOH	21.93	21.83	6.26	0.0102	-2.18	22.2181	2.83	**3a**
Mnz4y4	OOH		22.10	22.00	6.26	0.0102	-2.17	22.2181	2.99	**3b**
Mnzzy4		OO*H	23.06	23.01	6.24	0.0107	-2.08	22.2181	3.85	**4a-I**
Mnzzy4	OO*H		23.07	23.02	6.24	0.0107	-2.08	22.2181	3.84	**4b-I**
Mnxzy4		OO*	35.34	35.08	5.90	0.0104	-2.07	33.3271	4.55	**4a-II**
Mnz4yx	OO*		35.24	35.08	5.90	0.0103	-2.08	33.3271	4.57	**4b-II**
Mnzzyz	O_2		35.65	35.32	5.90	0.0111	-2.01	33.3271	4.58	**5**
Mnzzyz	O_2 (r = ∞)		35.78	35.36	5.86	0.0121	-1.94	33.3271	4.28	**6**

Final Gibbs free energies are obtained according to

$$\Delta G_{TZ,rel}(i) = \left(\Delta E_{TZ}(i) + \Delta H(i) - T\Delta S(i) - \Delta G^{H+}_{corr}(i)\right) - \Delta G_{TZ}(\mathbf{1}),$$

wherein $\Delta G_{TZ,rel}(i)$ is the Gibbs free energy of species *i* at the B3LYP/def2-SVP/def2-TZVP level of theory relative to $\Delta G_{TZ}(\mathbf{1})$, $\Delta E_{TZ}(i)$ is the electronic energy of species *i* at the B3LYP/def2-TZVP level of theory, $\Delta H(i)$ is the thermal correction of the enthalpy for species *i* obtained from frequency calculations at the B3LYP/def2-SVP level of theory, T = 298.150 K, $\Delta S(i)$ is the thermal correction to the entropy for species *i* obtained from frequency calculations at the B3LYP/def2-SVP level of theory, and $\Delta G^{H+}_{corr}(i)$ is the correction to the Gibbs energy arising from protons transferred to solution for species *i*. For simplicity, here we define

$$\Delta E_{TZ,rel}(i) = \Delta E_{TZ}(i) - \Delta G_{TZ,rel}(\mathbf{1}).$$

It should be noted that differences in Gibbs free energy between intermediates arise primarily from the difference in electronic energy (see Table S2). There is some small variance in enthalpic and entropic contributions that we ascribe to the differing number of protons between intermediates and is effectively compensated by the correction term for protons transferred to solution ΔG^{H+}_{corr}.

III. Nudged elastic band calculations

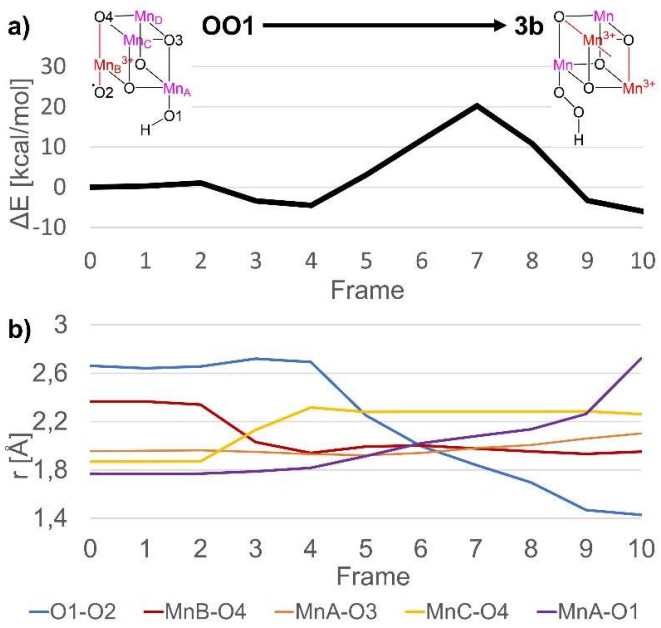

Figure S1: a) Energy changes along the minimum energy path (MEP) between **OO1** and **3b**. b) Bond lengths along the MEP between **OO1** and **3b**; O1-O2 in blue, Mn_B-O4 along z-axis in red, Mn_A-O3 along z-axis in orange, Mn_C-O4 along y-axis in yellow, and Mn_A-O1 in purple.

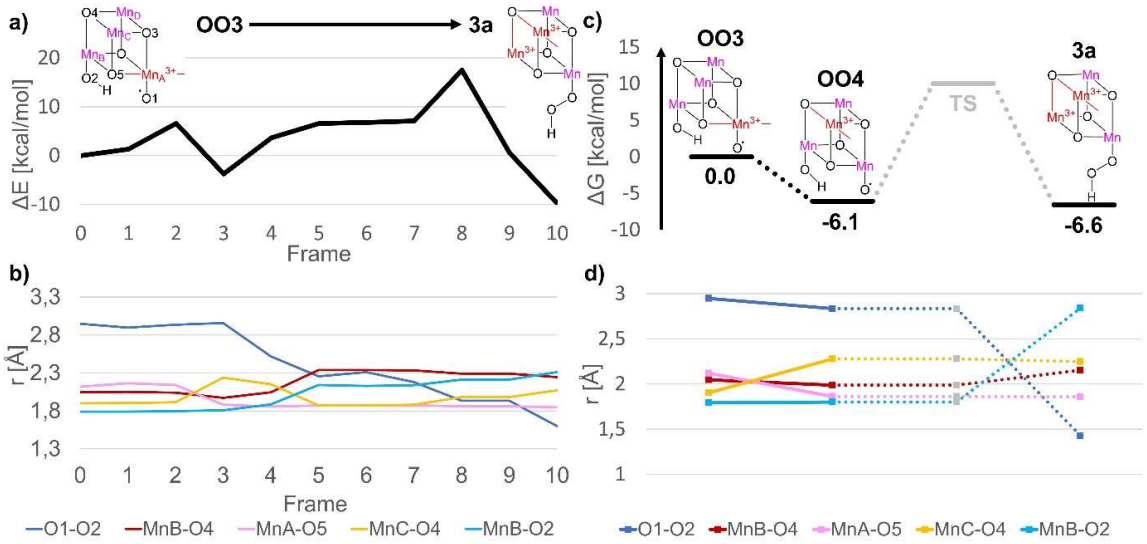

Figure S2: a) Energy changes along the minimum energy path (MEP) between **OO3** and **3a** (convergence: max(Fp)=0.02, RMS(FP)=0.01, max(FCI)=0.05, RMS(FCI)=0.002). b) Bond lengths along the MEP between **OO3** and **3a**; O1-O2 in blue, Mn_B-O4 along z-axis in red, Mn_A-O5 along x-axis in pink, Mn_C-O4 along y-axis in yellow, and Mn_B-O2 in cyan. c) Stationary points along the MEP for conversion of **3b** to **3a** and their relative energies in kcal/mol (TS could not be optimized, shown in grey). d) Bond lengths for stationary points along the MEP; color scheme as in b; TS could not be optimized, shown in grey).

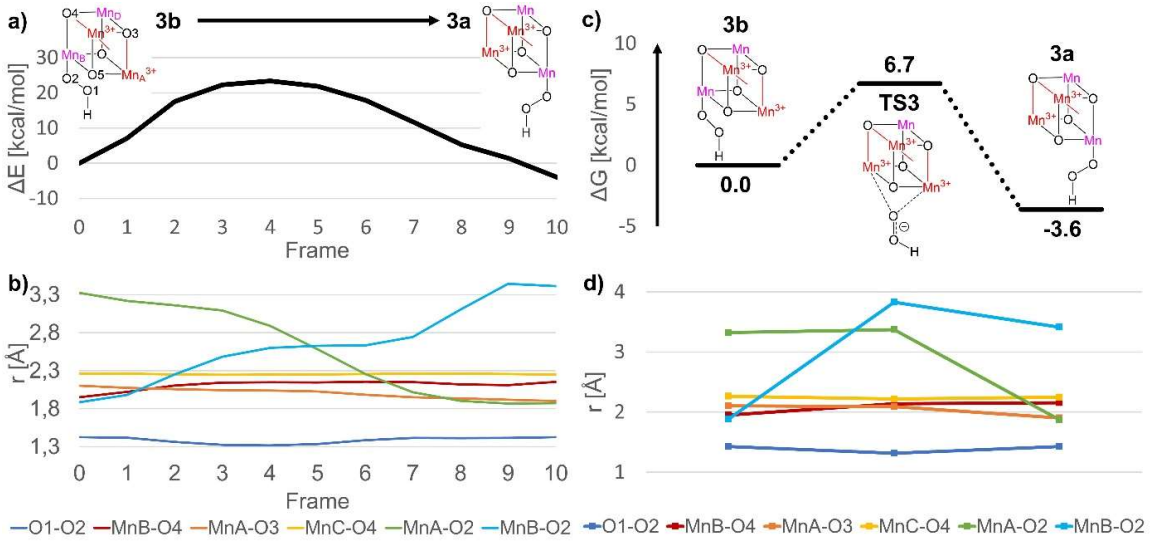

Figure S3: a) Energy changes along the minimum energy path (MEP) between **3b** and **3a**. b) Bond lengths along the MEP between **3b** and **3a**; O1-O2 in blue, Mn_B-O4 along z-axis in red, Mn_A-O3 along z-axis in orange, Mn_C-O4 along y-axis in yellow, and Mn_A-O2 in green, Mn_B-O2 in cyan. c) Stationary points along the MEP for conversion of **3b** to **3a** and their relative energies in kcal/mol. d) Bond lengths for stationary points along the MEP; color scheme as in b).

IV. List of O-O bond formation stationary points

Table S3: Stationary points along the MEPs for O-O bond formation. Columns from left to right: Redox and JT configuration of the cubane (e.g Mnx444, corresponding to a $Mn^{4+}{}_3Mn^{3+}$ configuration with a JT axis in x direction on Mn_A); configuration of reactive ligands on Mn_B and Mn_A; Gibbs free energy relative to **1**, computed at the B3LYP/def2-SVP/def2-TZVP level of theory (in eV); spin populations of Mn_{A-D} as well as the oxygen atoms of the reactive ligands, where O2 is bound to Mn_B and O1 is bound to Mn_A in **1**; O1-O2 distance in Å. Further notes: names of intermediates and TSs in bold.

Cubane redox state	Ligands		$\Delta G_{TZ,rel}$ [eV]	Spin populations						$r_{O\text{-}O}$ [Å]	Notes
	Mn_B-	Mn_A-		Mn_A	Mn_B	Mn_C	Mn_D	O2	O1		
Mn4z44	O*	OH	3.14	2.95	3.81	3.03	3.03	1.14	0.10	2.66	**OO1**
Mn44y4	O*	OH	2.76	2.98	2.92	3.88	3.02	1.03	0.08	2.84	**OO2**
Mn44y4	$O^{0.5}$	OH	4.10	3.56	2.95	3.89	3.03	0.53	0.01	1.84	**TS1**
Mnz4y4	OOH		2.99	3.91	3.05	3.90	3.03	-0.03	0.01	1.43	**3b**
Mnx444	OH	O*	3.12	3.86	2.98	3.01	3.01	0.04	1.01	2.95	**OO3**
Mn44y4	OH	O*	2.85	2.96	2.95	3.87	3.01	0.07	1.04	2.83	**OO4**
Mn4zy4		OOH	2.83	3.06	3.87	3.87	3.01	-0.01	0.01	1.43	**3a**
Mnzzy4	-OO*H-		3.41	3.91	3.89	3.89	3.02	-0.66	-0.33	1.32	**TS3**

V. Detailed energy breakdown, O-O bond formation stationary points

Table S4: Named intermediates and transition states along the MEPs of O-O bond formation in $[Mn_4V_4O_{17}(OAc)_3]^{3-}$, with detailed breakdown of electronic and thermochemical contributions to the Gibbs free energy. Columns from left to right: Redox and JT configuration of the cubane; configuration of reactive ligands on Mn_B and Mn_A; electronic energy relative to **1** at the B3LYP/def2-SVP level of theory; electronic energy relative to **1** at the B3LYP/def2-SVP/def2-TZVP level of theory; thermal correction to enthalpy; thermal correction to entropy; Grimme-D3 dispersion energy; energy correction for protons transferred to solution; final Gibbs free energy relative to **1** at the B3LYP/def2-SVP/def2-TZVP level of theory. All energy values are given in eV. Further notes: named intermediates, transition states in bold.

Cubane config	**Ligands**		$\Delta E_{DZ,rel}$ [eV]	$\Delta E_{TZ,rel}$ [eV]	ΔH [eV]	ΔS [eV]	$\Delta E_{D3,corr}$ [eV]	ΔG^{H+}_{corr} [eV]	$\Delta G_{TZ,rel}$ [eV]	**Notes**
	Mn_B-	**Mn_A-**								
Mn4z44	O*	OH	22.40	22.16	6.21	0.0101	-2.23	22.2181	3.14	**OO1**
Mn44y4	O*	OH	22.01	21.77	6.22	0.0101	-2.23	22.2181	2.76	**OO2**
Mn44y4	$O^{0.5}$	OH	23.31	23.12	6.19	0.0100	-2.19	22.2181	4.10	**TS1**
Mnz4y4	OOH		22.10	22.00	6.26	0.0102	-2.17	22.2181	2.99	**3b**
Mnx444	OH	O*	22.37	22.11	6.20	0.0100	-2.23	22.2181	3.12	**OO3**
Mn44y4	OH	O*	22.08	21,83	6.23	0.0100	-2.23	22.2181	2.85	**OO4**
Mn4zy4		OOH	21.93	21.83	6.26	0.0102	-2.18	22.2181	2.83	**3a**
Mnzzy4	-OO*H-		22.42	22.47	6.18	0.0102	-2.20	22.2181	3.41	**TS3**

A.3 Regeneration and Degradation in a Biomimetic Polyoxometalate Water Oxidation Catalyst

LUDWIG SCHWIEDRZIK, TINA RAJKOVIC, AND LETICIA GONZÁLEZ

ACS Catal., **2023**, 13, 3007-3019.
https://doi.org/10.1021/acscatal.2c06301

Contributions:

Ludwig Schwiedrzik designed the research, performed the research, analyzed the data, and wrote the paper.

Tina Rajkovic performed the research.

Leticia González designed the research and wrote the paper.

ACS Catalysis

pubs.acs.org/acscatalysis

Research Article

Regeneration and Degradation in a Biomimetic Polyoxometalate Water Oxidation Catalyst

Ludwig Schwiedrzik,* Tina Rajkovic, and Leticia González*

Cite This: *ACS Catal.* 2023, 13, 3007−3019

Read Online

ACCESS | Metrics & More | Article Recommendations | Supporting Information

ABSTRACT: Complete understanding of catalytic cycles is required to advance the design of water oxidation catalysts, but it is difficult to attain, due to the complex factors governing their reactivity and stability. In this study, we investigate the regeneration and degradation pathways of the highly active biomimetic water oxidation catalyst $[Mn^{3+}{}_2Mn^{4+}{}_2V_4O_{17}(OAc)_3]^{3-}$, thereby completing its catalytic cycle. Beginning with the deactivated species $[Mn^{3+}{}_4V_4O_{17}(OAc)_2]^{4-}$ left over after O_2 evolution, we scrutinize a network of reaction intermediates belonging to two alternative water oxidation cycles. We find that catalyst regeneration to the activated species $[Mn^{4+}{}_4V_4O_{17}(OAc)_2(OH)(H_2O)]^-$ proceeds via oxidation of each Mn center, with one water ligand being bound during the first oxidation step and a second water ligand being bound and deprotonated during the final oxidation step. $\Delta\Delta G$ values for this last oxidation are consistent with previous experimental results, while regeneration within an alternative catalytic cycle was found to be thermodynamically unfavorable. Extensive in silico sampling of catalyst structures also revealed two degradation processes: cubane opening and ligand dissociation, both of which have low barriers at highly reduced states of the catalyst due to the presence of Jahn−Teller effects. These mechanistic insights are expected to spur the development of more efficient and stable Mn cubane water oxidation catalysts.

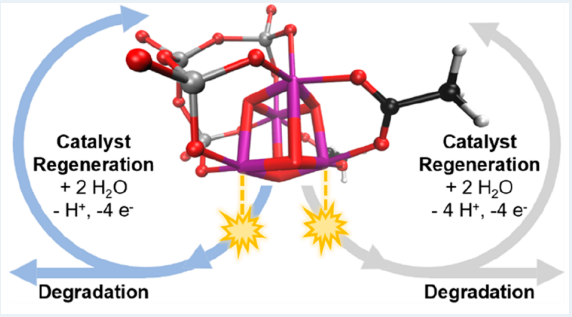

KEYWORDS: *artificial photosynthesis, polyoxometalate, Jahn−Teller axis, electrocatalysis, regeneration, degradation, density functional theory*

1. INTRODUCTION

Humanity's overreliance on fossil fuels is the main driver of the current climate and energy crises, the effects of which are increasingly being felt across the globe.[1−3] Searching for alternatives, researchers have worked for decades to develop new technologies for converting solar to chemical energy.[4,5] Among these, artificial water splitting plays a prominent role, promising to create renewable H_2 from water and sunlight.[6,7] Water splitting is a four-electron redox reaction consisting of two half-reactions: water oxidation and hydrogen evolution. Since water oxidation is considered the more challenging of the two, great efforts have been made to develop efficient water oxidation catalysts.[7−13] Inspired by the oxygen-evolving complex (OEC), which contains the tetramanganese cubane active center responsible for water oxidation in natural photosynthesis, a large number of biomimetic catalysts featuring four metal centers in a cubane arrangement have been synthesized and investigated.[13−28]

Among such systems, those featuring Co_4O_4 and Mn_4O_4 cubane cores have been intensively studied, often as model systems for the natural OEC or for heterogeneous catalysts relevant for industrial-scale water splitting. In this context, the cubanes' ability to flexibly redistribute electrons between metal centers has been leveraged to explain their high water oxidation activity.[18−20] Jahn−Teller (JT) effects have been noted to significantly alter the structure[29−37] and even the reactivity of Mn-containing catalysts featuring Mn^{3+} centers.[38−41] Such distortions are present in d^4 metal centers such as Mn^{3+} and lead to the elongation of one bond axis and concomitant shortening of the other two bond axes in an octahedral coordination environment. They represent a form of structural flexibility that, when taken together with the aforementioned facile electron redistribution, makes Mn-oxo cubane catalysts featuring Mn^{3+} centers particularly promising candidates for increasing the efficiency of the water oxidation reaction.[40−44]

In this work, we focus on the bioinspired water oxidation catalyst $[Mn^{3+}{}_2Mn^{4+}{}_2V_4O_{17}(OAc)_3]^{3-}$ (abbreviated as **3344-OAc**, where the numbers indicate the oxidation states of the

Received: December 21, 2022
Revised: January 30, 2023

Mn atoms; see Figure 1a).[45] This highly active multicenter catalyst (turnover number (TON) > 12 000; turnover

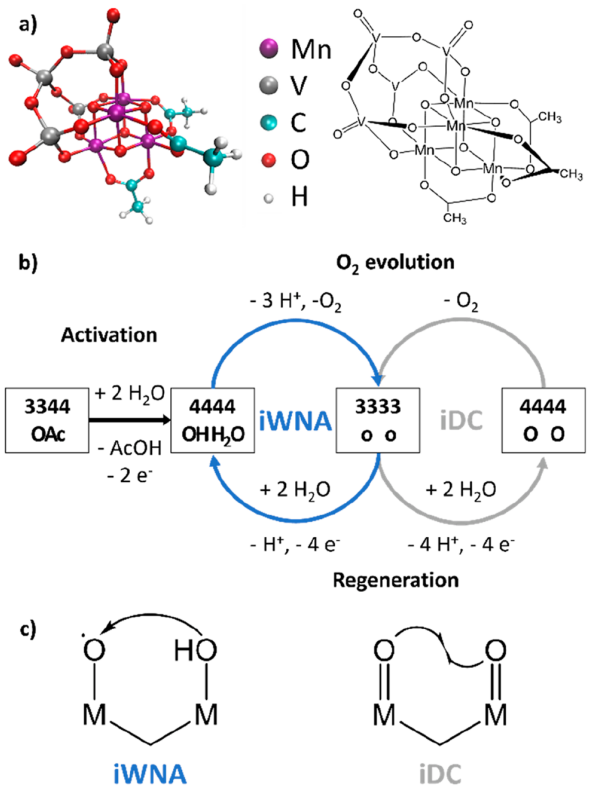

Figure 1. (a) Three-dimensional structure of $[Mn^{3+}_2Mn^{4+}_2V_4O_{17}(OAc)_3]^{3-}$ or **3344-OAc** with color legend (left) and its ChemDraw structure (right). (b) Reactivity scheme of **3344-OAc**, consisting of activation (black arrow), the proposed iWNA cycle between **4444-OH-H_2O** and **3333-o-o** (blue), and the alternative proposed iDC cycle between **4444-O-O** and **3333-o-o** (gray). O_2 evolution occurs in the upper half of each cycle, while the lower half corresponds to catalyst regeneration. (c) Different types of O−O bond formation mechanisms in multicenter water oxidation catalysts: intramolecular nucleophilic attack by an OH ligand on a neighboring terminal oxyl ligand (iWNA) and intramolecular direct coupling between two neighboring terminal oxo ligands (iDC).

frequency (TOF) > 200 min^{-1})[46] consists of an Mn_4O_4 cubane core, surrounded on three sides by a hexadentate V_4O_{13} vanadate ligand and three bidentate acetate ligands on the remaining sides. A prior combined experimental and theoretical study showed that **3344-OAc** is actually a precatalyst that must first undergo activation by oxidation of two Mn centers to yield an Mn^{4+}_4 configuration of the cubane core as well as exchange of one acetate with an OH and an H_2O ligand before the actual O_2 evolution can be catalyzed (Figure 1b, black arrow). The activated species was determined to be $[Mn^{4+}_4V_4O_{17}(OAc)_2(OH)(H_2O)]^-$ (**4444-OH-H_2O**).[40] Further theoretical work led to the proposal of a feasible mechanism for O_2 evolution, consisting of three proton-coupled electron transfers (PCET) and one electron transfer (ET) step (Figure 1b, upper half of blue cycle).[41] After O_2 evolution, the catalyst was found to remain as $[Mn^{3+}_4V_4O_{17}(OAc)_2]^{4-}$ (**3333-o-o**), a deactivated species with two cofacial open coordination sites (**o**) that must undergo regeneration before being able to catalyze another turnover. The question of how **4444-OH-H_2O** is regenerated from **3333-o-o** has thus far remained unanswered, leaving the understanding of the catalytic cycle incomplete.

In our proposed water oxidation cycle, O−O bond formation is achieved by the intramolecular attack of an OH ligand bound to one Mn center on a cofacial metal-oxyl group, as in the iWNA mechanism shown in Figure 1c.[41] This is one variant of the so-called "water nucleophilic attack" (WNA) type of mechanism, which has been often invoked to explain the reactivity of the OEC, as well as that of a large number of synthetic water oxidation catalysts.[8,12,13,47,48] In catalysts where multiple terminal metal-oxo groups are present in close proximity (including the OEC), an alternative form of O−O bonding has been proposed, coined a direct coupling (DC) type of mechanism—an intramolecular variant of which (iDC) is also shown in Figure 1c.[12,13,16,47,49,50] While no species featuring two cofacial oxo or oxyl ligands have been invoked so far for our tetramanganese catalyst, this does not rule out that an iDC-type water oxidation cycle could exist alongside the previously proposed iWNA-type. We hypothesize that O−O bond formation according to the iDC mechanism could best be achieved by first binding water ligands at a low redox state, followed by combined deprotonation and metal-centered oxidation through a series of PCET steps (Figure 1b, lower half of gray cycle), leading to a highly oxidized catalyst with terminal oxo ligands, $[Mn^{4+}_4V_4O_{17}(OAc)_2(O)_2]^{4-}$ (termed **4444-O-O**).

Previous work on **3344-OAc** paid particular attention to the role of JT effects in the reactivity of the catalyst. These effects have been noted to affect the structure and reactivity of the OEC as well as other synthetic catalysts containing d^4 metal centers;[29−39] JT effects have even been linked to increased water oxidation activity in heterogeneous catalysts.[42−44,51] In **3344-OAc**, we found that JT effects play a pivotal role in multiple reaction steps. During activation, JT-elongated bonds provided key weak points for water attack and subsequent ligand exchange.[40] We observed similar behavior for the O_2 dissociation step of the water oxidation mechanism.[41] Finally, we showed that during O_2 evolution, a reorientation of JT-distorted bonds precedes the formation of the O−O bond, which is itself concerted with an ET from the reactive ligands to a Mn center and the emergence of JT distortions at that same metal center.[41]

The obvious importance of JT effects for the reactivity of **3344-OAc** motivated some of us to study in depth the relative stability of structures featuring different orientations of JT-distorted bonds across all relevant redox states of the catalyst, resulting in a set of heuristic rules for the comparison among such structures.[52] In this context, we found that JT axes were energetically favorable when oriented toward the acetate or water ligands, but not toward the vanadate ligand, so that the vanadate appeared to stabilize the catalyst, which itself is overall quite flexible. The presence of a number of structures featuring open coordination sites as more stable alternatives to fully coordinated complexes at the lowest oxidation state of the catalyst (**3333**) was also noted and rationalized as an especially strong JT effect.[53]

In this work, we set out to investigate the regeneration mechanism of the **3344-OAc** catalyst from the deactivated **3333-o-o** form to the **4444-OH-H_2O** one (lower half of the blue cycle in Figure 1b), formally

https://doi.org/10.1021/acscatal.2c06301
ACS Catal. 2023, 13, 3007−3019

$$[Mn^{3+}{}_4V_4O_{17}(OAc)_2]^{4-} + 2H_2O \rightarrow [Mn^{4+}{}_4V_4O_{17}(OAc)_2(OH)(H_2O)]^{-} + H^+ + 4e^- \quad (1)$$

by sampling the large number of structures that could be involved in that process. To this end, we propose a network of intermediates that connect the two species, featuring a variety of ligand configurations from the two open coordination sites of the deactivated species to the H_2O and OH ligands of the activated catalyst. By comparing the stabilities of these various intermediates, we aim at uncovering a feasible regeneration mechanism for **3344-OAc**, thereby closing the proposed iWNA cyle. At the same time, we investigate the possibility of an iDC-type water oxidation cycle (shown in gray in Figure 1b). We focus on regeneration via binding of water ligands at a low oxidation state and a series of PCET steps, leading to a highly oxidized catalyst with terminal oxo ligands, **4444-O-O**, that is able to carry out O_2 evolution according to the iDC mechanism. Finally, we expect that the exhaustive sampling of reaction intermediate structures here undertaken can shed further light on the role of JT effects in the reactivity and stability of **3344-OAc** and its derivatives.

2. METHODS

2.1. Nomenclature. The presence of up to four Mn^{3+} centers across multiple oxidation states of our catalyst, which show distinctive JT bond distortions, necessitates sampling a large number of redox isomers (structures that differ in the assignment of oxidation states to specific Mn centers) and JT isomers (structures that differ in the *x*-, *y*-, or *z*-orientation of their elongated JT bond axes). To differentiate between these isomers, we use a specific nomenclature and abbreviated structural representation that is illustrated in Figure 2. Figure 2a shows the full and abbreviated ChemDraw structures of the most stable JT isomer of the deactivated species **3333-o-o**, which features four Mn^{3+} centers, each with a JT axis pointing to the *z*-direction (highlighted in red), and which will therefore be referred to as **zzzz-o-o**. Further representative examples with other oxidation states are shown in Figures 2b–d. Figure 2b is a **3334-o-o** structure, and because MnA, MnB, and MnD are Mn^{3+} centers with JT axes in the *z*-direction and MnC is an Mn^{4+} center without a JT axis, it is labeled as **zz4z-o-o**. Figure 2c is a **3344-o-o** species, where MnA and MnB are Mn^{4+} centers without JT axes, while MnC and MnD are Mn^{3+} centers with a JT axis in the *y*- and *z*-direction, respectively; it is therefore labeled as **44yz-o-o**. Finally, in Figure 2d, we depict a **3444-o-o** structure, with MnA, MnB, and MnC being Mn^{4+} centers and thus having no JT axes, and MnD being a Mn^{3+} center with a JT axis in the *x*-direction, thus labeled as **444x-o-o**. The **4444** oxidation state of the catalyst does not show redox or JT isomerism.

Furthermore, the catalyst was investigated in a variety of ligand configurations that are exemplified in Figure 3 for the oxidation state **4444**. Figure 3a shows the full and abbreviated ChemDraw structures of **4444-OH-H_2O**, a structure with an OH ligand bound to MnB and an H_2O ligand bound to MnA. Figure 3b displays **4444-o-o**, a structure with an open coordination site at each of the reactive centers MnA and MnB, while Figures 3c and 3d provide two examples each of structures with an open coordination site at MnA and a ligand bound to MnB (**4444-H_2O-o** and **4444-OH-o**) and vice versa (**4444-o-H_2O** and **4444-o-OH**). Finally, Figure 3e depicts a

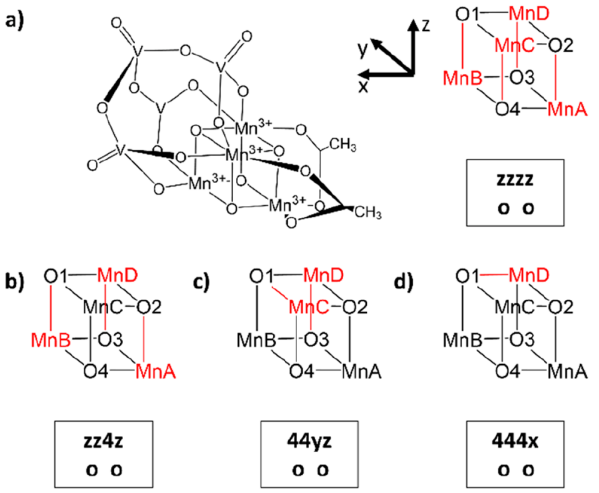

Figure 2. (a) Full ChemDraw structure of **zzzz-o-o**, the most stable isomer of the deactivated species **3333-o-o**, and its abbreviated ChemDraw structure with Mn centers labeled A–D and O atoms labeled 1–4. The Mn^{3+} centers and their respective JT axes are highlighted in red. The accompanying text box contains a descriptor consisting of two parts, the first with letters corresponding to the JT axis orientations at the Mn^{3+} centers ABCD (in this case, **zzzz**) and the second giving ligand configuration (in this case, **o o**, representing open coordination sites at MnB and MnA). (b–d) Abbreviated ChemDraw structures for **zz4z-o-o** (**3334** oxidation state), **44yz-o-o** (**3344**), and **444x-o-o** (**3444**), respectively.

structure with terminal oxo ligands bound to both MnA and MnB (**4444-O-O**). Other ligand configurations featuring, e.g., acetate ligands bound to MnA and MnB were not investigated here, as this would go beyond the scope of the present study; the reader is instead referred to other work covering the speciation of the catalyst both from an experimental and theoretical point of view.[40,45,46,52,54]

2.2. Sampling Procedure. In all investigated ligand configurations, the catalyst exhibits an idealized C_S symmetry, meaning that symmetry-equivalent structures were considered degenerate and therefore not sampled separately. Therefore, all Boltzmann populations are weighted by the degeneracy of the corresponding isomers. Even considering the idealized C_S symmetry of **3344-OAc** derivatives, the complete characterization of a single ligand configuration would have included 136 individual redox and JT isomers, an intractable task considering the number of ligand configurations investigated in this study. Therefore, we made use of the heuristic rules for the relative stability of redox and JT isomers derived by Mai et al.[52] to predict the most stable isomers for each oxidation state. In the case of the **4444** and **3444** oxidation states, the total number of symmetry-unique isomers is small enough so that all of them could be sampled. However, for the **3344**, **3334**, and **3333** oxidation states, only those isomers predicted by heuristics[52] to be within less than 12 kcal/mol of the most stable isomer within each oxidation state were targeted for sampling. A detailed analysis of the utility and accuracy of the heuristics used for sampling target selection can be found in section I in the Supporting Information (SI).

Sampling was performed according to a multistep protocol adapted from Mai et al.[52] Guess geometries for each isomer targeted for sampling were initially obtained from preoptimizations with geometric constraints, wherein a specific JT

https://doi.org/10.1021/acscatal.2c06301
ACS Catal. 2023, 13, 3007–3019

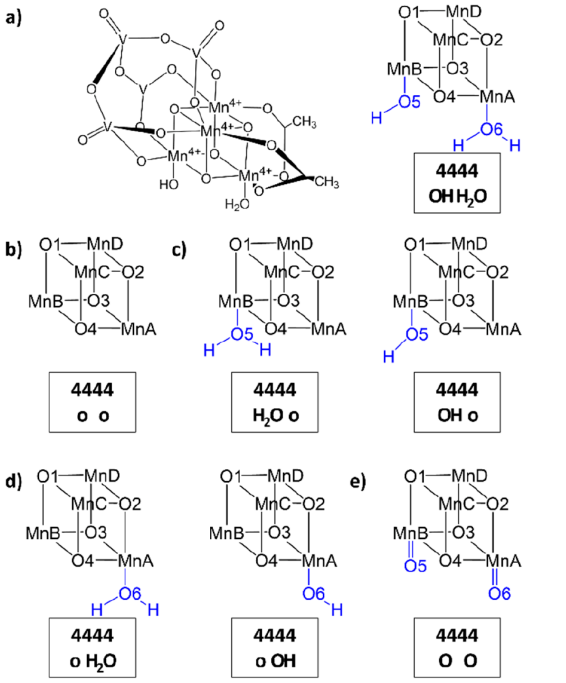

Figure 3. (a) Full ChemDraw structure of the activated species **4444-OH-H_2O**, showing the redox state of each Mn center, and its abbreviated ChemDraw structure with Mn centers labeled A-D, O atoms labeled 1−6. Ligands at MnA and MnB are highlighted in blue. The accompanying text box contains a descriptor consisting of two parts; in the first, each number corresponds to the redox state of the Mn^{4+} centers ABCD that have no JT axes (in this case, **4444**) and the ligand configuration (in this case, **OH H_2O**, representing the OH ligand at MnB and the H_2O ligand at MnA). (b−e) Abbreviated ChemDraw structures for **4444-o-o** (panel (b)), **4444-H_2O-o** and **4444-OH-o** (panel (c)), **4444-o-H_2O** and **4444-o-OH** (panel (d)), and **4444-O-O** (panel (e)).

configuration was enforced by setting the bond length of the corresponding Mn−O bond(s) within the cubane core to a value of 2.30 Å (in some cases, the opposing bond additionally had to be constrained to 2.20 Å; see section II in the SI for details). These guess geometries were then optimized without constraints, resulting in one or more stable isomers for the particular oxidation state and ligand configuration under investigation. As not every targeted isomer corresponded to a stable minimum on the potential energy surface, many of the unconstrained optimizations resulted in virtually identical structures; only the most stable of these for each redox and JT isomer is reported herein.

2.3. Computational Details. All single point, optimization, and frequency calculations were performed using the Orca 4.2.1 package,[55,56] with the zeroth order regular approximation (ZORA),[57−59] Grimme's D3 dispersion correction,[60] and the conductor-like polarized continuum model C-PCM for implicit solvation with surface type vdw_gaussian.[61] The resolution of identity for Coulomb integrals and numerical chain-of-sphere integration for the Hartree−Fock exchange integrals (RIJCOSX) was used to accelerate the calculations.[62] Constrained preoptimizations used the looseopt keyword for looser optimization convergence thresholds, with the unrestricted BP86 functional[63,64] and the ZORA-SVP basis set with def2/J general auxiliary basis set.[65] For simplicity, the C-PCM parameters of acetonitrile were used. Final unconstrained optimizations and numerical frequency calculations of isomers made use of the unrestricted B3LYP functional,[66,67] with the double-ζ ZORA-def2-SVP basis set and SARC/J decontracted auxiliary basis set.[65] To simulate the ACN:H_2O 9:1 (v/v) solvent mixture employed in experiments,[45,46] the C-PCM parameters for acetonitrile were combined with a custom epsilon value of 41.589 (9:1 weighted average of the epsilon values of ACN and H_2O).[41] Finally, single point electronic energies were refined using the larger triple-ζ ZORA-def2-TZVP basis set[65] with otherwise identical parameters to the final optimization protocol. The JT configuration of optimized structures was determined by comparing the lengths of Mn−O bonds within the cubane core, with the longest bond determining the *x*-, *y*-, or *z*-orientation of the JT axis on each Mn^{3+} center. All obtained structures were evaluated according to their numerically calculated vibrational frequencies; those showing negative frequencies were excluded from the results discussed herein. In all our calculations, an all-atom model of the complex using the high-spin configuration was employed, as is common in the literature.[40,41,52,54,68−70] Oxidation states are reported based on the Mulliken spin populations computed for individual atoms.

Final reported Gibbs energies are based on the refined electronic energies calculated using the ZORA-def2-TZVP basis set in combination with thermochemical corrections from the final optimizations and frequency calculations carried out using the ZORA-def2-SVP basis set. To account for energy differences between different ligand configurations, reference energies of the isolated ligands were calculated at the same final level of theory. Free energies in solution have been corrected for concentration effects using the package "GoodVibes",[71] setting the concentrations of all catalyst intermediates to a standard reference value of 1 M and the concentration of the 10% water in solution to 5.53 M.[72] Furthermore, to account for differing protonation states between structures, an energy correction term was calculated using the approach of Van Voorhis and co-workers, wherein the standard free energy of a proton in solution is added for each proton abstracted from the cluster.[8] As in our previous work,[41] we used a 9:1 weighted average of the standard free energy of a proton in acetonitrile (11.0622 eV) and of a proton in water (11.5305 eV)[73] to approximate the standard free energy of a proton in the ACN:H_2O 9:1 (v/v) solution mixture used in the experiment, giving 11.1090 eV.

In order to study possible instances of catalyst degradation, Climbing Image-Nudged Elastic Band (CI-NEB)[74] calculations, as implemented in ORCA 5.0.3,[55,56] were performed on several examples of intermediates showing various structural defects. Here, the unrestricted B3LYP functional[66,67] was used with the ZORA-def2-SVP basis set,[65] D3 dispersion correction,[60] and C-PCM (acetonitrile, epsilon = 41.589) with surface type vdw_gaussian.[61] Barrier heights for reactions studied using CI-NEB reported herein are calculated based on the electronic energy difference between the NEB climbing image and the reactant species, computed using ZORA-def2-SVP, and should therefore be taken as approximate, most likely upper bounds.

3. RESULTS

A total of 558 individual isomers were sampled across all oxidation states and ligand configurations, resulting in 159 stable minima. All investigated combinations of oxidation

https://doi.org/10.1021/acscatal.2c06301
ACS Catal. 2023, 13, 3007−3019

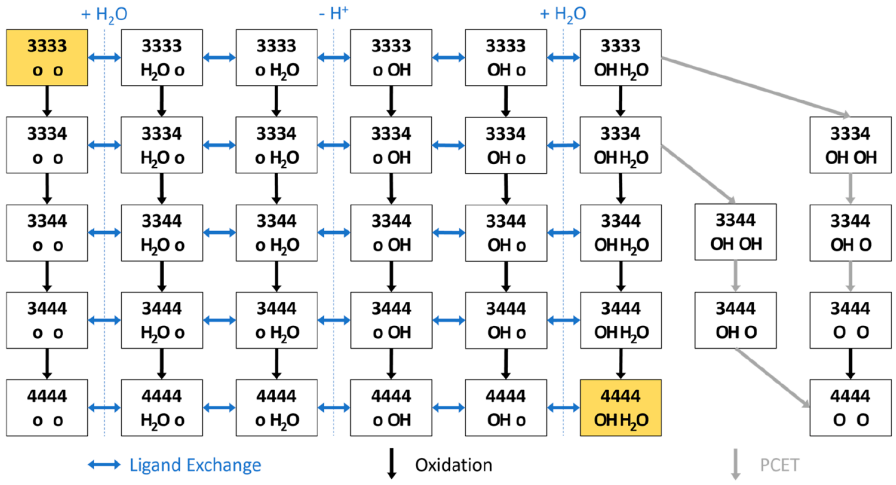

Figure 4. Scheme of all investigated oxidation pathways and their intermediates. Ligand exchange reactions are indicated by blue arrows, oxidation steps by black arrows, and proton-coupled electron transfer (PCET) steps by gray arrows. The starting **3333-o-o** and final **4444-OH-H_2O** structures (derived from prior work[40,41]) are highlighted in orange.

states and ligand configurations are shown in Figure 4. In the following, obtained results will be summarized for each ligand configuration, focusing on the most stable minima for each oxidation state—i.e., listing all structures with a Boltzmann population of at least 5% at thermal equilibrium (T = 298.15 K) for that ligand configuration and oxidation state. A full list of all optimized structures can be found in Tables S2−S9 in the SI.

Analysis of the bond lengths between each metal center and its coordinating atoms revealed several structures showing varying degrees of ligand dissociation; these structures are marked with an asterisk (*), and corresponding large interatomic distances are noted explicitly. To study the processes leading to the formation of such partially dissociated intermediates, NEB calculations were performed between representative examples of these intermediates and non-dissociated structures of identical oxidation state and comparable ligand configuration. The energy values given for intermediates and their various isomers are relative Gibbs energies calculated at the B3LYP-D3/ZORA-def2-TZVP//B3LYP-D3/ZORA-def2-SVP level of theory, while barrier heights are the relative electronic energy between the reactant and the climbing image of a CI-NEB simulation carried out only at the B3LYP-D3/ZORA-def2-SVP level of theory.

We begin at the lowest oxidation state with the ligand configuration featuring two open coordination sites, **3333-o-o**, which is the starting point of catalyst regeneration. The most stable isomer is **zzzz-o-o*** (0.0 eV relative Gibbs energy, 68% Boltzmann population at T = 298.15 K), which is used as a reference structure throughout this work. It features two slightly longer-than-average bond lengths within the cubane core caused by strong JT effects (r(MnC−O4) = 2.579 Å, r(MnD−O3) = 2.549 Å). Two other populated JT isomers were found: **zzyz-o-o*** (0.04 eV, 26%, r(MnD−O3) = 2.776 Å) and **zzzz-o-o** (0.06 eV, 5%). A NEB calculation between **zzzz-o-o** and **zzzz-o-o*** revealed a low kinetic barrier between them amounting to 0.25 eV or 5.7 kcal/mol. Oxidation to the **3334** state yields a mixed population consisting of **zz4z-o-o*** (3.95 eV, 90%, r(MnD−O3 = 2.519 Å) and **zz4x-o-o** (4.01 eV, 10%). A corresponding NEB calculation between **zz4x-o-o** and **zz4z-o-o*** showed that the elongation within the cubane core of the bond between MnD and O3 is effectively barrierless, with an activation energy of only 0.04 eV or 0.9 kcal/mol. Further oxidation states are dominated by single isomers: **zz44-o-o** (8.71 eV, 100%) for the **3344** oxidation state, **4z44-o-o** (14.49 eV, 100%) for the **3444** oxidation state, and finally **4444-o-o** (21.19 eV, 100%) for the **4444** oxidation state.

Moving on to the ligand configuration featuring a H_2O bound at MnB and an open coordination site at MnA, the most stable structures found at the lowest oxidation state (corresponding to **3333-H_2O-o** in Figure 4) are **xzxx-H_2O-o*** (0.05 eV, 57%, r(MnC−O2) = 2.548 Å, r(MnB−O5) = 3.526 Å, r(MnD−OAc) = 4.450 Å) and **zzzx-H_2O-o*** (0.05 eV, 43%, r(MnC−O4) = 2.884 Å, r(MnB−O5) = 3.851 Å). These structures, along with all but one of the others found for this ligand configuration and oxidation state, feature dissociated ligands—the sole exception being **zxyx-H_2O-o** (0.50 eV), which is however unpopulated at thermal equilibrium. At the **3334** oxidation state, two stable, populated intermediates could be identified: **z4yx-H_2O-o** (3.94 eV, 53%) and **zz4x-H_2O-o** (3.96 eV, 47%). The next oxidation leads to **z4y4-H_2O-o** (8.51 eV, 100%); further oxidation yields a mixture of **z444-H_2O-o** (13.95 eV, 79%) and **444x-H_2O-o** (14.00 eV, 21%); and finally **4444-H_2O-o** (20.22 eV, 100%) is obtained.

For the ligand configuration with an open coordination site at MnB and H_2O bound at MnA, the most stable isomer corresponding to **3333-o-H_2O** is **xzzx-o-H_2O*** (−0.37 eV, 100%, r(MnC−O4) = 3.014 Å), featuring an unusual combination of opened cubane core and protonated O4. A NEB calculation between the unpopulated **xzxx-o-H_2O** (0.43 eV) and **xzzx-o-H_2O*** reveals a very low barrier of only 0.17 eV or 3.8 kcal/mol for conversion to the O4-protonated species. The remaining oxidation states are dominated by only one populated species. Accordingly, starting at the **3334** oxidation state with **zzy4-o-H_2O** (3.92 eV, 98%), oxidation to the **3344** oxidation state yields **4z4x-o-H_2O** (8.38 eV, 100%), further oxidation to the **3444** oxidation state yields **4z44-o-H_2O** (13.57 eV, 100%), and finally oxidation to **4444** yields **4444-o-H_2O** (20,11 eV, 100%).

https://doi.org/10.1021/acscatal.2c06301
ACS Catal. 2023, 13, 3007−3019

Next, we examine the most stable intermediates for the ligand configuration featuring an open coordination site at MnB and OH bound at MnA. For the lowest oxidation state, the most stable isomer of **3333-o-OH** is **xzyz-o-OH** (1.86 eV, 95%). Oxidation to the **3334** oxidation state yields a mixed population of **yz4x-o-OH** (5.25 eV, 63%) and **yzy4-o-OH** (5.26 eV, 37%). Further oxidation to the **3344** oxidation state gives **4zy4-o-OH** (9.28 eV, 99%), then oxidation to the **3444** oxidation state gives **4z44-o-OH** (14.04 eV, 100%), and finally oxidation to the **4444** oxidation state gives **4444-o-OH** (20.23 eV, 100%).

All isomers found for **3333-OH-o**, the lowest oxidation state for the ligand configuration featuring OH bound at MnB and an open coordination site at MnA, have at least one partially dissociated ligand. The most stable isomers are **xxxx−OH-o*** (1.88 eV, 71%, r(MnB−O3) = 2.531 Å, r(MnD−OAc) = 4.810 Å) with an acetate ligand dissociated from one of its metal centers resulting in an open coordination site at MnD and **yyyx-OH-o*** (1.90 eV, 29%, r(MnB−O4) = 2.807 Å, r(MnC−OAc) = 6.651 Å) with a corresponding open coordination site at MnC. A NEB calculation was performed between the unpopulated isomers **zzyx-OH-o*** (2.84 eV, r(MnC−OAc) = 2.564 Å, r(MnD−OAc) = 2.556 Å) and **zxyx-OH-o*** (2.03 eV, r(MnD−OAc) = 4.157 Å) to investigate the transition between a strongly distorted and a fully dissociated Mn−OAc bond, finding a very low barrier of only 0.08 eV or 1.9 kcal/mol. Moving on to the **3334** oxidation state, only one populated isomer, **z4yz-OH-o** (5.44 eV, 99%), could be optimized. Oxidation to the **3344** oxidation state yields **z44x-OH-o** (9.50 eV, 100%); further oxidation to **3334** then results in **z444-OH-o** (14.45 eV, 100%), and finally oxidation to **4444** gives **4444-OH-o** (20.35 eV, 100%).

The final ligand configuration investigated as part of the regeneration half of the iWNA cycle from **3333-o-o** to **4444-OH-H_2O** features an OH and an H_2O ligand. One should note that the ligands at the two binding sites MnA and MnB are essentially interchangeable due to their hydrogen-bonded nature. However, thermodynamically it is more favorable to have H_2O bound to MnB for all oxidation states except the **4444** oxidation state. At the **3333** oxidation state, the most stable structures are **yzzx-H_2O-OH*** (1.91 eV, 93%, r(MnB−O5) = 3.166 Å) with a dissociated H_2O ligand and **xxyx-H_2O−OH** (1.98 eV, 5%). To obtain an approximate barrier height for the dissociation of an H_2O ligand, a NEB calculation was performed between **xxyx-H_2O-OH** and **yzzx-H_2O-OH***, resulting in a low barrier of 0.23 eV or 5.4 kcal/mol. Oxidizing to the **3334** oxidation state results in a mixed population of **yz4x-H_2O-OH** (5.13 eV, 84%) and **xz4x-H_2O-OH** (5,18 eV, 13%). Further oxidation to the **3344** oxidation state gives both **4z4x-H_2O-OH** (9.05 eV, 91%) and **44yx-H_2O-OH** (9.10 eV, 6%), while further oxidation to the **3444** oxidation state yields a mixture of **4z44-H_2O-OH** (13.69 eV, 58%) and **444x-H_2O-OH** (13.71 eV, 42%). The final oxidation step leads to **4444-OH-H_2O** (19.26 eV, 70%) and **4444-H_2O-OH** (19.28 eV, 30%), illustrating the typically small energy difference between the two protonation states.

We turn now to intermediates from a possible alternative iDC-type water oxidation cycle (gray in Figure 1b). The two iDC regeneration pathways we investigated (Figure 4) start from **3333-o-o** and proceed through the binding of water and a combination of PCET steps and one-electron oxidations all the way to **4444-O-O**, which contains two terminal oxo groups, ready to form an O−O bond by direct coupling. The initial intermediates of the first pathway feature an H_2O ligand bound to MnB and an OH ligand bound to MnA, resulting in two JT isomers: **yzzx-H_2O-OH*** (1.91 eV, 93%, r(MnB-O5) = 3.166 Å) and **xxyx-H_2O-OH** (1.98 eV, 5%). The first PCET step also results in a mixture of isomers, **yy4x-HO-HO** (7.09 eV, 54%), with O6 as the H-bond donor and O5 as the acceptor, and **xx4x-OH-OH** (7.10 eV, 40%) with O5 as the H-bond donor. Also at this step, a NEB calculation was performed between the unpopulated isomers **4xyx-OH-OH** (7.31 eV) and **4xxx-OH-OH*** (7.40 eV, r(MnD−OAc = 2.548 Å)), both with O5 as the H-bond donor and O6 as the H-bond acceptor. The barrier for the transition from the JT-distorted MnD−OAc bond of **4xyx-OH-OH** to the very strongly JT-distorted MnD−OAc bond of **4xxx-OH-OH*** was found to be very low at 0.17 eV or 4.0 kcal/mol. The second PCET step gives a mixed population of **4y4x-OH-O** (13.30 eV, 34%), **4x4x-OH-O** (13.30 eV, 27%), **x44x-O-OH** (13.31 eV, 18%), and **y44x-O-OH** (13.32 eV, 14%). The final PCET step yields **444x-O-O** (19.66 eV, 100%), which can be oxidized to **4444-O-O** (23.58 eV, 100%). Some spin delocalization across the Mn−O bonds can be observed for the deprotonated terminal oxo groups (see Table S8 in the SI).

Finally, the initial intermediates of the second iDC regeneration pathway investigated also feature an H_2O and an OH ligand: **yzzx-H_2O-OH*** (1.91 eV, 93%, r(MnB−O5) = 3.166 Å) and **xxyx-H_2O-OH** (1.98 eV, 5%), then **yz4x-H_2O-OH** (5.13 eV, 84%) and **xz4x-H_2O-OH** (5,18 eV, 13%). The first PCET step yields a mixed population of **y44x-HO-HO** (10.64 eV, 30%) with O6 being the H-bond donor and O5 the acceptor, **x44x-HO-HO** (10.65 eV, 24%) with the same H-bonding configuration, **y44x-OH-OH** (10.66 eV, 16%) with the inverted configuration of O5 being the H-bond donor and O6 the acceptor, **x44x-OH-OH** (10.66 eV, 11%) with the same inverted configuration, and **4x4x-HO-HO** (10.67 eV, 11%) once again having O6 as the donor. A further PCET step gives a mixture of **444x-OH-O** (16.90 eV, 87%) and **444x-O-OH** (16.95 eV, 13%). The final PCET step results in the same final product as the previous pathway, **4444-O-O** (23.58 eV, 100%). Again, some spin delocalization across the Mn−O bonds can be observed for the deprotonated terminal oxo groups (see Table S9 in the SI).

4. DISCUSSION

4.1. Structural Analysis. Analyzing the distributions of the interatomic distances between the Mn centers and each of their coordinating atoms reveals a common pattern (see section III in the SI), shown exemplarily in Figure 5a for r(MnB−O3). A peak at ∼1.9 Å represents both the undistorted bonds found at Mn^{4+} centers as well as the slightly shorter bonds not corresponding to the main JT axis at Mn^{3+} centers. A second peak at ∼2.3 Å represents bonds lengthened by JT distortions. Outliers above 2.5 Å correspond to structures featuring very strongly distorted or even fully dissociated bonds, which will be discussed in detail below.

This pattern of interatomic distance distributions marked by two main peaks is found essentially in all Mn centers and coordinating atoms, showing that JT distortions are possible along all bond axes, including those to the vanadate ligand (see Figure 5b). Overall, we predict 78 structures bearing at least one JT axis oriented toward the vanadate ligand, 18 of which have a Boltzmann population of >5% at thermal equilibrium, marking them as being among the most stable isomers. While the majority of these structures belong to the **3333** and **3334**

https://doi.org/10.1021/acscatal.2c06301
ACS Catal. 2023, 13, 3007−3019

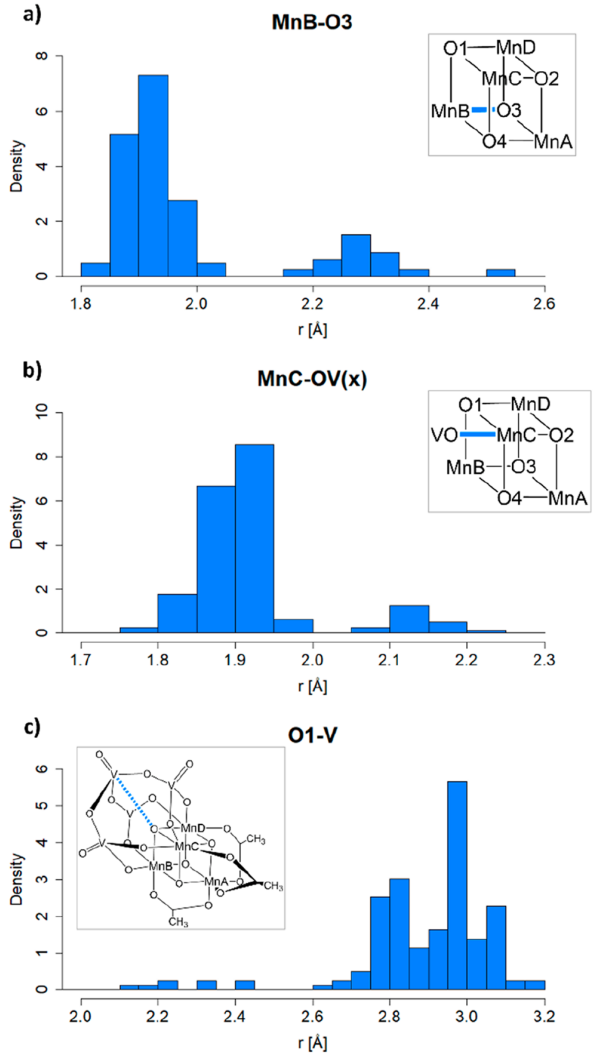

Figure 5. Interatomic distance distributions (in Å) for selected atom pairs highlighted in blue in the insets. (a) r(MnB−O3), showing two peaks: one at ∼2.3 Å for JT-distorted bonds and one around 1.9 Å for bonds not lengthened by JT effects. An outlier above 2.5 Å represents possibly dissociated structures. (b) r(MnC−OV), where OV is the nearest O atom of the vanadate ligand. The presence of a second peak of ∼2.1 Å indicates that bonds to the vanadate ligand are affected by JT distortions. (c) r(O1−V), where V is the nearest V atom of the vanadate ligand. Outliers below 2.6 Å show that an attractive interaction between these two atoms can pull them up to 0.4 Å closer together.

oxidation states, 17 such structures were found at the **3344** and 1 structure was found even at the **3444** oxidation state. This is a surprising result because it diverges somewhat from the assumption that the seemingly chemically inert vanadate ligand was unlikely to participate in the formation of JT axes.[52]

Rather, it appears that JT distortions in bonds to the vanadate ligand are possible, although they result in bonds that are more stable than is the case for other ligands (bonds to the vanadate lengthened by JT distortions are on average 0.1−0.2 Å shorter than JT-lengthened bonds to other ligands), and no instances of bond dissociation were observed for the vanadate ligand.

Interestingly, we obtained a number of structures featuring an interatomic distance smaller than 2.5 Å between O1 and one of the vanadium atoms (Figure 5c), indicating a certain degree of interaction between the two atoms. As previously noted by Mai et al., the experimental X-ray structure obtained at the **3344** oxidation state features three elongated Mn−O1 bonds, which were originally rationalized as being caused by attractive electrostatic interactions between O1 and the vanadate ligand,[45] but are more likely a result of dynamic disorder in the crystal structure between different JT isomers separated by low kinetic barriers.[52] Now, however, we find structures in the **3333** and **3334** oxidation state, all of which have three JT axes pointed at O1 and significantly lower than average distances between O1 and the vanadate ligand. This implies that the hypothesized attractive interaction of this pairing could be observed, but only at the lowest oxidation states and with the cooperation of three JT axes pushing O1 toward the vanadate ligand.

4.2. Catalyst Degradation. The appearance of numerous outliers in the interatomic distance analysis prompted us to investigate in depth structures featuring very strongly distorted or even fully dissociated bonds between Mn centers and their coordinating atoms. We discovered two types of potential catalyst degradation processes: (i) cubane opening, where intracubane Mn−O bonds are extended up to 3.0 Å, in one case followed by protonation of O4 by a neighboring H_2O ligand; and (ii) ligand dissociation, where Mn−OH_2 distances up to 3.9 Å and Mn−OAc distances up to 6.7 Å can be observed. Structures bearing one or even several of these distortions were found both in the **3334** oxidation state, where they appear in a small number of mostly unpopulated isomers, and in the **3333** oxidation state, where they are far more common and often among the most stable isomers obtained. In all these structures, Mn-ligand bond distortions and dissociations are consistent with the JT axes of their respective Mn^{3+} centers. Therefore, it is reasonable to assume that here, as in other parts of the catalytic cycles,[40,41] JT effects lower barriers for bond breakage and formation at Mn^{3+} centers, in this case potentially facilitating catalyst degradation through cubane opening and ligand dissociation.

To better understand the kinetics of these degradation processes, NEB calculations were performed between representative examples of structures bearing strongly distorted or dissociated bonds and nondissociated isomers of identical oxidation state and comparable ligand configuration. In this way, approximate barrier heights for different types of cubane opening and ligand dissociation processes could be obtained. Six such calculations were performed (see Figure 6 and section IV in the SI); in some cases (NEB 1, NEB 2), the minimum energy pathway obtained from the NEB calculation fluctuates between several JT isomers due to the near-degeneracy of many isomers at the **3333** oxidation state. However, the emergence of JT distortions consistent with the studied degradation process was observed before bond cleavage in two simulations (NEB 3, NEB 4), while in the remaining calculations, such JT distortions were already present in the reactant structure.

The barriers of all degradation processes investigated using NEB simulations were found to be small (<0.25 eV or 5.8 kcal/mol), pointing to the high reactivity of the catalyst at the **3333** and **3334** oxidation states. The catalyst's propensity for quickly dissociating ligands is enabled by the presence of JT effects at Mn^{3+} centers, which can extend Mn-ligand bonds and

https://doi.org/10.1021/acscatal.2c06301
ACS Catal. 2023, 13, 3007−3019

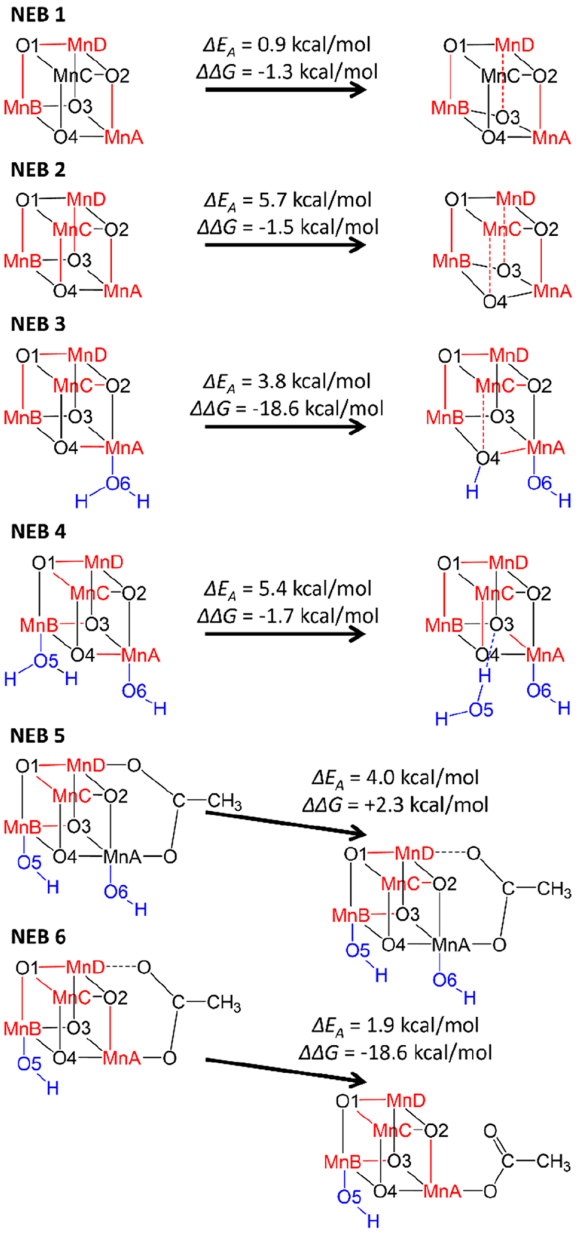

Figure 6. CI-NEB calculations carried out between relatively intact isomers and examples featuring at least one form of structural distortion. Mn^{3+} centers and their JT axes are marked in red; ligands at MnA and MnB are highlighted in blue. Activation energies ΔE_A (kcal/mol) correspond to the electronic energy of the climbing image relative to the reactant, computed at the B3LYP-D3/ZORA-def2-SVP level of theory. Gibbs energy differences $\Delta\Delta G$ (in kcal/mol) are calculated at the B3LYP-D3/ZORA-def2-TZVP//B3LYP-D3/ZORA-def2-SVP level of theory.

thereby lower reaction barriers for bond dissociation. Based on these results, it appears that all of these extremely fast reactions are potentially reversible, depending on the $\Delta\Delta G$ between reactant and product. For example, the products of NEB 1 and NEB 2 featuring extended intracubane Mn−O bonds, **zzzz-o-o*** and **zz4z-o-o***, are in equilibrium with their "intact" reactants. In these two cases, cubane opening does not seem to interfere with oxidative regeneration of the catalyst and is simply a form of a particularly strong JT effect. Similarly, the H_2O and acetate ligand dissociations studied in NEB 4 and NEB 5, respectively, appear to be reversible, showing that (partial) ligand dissociation does not necessarily impede regeneration. This is plausible in the case of H_2O, which is abundant in the reaction mixture under experimental conditions.[45,46] However, the dissociation of acetate from the complex bears further investigation (see below).

While NEB 5 shows that extreme distortion of an Mn−OAc bond (r(MnD−OAc) = 2.548 Å in the product) is reversible, this is not the case in NEB 6. In the latter, the bidentate acetate ligand is fully dissociated from MnD, with the remainder being bound as a monodentate ligand at MnA and leaving behind an additional open coordination site. This far more dramatic reaction is associated with a large negative $\Delta\Delta G$, pushing the system irreversibly toward the degraded product. NEB 3 falls into the same category; there, a combination of cubane opening and protonation by an H_2O ligand at O4 irreversibly results in the formation of a unique degradation product, **xzzx-o-H_2O***, that is fully 0.37 eV lower in energy than the next most stable isomer, **zzzz-o-o***. It would seem that this process could cause potentially irreversible damage to the catalyst, as the breaking of a μ-oxo bridge in the cubane core might interfere with the facile transfer of electrons between Mn centers, leading to a reduction in catalytic activity as this degradation product accumulates and possibly disintegrates even further. However, the irreversible protonation at O4 first requires H_2O to be bound as a ligand, which is thermodynamically quite unfavorable at the **3333** oxidation state: The most stable isomer that includes an H_2O ligand bound to either active site is the thermally unpopulated **xzyz-H2O-o*** (0.29 eV, r(MnD−O3) = 2.619 Å); this isomer, in turn, is 0.29 eV less stable than the reference structure without H_2O ligands, **zzzz-o-o***. Alternatively, O4 could be protonated by a solvent water molecule to form **xzzx-o-H_2O***. As the catalyst has been shown in experiments to catalyze over 12 000 turnovers,[46] we can safely assume that deactivation by solvent-based protonation of O4 must be associated with a substantial kinetic barrier. The further investigation of this intriguing process would require the inclusion of explicit solvent dynamics and is therefore beyond the scope of this work.

4.3. Catalyst Regeneration (iWNA Cycle). Leaving aside possible degradation products (in particular, **xzzx-o-H_2O***), we now turn to the question of how **4444-OH-H_2O** is regenerated from **3333-o-o** within the iWNA catalytic cycle of **3344-OAc**. As noted above, this regeneration reaction formally involves oxidation as well as ligand binding steps, making the detailed characterization of a single preferred reaction pathway extremely difficult. The binding of new water ligands to **3344-OAc** could occur at any oxidation state and has been shown to be subject to reaction barriers of widely differing heights in the context of catalyst activation.[40] Therefore, we choose to focus here solely on the thermodynamics of catalyst regeneration by identifying the most stable intermediates for each oxidation state and ligand configuration, shown in Figure 7.

To simplify the discussion, let us imagine that in place of the many JT and redox isomers that we have sampled, only the most stable isomer for each combination of redox state and ligand configuration were thermally populated. This would allow us to more easily compare intermediates featuring different ligand configurations at the same oxidation state, enabling us to estimate which of these intermediates could be

https://doi.org/10.1021/acscatal.2c06301
ACS Catal. 2023, 13, 3007−3019

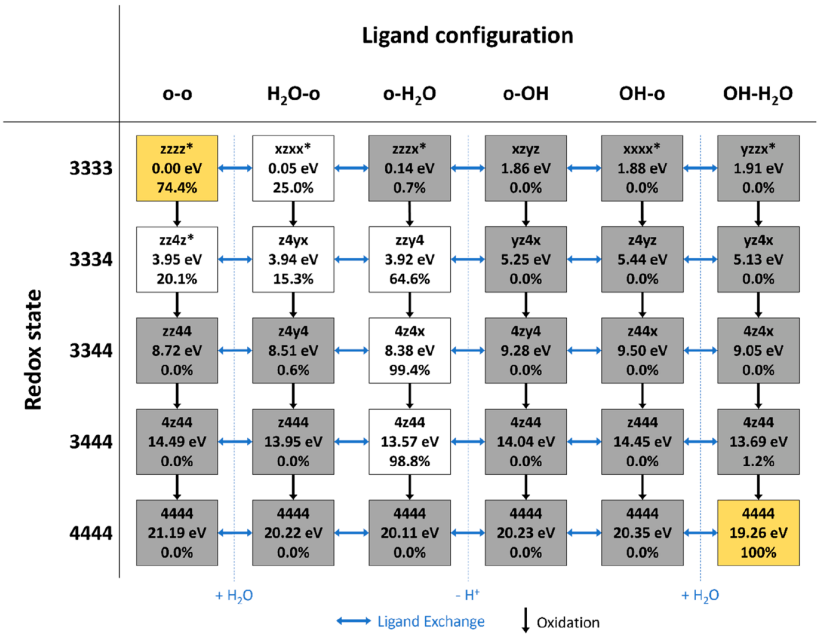

Figure 7. Most stable intermediates for each oxidation state (left) and ligand configuration (top), together comprising the most thermodynamically favorable regeneration pathways within the iWNA cycle. For each structure, the text box specifies JT isomer, relative Gibbs free energy (in eV), and relative Boltzmann population at 298.15 K within the given oxidation state. The starting **3333-o-o** and final **4444-OH-H_2O** structures are highlighted in orange, intermediates with a relative population smaller than 5.0% are shaded in gray. Ligand exchange reactions are indicated by blue arrows, and oxidation steps are indicated by black arrows.

populated at thermal equilibrium (orange and white boxes in Figure 7). Although unpopulated intermediates (gray boxes in Figure 7) may also play a role in catalyst regeneration depending on the reaction conditions (e.g., applied overpotential in electrocatalysis), a regeneration pathway featuring only the most stable intermediates would result in the lowest thermodynamic overpotential.[7,75,76]

Starting at the **3333** oxidation state, an isomer of the **o-o** ligand configuration (**zzzz-o-o***, 0.00 eV, 74.4%) is in thermodynamic equilibrium with a structure bearing dissociated H_2O and acetate ligands (**xzxx-H_2O-o***, 0.05 eV, 25.0%). It appears that having open coordination sites at both MnA and MnB is the most stable ligand configuration at the **3333** oxidation state. Oxidation to the **3334** state results in an equilibrium between structures with one open coordination site as well as one H_2O ligand, **zzy4-o-H_2O** (3.92 eV, 64.6%) and **z4yx-H_2O-o** (3.94 eV, 15.3%), and a structure with two open coordination sites, **zz4z-o-o*** (3.95 eV, 20.1%). Oxidizing to the **3344** oxidation state, the **o-H_2O** configuration with an open coordination site at MnB and H_2O bound to MnA becomes the most stable by far (**4z4x-o-H_2O**, 8.38 eV, 99.4%). This behavior is also found at the **3444** oxidation state, where **4z44-o-H_2O** (13.57 eV, 98.8%) is the only significantly populated intermediate. At the highest oxidation state **4444**, the expected final product **4444-OH-H_2O** (19.26 eV, 100%) is also the most stable structure.

Table 1 shows the oxidation potentials of the oxidation steps connecting the thermally populated intermediates in Figure 7 (ranges are given where several intermediates are populated). We note that the potential of the last oxidation step is the highest of the overall reaction: 1.41 V versus normal hydrogen electrode (NHE) for **4z44-o-H_2O** to **4444-OH-H_2O**. This value is just below the redox potential of the **3444-OH-H_2O** to

Table 1. Oxidation Potentials versus Normal Hydrogen Electrode E_{NHE} for Oxidation Steps between Thermally Populated Intermediates Shown in Figure 7

oxidation step	E_{NHE}[a] [V]
3333 → 3334	[−0.33; −0.41]
3334 → 3344	[0.15; 0.18]
3344 → 3444	0.91
3444 → 4444	1.41

[a]Potential ranges are given where several populated intermediates are present.

4444-OH-H_2O oxidation observed experimentally during catalyst activation, 1.47 eV vs NHE,[40] but slightly higher than the potential of the same oxidation step in a comparable OEC mimic, 1.3 V vs NHE.[77] These results indicate that oxidative regeneration of the **3344-OAc** catalyst is energetically comparable to its activation as well as to parallel processes in comparable structures.

4.4. Alternative Regeneration Pathways (iDC Cycle). Finally, we discuss two alternative regeneration pathways enabling an iDC-type water oxidation cycle. We hypothesized that O_2 evolution according to such a mechanism could best be enabled by first binding water ligands at a low redox state (**3333** or **3334**), followed by combined deprotonation and metal-centered oxidation through a series of PCET steps, leading to a highly oxidized catalyst with terminal oxo ligands (**4444-O-O**). For the pathway starting from **3333-H_2O-OH**, already the first PCET step leads to a structure (**yy4x-HO-HO**) that is 1.65 eV higher in energy than the next most stable isomer belonging to the iWNA cycle, **z4yz-OH-o**. A similar result is obtained when starting instead from **3334-H_2O-OH**, with the first PCET step leading to **y44x-HO-HO**, which is

https://doi.org/10.1021/acscatal.2c06301
ACS Catal. 2023, 13, 3007−3019

1.14 eV less stable than the next most stable isomer from the iWNA cycle, **z44x-OH-o**. All further intermediates from these two iDC regeneration pathways are also far less stable than iWNA regeneration intermediates at the same oxidation state. We therefore conclude that these particular iDC-type regeneration pathways play no significant role in the reactivity of our catalyst, although a different type of DC water oxidation cycle may, of course, yet be discovered.

5. CONCLUSION

We determined the most favorable regeneration mechanism of the biomimetic polyoxometalate water oxidation catalyst $[Mn^{3+}_2Mn^{4+}_2V_4O_{17}(OAc)_3]^{3-}$ (**3344-OAc**), thereby completing the iWNA-type catalytic cycle. Starting from its least oxidized **3333-o-o** form with two open coordination sides, the first H_2O ligand is able to bind at the **3334** oxidation state. This oxidation state shows the greatest diversity of populated ligand configurations. Afterward, the reaction converges to a single pathway leading via **3344-o-H_2O** and **3444-o-H_2O** back to the activated species **4444-OH-H_2O** as the final product. The second H_2O ligand is bound and deprotonated together with the final oxidation step. The catalyst's ability to access a variety of JT as well as redox isomers and ligand configurations is key to achieving a highly efficient catalytic cycle, starting with initial activation of the precatalyst **3344-OAc** to **4444-OH-H_2O**,[40] then O_2 evolution leaving behind the deactivated **3333-o-o**,[41] and finally regeneration of **4444-OH-H_2O**.

Additionally, we investigated the feasibility of an alternative iDC-type water oxidation cycle, initiated by binding water ligands to **3333-o-o** followed by a series of PCET steps to attain a highly oxidized species with two cofacial terminal oxo ligands (**4444-O-O**). However, this alternative regeneration pathway did not turn out to be thermodynamically favorable.

Since JT effects play a major role in determining the reactivity and stability of this polyoxometalate water oxidation catalyst, a tremendous in silico sampling effort was indispensable to characterize the involved structures, resulting in 159 individual stable minima found. This large-scale theoretical investigation not only offers unprecedented insight into the regeneration of **3344-OAc**, but has additionally produced several unforeseen results. Our sampling revealed that the vanadate ligand is far less inert than previously thought.[52] Having the ability to participate in the formation of surprisingly stable JT-distorted bonds, this hexadentate ligand even demonstrated an ability to additionally interact with the cubane core of the catalyst at the apical O1 atom, facilitated by three JT axes cooperatively pushing O1 toward the vanadate.

Equally unexpectedly, we found many strongly distorted or partially dissociated structures using our multistep sampling approach. Two types of degradation processes were identified: cubane opening and ligand dissociation. All barriers of investigated reactions were quite low, underlining the role of JT effects in facilitating the reactivity of the catalyst. Thus, in the **3333** and **3334** oxidation states, the catalyst in many ways appears to be less stable than at higher oxidation states; however, the majority of the investigated catalyst degradation reactions were found to be reversible. Only for specific ligand configurations in the **3333** oxidation state, some forms of ligand dissociation reactions may be irreversible. Most interestingly, a unique degradation product was discovered, which is most likely formed by protonation of O4 by solvent water. While the kinetics of this process remain unknown, we argue that a fairly high kinetic barrier is required to explain the high turnover observed in the experiments,[46] as the O4-protonated structure is more stable than the deactivated catalyst **3333-o-o**. Nevertheless, this unusual structure offers a first glimpse at how a loss of catalytic activity over time could occur in **3344-OAc**.

Looking to the future, greater understanding of the fundamental principles involved in catalyst degradation could be achieved through simulations in explicit solvation, thereby contributing to the goal of imbuing this highly efficient molecular catalyst with greater stability. From an experimental point of view, the proposal of a complete catalytic cycle for **3344-OAc** opens up many avenues for further investigation, both to verify the accuracy of our proposal as well as to operationalize the insights gained from these simulations. Chief among these is the importance of JT effects for increasing the water oxidation activity of catalysts that include d^4 metal centers. This structure−property relationship is already well-known in heterogeneous catalysis,[42−44,51] and it is high time it were applied to the development of molecular catalysts for artificial water splitting.

■ ASSOCIATED CONTENT

Supporting Information

The Supporting Information is available free of charge at https://pubs.acs.org/doi/10.1021/acscatal.2c06301.

Analysis of heuristics for sampling target selection, tables of stable isomers, interatomic distance analysis, and nudged elastic band simulation results (PDF)

Cartesian coordinates of relevant structures (PDF)

■ AUTHOR INFORMATION

Corresponding Authors

Ludwig Schwiedrzik − *Institute of Theoretical Chemistry, Faculty of Chemistry, University of Vienna, 1090 Vienna, Austria; Vienna Doctoral School in Chemistry (DoSChem), University of Vienna, 1090 Vienna, Austria;* orcid.org/0000-0002-9361-1032; Email: ludwig.schwiedrzik@univie.ac.at

Leticia González − *Institute of Theoretical Chemistry, Faculty of Chemistry, University of Vienna, 1090 Vienna, Austria;* orcid.org/0000-0001-5112-794X; Email: leticia.gonzalez@univie.ac.at

Author

Tina Rajkovic − *Institute of Theoretical Chemistry, Faculty of Chemistry, University of Vienna, 1090 Vienna, Austria*

Complete contact information is available at: https://pubs.acs.org/10.1021/acscatal.2c06301

Author Contributions

L.S. and L.G designed the research. L.S. and T.R. performed the research. L.S. analyzed the data. L.S and L.G. wrote the paper.

Funding

Open Access is funded by the Austrian Science Fund (FWF).

Notes

The authors declare no competing financial interest.

■ ACKNOWLEDGMENTS

This work is supported by the Austrian Science Fund FWF (Project Nos. I3987-N28 and I6116−N) and the Deutsche Forschungsgemeinschaft DFG (TRR234 "CataLight", Project

ID No. 364549901, subproject C3). The authors thank the Vienna Scientific Cluster for the generous allocation of computational resources and the University of Vienna for continuous support.

REFERENCES

(1) Chow, J.; Kopp, R. J.; Portney, P. R. Energy Resources and Global Development. *Science* **2003**, *302* (5650), 1528−1531.
(2) Friedlingstein, P.; Jones, M. W.; O'Sullivan, M.; Andrew, R. M.; Bakker, D. C. E.; Hauck, J.; Le Quéré, C.; Peters, G. P.; Peters, W.; Pongratz, J.; Sitch, S.; Canadell, J. G.; Ciais, P.; Jackson, R. B.; Alin, S. R.; Anthoni, P.; Bates, N. R.; Becker, M.; Bellouin, N.; Bopp, L.; Chau, T. T. T.; Chevallier, F.; Chini, L. P.; Cronin, M.; Currie, K. I.; Decharme, B.; Djeutchouang, L. M.; Dou, X.; Evans, W.; Feely, R. A.; Feng, L.; Gasser, T.; Gilfillan, D.; Gkritzalis, T.; Grassi, G.; Gregor, L.; Gruber, N.; Gürses, Ö.; Harris, I.; Houghton, R. A.; Hurtt, G. C.; Iida, Y.; Ilyina, T.; Luijkx, I. T.; Jain, A.; Jones, S. D.; Kato, E.; Kennedy, D.; Klein Goldewijk, K.; Knauer, J.; Korsbakken, J. I.; Körtzinger, A.; Landschützer, P.; Lauvset, S. K.; Lefèvre, N.; Lienert, S.; Liu, J.; Marland, G.; McGuire, P. C.; Melton, J. R.; Munro, D. R.; Nabel, J. E. M. S.; Nakaoka, S.-I.; Niwa, Y.; Ono, T.; Pierrot, D.; Poulter, B.; Rehder, G.; Resplandy, L.; Robertson, E.; Rödenbeck, C.; Rosan, T. M.; Schwinger, J.; Schwingshackl, C.; Séférian, R.; Sutton, A. J.; Sweeney, C.; Tanhua, T.; Tans, P. P.; Tian, H.; Tilbrook, B.; Tubiello, F.; van der Werf, G. R.; Vuichard, N.; Wada, C.; Wanninkhof, R.; Watson, A. J.; Willis, D.; Wiltshire, A. J.; Yuan, W.; Yue, C.; Yue, X.; Zaehle, S.; Zeng, J. Global Carbon Budget 2021. *Earth Syst. Sci. Data* **2022**, *14* (4), 1917−2005.
(3) Pörtner, H.-O., Roberts, D. C., Tignor, M., Poloczanska, E. S., Mintenbeck, K., Alegría, A., Craig, M., Langsdorf, S., Löschke, S., Möller, V., Okem, A., Rama, B., Eds. IPCC. *Climate Change 2022: Impacts, Adaptation, and Vulnerability. Contribution of Working Group II to the Sixth Assessment Report of the Intergovernmental Panel on Climate Change*; Cambridge University Press: Cambridge, U.K. and New York, 2022; p 3056.
(4) Cook, T. R.; Dogutan, D. K.; Reece, S. Y.; Surendranath, Y.; Teets, T. S.; Nocera, D. G. Solar Energy Supply and Storage for the Legacy and Nonlegacy Worlds. *Chem. Rev.* **2010**, *110* (11), 6474−6502.
(5) Faunce, T. A.; Lubitz, W.; Rutherford, A. W.; MacFarlane, D.; Moore, G. F.; Yang, P.; Nocera, D. G.; Moore, T. A.; Gregory, D. H.; Fukuzumi, S.; Yoon, K. B.; Armstrong, F. A.; Wasielewski, M. R.; Styring, S. Energy and Environment Policy Case for a Global Project on Artificial Photosynthesis. *Energy Environ. Sci.* **2013**, *6* (3), 695−698.
(6) Lubitz, W.; Reijerse, E. J.; Messinger, J. Solar Water-Splitting into H_2 and O_2: Design Principles of Photosystem II and Hydrogenases. *Energy Environ. Sci.* **2008**, *1* (1), 15−31.
(7) Dau, H.; Limberg, C.; Reier, T.; Risch, M.; Roggan, S.; Strasser, P. The Mechanism of Water Oxidation: From Electrolysis via Homogeneous to Biological Catalysis. *ChemCatChem.* **2010**, *2* (7), 724−761.
(8) Wang, L.-P.; Wu, Q.; Van Voorhis, T. Acid−Base Mechanism for Ruthenium Water Oxidation Catalysts. *Inorg. Chem.* **2010**, *49* (10), 4543−4553.
(9) Schilling, M.; Böhler, M.; Luber, S. Towards the Rational Design of the PyS-Ligand Framework for Ruthenium-Based Water Oxidation Catalysts. *Dalton Trans.* **2018**, *47* (31), 10480−10490.
(10) Betley, T. A.; Wu, Q.; Van Voorhis, T.; Nocera, D. G. Electronic Design Criteria for O−O Bond Formation via Metal−Oxo Complexes. *Inorg. Chem.* **2008**, *47* (6), 1849−1861.
(11) Rivalta, I.; Brudvig, G. W.; Batista, V. S. Oxomanganese Complexes for Natural and Artificial Photosynthesis. *Curr. Opin. Chem. Biol.* **2012**, *16* (1), 11−18.
(12) Shaffer, D. W.; Xie, Y.; Concepcion, J. J. O−O Bond Formation in Ruthenium-Catalyzed Water Oxidation: Single-Site Nucleophilic Attack vs. O−O Radical Coupling. *Chem. Soc. Rev.* **2017**, *46* (20), 6170−6193.
(13) Schilling, M.; Luber, S. Computational Modeling of Cobalt-Based Water Oxidation: Current Status and Future Challenges. *Front. Chem.* **2018**, *6*, 100.
(14) Li, X.; Siegbahn, P. E. M. Water Oxidation Mechanism for Synthetic Co−Oxides with Small Nuclearity. *J. Am. Chem. Soc.* **2013**, *135* (37), 13804−13813.
(15) McCool, N. S.; Robinson, D. M.; Sheats, J. E.; Dismukes, G. C. A Co4O4 "Cubane" Water Oxidation Catalyst Inspired by Photosynthesis. *J. Am. Chem. Soc.* **2011**, *133* (30), 11446−11449.
(16) Wang, L.-P.; Van Voorhis, T. Direct-Coupling O2 Bond Forming a Pathway in Cobalt Oxide Water Oxidation Catalysts. *J. Phys. Chem. Lett.* **2011**, *2* (17), 2200−2204.
(17) Fernando, A.; Aikens, C. M. Reaction Pathways for Water Oxidation to Molecular Oxygen Mediated by Model Cobalt Oxide Dimer and Cubane Catalysts. *J. Phys. Chem. C* **2015**, *119* (20), 11072−11085.
(18) Nguyen, A. I.; Ziegler, M. S.; Oña-Burgos, P.; Sturzbecher-Hohne, M.; Kim, W.; Bellone, D. E.; Tilley, T. D. Mechanistic Investigations of Water Oxidation by a Molecular Cobalt Oxide Analogue: Evidence for a Highly Oxidized Intermediate and Exclusive Terminal Oxo Participation. *J. Am. Chem. Soc.* **2015**, *137* (40), 12865−12872.
(19) Hodel, F. H.; Luber, S. What Influences the Water Oxidation Activity of a Bioinspired Molecular CoII4O4 Cubane? An In-Depth Exploration of Catalytic Pathways. *ACS Catal.* **2016**, *6* (3), 1505−1517.
(20) Hodel, F. H.; Luber, S. Redox-Inert Cations Enhancing Water Oxidation Activity: The Crucial Role of Flexibility. *ACS Catal.* **2016**, *6* (10), 6750−6761.
(21) Soriano-López, J.; Musaev, D. G.; Hill, C. L.; Galán-Mascarós, J. R.; Carbó, J. J.; Poblet, J. M. Tetracobalt-Polyoxometalate Catalysts for Water Oxidation: Key Mechanistic Details. *J. Catal.* **2017**, *350*, 56−63.
(22) Liao, R.-Z.; Kärkäs, M. D.; Lee, B.-L.; Åkermark, B.; Siegbahn, P. E. M. Photosystem II Like Water Oxidation Mechanism in a Bioinspired Tetranuclear Manganese Complex. *Inorg. Chem.* **2015**, *54* (1), 342−351.
(23) Dismukes, G. C.; Brimblecombe, R.; Felton, G. A. N.; Pryadun, R. S.; Sheats, J. E.; Spiccia, L.; Swiegers, G. F. Development of Bioinspired Mn4O4−Cubane Water Oxidation Catalysts: Lessons from Photosynthesis. *Acc. Chem. Res.* **2009**, *42* (12), 1935−1943.
(24) Mukherjee, S.; Stull, J. A.; Yano, J.; Stamatatos, T. C.; Pringouri, K.; Stich, T. A.; Abboud, K. A.; Britt, R. D.; Yachandra, V. K.; Christou, G. Synthetic Model of the Asymmetric [Mn3CaO4] Cubane Core of the Oxygen-Evolving Complex of Photosystem II. *Proc. Natl. Acad. Sci. U. S. A.* **2012**, *109* (7), 2257−2262.
(25) Kanady, J. S.; Lin, P.-H.; Carsch, K. M.; Nielsen, R. J.; Takase, M. K.; Goddard, W. A.; Agapie, T. Toward Models for the Full Oxygen-Evolving Complex of Photosystem II by Ligand Coordination To Lower the Symmetry of the Mn3CaO4 Cubane: Demonstration That Electronic Effects Facilitate Binding of a Fifth Metal. *J. Am. Chem. Soc.* **2014**, *136* (41), 14373−14376.
(26) Zhang, C.; Chen, C.; Dong, H.; Shen, J.-R.; Dau, H.; Zhao, J. A Synthetic Mn4Ca-Cluster Mimicking the Oxygen-Evolving Center of Photosynthesis. *Science* **2015**, *348* (6235), 690−693.
(27) Lee, H. B.; Agapie, T. Redox Tuning via Ligand-Induced Geometric Distortions at a YMn3O4 Cubane Model of the Biological Oxygen Evolving Complex. *Inorg. Chem.* **2019**, *58* (22), 14998−15003.
(28) Li, M.; Liao, R.-Z. Water Oxidation Catalyzed by a Bioinspired Tetranuclear Manganese Complex: Mechanistic Study and Prediction. *ChemSusChem* **2022**, *15* (15), No. e202200187.
(29) Kanady, J. S.; Tsui, E. Y.; Day, M. W.; Agapie, T. A Synthetic Model of the Mn_3Ca Subsite of the Oxygen-Evolving Complex in Photosystem II. *Science* **2011**, *333* (6043), 733−736.
(30) Gatt, P.; Petrie, S.; Stranger, R.; Pace, R. J. Rationalizing the 1.9 Å Crystal Structure of Photosystem II—A Remarkable Jahn−Teller Balancing Act Induced by a Single Proton Transfer. *Angew. Chem., Int. Ed.* **2012**, *51* (48), 12025−12028.

https://doi.org/10.1021/acscatal.2c06301
ACS Catal. 2023, 13, 3007−3019

(31) Krewald, V.; Neese, F.; Pantazis, D. A. On the Magnetic and Spectroscopic Properties of High-Valent Mn3CaO4 Cubanes as Structural Units of Natural and Artificial Water-Oxidizing Catalysts. *J. Am. Chem. Soc.* **2013**, *135* (15), 5726−5739.
(32) Tsui, E. Y.; Agapie, T. Reduction Potentials of Heterometallic Manganese−Oxido Cubane Complexes Modulated by Redox-Inactive Metals. *Proc. Natl. Acad. Sci. U. S. A.* **2013**, *110* (25), 10084−10088.
(33) Yamaguchi, K.; Yamanaka, S.; Isobe, H.; Saito, T.; Kanda, K.; Umena, Y.; Kawakami, K.; Shen, J.-R.; Kamiya, N.; Okumura, M.; Nakamura, H.; Shoji, M.; Yoshioka, Y. The Nature of Chemical Bonds of the CaMn4O5 Cluster in Oxygen Evolving Complex of Photosystem II: Jahn-Teller Distortion and Its Suppression by Ca Doping in Cubane Structures. *Int. J. Quantum Chem.* **2013**, *113* (4), 453−473.
(34) Lee, C.; Aikens, C. M. Water Splitting Processes on Mn4O4 and CaMn3O4 Model Cubane Systems. *J. Phys. Chem. A* **2015**, *119* (35), 9325−9337.
(35) Krewald, V.; Retegan, M.; Cox, N.; Messinger, J.; Lubitz, W.; DeBeer, S.; Neese, F.; Pantazis, D. A. Metal Oxidation States in Biological Water Splitting. *Chem. Sci.* **2015**, *6* (3), 1676−1695.
(36) Fernando, A.; Aikens, C. M. Theoretical Investigation of Water Oxidation Catalysis by a Model Manganese Cubane Complex. *J. Phys. Chem. C* **2016**, *120* (38), 21148−21161.
(37) Yamaguchi, K.; Shoji, M.; Isobe, H.; Yamanaka, S.; Umena, Y.; Kawakami, K.; Kamiya, N. On the Guiding Principles for Understanding of Geometrical Structures of the CaMn4O5 Cluster in Oxygen-Evolving Complex of Photosystem II. Proposal of Estimation Formula of Structural Deformations via the Jahn−Teller Effects. *Mol. Phys.* **2017**, *115* (5), 636−666.
(38) Kanady, J. S.; Mendoza-Cortes, J. L.; Tsui, E. Y.; Nielsen, R. J.; Goddard, W. A.; Agapie, T. Oxygen Atom Transfer and Oxidative Water Incorporation in Cuboidal Mn3MO*n* Complexes Based on Synthetic, Isotopic Labeling, and Computational Studies. *J. Am. Chem. Soc.* **2013**, *135* (3), 1073−1082.
(39) Drosou, M.; Zahariou, G.; Pantazis, D. A. Orientational Jahn−Teller Isomerism in the Dark-Stable State of Nature's Water Oxidase. *Angew. Chem., Int. Ed.* **2021**, *60* (24), 13493−13499.
(40) Cárdenas, G.; Trentin, I.; Schwiedrzik, L.; Hernández-Castillo, D.; Lowe, G. A.; Kund, J.; Kranz, C.; Klingler, S.; Stach, R.; Mizaikoff, B.; Marquetand, P.; Nogueira, J. J.; Streb, C.; González, L. Activation by Oxidation and Ligand Exchange in a Molecular Manganese Vanadium Oxide Water Oxidation Catalyst. *Chem. Sci.* **2021**, *12* (39), 12918−12927.
(41) Schwiedrzik, L.; Brieskorn, V.; González, L. Flexibility Enhances Reactivity: Redox Isomerism and Jahn−Teller Effects in a Bioinspired Mn_4O_4 Cubane Water Oxidation Catalyst. *ACS Catal.* **2021**, *11* (21), 13320−13329.
(42) Robinson, D. M.; Go, Y. B.; Mui, M.; Gardner, G.; Zhang, Z.; Mastrogiovanni, D.; Garfunkel, E.; Li, J.; Greenblatt, M.; Dismukes, G. C. Photochemical Water Oxidation by Crystalline Polymorphs of Manganese Oxides: Structural Requirements for Catalysis. *J. Am. Chem. Soc.* **2013**, *135* (9), 3494−3501.
(43) Maitra, U.; Naidu, B. S.; Govindaraj, A.; Rao, C. N. R. Importance of Trivalency and the Eg1 Configuration in the Photocatalytic Oxidation of Water by Mn and Co Oxides. *Proc. Natl. Acad. Sci. U. S. A.* **2013**, *110* (29), 11704−11707.
(44) Indra, A.; Menezes, P. W.; Driess, M. Uncovering Structure−Activity Relationships in Manganese-Oxide-Based Heterogeneous Catalysts for Efficient Water Oxidation. *ChemSusChem* **2015**, *8* (5), 776−785.
(45) Schwarz, B.; Forster, J.; Goetz, M. K.; Yücel, D.; Berger, C.; Jacob, T.; Streb, C. Visible-Light-Driven Water Oxidation by a Molecular Manganese Vanadium Oxide Cluster. *Angew. Chem., Int. Ed.* **2016**, *55* (21), 6329−6333.
(46) Huber, F. L.; Amthor, S.; Schwarz, B.; Mizaikoff, B.; Streb, C.; Rau, S. Multi-Phase Real-Time Monitoring of Oxygen Evolution Enables in Operando Water Oxidation Catalysis Studies. *Sustain. Energy Fuels* **2018**, *2* (9), 1974−1978.
(47) Guo, Y.; Li, H.; He, L.-L.; Zhao, D.-X.; Gong, L.-D.; Yang, Z.-Z. The Open-Cubane Oxo−Oxyl Coupling Mechanism Dominates Photosynthetic Oxygen Evolution: A Comprehensive DFT Investigation on O−O Bond Formation in the S4 State. *Phys. Chem. Chem. Phys.* **2017**, *19* (21), 13909−13923.
(48) Vinyard, D. J.; Khan, S.; Brudvig, G. W. Photosynthetic Water Oxidation: Binding and Activation of Substrate Waters for O−O Bond Formation. *Faraday Discuss.* **2015**, *185*, 37−50.
(49) Siegbahn, P. E. M. Theoretical Studies of O−O Bond Formation in Photosystem II. *Inorg. Chem.* **2008**, *47* (6), 1779−1786.
(50) Sproviero, E. M.; Gascón, J. A.; McEvoy, J. P.; Brudvig, G. W.; Batista, V. S. Quantum Mechanics/Molecular Mechanics Study of the Catalytic Cycle of Water Splitting in Photosystem II. *J. Am. Chem. Soc.* **2008**, *130* (11), 3428−3442.
(51) Yu, X.; Qian, K.; Du, L.; Zhang, J.; Lu, N.; Miao, Z.; Li, Y.; Kobayashi, H.; Yan, X.; Li, R. A Strong Jahn−Teller Distortion in Mn3O4−MnO Heterointerfaces for Enhanced Silver Catalyzed Formaldehyde Reforming into Hydrogen. *Sustain. Energy Fuels* **2022**, *6* (12), 3068−3077.
(52) Mai, S.; Holzer, M.; Andreeva, A.; González, L. Jahn-Teller Effects in a Vanadate-Stabilized Manganese-Oxo Cubane Water Oxidation Catalyst. *Chem.−Eur. J.* **2021**, *27* (68), 17066−17077.
(53) Dau, H.; Liebisch, P.; Haumann, M. The Manganese Complex of Oxygenic Photosynthesis: Conversion of Five-Coordinated Mn-(III) to Six-Coordinated Mn(IV) in the S2−S3 Transition Is Implied by XANES Simulations. *Phys. Scr.* **2005**, *2005* (T115), 844.
(54) Mai, S.; Klingler, S.; Trentin, I.; Kund, J.; Holzer, M.; Andreeva, A.; Stach, R.; Kranz, C.; Streb, C.; Mizaikoff, B.; González, L. Spectral Signatures of Oxidation States in a Manganese-Oxo Cubane Water Oxidation Catalyst. *Chem.−Eur. J.* **2021**, *27*, 17078−17086.
(55) Neese, F. The ORCA Program System. *WIREs Comput. Mol. Sci.* **2012**, *2* (1), 73−78.
(56) Neese, F. Software Update: The ORCA Program System, Version 4.0. *WIREs Comput. Mol. Sci.* **2018**, *8* (1), No. e1327.
(57) Pantazis, D. A.; Chen, X.-Y.; Landis, C. R.; Neese, F. All-Electron Scalar Relativistic Basis Sets for Third-Row Transition Metal Atoms. *J. Chem. Theory Comput.* **2008**, *4* (6), 908−919.
(58) van Lenthe, E.; Baerends, E. J.; Snijders, J. G. Relativistic Regular Two-component Hamiltonians. *J. Chem. Phys.* **1993**, *99* (6), 4597−4610.
(59) van Lenthe, E.; Baerends, E. J.; Snijders, J. G. Relativistic Total Energy Using Regular Approximations. *J. Chem. Phys.* **1994**, *101* (11), 9783−9792.
(60) Grimme, S.; Antony, J.; Ehrlich, S.; Krieg, H. A Consistent and Accurate Ab Initio Parametrization of Density Functional Dispersion Correction (DFT-D) for the 94 Elements H-Pu. *J. Chem. Phys.* **2010**, *132* (15), 154104.
(61) Barone, V.; Cossi, M. Quantum Calculation of Molecular Energies and Energy Gradients in Solution by a Conductor Solvent Model. *J. Phys. Chem. A* **1998**, *102* (11), 1995−2001.
(62) Helmich-Paris, B.; de Souza, B.; Neese, F.; Izsák, R. An Improved Chain of Spheres for Exchange Algorithm. *J. Chem. Phys.* **2021**, *155* (10), 104109.
(63) Perdew, J. P. Density-Functional Approximation for the Correlation Energy of the Inhomogeneous Electron Gas. *Phys. Rev. B* **1986**, *33* (12), 8822−8824.
(64) Becke, A. D. Density-Functional Exchange-Energy Approximation with Correct Asymptotic Behavior. *Phys. Rev. A* **1988**, *38* (6), 3098−3100.
(65) Weigend, F.; Ahlrichs, R. Balanced Basis Sets of Split Valence, Triple Zeta Valence and Quadruple Zeta Valence Quality for H to Rn: Design and Assessment of Accuracy. *Phys. Chem. Chem. Phys.* **2005**, *7* (18), 3297−3305.
(66) Becke, A. D. Density-functional Thermochemistry. III. The Role of Exact Exchange. *J. Chem. Phys.* **1993**, *98* (7), 5648−5652.
(67) Lee, C.; Yang, W.; Parr, R. G. Development of the Colle-Salvetti Correlation-Energy Formula into a Functional of the Electron Density. *Phys. Rev. B* **1988**, *37* (2), 785−789.

(68) Siegbahn, P. E. M. O−O Bond Formation in the S4 State of the Oxygen-Evolving Complex in Photosystem II. *Chem.−Eur. J.* **2006**, *12* (36), 9217−9227.
(69) Siegbahn, P. E. M. Substrate Water Exchange for the Oxygen Evolving Complex in PSII in the S1, S2, and S3 States. *J. Am. Chem. Soc.* **2013**, *135* (25), 9442−9449.
(70) Siegbahn, P. E. M. The S2 to S3 Transition for Water Oxidation in PSII (Photosystem II), Revisited. *Phys. Chem. Chem. Phys.* **2018**, *20* (35), 22926−22931.
(71) Luchini, G.; Alegre-Requena, J. V.; Funes-Ardoiz, I.; Paton, R. S. GoodVibes: Automated Thermochemistry for Heterogeneous Computational Chemistry Data. *F1000Res.* **2020**, *9*, 291.
(72) Harvey, J. N.; Himo, F.; Maseras, F.; Perrin, L. Scope and Challenge of Computational Methods for Studying Mechanism and Reactivity in Homogeneous Catalysis. *ACS Catal.* **2019**, *9* (8), 6803−6813.
(73) Rossini, E.; Knapp, E.-W. Proton Solvation in Protic and Aprotic Solvents. *J. Comput. Chem.* **2016**, *37* (12), 1082−1091.
(74) Henkelman, G.; Uberuaga, B. P.; Jónsson, H. A Climbing Image Nudged Elastic Band Method for Finding Saddle Points and Minimum Energy Paths. *J. Chem. Phys.* **2000**, *113* (22), 9901−9904.
(75) Nørskov, J. K.; Rossmeisl, J.; Logadottir, A.; Lindqvist, L.; Kitchin, J. R.; Bligaard, T.; Jónsson, H. Origin of the Overpotential for Oxygen Reduction at a Fuel-Cell Cathode. *J. Phys. Chem. B* **2004**, *108* (46), 17886−17892.
(76) Nørskov, J. K.; Bligaard, T.; Rossmeisl, J.; Christensen, C. H. Towards the Computational Design of Solid Catalysts. *Nat. Chem.* **2009**, *1*, 37−46.
(77) Yao, R.; Li, Y.; Chen, Y.; Xu, B.; Chen, C.; Zhang, C. Rare-Earth Elements Can Structurally and Energetically Replace the Calcium in a Synthetic Mn4CaO4-Cluster Mimicking the Oxygen-Evolving Center in Photosynthesis. *J. Am. Chem. Soc.* **2021**, *143* (42), 17360−17365.

Supporting Information:

Regeneration and Degradation in a Biomimetic Polyoxometalate Water Oxidation Catalyst

Ludwig Schwiedrzik,[a,b,*] Tina Rajkovic,[a] Leticia González[a,*]

[a] Institute of Theoretical Chemistry, Faculty of Chemistry, University of Vienna, Währinger Straße 17, 1090 Vienna, Austria

[b] Vienna Doctoral School in Chemistry (DoSChem), University of Vienna, Währinger Str. 42, 1090 Vienna, Austria

[*] ludwig.schwiedrzik@univie.ac.at, leticia.gonzalez@univie.ac.at

Contents

I.	Analysis of heuristics for sampling target selection	S2
II.	Tables of stable isomers	S4
III.	Interatomic distance analysis	S12
IV.	Nudged elastic band simulation results	S16

I. Analysis of heuristics for sampling target selection

In selecting which structures to target for sampling, we made use of a set of heuristic rules derived by Mai et al. for the relative stability of Jahn-Teller (JT) and redox isomers of the **3344-OAc** catalyst and its derivatives.[1] These rules were developed on the basis of optimized structures covering all oxidation states of the catalyst (**3333**, **3334**, **3344**, **3444**, **4444**) with one H_2O and one OH ligand. They take the form of absolute energy values for each type of JT axis that a structure might contain:

1. JT axes at MnA cost 7.5 kcal/mol.
2. A crossing of two JT axes costs 5 kcal/mol.
3. JT axes to the vanadate ligand cost 12 kcal/mol.
4. A crossing of three JT axes costs 17 kcal/mol.

In practice, these rules allow us to predict the energy of every conceivable isomer (relative to a structure without JT distortions) by adding up the respective value for every JT axis in that isomer. For example, **z444-OH-H_2O** has a predicted energy of 7.5 kcal/mol, while **z44y-OH-H_2O** has a predicted relative energy of 24.5 kcal/mol. We thus created an energy ranking of all isomers for each oxidation state of the catalyst. In the case of the **4444** and **3444** oxidation states, the total number of symmetry-unique isomers is small enough so that all of them could be sampled. For the **3344**, **3334**, and **3333** oxidation states, we decided to limit our sampling to those isomers within less than 12 kcal/mol of the most stable isomer for each oxidation state, thereby greatly reducing the computational cost of our study.

Having obtained a large number of optimized geometries and their respective Gibbs energies, we now wanted to evaluate the utility and accuracy of the heuristic-based target selection by comparing the predicted energies obtained using the heuristic rules E_{pred} to the calculated energies from our DFT calculations E_{calc}. To this end, we split the optimized geometries into six groups according to their ligand configurations: **o-o** contains all structures listed in table S2; **H_2O-o/o-H_2O** contains all structures from tables S3 and S4; **OH-o/o-OH** contains all structures from tables S5 and S6; **OH-H_2O** contains all structures listed in table S7; **PCET 1** contains all structures from table S8; and **PCET 2** contains all structures from table S9 (see section II). Within each of these groups, the most stable isomer belonging to a specific ligand configuration and oxidation state is used as a reference for that combination of ligand configuration and oxidation state by defining its E_{calc} as equal to its E_{pred}. Other structures of the same ligand configuration and oxidation state then have their E_{calc} defined relative to this reference, allowing us to compare values across multiple oxidation states and ligand configurations. These reference structures are omitted in the linear fits shown in figure S1, as they have an absolute error of 0.0 kcal/mol by definition.

Figure S1 shows linear fits obtained by plotting E_{pred} vs E_{calc} for each of the six groups of structures, while Table S1 shows the fit parameters: slope, intercept, R^2, and the mean absolute error (MAE). Ideally, these linear fits should have a slope of 1, an intercept of 0, $R^2 = 1.0$, and MAE = 0.0; this would indicate that the heuristics-derived energies perfectly predict the DFT-calculated energies. Deviations from these ideal values allow us to evaluate the accuracy and precision of the heuristic predictions.

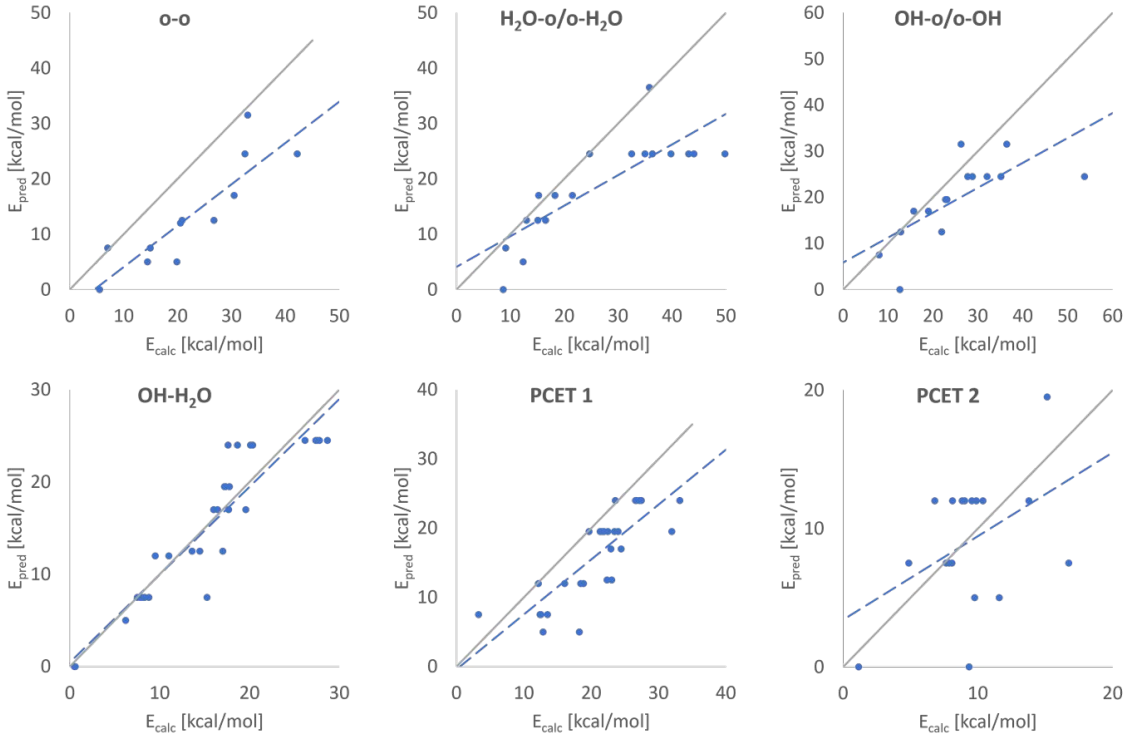

Figure S1: Linear fits of heuristics-predicted E_{pred} vs DFT-calculated E_{calc} (in kcal/mol) for all six groups of structures. The blue dashed lines represent the linear fits, while the grey unbroken line represents an ideal fit with a slope of 1 and intercept of 0.

Table S1: Parameters of the linear fits shown in figure S1: number of structures, slope, intercept, R^2, and MAE (in kcal/mol). In the latter four categories, the values closest to an ideal fit are highlighted in bold.

Group	**o-o**	**H_2O-o/ o-H_2O**	**OH-o/ o-OH**	**OH-H_2O**	**PCET 1**	**PCET 2**
Structures	12	18	15	31	29	18
Slope	0,75	0,55	0,54	**0,95**	0,79	0,60
Intercept	-3,37	4,06	5,88	0,45	**-0,43**	3,40
R^2	0,76	0,68	0,52	**0,86**	0,66	0,20
MAE	10,94	14,23	9,82	7,02	14,61	**6,24**

For all six groups of structures, the linear fits show that the predicted energies are able to at least qualitatively reproduce the calculated energies: all slopes are positive, showing that the energy ranking from low- to high-energy structure is comparable between predicted and calculated energy values. Non-zero intercept values are a lesser concern, as they represent an overall bias in the prediction affecting all structures equally and therefore not interfering with the correct energy ranking. In all cases, the energies of less stable structures with a greater number of JT axes are at least slightly underestimated, shown by the downward deviation of the linear fits (blue dashed lines) from the ideal fit (grey unbroken line) in figure S1. A small degree of overestimation of relative energies can be observed for structures under 10 kcal/mol calculated energy in the **H_2O-o/o-H_2O**, **OH-o/o-OH**, and **PCET 2** groups, but as only structures occupying the higher oxidation states of the catalyst (of which all possible isomers

were sampled) occupy this energy range, this overestimation does not reflect negatively on the practical accuracy of our heuristics. The highest precision is achieved in the **OH-H_2O** group, which was to be expected as this is the ligand configuration the heuristic rules were developed for. As already noted by Mai et al., the energy "costs" associated with each type of JT axis are heavily dependent on the ligand configuration of the system.[1] This observation is confirmed by the significantly lower R^2 values obtained for the other five groups of structures. Finally, the MAE values allow us to quantify the error separating predicted and calculated energies in terms of a mean absolute deviation in kcal/mol for each of the groups of structures. Again, the **OH-H_2O** group has the lowest value among the first four groups, which each cover all investigated oxidation states of the catalyst. The MAE of the **PCET 2** group is even lower, but this is mainly because this group only contains structures from the **3344**, **3444**, and **4444** oxidation states bearing fewer JT axes.

II. Tables of stable isomers

In the following, a table for each ligand configuration in the different oxidation states is provided, collecting relative Gibbs energies, relative Boltzmann populations at thermal equilibrium (T = 298.15 K) and spin populations.

Table S2: Unique isomers for the ligand configuration with two open coordination sites (**o-o**), grouped according to the overall oxidation state of the cubane core, charge q and multiplicity 2S+1. Columns from left to right: Oxidation state of the cubane core; name of isomer; Gibbs free energy relative to **zzzz-o-o*** (in eV); relative Boltzmann population at thermal equilibrium (T = 298.15 K); spin populations of MnA-D. Further notes: other spin populations over 0.15 with their atom name and number, † = structure obtained by applying two constraints along at least one JT axis. Structures with Boltzmann populations over 5.0% are highlighted in bold.

Ox. state	Isomer	ΔG_{rel} [eV]	Pop.	Spin populations MnA	MnB	MnC	MnD	Notes
4444	q = 0	2S+1 = 13						
	4444-o-o	21.19	**100%**	3.04	2.95	2.85	2.85	
3444	q = -1	2S+1 = 14						
	z444-o-o	14.79	0.0%	3.95	2.97	2.93	2.93	†
	444x-o-o	14.73	0.0%	3.03	2.97	2.92	3.86	†
	4z44-o-o	14.49	**100%**	3.04	3.88	2.92	2.92	†
3344	q = -2	2S+1 = 15						
	44yz-o-o	9.28	0.0%	3.01	2.97	3.86	3.86	†
	44yx-o-o	9.25	0.0%	3.02	2.93	3.86	3.86	†
	z44x-o-o	9.04	0.0%	3.89	2.98	2.98	3.89	†
	4z4x-o-o	9.02	0.0%	3.03	3.86	2.96	3.85	†
	zz44-o-o	8.72	**100%**	3.90	3.89	2.99	2.99	†
3334	q = -3	2S+1 = 16						
	4zyz-o-o*	4.43	0.0%	3.00	3.84	3.86	3.87	O1 0.17, †
	z4yx-o-o	4.27	0.0%	3.89	2.94	3.89	3.89	†
	zz4x-o-o	4.01	**9.7%**	3.90	3.87	3.00	3.88	O1 0.15, †
	zz4z-o-o*	3.95	**90.3%**	3.93	3.88	3.03	3.87	†
3333	q = -4	2S+1 = 17						

	zzyx-o-o*	0.46	0.0%	3.96	3.93	3.87	3.87	O1 0.25
	zzzz-o-o	0.06	**5.5%**	3.91	3.87	3.88	3.88	†
	zzyz-o-o*	0.04	**26.3%**	3.91	3.86	3.90	3.87	O1 0.18, †
	zzzz-o-o*	0.00	**68.2%**	3.91	3.92	3.88	3.88	†

Table S3: Unique isomers for the ligand configuration with H_2O bound to MnB and and open coordination site at MnA (**H_2O-o**), grouped according to the overall oxidation state of the cubane core, charge q and multiplicity 2S+1. Columns from left to right: Oxidation state of the cubane core; name of isomer; Gibbs free energy relative to **zzzz-o-o*** (in eV); relative Boltzmann population at thermal equilibrium (T = 298.15 K); spin populations of MnA-D. Further notes: other spin populations over 0.15 with their atom name and number, † = structure obtained by applying two constraints along at least one JT axis. Structures with Boltzmann populations over 5.0% are highlighted in bold.

Ox. state	Structure	ΔG_{rel} [eV]	Pop.	Spin populations MnA	MnB	MnC	MnD	Notes
4444	q = 0	2S+1 = 13						
	4444-H_2O-o	20.22	**100%**	3.04	2.93	2.87	2.87	
3444	q = -1	2S+1 = 14						
	444x-H_2O-o	14.00	**21.4%**	3.04	2.98	2.94	3.86	
	z444-H_2O-o	13.95	**78.6%**	3.90	2.96	2.95	2.95	
3344	q = -2	2S+1 = 15						
	z4y4-H_2O-o	8.51	**100%**	3.90	3.00	3.89	2.99	
3334	q = -3	2S+1 = 16						
	zz4x-H_2O-o	3.96	**46.9%**	3.90	3.89	3.00	3.89	
	z4yx-H_2O-o	3.94	**53.1%**	3.90	2.98	3.89	3.89	
3333	q = -4	2S+1 = 17						
	zzxz-H_2O-o*	0.54	0.0%	3.92	3.87	3.87	3.88	O2 0.20
	zxyx-H_2O-o	0.50	0.0%	3.94	3.86	3.89	3.90	O1 0.15
	zzyx-H_2O-o*	0.39	0.0%	3.95	3.84	3.87	3.87	O1 0.31
	zzzx-H_2O-o*	0.05	**42.6%**	3.91	3.86	3.87	3.90	O1 0.19
	xzxx-H_2O-o*	0.05	**57.4%**	3.93	3.87	3.87	3.85	O1 0.22

Table S4: Unique isomers for the ligand configuration with an open coordination site at MnB and H_2O bound to MnA (**o-H_2O**), grouped according to the overall oxidation state of the cubane core, charge q and multiplicity 2S+1. Columns from left to right: Oxidation state of the cubane core; name of isomer; Gibbs free energy relative to **zzzz-o-o*** (in eV); relative Boltzmann population at thermal equilibrium (T = 298.15 K); spin populations of MnA-D. Further notes: other spin populations over 0.15 with their atom name and number, † = structure obtained by applying two constraints along at least one JT axis. Structures with Boltzmann populations over 5.0% are highlighted in bold.

Ox. state	Structure	ΔG_{rel} [eV]	Pop.	Spin populations MnA	MnB	MnC	MnD	Notes

4444	q = 0	2S+1 = 13						
	4444-o-H_2O	20.11	**100%**	3.04	2.95	2.88	2.88	
3444	q = -1	2S+1 = 14						
	4z44-o-H_2O	13.57	**100%**	3.04	3.88	2.94	2.94	
3344	q = -2	2S+1 = 15						
	44yx-o-H_2O	8.70	0.0%	3.04	2.93	3.87	3.87	
	xz44-o-H_2O	8.56	0.1%	3.91	3.91	2.99	3.00	
	4z4x-o-H_2O	8.38	**99.9%**	3.04	3.86	2.97	3.86	O1 0.15
3334	q = -3	2S+1 = 16						
	4zyx-o-H_2O*	4.32	0.0%	3.04	3.80	3.84	3.84	O1 0.34
	4zxx-o-H_2O	4.17	0.0%	3.00	3.85	3.88	3.87	O1 0.16
	xz4x-o-H_2O	4.10	0.1%	3.92	3.88	3.01	3.89	O1 0.15
	4zzx-o-H_2O	4.04	1.0%	3.01	3.84	3.88	3.86	O1 0.17
	xzy4-o-H_2O	4.04	1.2%	3.91	3.88	3.89	3.03	
	zzy4-o-H_2O	3.92	**97.7%**	3.92	3.87	3.89	3.01	O1 0.16
3333	q = -4	2S+1 = 17						
	xzyx-o-H_2O*	0.72	0.0%	3.92	3.93	3.88	3.87	O1 0.24
	xzyy-o-H_2O	0.47	0.0%	3.92	3.94	3.90	3.89	
	xzxx-o-H_2O	0.43	0.0%	3.92	3.87	3.87	3.89	O1 0.19
	xzyz-o-H_2O*	0.29	0.0%	3.95	3.92	3.90	3.89	
	zzzx-o-H_2O*	0.14	0.0%	3.93	3.91	3.87	3.90	O1 0.17
	xzzx-o-H_2O*	-0.37	**100%**	3.91	3.90	3.87	3.89	O1 0.15

Table S5: Unique isomers for the ligand configuration with an open coordination site at MnB and OH bound to MnA (**o-OH**), grouped according to the overall oxidation state of the cubane core, charge q and multiplicity 2S+1. Columns from left to right: Oxidation state of the cubane core; name of isomer; Gibbs free energy relative to **zzzz-o-o*** (in eV); relative Boltzmann population at thermal equilibrium (T = 298.15 K); spin populations of MnA-D. Further notes: other spin populations over 0.15 with their atom name and number, † = structure obtained by applying two constraints along at least one JT axis. Structures with Boltzmann populations over 5.0% are highlighted in bold.

Ox. state	Structure	ΔG_{rel} [eV]	Pop.	Spin populations MnA	MnB	MnC	MnD	Notes
4444	q = -1	2S+1 = 13						
	4444-o-OH	20.23	**100%**	2.94	2.97	2.92	2.91	
3444	q = -2	2S+1 = 14						
	4z44-o-OH	14.04	**100%**	2.97	3.89	2.98	2.98	
3344	q = -3	2S+1 = 15						
	yz44-o-OH	9.41	0.6%	3.88	3.91	3.02	3.02	
	4zy4-o-OH	9.28	**99.4%**	3.02	3.87	3.88	2.99	O1 0.16
3334	q = -4	2S+1 = 16						

	4zxx-o-OH	5.53	0.0%	3.02	3.86	3.87	3.88	O1 0.16
	4zyz-o-OH	5.39	0.3%	3.01	3.85	3.88	3.89	O1 0.17
	yzy4-o-OH	5.26	**36.9%**	3.94	3.89	3.90	3.03	O1 0.16
	yz4x-o-OH	5.25	**62.9%**	3.93	3.89	3.04	3.90	
	q = -5	2S+1 = 17						
	yzyx-o-OH*	2.05	0.1%	3.95	3.85	3.89	3.89	O1 0.28
3333	xzxx-o-OH	2.00	0.4%	3.93	3.88	3.88	3.89	O1 0.18
	xzxz-o-OH	1.94	4.9%	3.91	3.92	3.89	3.90	
	xzyz-o-OH	1.86	**94.6%**	3.93	3.86	3.90	3.90	O1 0.16

Table S6: Unique isomers for the ligand configuration with OH bound to MnB and an open coordination site at MnA (**OH-o**), grouped according to the overall oxidation state of the cubane core, charge q and multiplicity 2S+1. Columns from left to right: Oxidation state of the cubane core; name of isomer; Gibbs free energy relative to **zzzz-o-o*** (in eV); relative Boltzmann population at thermal equilibrium (T = 298.15 K); spin populations of MnA-D. Further notes: other spin populations over 0.15 with their atom name and number, † = structure obtained by applying two constraints along at least one JT axis. Structures with Boltzmann populations over 5.0% are highlighted in bold.

Ox. state	Structure	ΔG_{rel} [eV]	Pop.	Spin populations MnA	MnB	MnC	MnD	Notes
4444	q = -1	2S+1 = 13						
	4444-OH-o	20.35	**100%**	3.04	2.90	2.91	2.91	
	q = -2	2S+1 = 14						
3444	444x-OH-o	14.67	0.0%	3.04	2.95	2.96	3.86	
	z444-OH-o	14.45	**100%**	3.90	2.94	2.98	2.98	
3344	q = -3	2S+1 = 15						
	z44x-OH-o	9.50	**100%**	3.90	2.99	3.01	3.89	
	q = -4	2S+1 = 16						
	zxy4-OH-o	5.60	0.2%	3.89	3.89	3.90	3.03	
3334	zx4x-OH-o	5.59	0.4%	3.94	3.88	3.03	3.90	
	z4yx-OH-o	5.55	0.8%	3.91	3.03	3.87	3.87	O1 0.15
	z4yz-OH-o	5.44	**98.6%**	3.93	3.05	3.91	3.88	
	q = -5	2S+1 = 17						
	zzyx-OH-o*	2.84	0.0%	3.95	3.87	3.88	3.88	O1 0.19
3333	zxzx-OH-o*	2.09	0.0%	3.89	3.91	3.88	3.89	
	zxyx-OH-o*	2.03	0.1%	3.92	3.91	3.88	3.85	O1 0.18
	yyyx-OH-o*	1.90	**28.9%**	3.89	3.91	3.84	3.88	O1 0.18
	xxxx-OH-o*	1.88	**71.0%**	3.90	3.89	3.89	3.87	

Table S7: Unique isomers for the ligand configuration with an OH and an H_2O ligand, grouped according to the overall oxidation state of the cubane core, charge q and multiplicity 2S+1. Columns from left to right: Oxidation state of the cubane core; name of isomer; Gibbs free energy relative to **zzzz-o-o*** (in eV); relative Boltzmann population at thermal equilibrium (T = 298.15 K); spin populations of MnA-D. Further notes: other spin populations over 0.15 with their atom name and number, † = structure obtained by applying two constraints along at least one JT axis. Structures with Boltzmann populations over 5.0% are highlighted in bold.

Ox. state	Structure	ΔG_{rel} [eV]	Pop.	Spin populations MnA	MnB	MnC	MnD	Notes
	q = -1	2S+1 = 13						
4444	**4444-H_2O-OH**	19.28	**29.6%**	2.98	2.94	2.93	2.93	
	4444-OH-H_2O	19.26	**70.4%**	3.03	2.93	2.93	2.93	
	q = -2	2S+1 = 14						
	x444-OH-H_2O	14.04	0.0%	3.91	2.98	2.98	2.98	
3444	z444-OH-H_2O	14.03	0.0%	3.91	2.97	2.99	2.99	
	444x-H_2O-OH	13.71	**41.9%**	3.03	2.99	2.99	3.88	
	4z44-H_2O-OH	13.69	**58.1%**	3.01	3.88	2.99	2.99	†
	q = -3	2S+1 = 15						
	zz44-OH-H_2O	9.50	0.0%	3.92	3.86	3.03	3.03	
	44xx-OH-H_2O	9.31	0.0%	3.02	3.01	3.86	3.88	†
	4x4x-OH-H_2O	9.25	0.0%	3.03	3.88	2.99	3.88	†
	z44x-OH-H_2O	9.21	0.1%	3.92	3.02	3.02	3.90	
3344	x44x-H_2O-OH	9.19	0.3%	3.90	3.03	3.03	3.90	
	y44x-H_2O-OH	9.17	0.8%	3.91	3.03	3.03	3.90	
	xz44-H_2O-OH	9.16	1.3%	3.89	3.92	3.02	3.02	
	44yx-H_2O-OH	9.10	**5.9%**	3.05	2.98	3.88	3.88	
	4z4x-H_2O-OH	9.05	**91.5%**	3.04	3.88	2.99	3.88	
	q = -4	2S+1 = 16						
	4xxx-H_2O-OH*	5.47	0.0%	3.02	3.87	3.88	3.89	†
	4xyy-H_2O-OH	5.46	0.0%	3.02	3.88	3.88	3.89	†
	4zyx-H_2O-OH*	5.44	0.0%	3.07	3.85	3.85	3.85	O1 0.28
	4zzz-H_2O-OH	5.40	0.0%	3.01	3.88	3.88	3.88	†
	zx4x-OH-H_2O	5.36	0.0%	3.92	3.89	3.03	3.90	†
	4zxx-H_2O-OH	5.36	0.0%	3.03	3.88	3.88	3.87	†
	4xzx-H_2O-OH	5.35	0.0%	3.03	3.88	3.89	3.88	†
3334	zy4x-OH-H_2O	5.34	0.0%	3.92	3.90	3.04	3.91	†
	x4yz-OH-H_2O	5.34	0.0%	3.92	3.06	3.90	3.90	†
	z4yx-OH-H_2O	5.33	0.0%	3.93	3.04	3.89	3.89	†
	4xyx-H_2O-OH	5.30	0.1%	3.04	3.87	3.88	3.87	†
	4zyz-H_2O-OH	5.28	0.2%	3.03	3.87	3.87	3.88	†
	x4yx-H_2O-OH	5.22	3.0%	3.92	3.01	3.90	3.90	
	xz4x-H_2O-OH	5.18	**12.7%**	3.91	3.91	3.02	3.90	†
	yz4x-H_2O-OH	5.13	**83.8%**	3.91	3.91	3.03	3.90	

	q = -5	2S+1 = 17						
	zxyx-OH-H_2O*	2.09	0.1%	3.92	3.89	3.89	3.88	†
	yzyx-H_2O-OH*	2.05	0.4%	3.93	3.87	3.88	3.88	O1 0.25
3333	yzyy-H_2O-OH*	2.04	0.5%	3.91	3.88	3.89	3.87	O1 0.18, †
	xzyy-H_2O-OH*	2.03	0.7%	3.91	3.89	3.89	3.88	O1 0.16, †
	xxyx-H_2O-OH	1.98	**5.5%**	3.93	3.87	3.90	3.89	O1 0.16, †
	yzzx-H_2O-OH*	1.91	**92.8%**	3.93	3.86	3.90	3.90	O1 0.16, †

Table S8: Unique isomers from the first PCET pathway, comprising those with two OH ligands, those with one oxo and one OH ligand, and those with two oxo ligands; grouped according to the overall oxidation state of the cubane core, charge q and multiplicity 2S+1. Columns from left to right: Oxidation state of the cubane core; name of isomer; Gibbs free energy relative to **zzzz-o-o*** (in eV); relative Boltzmann population at thermal equilibrium (T = 298.15 K); spin populations of MnA-D. Further notes: other spin populations over 0.15 with their atom name and number, † = structure obtained by applying two constraints along at least one JT axis. Structures with Boltzmann populations over 5.0% are highlighted in bold.

Ox. state	Structure	ΔG_{rel} [eV]	Pop.	Spin populations MnA	MnB	MnC	MnD	Notes
	q = -5	2S+1 = 14						
3444	x444-O-O	19.80	0.4%	3.76	2.71	3.04	3.04	O5 0.35, O6 0.17
	444x-O-O	19.66	**99.6%**	2.71	2.67	3.01	3.89	O5 0.39, O6 0.38, †
	q = -5	2S+1 = 15						
	xx44-OH-O	13.70	0.0%	3.77	3.87	3.02	2.99	O6 0.15, †
	44xx-O-OH	13.59	0.0%	3.02	2.75	3.87	3.87	O5 0.30, †
	4x4x-O-OH	13.58	0.0%	3.01	3.78	3.00	3.89	†
	44yx-O-OH	13.57	0.0%	3.03	2.76	3.85	3.85	O1 0.18, O5 0.30
3344	44yz-O-OH	13.47	0.0%	3.02	2.76	3.88	3.87	O5 0.30, †
	x44x-OH-O	13.36	2.7%	3.78	3.03	3.04	3.91	
	44yx-OH-O	13.33	4.1%	2.76	3.04	3.88	3.88	O6 0.33
	y44x-O-OH	13.32	**14.4%**	3.90	2.77	3.02	3.90	O5 0.29, †
	x44x-O-OH	13.31	**17.5%**	3.90	2.77	3.02	3.90	O5 0.29
	4x4x-OH-O	13.30	**26.7%**	2.76	3.88	3.03	3.90	O6 0.30, †
	4y4x-OH-O	13.30	**34.4%**	2.76	3.90	3.03	3.90	O6 0.31, †

	q = -5	2S+1 = 16						
	4zzz-HO-HO	7.68	0.0%	3.01	3.87	3.87	3.87	†
	xz4z-HO-HO	7.63	0.0%	3.90	3.88	3.03	3.88	†
	4xyy-OH-OH	7.44	0.0%	3.01	3.90	3.88	3.89	†
	4xyy-HO-HO	7.42	0.0%	3.04	3.91	3.88	3.89	†
	4xxx-OH-OH*	7.40	0.0%	3.02	3.89	3.88	3.88	†
	4xxx-HO-HO*	7.40	0.0%	3.03	3.89	3.88	3.89	†
	4xyx-OH-OH	7.31	0.0%	3.04	3.89	3.87	3.86	†
	x4xx-OH-OH	7.29	0.0%	3.91	3.06	3.88	3.89	†
3334	4xzx-HO-HO	7.27	0.1%	3.03	3.91	3.88	3.89	†
	x4xx-HO-HO	7.26	0.1%	3.91	3.06	3.88	3.90	†
	y4yx-OH-OH	7.25	0.1%	3.92	3.05	3.88	3.89	O1 0.16
	4yyx-HO-HO	7.24	0.2%	3.04	3.89	3.87	3.88	†
	yy4x-OH-OH	7.22	0.4%	3.90	3.90	3.04	3.91	†
	y4yx-HO-HO	7.22	0.4%	3.91	3.05	3.89	3.89	O1 0.16
	x4yz-OH-OH	7.20	0.9%	3.92	3.05	3.90	3.90	†
	xx4x-HO-HO	7.19	1.4%	3.90	3.88	3.03	3.90	†
	x4yz-HO-HO	7.17	2.5%	3.93	3.05	3.90	3.90	†
	xx4x-OH-OH	7.10	**40.1%**	3.91	3.88	3.03	3.90	†
	yy4x-HO-HO	7.09	**53.7%**	3.92	3.89	3.04	3.92	†

Table S9: Unique isomers from the second PCET pathway, comprising those with two OH ligands, those with one oxo and one OH ligand, and those with two oxo ligands; grouped according to the overall oxidation state of the cubane core, charge q and multiplicity 2S+1. Columns from left to right: Oxidation state of the cubane core; name of isomer; Gibbs free energy relative to **zzzz-o-o*** (in eV); relative Boltzmann population at thermal equilibrium (T = 298.15 K); spin populations of MnA-D. Further notes: other spin populations over 0.15 with their atom name and number, † = structure obtained by applying two constraints along at least one JT axis. Structures with Boltzmann populations over 5.0% are highlighted in bold.

Ox. state	Structure	ΔG_{rel} [eV]	Pop.	Spin populations MnA	MnB	MnC	MnD	Notes
4444	q = -4	2S+1 = 13						
	4444-O-O	23.58	**100%**	2.63	2.61	3.02	3.02	O5 0.42 O6 0.43
3444	q = -4	2S+1 = 14						
	4z44-O-OH	17.31	0.0%	2.98	3.77	3.01	3.01	†
	4x44-OH-O	17.20	0.0%	2.69	3.87	3.01	3.02	O6 0.36, †
	y444-O-OH	17.12	0.0%	3.88	2.71	3.01	3.01	O5 0.32
	444x-O-OH	16.95	**12.6%**	3.00	2.70	2.99	3.88	O5 0.34
	444x-OH-O	16.90	**87.4%**	2.70	2.99	3.02	3.89	O6 0.37

	q = -4	2S+1 = 15						
	yz44-HO-HO	11.04	0.0%	3.88	3.87	3.04	3.04	†
	xx44-OH-OH	10.97	0.0%	3.89	3.87	3.01	3.02	†
	44xx-OH-OH	10.91	0.0%	3.02	3.00	3.87	3.88	†
	44yx-OH-OH	10.82	0.0%	3.04	3.01	3.86	3.86	
	44yz-OH-OH	10.76	0.2%	3.02	3.02	3.88	3.88	†
	4y4x-OH-OH	10.74	0.5%	3.02	3.88	3.02	3.89	†
3344	44yx-HO-HO	10.74	0.3%	3.02	3.02	3.87	3.87	
	44yz-HO-HO	10.73	1.0%	3.02	3.03	3.88	3.88	†
	4x4x-OH-OH	10.71	2.3%	3.02	3.87	3.01	3.89	†
	4y4x-HO-HO	10.70	3.2%	3.02	3.89	3.02	3.89	†
	4x4x-HO-HO	10.67	**10.8%**	3.01	3.88	3.02	3.89	†
	x44x-OH-OH	10.66	**11.3%**	3.90	3.03	3.03	3.90	
	y44x-OH-OH	10.66	**16.2%**	3.91	3.03	3.03	3.90	
	x44x-HO-HO	10.65	**23.9%**	3.90	3.03	3.03	3.90	
	y44x-HO-HO	10.64	**30.2%**	3.89	3.03	3.03	3.90	†

III. Interatomic distance analysis

In the following, histograms of the interatomic distances between each Mn center and every one of its coordinating atoms is provided. For the most part, these show a common pattern: two peaks representing bonds not lengthened by JT distortions and JT-distorted bonds, respectively, and outliers above 2.5 Å representing partly dissociated structures.

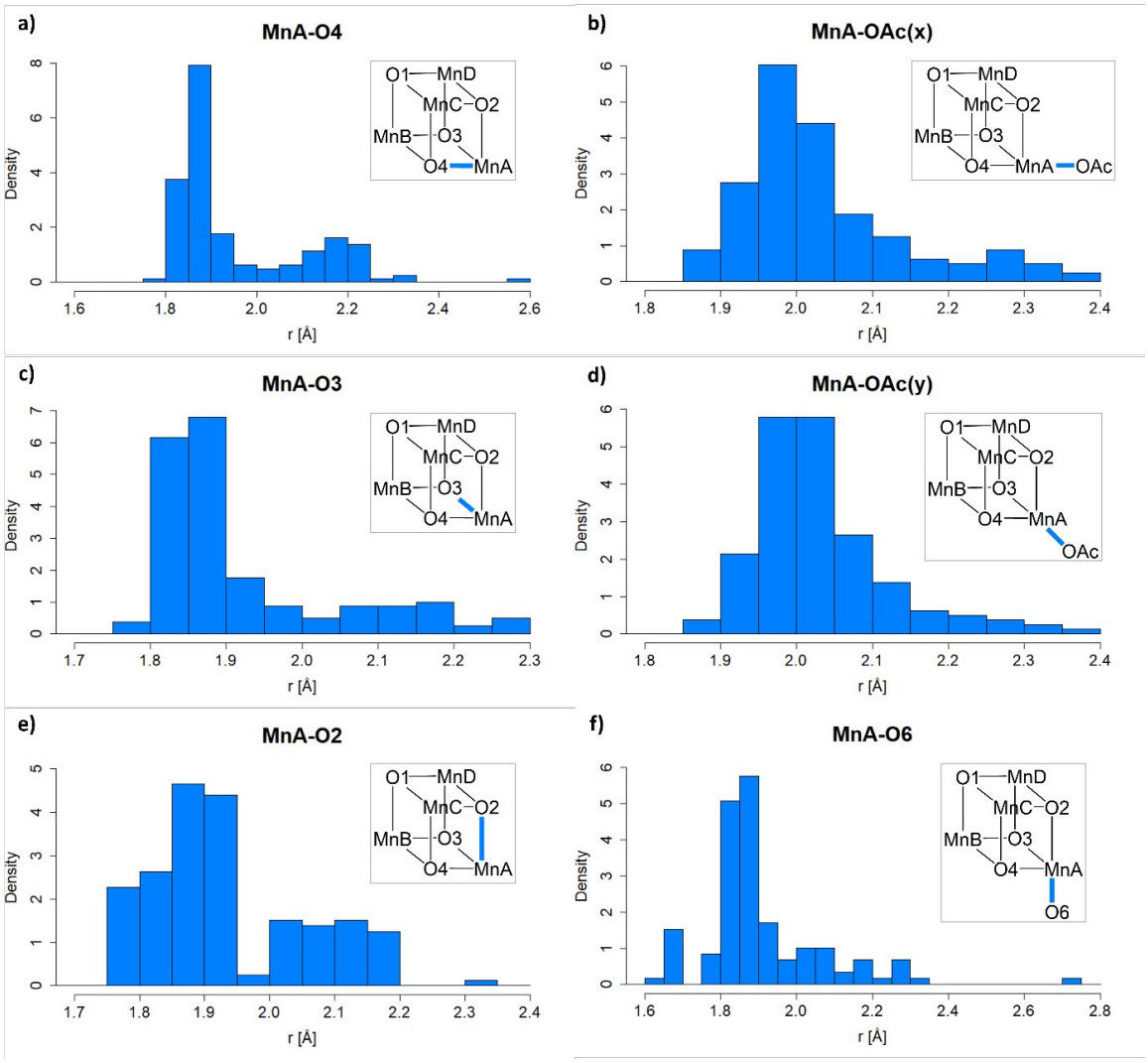

Figure S2: Interatomic distance distributions (in Å) for MnA and its coordination partners (bonds highlighted in blue in the insets). a) r(MnA-O4), b) r(MnA-OAc) along x axis, c) r(MnA-O3), d) r(MnA-OAc) along y axis, e) r(MnA-O2), f) r(MnA-O6).

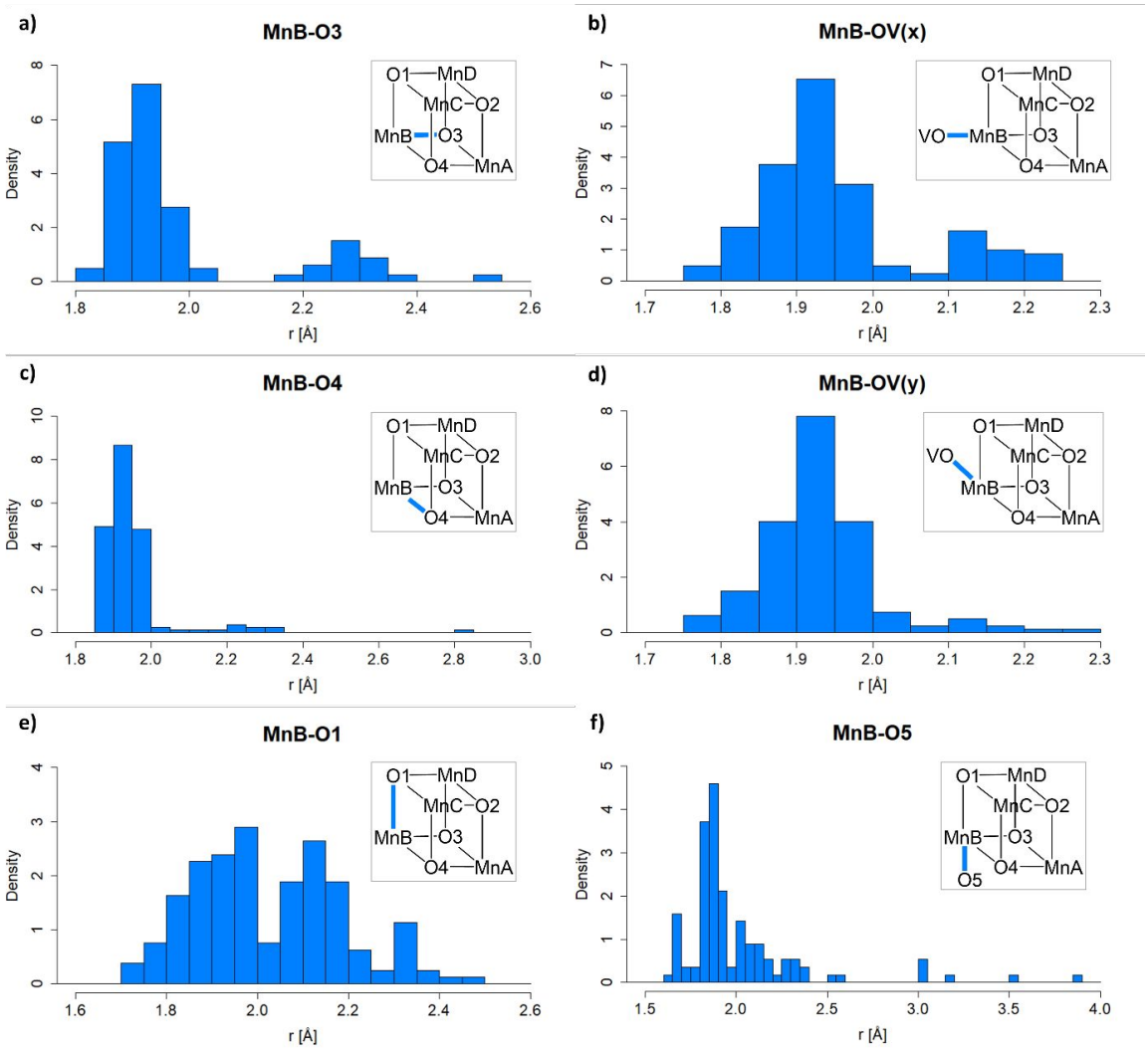

Figure S3: Interatomic distance distributions (in Å) for MnB and its coordination partners (bonds highlighted in blue in the insets). a) r(MnB-O3), b) r(MnB-OV) along x axis, c) r(MnB-O4), d) r(MnB-OV) along y axis, e) r(MnB-O1), f) r(MnB-O5).

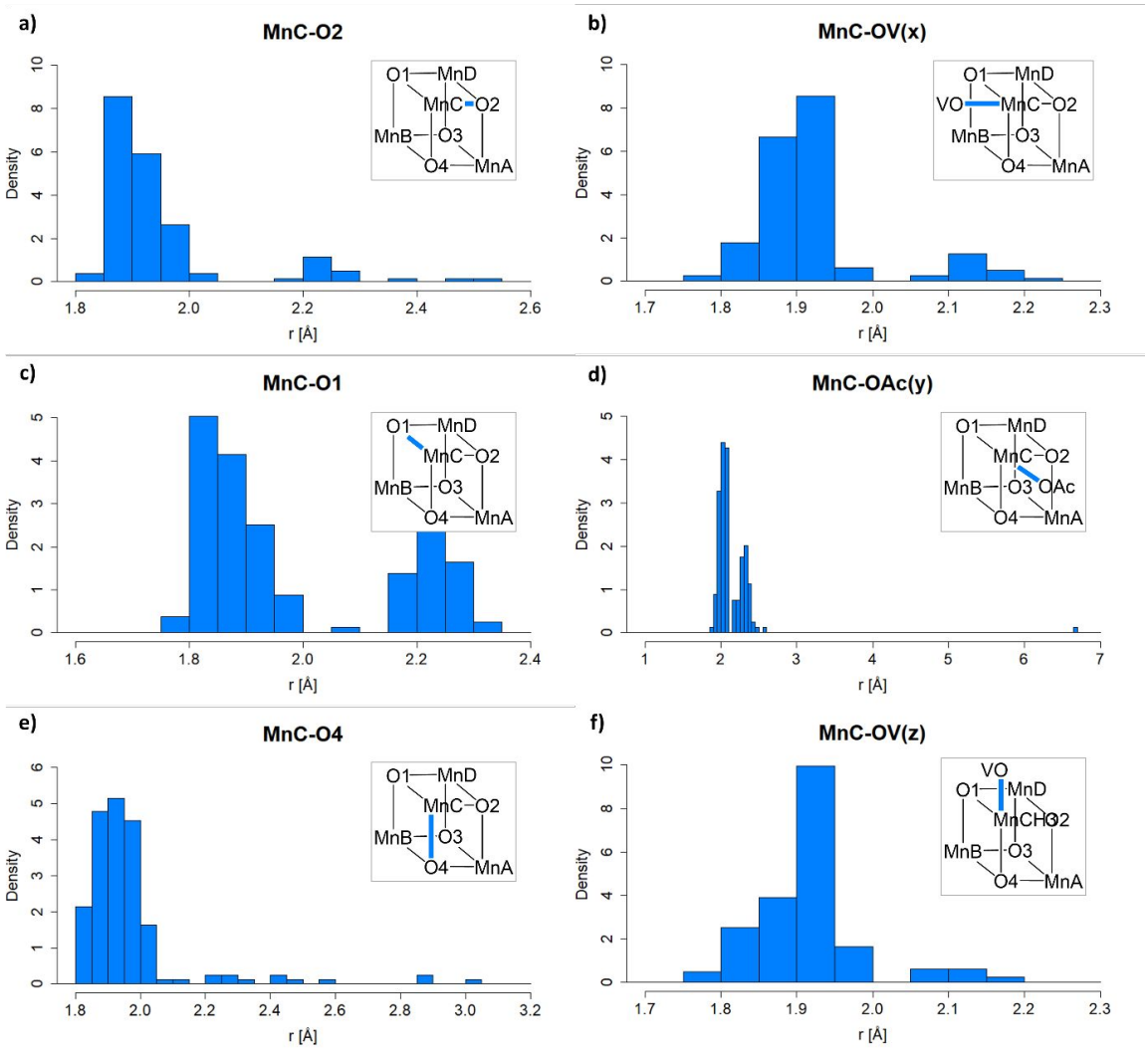

Figure S4: Interatomic distance distributions (in Å) for MnC and its coordination partners (bonds highlighted in blue in the insets). a) r(MnC-O2), b) r(MnC-OV) along x axis, c) r(MnC-O1), d) r(MnC-OAc) along y axis, e) r(MnC-O4), f) r(MnC-OV) along z axis.

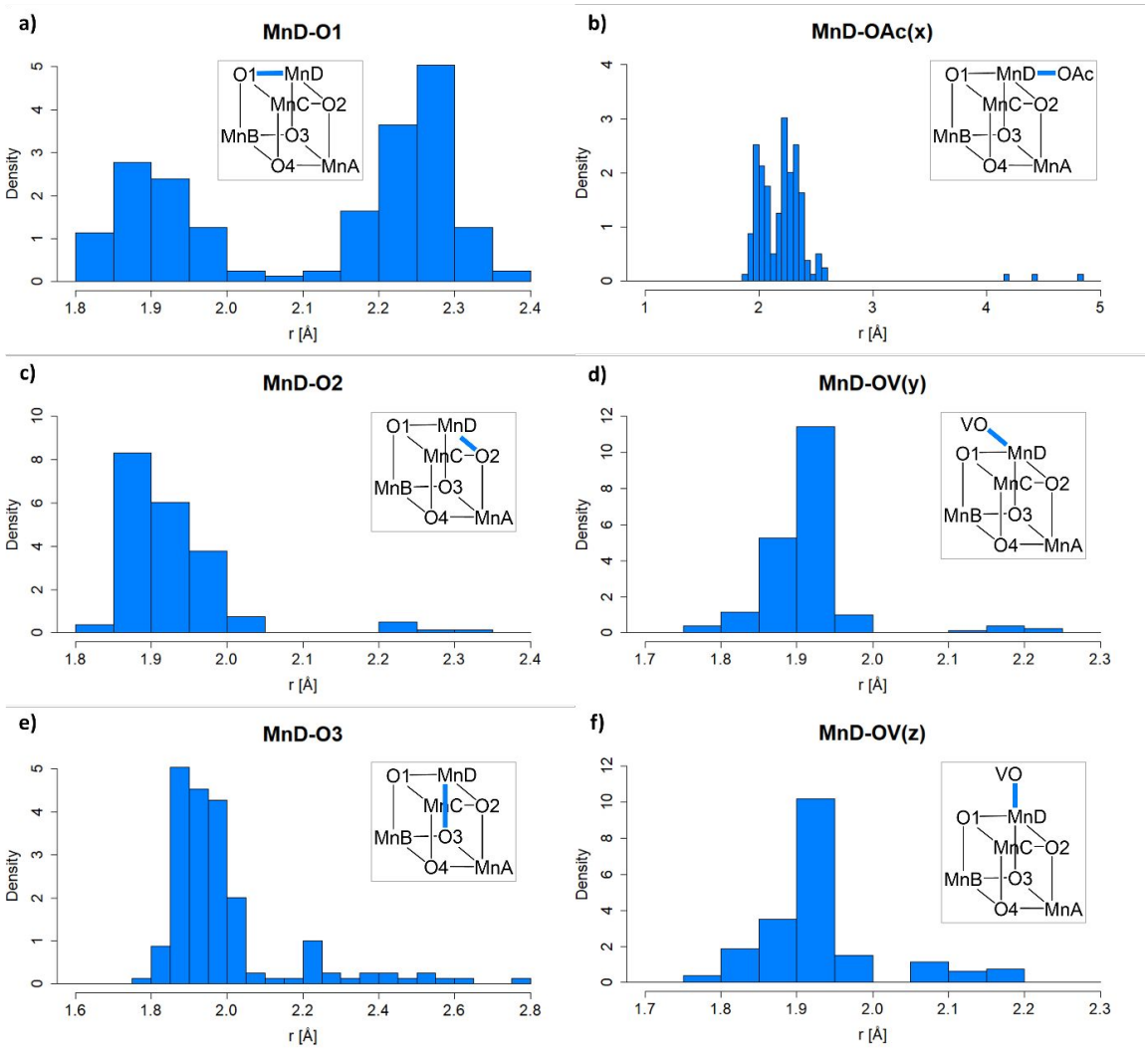

Figure S5: Interatomic distance distributions (in Å) for MnD and its coordination partners (bonds highlighted in blue in the insets). a) r(MnD-O1), b) r(MnD-OAc) along x axis, c) r(MnD-O2), d) r(MnD-OV) along y axis, e) r(MnD-O3), f) r(MnD-OV) along z axis.

IV. Nudged elastic band simulation results

In the following, figures summarizing the results of the nudged elastic band calculations NEB 1-6 are provided, showing the reactant and product structures, electronic energy changes along the minimum energy pathways, and significant bond distance changes along the minimum energy pathways indicating a reaction has taken place. Small changes in Mn-O interatomic distances (below 0.4 Å) typically represent a JT or redox isomerization, while larger changes point toward bond dissociations.

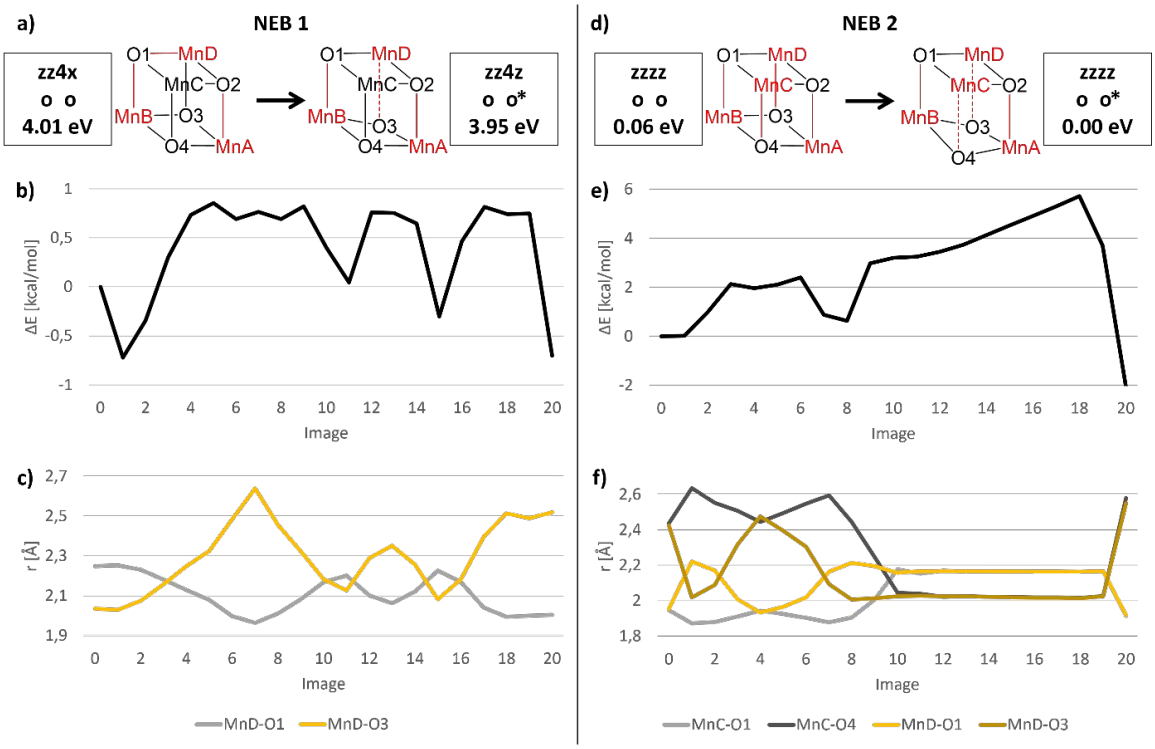

Figure S6: Results summary of the NEB 1 and NEB 2 calculations. a,d) Reactant and product structures with energies calculated at the B3LYP-D3/ZORA-def2-TZVP//B3LYP-D3/ZORA-def2-SVP level of theory. b,e) Energy changes along the minimum energy paths, calculated at the B3LYP-D3/ZORA-def2-SVP level of theory. c,f) Bond length changes along the minimum energy paths, in both cases showing fluctuation between two JT minima.

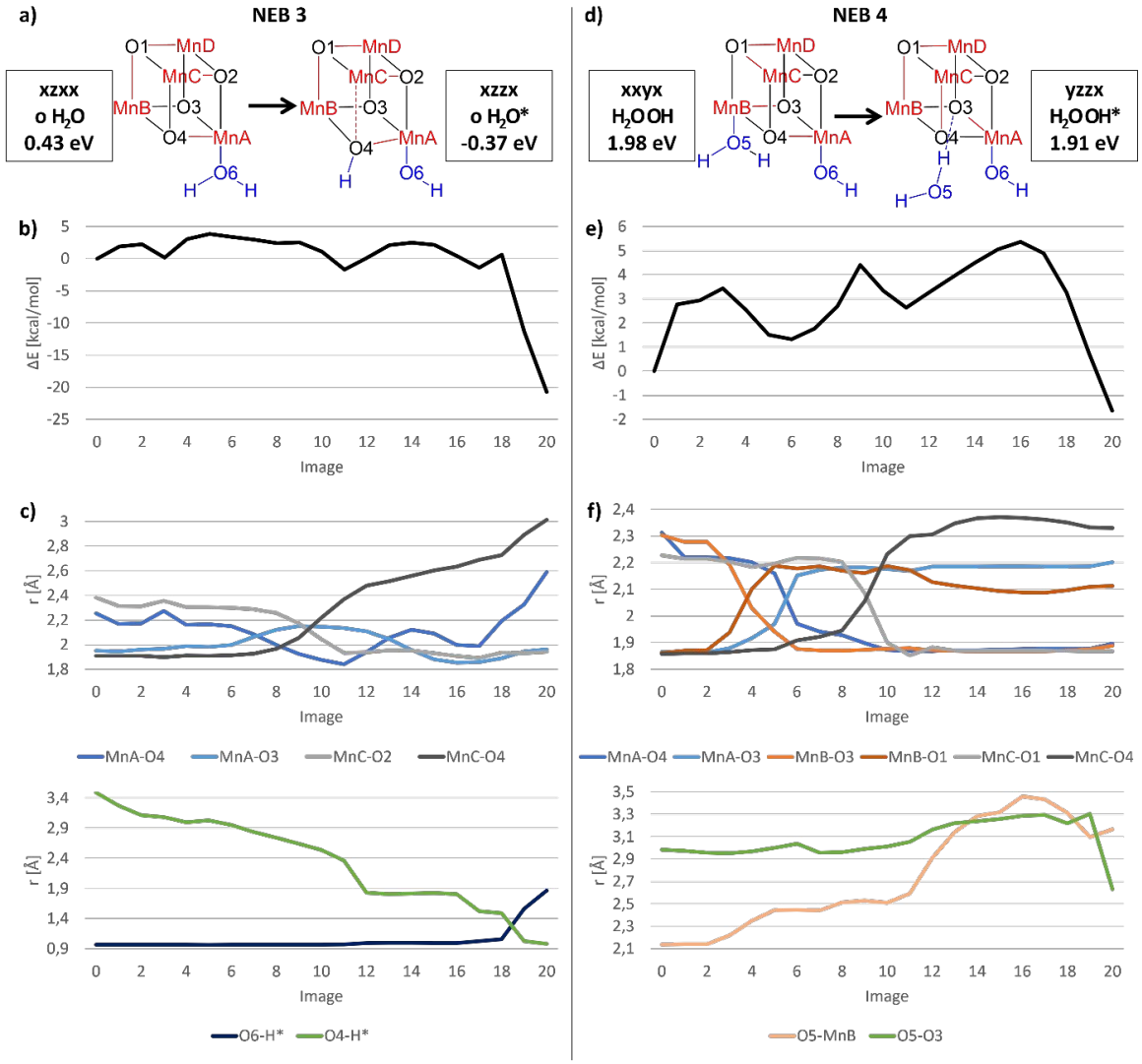

Figure S7: Results summary of the NEB 3 and NEB 4 calculations. a,d) Reactant and product structures with energies calculated at the B3LYP-D3/ZORA-def2-TZVP//B3LYP-D3/ZORA-def2-SVP level of theory. b,e) Energy changes along the minimum energy paths, calculated at the B3LYP-D3/ZORA-def2-SVP level of theory. c,f) Bond length changes along the minimum energy paths, in both cases the emergence of JT distortions in line with the studied degradation process can be observed before bond cleavage.

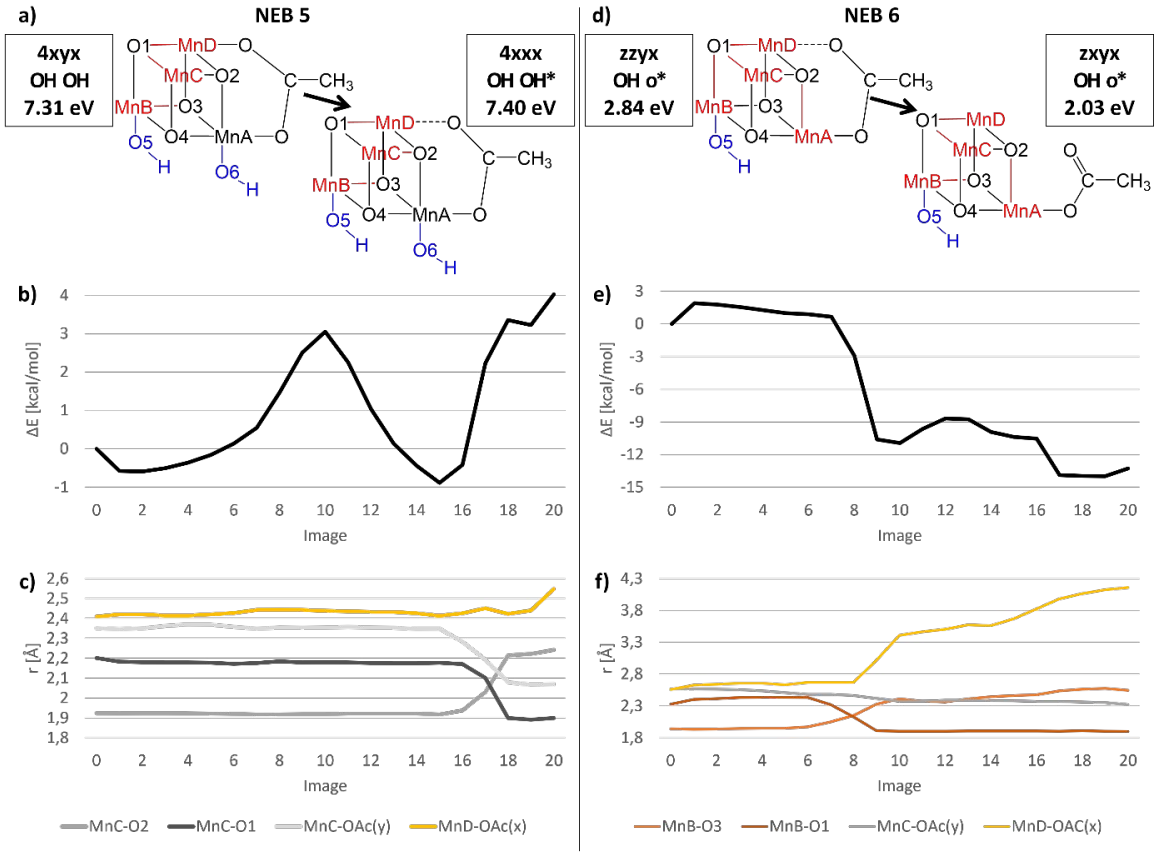

Figure S8: Results summary of the NEB 5 and NEB 6 calculations. a,d) Reactant and product structures with energies calculated at the B3LYP-D3/ZORA-def2-TZVP//B3LYP-D3/ZORA-def2-SVP level of theory. b,e) Energy changes along the minimum energy paths, calculated at the B3LYP-D3/ZORA-def2-SVP level of theory. c,f) Bond length changes along the minimum energy paths, in both cases JT distortions in line with the studied degradation are present in both the reactant and product structure.

Sources

(1) Mai, S.; Holzer, M.; Andreeva, A.; González, L. Jahn-Teller Effects in a Vanadate-Stabilized Manganese-Oxo Cubane Water Oxidation Catalyst. *Chemistry – A European Journal* **2021**, *27* (68), 17066–17077. https://doi.org/10.1002/chem.202102539.

Bibliography

[1] J. Chow, R. J. Kopp, and P. R. Portney, "Energy Resources and Global Development," *Science*, vol. 302, no. 5650, pp. 1528–1531, 2003.

[2] E. Regnier, "Oil and energy price volatility," *Energy Economics*, vol. 29, no. 3, pp. 405–427, 2007.

[3] H.-O. Pörtner, D. Roberts, H. Adams, I. Adelekan, C. Adler, R. Adrian, P. Aldunce, E. Ali, R. A. Begum, B. B. Friedl, R. B. Kerr, R. Biesbroek, J. Birkmann, K. Bowen, M. Caretta, J. Carnicer, E. Castellanos, T. Cheong, W. Chow, G. C. G. Cissé, and Z. Z. Ibrahim, *Climate Change 2022: Impacts, Adaptation and Vulnerability*. Cambridge, UK and New York, USA: Cambridge University Press, 2022.

[4] International Energy Agency, *CO2 Emissions from Fuel Combustion 2017*. International Energy Agency, 2017.

[5] T. R. Cook, D. K. Dogutan, S. Y. Reece, Y. Surendranath, T. S. Teets, and D. G. Nocera, "Solar Energy Supply and Storage for the Legacy and Nonlegacy Worlds," *Chemical Reviews*, vol. 110, no. 11, pp. 6474–6502, 2010.

[6] A. Züttel, A. Remhof, A. Borgschulte, and O. Friedrichs, "Hydrogen: the future energy carrier," *Philosophical Transactions of the Royal Society A: Mathematical, Physical and Engineering Sciences*, vol. 368, no. 1923, pp. 3329–3342, 2010.

[7] H. Dau, C. Limberg, T. Reier, M. Risch, S. Roggan, and P. Strasser, "The Mechanism of Water Oxidation: From Electrolysis via Homogeneous to Biological Catalysis," *ChemCatChem*, vol. 2, no. 7, pp. 724–761, 2010.

[8] W. Lubitz, E. J. Reijerse, and J. Messinger, "Solar water-splitting into H_2 and O_2: design principles of photosystem II and hydrogenases," *Energy & Environmental Science*, vol. 1, no. 1, pp. 15–31, 2008.

[9] M. Yagi, E. Tomita, and T. Kuwabara, "Remarkably high activity of electrodeposited IrO_2 film for electrocatalytic water oxidation," *Journal of Electroanalytical Chemistry*, vol. 579, no. 1, pp. 83–88, 2005.

[10] S. W. Gersten, G. J. Samuels, and T. J. Meyer, "Catalytic oxidation of water by an oxo-bridged ruthenium dimer," *Journal of the American Chemical Society*, vol. 104, no. 14, pp. 4029–4030, 1982.

[11] J. A. Gilbert, D. S. Eggleston, W. R. J. Murphy, D. A. Geselowitz, S. W. Gersten, D. J. Hodgson, and T. J. Meyer, "Structure and redox properties of the water-oxidation catalyst $[(bpy)_2(OH_2)RuORu(OH_2)(bpy)_2]^{4+}$," *Journal of the American Chemical Society*, vol. 107, no. 13, pp. 3855–3864, 1985.

[12] C. W. Chronister, R. A. Binstead, J. Ni, and T. J. Meyer, "Mechanism of water oxidation catalyzed by the mu-oxo dimer $[(bpy)_2(OH_2)Ru^{III}ORu^{III}(OH_2)(bpy)_2]^{4+}$," *Inorganic Chemistry*, vol. 36, no. 18, pp. 3814–3815, 1997.

[13] C. Ma, S. Piccinin, and S. Fabris, "Interface structure and reactivity of water-oxidation Ru–polyoxometalate catalysts on functionalized graphene electrodes," *Physical Chemistry Chemical Physics*, vol. 16, no. 11, pp. 5333–5341, 2014.

[14] G. Y. Lee, I. Kim, J. Lim, M. Y. Yang, D. S. Choi, Y. Gu, Y. Oh, S. H. Kang, Y. S. Nam, and S. O. Kim, "Spontaneous linker-free binding of polyoxometalates on nitrogen-doped carbon nanotubes for efficient water oxidation," *Journal of Materials Chemistry A*, vol. 5, no. 5, pp. 1941–1947, 2017.

[15] Y. Guo, H. Li, L.-L. He, D.-X. Zhao, L.-D. Gong, and Z.-Z. Yang, "The open-cubane oxo–oxyl coupling mechanism dominates photosynthetic oxygen evolution: a comprehensive DFT investigation on O–O bond formation in the S4 state," *Physical Chemistry Chemical Physics*, vol. 19, no. 21, pp. 13909–13923, 2017.

[16] D. J. Vinyard, S. Khan, and G. W. Brudvig, "Photosynthetic water oxidation: binding and activation of substrate waters for O–O bond formation," *Faraday Discussions*, vol. 185, pp. 37–50, 2015.

[17] P. E. M. Siegbahn, "Theoretical Studies of O-O Bond Formation in Photosystem II," *Inorganic Chemistry*, vol. 47, no. 6, pp. 1779–1786, 2008.

[18] E. M. Sproviero, J. A. Gascón, J. P. McEvoy, G. W. Brudvig, and V. S. Batista, "Quantum Mechanics/Molecular Mechanics Study of the Catalytic Cycle of Water Splitting in Photosystem II," *Journal of the American Chemical Society*, vol. 130, no. 11, pp. 3428–3442, 2008.

[19] M. Suga, F. Akita, K. Hirata, G. Ueno, H. Murakami, Y. Nakajima, T. Shimizu, K. Yamashita, M. Yamamoto, H. Ago, and J.-R. Shen, "Native structure of photosystem II at 1.95 Å resolution viewed by femtosecond X-ray pulses," *Nature*, vol. 517, no. 7532, pp. 99–103, 2015.

[20] A. I. Nguyen, M. S. Ziegler, P. Oña-Burgos, M. Sturzbecher-Hohne, W. Kim, D. E. Bellone, and T. D. Tilley, "Mechanistic Investigations of Water Oxidation by a Molecular Cobalt Oxide Analogue: Evidence for a Highly Oxidized Intermediate and Exclusive Terminal Oxo Participation," *Journal of the American Chemical Society*, vol. 137, no. 40, pp. 12865–12872, 2015.

[21] F. H. Hodel and S. Luber, "What Influences the Water Oxidation Activity of a Bioinspired Molecular $Co_4^{II}O_4$ Cubane? An In-Depth Exploration of Catalytic Pathways," *ACS Catalysis*, vol. 6, no. 3, pp. 1505–1517, 2016.

[22] F. H. Hodel and S. Luber, "Redox-Inert Cations Enhancing Water Oxidation Activity: The Crucial Role of Flexibility," *ACS Catalysis*, vol. 6, no. 10, pp. 6750–6761, 2016.

[23] M. Schilling and S. Luber, "Computational Modeling of Cobalt-Based Water Oxidation: Current Status and Future Challenges," *Frontiers in Chemistry*, vol. 6, p. 100, 2018.

[24] X. Li and P. E. M. Siegbahn, "Water Oxidation Mechanism for Synthetic Co–Oxides with Small Nuclearity," *Journal of the American Chemical Society*, vol. 135, no. 37, pp. 13804–13813, 2013.

[25] N. S. McCool, D. M. Robinson, J. E. Sheats, and G. C. Dismukes, "A Co_4O_4 'Cubane' Water Oxidation Catalyst Inspired by Photosynthesis," *Journal of the American Chemical Society*, vol. 133, no. 30, pp. 11446–11449, 2011.

[26] L.-P. Wang and T. Van Voorhis, "Direct-Coupling O_2 Bond Forming a Pathway in Cobalt Oxide Water Oxidation Catalysts," *The Journal of Physical Chemistry Letters*, vol. 2, no. 17, pp. 2200–2204, 2011.

[27] A. Fernando and C. M. Aikens, "Reaction Pathways for Water Oxidation to Molecular Oxygen Mediated by Model Cobalt Oxide Dimer and Cubane Catalysts," *The Journal of Physical Chemistry C*, vol. 119, no. 20, pp. 11072–11085, 2015.

[28] J. Soriano-López, D. G. Musaev, C. L. Hill, J. R. Galán-Mascarós, J. J. Carbó, and J. M. Poblet, "Tetracobalt-polyoxometalate catalysts for water oxidation: Key mechanistic details," *Journal of Catalysis*, vol. 350, pp. 56–63, 2017.

[29] R.-Z. Liao, M. D. Kärkäs, B.-L. Lee, B. Åkermark, and P. E. M. Siegbahn, "Photosystem II Like Water Oxidation Mechanism in a Bioinspired Tetranuclear Manganese Complex," *Inorganic Chemistry*, vol. 54, no. 1, pp. 342–351, 2015.

[30] G. C. Dismukes, R. Brimblecombe, G. A. N. Felton, R. S. Pryadun, J. E. Sheats, L. Spiccia, and G. F. Swiegers, "Development of Bioinspired Mn4O4-Cubane Water Oxidation Catalysts: Lessons from Photosynthesis," *Accounts of Chemical Research*, vol. 42, no. 12, pp. 1935–1943, 2009.

[31] S. Mukherjee, J. A. Stull, J. Yano, T. C. Stamatatos, K. Pringouri, T. A. Stich, K. A. Abboud, R. D. Britt, V. K. Yachandra, and G. Christou, "Synthetic model of the asymmetric [Mn_3CaO_4] cubane core of the oxygen-evolving complex of photosystem II," *Proceedings of the National Academy of Sciences*, vol. 109, no. 7, pp. 2257–2262, 2012.

[32] J. S. Kanady, P.-H. Lin, K. M. Carsch, R. J. Nielsen, M. K. Takase, W. A. Goddard, and T. Agapie, "Toward Models for the Full Oxygen-Evolving Complex of Photosystem II by Ligand Coordination To Lower the Symmetry of the Mn_3CaO_4 Cubane: Demonstration That Electronic Effects Facilitate Binding of a Fifth Metal," *Journal of the American Chemical Society*, vol. 136, no. 41, pp. 14373–14376, 2014.

[33] C. Zhang, C. Chen, H. Dong, J.-R. Shen, H. Dau, and J. Zhao, "A synthetic Mn_4Ca-cluster mimicking the oxygen-evolving center of photosynthesis," *Science*, vol. 348, no. 6235, pp. 690–693, 2015.

[34] H. B. Lee and T. Agapie, "Redox Tuning via Ligand-Induced Geometric Distortions at a YMn_3O_4 Cubane Model of the Biological Oxygen Evolving Complex," *Inorganic Chemistry*, vol. 58, no. 22, pp. 14998–15003, 2019.

[35] P.-E. Car, M. Guttentag, K. K. Baldridge, R. Alberto, and G. R. Patzke, "Synthesis and characterization of open and sandwich-type polyoxometalates reveals visible-light-driven water oxidation via POM-photosensitizer complexes," *Green Chemistry*, vol. 14, no. 6, pp. 1680–1688, 2012.

[36] A. Sartorel, P. Miró, E. Salvadori, S. Romain, M. Carraro, G. Scorrano, M. D. Valentin, A. Llobet, C. Bo, and M. Bonchio, "Water Oxidation at a Tetraruthenate Core Stabilized by Polyoxometalate Ligands: Experimental and Computational Evidence To Trace the Competent Intermediates," *Journal of the American Chemical Society*, vol. 131, no. 44, pp. 16051–16053, 2009.

[37] K. Nishiki, N. Umehara, Y. Kadota, X. López, J. M. Poblet, C. A. Mezui, A.-L. Teillout, I. M. Mbomekalle, P. d. Oliveira, M. Miyamoto, T. Sano, and M. Sadakane, "Preparation of α1- and α2-isomers of mono-Ru-substituted Dawson-type phosphotungstates with an aqua ligand and comparison of their redox potentials, catalytic activities, and thermal stabilities with Keggin-type derivatives," *Dalton Transactions*, vol. 45, no. 9, pp. 3715–3726, 2016.

[38] Z.-L. Lang, G.-C. Yang, N.-N. Ma, S.-Z. Wen, L.-K. Yan, W. Guan, and Z.-M. Su, "DFT characterization on the mechanism of water splitting catalyzed by single-Ru-substituted polyoxometalates," *Dalton Transactions*, vol. 42, no. 29, pp. 10617–10625, 2013.

[39] A. E. Kuznetsov, Y. V. Geletii, C. L. Hill, K. Morokuma, and D. G. Musaev, "Dioxygen and Water Activation Processes on Multi-Ru-Substituted Polyoxometalates: Comparison with the 'Blue-Dimer' Water Oxidation Catalyst," *Journal of the American Chemical Society*, vol. 131, no. 19, pp. 6844–6854, 2009.

[40] D. Quiñonero, A. L. Kaledin, A. E. Kuznetsov, Y. V. Geletii, C. Besson, C. L. Hill, and D. G. Musaev, "Computational Studies of the Geometry and Electronic Structure of an All-Inorganic and Homogeneous Tetra-Ru-Polyoxotungstate Catalyst for Water Oxidation and Its Four Subsequent One-Electron Oxidized Forms," *The Journal of Physical Chemistry A*, vol. 114, no. 1, pp. 535–542, 2010.

[41] S. Piccinin and S. Fabris, "A first principles study of water oxidation catalyzed by a tetraruthenium-oxo core embedded in polyoxometalate ligands," *Physical Chemistry Chemical Physics*, vol. 13, no. 17, pp. 7666–7674, 2011.

[42] S. Piccinin, A. Sartorel, G. Aquilanti, A. Goldoni, M. Bonchio, and S. Fabris, "Water oxidation surface mechanisms replicated by a totally inorganic tetraruthenium–oxo molecular complex," *Proceedings of the National Academy of Sciences*, vol. 110, no. 13, pp. 4917–4922, 2013. Publisher: National Academy of Sciences Section: Physical Sciences.

[43] S. Piccinin and S. Fabris, "Water Oxidation by Ru-Polyoxometalate Catalysts: Overpotential Dependency on the Number and Charge of the Metal Centers," *Inorganics*, vol. 3, no. 3, pp. 374–387, 2015. Number: 3 Publisher: Multidisciplinary Digital Publishing Institute.

[44] X.-F. Su, W. Guan, L.-K. Yan, Z.-L. Lang, and Z.-M. Su, "Evidence of two-state reactivity in water oxidation catalyzed by polyoxometalate-based complex $[Mn_3(H_2O)_3(SbW_9O_{33})_2]^{12-}$," *Journal of Catalysis*, vol. 376, pp. 146–149, 2019.

[45] X.-F. Su, L.-K. Yan, and Z.-M. Su, "Theoretical Insight into the Performance of $Mn^{II/III}$-Monosubstituted Heteropolytungstates as Water Oxidation Catalysts," *Inorganic Chemistry*, vol. 58, no. 23, pp. 15751–15757, 2019.

[46] T. A. Betley, Q. Wu, T. Van Voorhis, and D. G. Nocera, "Electronic Design Criteria for O-O Bond Formation via Metal-Oxo Complexes," *Inorganic Chemistry*, vol. 47, no. 6, pp. 1849–1861, 2008.

[47] J. K. Nørskov, J. Rossmeisl, A. Logadottir, L. Lindqvist, J. R. Kitchin, T. Bligaard, and H. Jónsson, "Origin of the Overpotential for Oxygen Reduction at a Fuel-Cell Cathode," *The Journal of Physical Chemistry B*, vol. 108, no. 46, pp. 17886–17892, 2004.

[48] I. C. Man, H.-Y. Su, F. Calle-Vallejo, H. A. Hansen, J. I. Martínez, N. G. Inoglu, J. Kitchin, T. F. Jaramillo, J. K. Nørskov, and J. Rossmeisl, "Universality in Oxygen Evolution Electrocatalysis on Oxide Surfaces," *ChemCatChem*, vol. 3, no. 7, pp. 1159–1165, 2011.

[49] M. Blasco-Ahicart, J. Soriano-López, J. J. Carbó, J. M. Poblet, and J. R. Galan-Mascaros, "Polyoxometalate electrocatalysts based on earth-abundant metals for efficient water oxidation in acidic media," *Nature Chemistry*, vol. 10, no. 1, pp. 24–30, 2018.

[50] L. Schwiedrzik, T. Rajkovic, and L. González, "Regeneration and Degradation in a Biomimetic Polyoxometalate Water Oxidation Catalyst," *ACS Catalysis*, vol. 13, no. 5, pp. 3007–3019, 2023.

[51] B. Schwarz, J. Forster, M. K. Goetz, D. Yücel, C. Berger, T. Jacob, and C. Streb, "Visible-Light-Driven Water Oxidation by a Molecular Manganese Vanadium Oxide Cluster," *Angewandte Chemie International Edition*, vol. 55, no. 21, pp. 6329–6333, 2016.

[52] F. L. Huber, S. Amthor, B. Schwarz, B. Mizaikoff, C. Streb, and S. Rau, "Multi-phase real-time monitoring of oxygen evolution enables in operando water oxidation catalysis studies," *Sustainable Energy & Fuels*, vol. 2, no. 9, pp. 1974–1978, 2018.

[53] S. Mai, S. Klingler, I. Trentin, J. Kund, M. Holzer, A. Andreeva, R. Stach, C. Kranz, C. Streb, B. Mizaikoff, and L. González, "Spectral Signatures of Oxidation States in a Manganese-Oxo Cubane Water Oxidation Catalyst," *Chemistry – A European Journal*, vol. 27, p. 17078, 2021.

[54] G. Cárdenas, I. Trentin, L. Schwiedrzik, D. Hernández-Castillo, G. A. Lowe, J. Kund, C. Kranz, S. Klingler, R. Stach, B. Mizaikoff, P. Marquetand, J. J. Nogueira, C. Streb, and L. González, "Activation by oxidation and ligand exchange in a molecular manganese vanadium oxide water oxidation catalyst," *Chemical Science*, vol. 12, no. 39, pp. 12918–12927, 2021.

[55] L. Schwiedrzik, V. Brieskorn, and L. González, "Flexibility Enhances Reactivity: Redox Isomerism and Jahn–Teller Effects in a Bioinspired Mn_4O_4 Cubane Water Oxidation Catalyst," *ACS Catalysis*, vol. 11, no. 21, pp. 13320–13329, 2021.

[56] J. S. Kanady, E. Y. Tsui, M. W. Day, and T. Agapie, "A Synthetic Model of the Mn_3Ca Subsite of the Oxygen-Evolving Complex in Photosystem II," *Science*, vol. 333, no. 6043, pp. 733–736, 2011.

[57] P. Gatt, S. Petrie, R. Stranger, and R. J. Pace, "Rationalizing the 1.9 Å Crystal Structure of Photosystem II—A Remarkable Jahn–Teller Balancing Act Induced by a Single Proton Transfer," *Angewandte Chemie International Edition*, vol. 51, no. 48, pp. 12025–12028, 2012.

[58] V. Krewald, F. Neese, and D. A. Pantazis, "On the Magnetic and Spectroscopic Properties of High-Valent Mn_3CaO_4 Cubanes as Structural Units of Natural and Artificial Water-Oxidizing Catalysts," *Journal of the American Chemical Society*, vol. 135, no. 15, pp. 5726–5739, 2013.

[59] E. Y. Tsui and T. Agapie, "Reduction potentials of heterometallic manganese–oxido cubane complexes modulated by redox-inactive metals," *Proceedings of the National Academy of Sciences*, vol. 110, no. 25, pp. 10084–10088, 2013.

[60] K. Yamaguchi, S. Yamanaka, H. Isobe, T. Saito, K. Kanda, Y. Umena, K. Kawakami, J.-R. Shen, N. Kamiya, M. Okumura, H. Nakamura, M. Shoji, and Y. Yoshioka, "The nature of chemical bonds of the $CaMn_4O_5$ cluster in oxygen evolving complex of photosystem II: Jahn-Teller distortion and its suppression by Ca doping in cubane structures," *International Journal of Quantum Chemistry*, vol. 113, no. 4, pp. 453–473, 2013.

[61] C. Lee and C. M. Aikens, "Water Splitting Processes on Mn_4O_4 and $CaMn_3O_4$ Model Cubane Systems," *The Journal of Physical Chemistry A*, vol. 119, no. 35, pp. 9325–9337, 2015.

[62] A. Fernando and C. M. Aikens, "Theoretical Investigation of Water Oxidation Catalysis by a Model Manganese Cubane Complex," *The Journal of Physical Chemistry C*, vol. 120, no. 38, pp. 21148–21161, 2016.

[63] K. Yamaguchi, M. Shoji, H. Isobe, S. Yamanaka, Y. Umena, K. Kawakami, and N. Kamiya, "On the guiding principles for understanding of geometrical structures of the $CaMn_4O_5$ cluster in oxygen-evolving complex of photosystem II. Proposal of estimation formula of structural deformations via the Jahn–Teller effects," *Molecular Physics*, vol. 115, no. 5, pp. 636–666, 2017.

[64] V. Krewald, M. Retegan, N. Cox, J. Messinger, W. Lubitz, S. DeBeer, F. Neese, and D. A. Pantazis, "Metal oxidation states in biological water splitting," *Chemical Science*, vol. 6, no. 3, pp. 1676–1695, 2015.

[65] D. M. Robinson, Y. B. Go, M. Mui, G. Gardner, Z. Zhang, D. Mastrogiovanni, E. Garfunkel, J. Li, M. Greenblatt, and G. C. Dismukes, "Photochemical Water Oxidation by Crystalline Polymorphs of Manganese Oxides: Structural Requirements for Catalysis," *Journal of the American Chemical Society*, vol. 135, no. 9, pp. 3494–3501, 2013.

[66] U. Maitra, B. S. Naidu, A. Govindaraj, and C. N. R. Rao, "Importance of trivalency and the e_g^1 configuration in the photocatalytic oxidation of water by Mn and Co oxides," *Proceedings of the National Academy of Sciences*, vol. 110, no. 29, pp. 11704–11707, 2013.

[67] A. Indra, P. W. Menezes, and M. Driess, "Uncovering Structure–Activity Relationships in Manganese-Oxide-Based Heterogeneous Catalysts for Efficient Water Oxidation," *ChemSusChem*, vol. 8, no. 5, pp. 776–785, 2015.

[68] M. Drosou, G. Zahariou, and D. A. Pantazis, "Orientational Jahn–Teller Isomerism in the Dark-Stable State of Nature's Water Oxidase," *Angewandte Chemie International Edition*, vol. 60, no. 24, pp. 13493–13499, 2021.

[69] S. Mai, M. Holzer, A. Andreeva, and L. González, "Jahn-Teller Effects in a Vanadate-Stabilized Manganese-Oxo Cubane Water Oxidation Catalyst," *Chemistry – A European Journal*, vol. 27, no. 68, pp. 17066–17077, 2021.

[70] L.-P. Wang, Q. Wu, and T. Van Voorhis, "Acid-Base Mechanism for Ruthenium Water Oxidation Catalysts," *Inorganic Chemistry*, vol. 49, no. 10, pp. 4543–4553, 2010.

[71] D. W. Shaffer, Y. Xie, and J. J. Concepcion, "O–O bond formation in ruthenium-catalyzed water oxidation: single-site nucleophilic attack vs. O–O radical coupling," *Chemical Society Reviews*, vol. 46, no. 20, pp. 6170–6193, 2017.

[72] A. D. Becke, "Density-functional thermochemistry. III. The role of exact exchange," *The Journal of Chemical Physics*, vol. 98, no. 7, pp. 5648–5652, 1993.

[73] C. Lee, W. Yang, and R. G. Parr, "Development of the Colle-Salvetti correlation-energy formula into a functional of the electron density," *Physical Review B*, vol. 37, no. 2, pp. 785–789, 1988.

[74] V. Krewald and D. A. Pantazis, "Understanding and tuning the properties of redox-accumulating manganese helicates," *Dalton Transactions*, vol. 45, no. 47, pp. 18900–18908, 2016.

[75] F. Weigend and R. Ahlrichs, "Balanced basis sets of split valence, triple zeta valence and quadruple zeta valence quality for H to Rn: Design and assessment of accuracy," *Physical Chemistry Chemical Physics*, vol. 7, no. 18, pp. 3297–3305, 2005.

[76] V. Barone and M. Cossi, "Quantum Calculation of Molecular Energies and Energy Gradients in Solution by a Conductor Solvent Model," *The Journal of Physical Chemistry A*, vol. 102, no. 11, pp. 1995–2001, 1998.

[77] E. Rossini and E.-W. Knapp, "Proton solvation in protic and aprotic solvents," *Journal of Computational Chemistry*, vol. 37, no. 12, pp. 1082–1091, 2016.

[78] L.-P. Wang, A. Titov, R. McGibbon, F. Liu, V. S. Pande, and T. J. Martínez, "Discovering chemistry with an ab initio nanoreactor," *Nature Chemistry*, vol. 6, no. 12, pp. 1044–1048, 2014.

[79] L.-P. Wang, R. T. McGibbon, V. S. Pande, and T. J. Martinez, "Automated discovery and refinement of reactive molecular dynamics pathways," *Journal of Chemical Theory and Computation*, vol. 12, no. 2, pp. 638–649, 2016.

[80] I. S. Ufimtsev and T. J. Martínez, "Quantum chemistry on graphical processing units. 1. strategies for two-electron integral evaluation," *Journal of Chemical Theory and Computation*, vol. 4, no. 2, pp. 222–231, 2008.

[81] I. S. Ufimtsev and T. J. Martinez, "Quantum chemistry on graphical processing units. 2. direct self-consistent-field implementation," *Journal of Chemical Theory and Computation*, vol. 5, no. 4, pp. 1004–1015, 2009.

[82] I. S. Ufimtsev and T. J. Martinez, "Quantum Chemistry on Graphical Processing Units. 3. Analytical Energy Gradients, Geometry Optimization, and First Principles Molecular Dynamics," *Journal of Chemical Theory and Computation*, vol. 5, no. 10, pp. 2619–2628, 2009.

[83] S. Seritan, C. Bannwarth, B. S. Fales, E. G. Hohenstein, C. M. Isborn, S. I. L. Kokkila-Schumacher, X. Li, F. Liu, N. Luehr, J. W. Snyder Jr., C. Song, A. V. Titov, I. S. Ufimtsev, L.-P. Wang, and T. J. Martínez, "Terachem: A graphical processing unit-accelerated electronic structure package for large-scale ab initio molecular dynamics," *WIREs Computational Molecular Science*, vol. 11, no. 2, p. e1494, 2021.

[84] M. D. Wodrich, A. Fabrizio, B. Meyer, and C. Corminboeuf, "Data-powered augmented volcano plots for homogeneous catalysis," *Chemical Science*, vol. 11, no. 44, pp. 12070–12080, 2020.

[85] J. P. Janet, C. Duan, A. Nandy, F. Liu, and H. J. Kulik, "Navigating Transition-Metal Chemical Space: Artificial Intelligence for First-Principles Design," *Accounts of Chemical Research*, vol. 54, no. 3, pp. 532–545, 2021.

[86] D. R. Harper and H. J. Kulik, "Computational Scaling Relationships Predict Experimental Activity and Rate-Limiting Behavior in Homogeneous Water Oxidation," *Inorganic Chemistry*, vol. 61, no. 4, pp. 2186–2197, 2022.